MULTI-BODY TRAJECTORY DESIGN STRATEGIES

BASED ON PERIAPSIS POINCARÉ MAPS

A Dissertation

Submitted to the Faculty

of

Purdue University

by

Diane Elizabeth Craig Davis

In Partial Fulfillment of the

Requirements for the Degree

of

Doctor of Philosophy

August 2011

Purdue University

West Lafayette, Indiana

To my husband and children

ACKNOWLEDGMENTS

I would like to thank my advisor, Professor Kathleen Howell, for her support and guidance. She has been an invaluable source of knowledge and ideas throughout my studies at Purdue, and I have truly enjoyed our collaborations. She is an inspiration to me.

I appreciate the insight and support from my committee members, Professor James Longuski, Professor Martin Corless, and Professor Daniel DeLaurentis.

I would like to thank the members of my research group, past and present, for their friendship and collaboration, including Geoff Wawrzyniak, Chris Patterson, Lindsay Millard, Dan Grebow, Marty Ozimek, Lucia Irrgang, Masaki Kakoi, Raoul Rausch, Matt Vavrina, Todd Brown, Amanda Haapala, Cody Short, Mar Vaquero, Tom Pavlak, Wayne Schlei, Aurelie Heritier, Amanda Knutson, and Jeff Stuart.

I thank my parents, David and Jeanne Craig, for their encouragement and love throughout my academic career. They have cheered me on through many years of studies.

I am grateful for the love and encouragement of my husband, Jonathan. His never-ending patience and friendship have been a constant source of support.

Finally, I owe thanks to the organizations that have provided the funding opportunities that have supported me through my studies, including the Clare Booth Luce Foundation, Zonta International, and Purdue University and the School of Aeronautics and Astronautics through the Graduate Assistance in Areas of National Need and the Purdue Forever Fellowships.

TABLE OF CONTENTS

Page

Page

Page

LIST OF TABLES

LIST OF FIGURES

Figure Page

Figure Page

Figure Page

Figure Page

Figure Page

Figure Page

Figure Page

Figure Page

Figure Page

ABSTRACT

Davis, Diane Elizabeth Craig Ph.D., Purdue University, August 2011. Multi-Body Trajectory Design Strategies Based on Periapsis Poincaré Maps. Major Professor: Kathleen C. Howell.

Incorporating multi-body dynamics into preliminary spacecraft trajectory design expands the design space and provides trajectory options that may not otherwise be available. However, multi-body environments are not as well understood as those involving a single gravitational body, and preliminary design in these complicated scenarios is challenging. The current investigation focuses on preliminary design of orbits in the vicinity of the second primary in a 3- or 4-body model, for example, trajectories near a planet in a Sun-planet-moon system.

The tidal acceleration due to the distant larger primary (P_1) has significant influence on large orbits about the second primary (P_2). The effects on individual orbits are explored before the investigation is expanded to include large groups of orbits. Periapsis Poincaré maps are employed to simplify and organize the design space. By parameterizing trajectories in terms of periapse radius and orientation relative to the P_1-P_2 line, the short- and long-term behaviors of many trajectories are predictable based on initial conditions. Trajectories that impact P_2 or escape its vicinity are easily identified. Initial conditions that lead to long-term orbits with particular characteristics, for example, periodic or quasi-periodic orbits, as well as quasi-frozen orbits, are selected from the maps. The existence of various types of trajectories at different spacecraft energy levels and in different P_1-P_2 systems is explored. The expanded knowledge of the design space in the vicinity of P_2 is then applied to various mission design objectives. By employing periapsis Poincaré maps, mission objectives are satisfied in a simple, methodical process.

In the same way, an examination of flybys from a multi-body perspective is insightful. Before adding the influence of a gravity assist body to the larger problem, the flyby itself is explored within the context of the 3-body problem. Then, the flyby design is combined with a tidally-influenced orbit to produce a trajectory that takes full advantage of its multi-body environment.

1. INTRODUCTION

Increasingly complex spacecraft mission scenarios demand innovative trajectory design concepts and the development of computational tools that incorporate the dynamical structure of the design space. In support of wide-ranging exploration goals, any one vehicle may fly through various types of dynamical regimes during a single mission. Exploiting the dynamical structure in different force environments may offer advantages in trajectory design. In regimes where multiple bodies impact the spacecraft behavior to a similar degree, the gravity fields must be simultaneously considered even for preliminary design. However, multi-body environments are not as well understood as those involving a single gravitational body, and preliminary design in these complicated scenarios is challenging.

A major barrier to the development of a simple orbit design process is the complexity of the design space. With the addition of only one gravitational body, an analytical solution to the orbit problem is no longer available, and for large orbits, the ordered world of conic sections becomes an apparently chaotic regime, where predicting the long-term behavior of a trajectory based on its initial state is not straightforward. Even in the Circular Restricted 3-Body Problem (CR3BP), orbit design remains challenging due to the chaotic and varied nature of trajectories that are simultaneously influenced by two gravitational bodies. To effectively select a trajectory to satisfy a given mission requirement, it is necessary to simplify and organize the design space. Concentrating on the region close to the smaller primary, this effort focuses on the development of strategies that facilitate preliminary trajectory design in the CR3BP. Rather than attempting to cancel out the multi-body gravitational perturbations, these schemes exploit the additional gravitational forces to facilitate the design of trajectories that may otherwise be infeasible.

1.1. Problem Definition

The goal of this research investigation is a methodical process for designing trajectories in a multi-body regime. The basic scenario involves a large orbit about a smaller primary, one that is

significantly affected by the tidal acceleration of a distant larger primary, for example, a Saturn-centered orbit perturbed by solar gravity. Next, an additional small primary — a flyby body — is added to the system. A close approach to the flyby body can significantly affect the trajectory. In this scenario, for example, a spacecraft in a Saturn-centered orbit encounters the moon Titan, which sends it into a large orbit perturbed by the Sun. Selection of the pre-flyby trajectory that leads to the desired ultimate outcome, after the tidal acceleration has influenced the orbit, is a typical design objective.

Before proceeding with a direct search for orbits that fulfill certain mission requirements, however, it is necessary to better understand the underlying dynamical structure in the problem. Once this foundation is in place, it serves as the framework for the development of orbit selection tools. In more detail, the research objectives are as follows:

(i) Examine natural trajectories near a relatively small gravitational body (P_2) influenced by a distant larger body (P_1). Large trajectories centered at P_2 exhibit behavior over time that is difficult to predict. Before designing trajectories in this space, a better understanding of the gravitational effects of P_1 on the orbit is required. After characterizing the effects of the tidal acceleration on the orbital elements of individual orbits, the study is expanded to investigate the behavior of larger sets of trajectories. Both long- and short-term propagations are examined. Despite the chaotic appearance of the design space, a dynamical structure emerges that allows the prediction of the trajectory evolution based on an initial state at periapsis.

(ii) Apply the understanding of the dynamical structure to the design of tidally influenced P_2-centered trajectories. With the design space better understood, it is now necessary to organize the information so that it can be used for trajectory design. Maps relating an initial periapse state to trajectory behavior over both short and long time spans are applied to the selection of trajectories that satisfy various mission requirements.

(iii) Add the influence of an additional smaller primary. First, flyby trajectories are examined in the CR3BP. This complicated problem is facilitated by the use of the kick function, an approximation to the CR3BP equations of motion that supplies a valuable initial guess in the design of flyby trajectories in the three-body model. Then, by patching together two CR3BP scenarios — a Sun-planet and a planet-moon problem — maps are developed to allow the selection of initial conditions to fulfill design objectives. By incorporating the influence of a distant larger primary together with the effects from close encounters with a smaller primary, a designer can create trajectories that truly exploit the multi-body environment.

1.2. Previous Work

1.2.1. Understanding the Tidally-Influenced Environment

The impact of the gravity of a distant larger primary in the design of spacecraft trajectories is familiar, of course, either as a perturbation or as a dominant force that shapes the path. Inclusion of such a gravitational force as a perturbation to a reference trajectory has a long history, and the study of its influence is extensive. A variety of methods can be employed for the analysis of lower-altitude orbits. The Lagrange Planetary Equations (LPEs) are commonly used to describe the effects of gravitational perturbations on the orbital elements. Examples include Broucke[1] and Prado[2,3], who employ the LPEs to estimate the luni-solar perturbations on an Earth orbiter. Scheeres, Guman, and Villac[4] as well as Paskowitz and Scheeres[5] analyze the stability of a Europa orbiter in a low, near-polar orbit, including the third-body effects of Jupiter as well as the J_2 and J_3 perturbations from Europa. The LPEs are most effective in estimating the effects of tidal acceleration when the orbit remains close to the second primary.

For somewhat larger orbits, another method of analysis is offered by Villac, Scheeres, D'Amario, and Guman.[6] They apply the first step of Picard's method of successive approximations[7] to the Hill 3-body Problem (H3BP) equations of motion, producing estimates of the changes in energy and angular momentum that are, in turn, used to calculate changes in semi-major axis, eccentricity, and inclination over one revolution of the spacecraft in its orbit. The authors note that the method is beneficial for the selection of initial conditions to be used in higher-fidelity models. Scheeres, Williams, and Miller[8] as well as Scheeres, Miller, and Yeomans[9] employ this technique in an investigation of the orbital dynamics near the asteroid 433 Eros.

In a regime where neither P_1 nor P_2 may be considered merely a perturbing body, the above approximations become less accurate. Numerous studies exploit the dynamics of the CR3BP or the H3BP to explore the long-term behavior of trajectories near the smaller primary in the restricted three-body problem. Hénon,[10-14] a pioneer in the study of multi-body orbits, investigates the existence and stability of periodic and non-periodic orbits about P_2 in the HR3BP. His work extends from the late 1960s through the mid 2000s. Benest[15] investigates the existence and stability of retrograde satellites in the CR3BP as the mass ratio increases in a paper from 1974. In research from the 1980s, Robin and Markellos[16] and Kazantizis[17] numerically determine families of three-dimensional periodic orbits near Jupiter in the Sun-Jupiter CR3BP. Advances in

computing power over time allow more comprehensive searches for periodic trajectories. More recently, Lam and Whiffen[18] explore the stability of distant retrograde orbits around Europa, proposing this type of trajectory as a safe end-of-life option for missions including the proposed Jupiter Icy Moons Orbiter. Russell[19] employs a thorough grid search to catalog numerous planar and 3-dimensional periodic trajectory families about Europa in the Jupiter-Europa CR3BP. Tsirogiannis, Perdios, and Markellos[20] expand on Russell's work, presenting an updated, adaptive grid search approach along with a classification method for the resulting periodic orbits. Lara and Russell[21] thoroughly investigate one particular family (the egg-shaped "g" family) of periodic orbits in the CR3BP for varying values of mass parameter. Lara, Russell, and Villac[22, 23] investigate the stability regions of both prograde and retrograde trajectories about Europa and examine the robustness of various orbits, evaluating them as candidate solutions for Europa orbiter design.

The evolution of a trajectory centered at the smaller primary is also investigated in the astronomy community. For example, Chauvineau and Mignard[24] employ Poincaré maps in the Hill problem to investigate the existence of periodic, quasi-periodic, and chaotic but bounded trajectories about an asteroid in terms of Jacobi Constant. Their results are applied to a discussion of the existence of binary asteroids. Hamilton and Burns[25] investigate zones of stability for orbital debris about asteroids. The authors depict the components of acceleration due to solar gravitational perturbations as viewed in the rotating frame. In regions where these perturbations are significant, the existence of stable, unstable, and quasi-periodic orbits is discussed. They examine the stability of prograde versus retrograde trajectories, offering an explanation for the differences in terms of the direction of the Coriolis acceleration. The time histories of the orbital elements for sample orbits are also analyzed; however, their analysis is mainly limited to trajectories with an initial eccentricity of zero and an initial periapsis located on the Sun-asteroid line. Hamilton and Krivov[26] provide a further investigation of the stability of natural satellites in various orbits about asteroids. The authors formulate the Tisserand Constant in terms of P_2-centered coordinates and use the expression to analytically demonstrate that distant retrograde orbits about asteroids are more stable than equivalent prograde trajectories. The authors note that the elongation of trajectories, as viewed in a rotating frame, is along the *x*-axis in the prograde case and along the *y*-axis in the retrograde case. Several authors discuss the effects of solar gravity on the capture and stability of irregular satellites about the outer planets. Using long-term integrations, Carruba, Burns, Nicholson, and Gladman[27] detail the range of inclinations at which irregular satellites can exist. Sheppard[28] relates the findings of Hamilton

and Krivov[26] regarding the stability zones of prograde and retrograde orbits to the existence of natural planetary satellites. Astakhov, Burbanks, Wiggins, and Farrelly[29, 30] investigate the capture of the irregular satellites. They conclude that the bodies are initially captured into long-lived chaotic trajectories, and energy dissipation transitions these chaotic orbits into quasiperiodic trajectories that remain bounded. For lower energies, prograde capture is possible, while at higher energies irregular satellites are increasingly captured into retrograde orbits. However, since prograde trajectories tend to possess smaller periapse radii, they are more effectively swept away by regular moons in a planetary system. This phenomenon is particularly apparent in a comparison between the Jupiter system, which contains few prograde irregular satellites, and the Saturn system, which includes a larger number of prograde irregulars. The difference is due to the effects of the Galilean satellites: the orbit of Callisto, for example, encompasses a larger fraction of the Jupiter's Hill sphere than does Titan in the Saturn system.

1.2.2. Designing Trajectories in the Tidally-Influenced Environment

Previous investigations have employed tidal acceleration to gain insight into mission design. For example, Belbruno[31] develops the concept of ballistic lunar transfers, which enlist the Sun's gravity to pull a spacecraft from the vicinity of the Earth out to the vicinity of the Moon. This type of transfer, one that requires significantly less ΔV than a traditional Hohmann transfer, was employed by the Japanese spacecraft Hiten to reach the Moon in 1991, as described by Belbruno and Miller.[32] Yamakawa, Kawaguchi, Ishii, and Matsuo[33] present an approach to the design of such trajectories, investigating the tidal acceleration of P_1 on an orbiter at P_2. Defining a set of quadrants in a P_2-centered rotating frame, they depict the direction of the tidal acceleration and describe its effects on osculating C3 (total energy in a conic sense). The authors then apply their findings to the problem of designing an Earth-Moon transfer trajectory in the Sun-Earth-Moon problem. In a further study by Kawaguchi, Yamakawa, Uesugi, and Matsuo,[34] the methods are applied to the design of trajectories for the LUNAR-A mission to the Moon and the PLANET-B mission to Mars. The goal is to lower ΔV costs and, thus, increase the mass budget for the scientific payloads. The authors note that "trajectory design with ballistic capture is comparatively difficult owing to its high sensitivity to initial fluctuation," and they present an iterative corrections method to solve the transfer problem. The authors determine that a cost savings is generated for an Earth-Moon transfer on the order of 150 m/s compared to a Hohmann transfer, which corresponds to a savings of up to 10% of the spacecraft mass. Belbruno and

Carrico[35] use a numerical targeting algorithm available in the standard STK/Astrogator© software to compute ballistic lunar transfers.

In an attempt to better understand the dynamics involved in the three-body problem and to facilitate trajectory design, manifolds associated with periodic orbits in the CR3BP have been increasingly used to predict the long-term behavior of trajectories that originate near the smaller primary. Many examples of this type of analysis exist in the literature. Howell and Kakoi[36] compute free connections between Earth-Moon libration point orbits and Sun-Earth libration point orbits by connecting the manifolds of the two types of orbits. Koon, Lo, Marsden and Ross,[37] as well as Gómez, Koon, Lo, Marsden, Masdemont, and Ross[38, 39] connect stable and unstable manifolds in the various Jupiter-moon systems to produce a "Petit Grand Tour" of the moons, which includes flybys of Europa and Ganymede, that require low ΔV. Parker and Born[40] approach the ballistic lunar transfer problem in terms of manifolds in the Sun-Earth and Earth-Moon systems. Russell and Lam[41] select several large, unstable orbits about P_2, and using the associated stable manifolds, design transfer trajectories into each periodic orbit. Applying multi-body dynamics to the study of natural bodies, Howell, Marchand, and Lo[42] describe the behavior of comets Oterma and Helin-Roman-Crocket in terms of stable and unstable halo manifolds in the Sun-Jupiter system.

One major challenge involved in orbit design within the context of the CR3BP is the organization of the vast set of options that is available within the design space; it is challenging to locate the specific initial conditions that lead to a trajectory with particular characteristics. One method for visualizing the space is the use of Poincaré maps, which reduce the dimensionality of the problem. Commonly, maps are projected onto a physical plane. In the CR3BP, such a projection is often realized on the plane defined by $y = 0$, and the returns to the map are plotted for trajectories with a particular Jacobi Constant. Such maps are successfully employed in analyses such as Howell and Kakoi,[36] Koon et al.,[37] Gómez et al.,[38, 39] Howell et al.,[42] Chauvineau and Mignard,[24] and Astakhov et al.,[29, 30] all discussed above. A slightly different approach is to define the surface of section at the plane corresponding to periapsis. This type of map is denoted as a periapsis Poincaré map and is employed by Villac and Scheeres[43] to relate a trajectory escaping the vicinity of P_2 back to its previous periapsis in the planar Hill problem. The maps produce lobes corresponding to immediate escape; any trajectory at a given value of Jacobi Constant that achieves periapsis within the corresponding lobe is guaranteed to escape before reaching a subsequent periapsis. The authors apply this observation to the design of escape trajectories from a circular orbit about Europa and other planetary satellites. Paskowitz and

Scheeres[44] extend this analysis, using periapsis Poincaré maps to define lobes corresponding to the first four periapse passages after capture into orbit about P_2. For application to the Europa orbiter problem, they define "safe zones" where a spacecraft is predicted to neither escape nor impact the surface of the satellite for a specified period of time. Within these safe zones, particular trajectories are selected for transfers into long-term stable science orbits. The majority of their analysis is planar, though they do offer a preliminary analysis of the 3-dimensional capture lobes. Villac and Scheeres[45] also use periapsis Poincaré maps in the design of optimal plane change maneuvers, utilizing third-body forces to change the inclination of a trajectory with minimal ΔV. They carefully orient the orbit such that the tidal acceleration changes the inclination without affecting the periapse radius; the resulting trajectories represent a ΔV savings of 15% compared to a traditional parabolic transfer and 70% compared to a single-impulse plane change. The periapsis Poincaré maps represent a significant step forward in both the characterization of the design space near P_2 and in the design of trajectories in its vicinity.

1.2.3. Adding the Influence of an Additional Smaller Primary

The study of flybys has an extensive history and much success in practice. A summary of the dynamics associated with the patched conic gravity assist technique is available in Broucke,[46] who notes that in 1847, Leverrier already understood the basic principles behind the gravity assist as it is applied to Jupiter's effects on comets. Strange and Longuski[47] present a valuable technique for the design of flyby tours, the Tisserand plot. Using contours of constant V_∞ on a plot of period versus periapse radius, the Tisserand plot allows a mission designer to hop between resonant orbits about one or many flyby bodies using patched conic analysis. This principle is extended by Kloster, Petropoulos, and Longuski[48] to include information on the radiation environment in the Jupiter system, such that a Jupiter tour is designed while maintaining a safe level of radiation for the spacecraft. Campagnola and Russell[49] extend the Tisserand plot to include low energy contours of the Tisserand Constant, allowing analysis of trajectories in regions where $V_\infty^2 < 0$ in the patched conic model. The authors use the resulting Tisserand-Poincaré graph to identify a low energy transfer between Ganymede and Europa. Howell and Guzmán[50] incorporate flybys in an accurate multi-body model; while successful, its high level of accuracy and semi-analytical formulation is too complex for inclusion in an initial design process that seeks a quick and methodical strategy. An energy kick function is an alternative intermediate step between a patched-conic approximation and an integrated multi-body propagation. While

the effect of the flyby is modeled with the kick function as a discrete event occurring at the spacecraft's closest approach to the flyby body, the expression for the energy kick function is derived from the Jacobi Constant in the three-body problem rather than the analytical relationships in the conic solution. Various investigations of orbits in multi-body regimes, including comets and other solar system particles, as well as spacecraft, employ the kick function to lend insight to the problem. Malyshkin and Tremaine[51] represent the kick function as a continuous interpolation function determined from a numerically integrated set of trajectories and apply it to the problem of the orbital evolution of comet trajectories, considering the probabilities of cometary survival. Zhou, Sun, Zheng, and Valtonen[52] derive the kick function from an expansion of the equations of motion in the CR3BP and employ it to study the transfer of comets from the Oort cloud to the inner solar system due to the gravitational effects of Jupiter. Pan and Sari[53] integrate the torque exerted on a particle by the gravity of a perturbing body. Then, their resulting kick function is the basis for an investigation of the motion of particles originally in nearly circular orbits around a star that encounter a planet and are perturbed into highly eccentric orbits. Ross and Scheeres[54] generate the kick function using Picard's method of successive approximations and apply it to distant flybys of a perturbing moon; a spacecraft remains outside of the Hill sphere in the planet-moon system and the periapsis of the spacecraft orbit also remains beyond the moon's orbital radius. Gawlik, Marsden, Campagnola, and Moore[55] combine the flyby kick function with the Tisserand-Poincaré graph described by Campagnola and Russell[49] to design a resonant gravity assist tour in the Saturn-Titan system.

The patched three-body model has been used by many researchers to combine multiple circular restricted problems into a single design space. Examples include Gómez et al.[38, 39] and Campagnola and Russell,[49] who patch together several planet-moon systems to produce transfers between moons of the same planet, and Howell and Kakoi[36] followed by Parker and Born,[40] who patch the Earth-Moon CR3BP with the Sun-Earth CR3BP.

1.3. Scope of the Present Work

The focus of the current investigation is on the dynamics and design of trajectories in the vicinity of the second primary in a 3- or 4-body model. The effects of tidal acceleration on individual trajectory characteristics are considered before broadening the investigation through the use of Poincaré maps. With the introduction of periapsis Poincaré maps, the design space is thoroughly explored, and both the short- and long-term behavior of P_2-centered trajectories is

characterized. After developing a better understanding of the traits of both escaping trajectories as well as orbits that remain captured over long-term propagations, maps are generated that facilitate the selection of initial conditions that produce trajectories to satisfy a variety of mission design objectives. Extending the map-based strategy, an additional primary is added to the problem. With the inclusion of a flyby body, the investigation focuses on designing the final pre-flyby orbit to yield particular trajectory characteristics after a full post-flyby revolution strongly affected by tidal acceleration. The study is organized as follows:

- Chapter 2: The dynamical models used in the investigation are introduced. The CR3BP is derived, and the characteristics of the differential equations of motion are examined. The Poincaré map is presented, and the periapsis Poincaré map, which forms the backbone of the dynamical investigations in later chapters, is described. The Cassini mission, one of the original sources of inspiration for the study, is introduced.

- Chapter 3: The concept of tidal acceleration is introduced. The orientation of an orbit within a set of quadrants centered at the second primary, P_2, determines the effects of tidal acceleration on the orbital elements. The effects of the tidal perturbations on individual trajectories are investigated within this framework. The influence of the Coriolis acceleration on retrograde trajectories is briefly considered. Then, the tidal kick function is derived. This function provides an approximation for the changes in orbital elements due to tidal acceleration over one spacecraft revolution. The accuracy of the resulting estimates is investigated. The influence of tidal acceleration on various orbits over time is then explored, including a look at orbits that escape from the vicinity of the second primary as compared to orbits that remain in the vicinity indefinitely.

- Chapter 4: Given a framework that isolates the impact of tidal acceleration on individual orbits, the investigation is expanded. Periapsis Poincaré maps are employed to facilitate the examination of large groups of trajectories in the vicinity of the second primary. The short term behavior of orbits, over one or a handful of revolutions, is examined. Well-defined regions identify initial conditions that lead to escape and impact trajectories, as well as orbits that remain captured about P_2 for one or many revolutions. The evolution of these regions is observed as parameters change, for example, trajectory energy or the system mass parameter. The focus then shifts to trajectories that remain captured in the

P_2 vicinity for many revolutions. Long-term periapsis Poincaré maps are developed that reveal the existence of periodic and quasi-periodic orbits.

- Chapter 5: After developing a better understanding of the underlying dynamics of the problem, the investigation evolves to employ periapsis Poincaré maps for trajectory design. The point solutions resulting from a 2007 Cassini end-of-life study are summarized, including impact and escape trajectories as well as long-term orbit options. Long-term periapsis Poincaré maps are introduced that facilitate the identification of quasi-periodic orbits as well as other trajectories of interest. Both short- and long-term maps are then applied to the Cassini end-of-life problem, providing a methodical procedure for designing long-period Saturn impact trajectories and orbits that escape from Saturn either towards the inner or outer solar system. The maps deliver a process for the design of quasi-periodic orbits that remain beyond the orbit of the distant moon Phoebe for long-term propagations. Other applications are then investigated, including mission design for capture around the large moon Titan, as well as designing transfer trajectories from Earth orbit to the vicinity of the Moon.

- Chapter 6: The problem is expanded to include the influence of a flyby body. Initially, the tidal acceleration is neglected, and the flyby is investigated in terms of the P_2-flyby body CR3BP. An analytical approach for approximating the effects on the orbital elements due to the flyby is introduced. Predictions via the flyby kick function are compared to the results from CR3BP propagations. Then, the effectiveness of orbit changes due to inbound flybys at a particular altitude is compared to the results of equivalent outbound flybys as well as to patched-conic predictions. The effects of tidal acceleration on the post-flyby trajectory are then included in the simulations. Periapsis Poincaré maps are produced that relate the pre-flyby trajectory to the orbit following a full post-flyby revolution. Incorporating tidal acceleration into the problem of V_∞ leveraging is then investigated. Finally, periapsis Poincaré maps are used to target a second flyby at a significantly reduced value of V_∞ with no maneuver involved.

- Chapter 7: Concluding remarks are offered along with recommendations for future research.

2. BACKGROUND

A design strategy for trajectories under the influence of multiple gravity fields begins with the definition of a dynamical model. From the relative equations of motion as derived from the Law of Gravitation, the Circular Restricted Three-Body Problem (CR3BP) is defined. While the CR3BP equations of motion cannot be solved analytically, particular characteristics of the problem exist that help define the motion of a spacecraft, for example, a constant of the motion, equilibrium solutions, and periodic orbits. These and other properties of the CR3BP are investigated. Then the Poincaré map is introduced, including a specific formulation, the periapsis Poincaré map, which is particularly useful for the design of multi-body trajectories in the vicinity of the smaller primary. Finally, the Cassini mission, an inspiration for this investigation, is introduced along with the Saturnian system, as well as numerical integration models.

2.1. The Circular Restricted Three-Body Problem

The equations of motion for a vehicle moving under the influence of multiple gravity fields are formulated in terms of various coordinates and reference frames. Most familiar, perhaps, is the motion in an inertial reference frame where the position of the spacecraft relative to an inertially fixed point is expressed in terms of a set of inertial coordinates X, Y, and Z. Then, the equations of motion of a spacecraft relative to an inertially-fixed point, under the influence of N gravity fields, are written

$$\begin{aligned} X'' &= \frac{-GM_1X_1}{r_1^3} - \frac{GM_2X_2}{r_2^3} - \cdots - \frac{GM_NX_N}{r_N^3} \\ Y'' &= \frac{-GM_1Y_1}{r_1^3} - \frac{GM_2Y_2}{r_2^3} - \cdots - \frac{GM_NY_N}{r_N^3} \\ Z'' &= \frac{-GM_1Z_1}{r_1^3} - \frac{GM_2Z_2}{r_2^3} - \cdots - \frac{GM_NZ_N}{r_N^3} \end{aligned} \tag{2.1}$$

or, in vector form

$$\bar{R}'' = \frac{-GM_1\bar{R}_1}{r_1^3} - \frac{GM_2\bar{R}_2}{r_2^3} - \cdots - \frac{GM_N\bar{R}_N}{r_N^3} \tag{2.2}$$

where $\bar{R}_i$ is the position vector from gravitational body P_i to the spacecraft and R_i is the magnitude of the position vector. (Note that vectors are indicated with an overbar.) The double prime indicates the second derivative with respect to time, *t*. While a familiar analytical solution exists for the problem of two bodies, the presence of even a single additional body renders the equations of motion unsolvable in closed form.

For the problem of three bodies, a rotating reference frame along with certain assumptions supplies insight to the problem. Initially, let there be three bodies in the system: two large primaries and a spacecraft. The motion of the spacecraft is then described in terms of the CR3BP. In this model, the origin is set at the barycenter of the two large primaries, P_1 and P_2. The two large primaries are assumed to be orbiting their barycenter on circular paths, while the spacecraft is assumed to possess negligible mass. That is, while P_1 and P_2 gravitationally influence each other as well as the spacecraft, the spacecraft has no influence on P_1 or P_2, which exhibit circular conic motion. A set of rotating axes appears in Figure 2.1 and moves with the P_1-P_2 system. The *x*-axis is directed from P_1 to P_2, the *z*-axis is normal to the plane of motion of the two primaries and parallel to the primary orbital angular momentum, and the *y*-axis completes the right-handed system. The inertial and rotating frames are related through the angle *Nt*, which changes at a constant rate, *N*, where *N* is the mean motion of the two large primaries in their circular orbits.

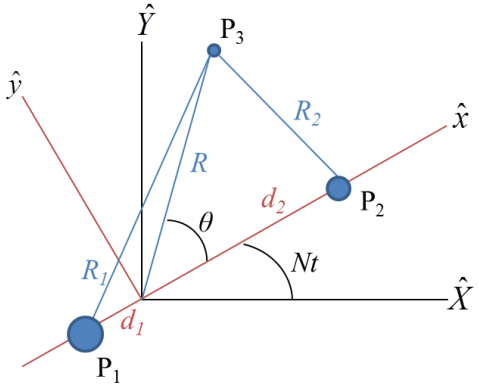

Figure 2.1 Inertial and rotating reference frames in the CR3BP.

2.1.1. Characteristic Quantities and Nondimensionalization

Before formulating the equations of motion in the CR3BP, several characteristic quantities are introduced to nondimensionalize the problem. The characteristic length is defined as the total distance between P_1 and P_2,

$$l^* = d_1 + d_2 \tag{2.3}$$

and the characteristic mass is the total mass of the two large primaries,

$$m^* = m_1 + m_2 . \tag{2.4}$$

The characteristic time is then defined as

$$t^* = \left[\frac{l^{*3}}{Gm^*} \right]^{1/2} \tag{2.5}$$

where G is the gravitational constant. These characteristic quantities are used to simplify the CR3BP computations. Nondimensional constants and variables are now defined. The mass parameter of the system,

$$\mu = \frac{m_2}{m^*} \tag{2.6}$$

is the mass of P_2 as well as the distance between the barycenter and P_1. The mass of P_1 is equal to $1-\mu$; this nondimensional quantity is also equal to the distance between the barycenter and P_2. The nondimensional distance between the two primaries is then simply equal to one. The nondimensional gravitational parameter,

$$G^* = \frac{Gm^* t^{*2}}{l^{*3}} \tag{2.7}$$

and the nondimensional mean motion of the two primaries,

$$n = t^* \left[\frac{Gm^*}{l^{*3}} \right]^{1/2} \tag{2.8}$$

are also equal to one. Nondimensional time, τ, is the dimensional time divided by the characteristic time t^*.

2.1.2. The CR3BP Equations of Motion

The nondimensional quantities are now used in the formulation of the CR3BP equations of motion. In rotating coordinates, the equations of motion in Eq. (2.2) are nondimensionalized to become

$$\ddot{\bar{r}} = \frac{-(1-\mu)\bar{r}_1}{r_1^3} - \frac{\mu \bar{r}_2}{r_2^3} \tag{2.9}$$

where the double dot signifies the second derivative with respect to nondimensional time, τ. To write this equation in terms of rotating components x, y, and z, it is noted that

$$\bar{r} = x\hat{x} + y\hat{y} + z\hat{z} \tag{2.10}$$

$$\bar{r}_1 = (x+\mu)\hat{x} + y\hat{y} + z\hat{z} \tag{2.11}$$

and

$$\bar{r}_2 = (x-(1-\mu))\hat{x} + y\hat{y} + z\hat{z}\,. \tag{2.12}$$

The first derivative of $\bar{r}$ with respect to nondimensional time is

$$\dot{\bar{r}} = \frac{{}^I d\bar{r}}{d\tau} = \frac{{}^R d\bar{r}}{d\tau} + {}^I\bar{\omega}^R \times \bar{r} \tag{2.13}$$

where the superscript I denotes the derivative as observed in the inertial frame and the superscript R refers to the derivative observed from the rotating frame. The angular velocity of the rotating frame with respect to the inertial frame is

$${}^I\bar{\omega}^R = n\hat{z} \tag{2.14}$$

given the nondimensional rate n and where nt is the angle between the rotating and inertial reference frames as in Figure 2.1. The first derivative of $\bar{r}$ then becomes

$$\dot{\bar{r}} = (\dot{x} - yn)\hat{x} + (\dot{y} + xn)\hat{y} + \dot{z}\hat{z}\,. \tag{2.15}$$

Differentiating with respect to nondimensional time once more,

$$\ddot{\bar{r}} = \frac{{}^R d\dot{\bar{r}}}{d\tau} + {}^I\bar{\omega}^R \times \dot{\bar{r}} = \frac{{}^R d^2\bar{r}}{d\tau^2} + 2\,{}^I\bar{\omega}^R \times \frac{{}^R d\bar{r}}{d\tau} + {}^I\bar{\omega}^R \times \left({}^I\bar{\omega}^R \times \bar{r}\right). \tag{2.16}$$

Then, in terms of rotating coordinates,

$$\ddot{\bar{r}} = \left(\ddot{x} - 2yn - xn^2\right)\hat{x} + \left(\ddot{y} + 2xn - yn^2\right)\hat{y} + \ddot{z}\hat{z} \tag{2.17}$$

where $\frac{d(nt)}{dt} = n$ is the constant nondimensional mean motion of the primaries. Then substituting Eq. (2.17) into Eq. (2.9), and recalling that $n = 1$,

$$\begin{aligned}
\ddot{x} - 2\dot{y} - x &= \frac{-(1-\mu)(x+\mu)}{r_1^3} - \frac{\mu\left(x-(1-\mu)\right)}{r_2^3} \\
\ddot{y} + 2\dot{x} - y &= \frac{-(1-\mu)y}{r_1^3} - \frac{\mu y}{r_2^3} \\
\ddot{z} &= \frac{-(1-\mu)z}{r_1^3} - \frac{\mu z}{r_2^3}.
\end{aligned} \tag{2.18}$$

Equation (2.18) represents the scalar nondimensional equations of motion in the CR3BP. These equations describe the motion of a spacecraft under the influence of two gravitational primaries in terms of rotating coordinates, relative to the barycenter of the two primaries.

By substituting Eq. (2.16) into Eq. (2.9), the components of the acceleration are investigated. The substitution yields

$$\frac{{}^R d^2\bar{r}}{d\tau^2} = \frac{\mu\bar{r}_2}{r_2^3} + \frac{(1-\mu)\bar{r}_1}{r_1^3} - {}^I\bar{\omega}^R \times \left({}^I\bar{\omega}^R \times \bar{r}\right) - 2\,{}^I\bar{\omega}^R \times \frac{{}^R d\bar{r}}{d\tau}. \tag{2.19}$$

Consider a spacecraft located near the smaller primary, P_2. On the right side, the first term (colored blue) is the direct acceleration due to the close, smaller primary, P_2. The last term (in green) is the Coriolis acceleration, originating from the rotation of the frame and the velocity of the spacecraft. The second term is the acceleration due to the distant larger primary, P_1, and the third term is the centripetal acceleration, caused by the rotation of the reference frame. Together, the second and third terms (colored red) are known as the tidal acceleration,[6]

$$a_{tidal} = \frac{(1-\mu)\bar{r}_1}{r_1^3} - n\hat{z} \times \left(n\hat{z} \times \bar{r}\right). \tag{2.20}$$

If the spacecraft is located sufficiently close to P_2, the tidal acceleration is modeled as a perturbation in some analyses. However, in other cases, for example when the orbit of the spacecraft ranges far from P_2, the tidal acceleration has a significant effect on the spacecraft

trajectory and can no longer accurately be treated simply as a perturbation. The effects of tidal acceleration are thoroughly investigated in the following chapters.

2.1.3. Frame Transformations

The equations of motion in Eq. (2.18) are written in terms of rotating coordinates, however, it is often necessary to express the position and velocity of the spacecraft in inertial coordinates. A transformation matrix between the frames is straightforward to derive. Defining the inertial and rotating states in terms of column vectors,

$$\begin{aligned} \bar{\mathbb{R}} &= \left[X, Y, Z, \dot{X}, \dot{Y}, \dot{Z} \right]^T \\ \bar{\rho} &= \left[x, y, z, \dot{x}, \dot{y}, \dot{z} \right]^T \end{aligned} \tag{2.21}$$

the transformation is written

$$\bar{\mathbb{R}} = C \ \ \bar{\rho} \tag{2.22}$$

where the matrix C is defined as

$$C = \begin{pmatrix} c_{11} & 0_{3x3} \\ c_{21} & c_{22} \end{pmatrix}. \tag{2.23}$$

Assume the inertial and rotating axes are aligned at time $\tau = \tau_0$. Then the submatrices of C are

$$c_{11} = c_{22} = \begin{pmatrix} \cos(\tau - \tau_0) & -\sin(\tau - \tau_0) & 0 \\ \sin(\tau - \tau_0) & \cos(\tau - \tau_0) & 0 \\ 0 & 0 & 1 \end{pmatrix} \tag{2.24}$$

and

$$c_{21} = \dot{c}_{11} = \begin{pmatrix} -\sin(\tau - \tau_0) & -\cos(\tau - \tau_0) & 0 \\ \cos(\tau - \tau_0) & -\sin(\tau - \tau_0) & 0 \\ 0 & 0 & 0 \end{pmatrix}. \tag{2.25}$$

The inverse of C then transforms the inertial state into rotating coordinates,

$$\bar{\rho} = C^{-1} \bar{\mathbb{R}}. \tag{2.26}$$

The rotation matrices allow the expression of the spacecraft state in both the rotating and inertial frames of reference.

2.1.4. The Jacobi and Tisserand Constants

The equations of motion in the CR3BP, represented by Eq. (2.18), incorporate a pair of important approximations. First, it is assumed that the mass of the spacecraft does not affect the orbits of the two primaries, which move on Keplerian arcs; this assumption results in the *Restricted* 3-Body Problem. Second, P_1 and P_2 are assumed to be in circular motion about their barycenter, reducing the problem to the *Circular* Restricted 3-Body Problem. Despite these simplifications, there remains no closed-form solution. However, one integral of the motion in the CR3BP does exist, i.e., the Jacobi Integral; it provides valuable insight into the motion of the spacecraft.

The Jacobi Integral is derived from the CR3BP equations of motion. First, define a pseudopotential U^* such that

$$U^* = \frac{(1-\mu)}{r_1} - \frac{\mu}{r_2} + \frac{1}{2}\left(x^2 + y^2\right) \tag{2.27}$$

Then, the equations of motion in Eq. (2.18) are rewritten in terms of U^* to yield

$$\begin{aligned} \ddot{x} - 2\dot{y} &= \frac{\partial U^*}{\partial x} \\ \ddot{y} + 2\dot{x} &= \frac{\partial U^*}{\partial y} \\ \ddot{z} &= \frac{\partial U^*}{\partial z}. \end{aligned} \tag{2.28}$$

Multiplying the three equations in Eq. (2.28) by $\dot{x}$, $\dot{y}$, and $\dot{z}$ respectively, and adding the results, yields

$$\dot{x}\ddot{x} + \dot{y}\ddot{y} + \dot{z}\ddot{z} = \frac{\partial U^*}{\partial x}\frac{\partial x}{\partial \tau} + \frac{\partial U^*}{\partial y}\frac{\partial y}{\partial \tau} + \frac{\partial U^*}{\partial z}\frac{\partial z}{\partial \tau}. \tag{2.29}$$

The term on the right side is a perfect differential since U^* is a function of x, y, and z only. Equation (2.29) is, thus, integrated to yield

$$\dot{x}^2 + \dot{y}^2 + \dot{z}^2 = 2U^* - J \tag{2.30}$$

where J is the Jacobi Constant. It can also be written

$$J = x^2 + y^2 + \frac{2(1-\mu)}{r_1} + \frac{2\mu}{r_2} - v^2 \tag{2.31}$$

where v is the magnitude of the spacecraft velocity relative to the rotating frame. The Jacobi Constant, or Jacobi Integral, is an energy-like quantity that remains constant along a spacecraft

trajectory, barring the inclusion of other forces (such as another gravitational body or a maneuver).

If the gravitational parameter μ is small, and if the distances r and r_2 are large, the Jacobi Constant is approximated well by the Tisserand Constant. Expressing J in terms of inertial coordinates,

$$J = 2\left(X\dot{Y} - Y\dot{X}\right) + 2\left(\frac{(1-\mu)}{r_1} + \frac{\mu}{r_2}\right) - \dot{X}^2 - \dot{Y}^2 - \dot{Z}^2 . \tag{2.32}$$

The vis viva equation states that

$$\dot{X}^2 + \dot{Y}^2 + \dot{Z}^2 = \frac{2}{r_1} - \frac{1}{a} \tag{2.33}$$

and the angular momentum per unit mass of the spacecraft orbit is defined as

$$\bar{h} = \bar{r} \times \dot{\bar{r}} . \tag{2.34}$$

If i is the inclination of the spacecraft orbit relative to the plane of motion of the primaries, the Z-component of the angular momentum vector is evaluated by

$$X\dot{Y} - Y\dot{X} = h\cos i . \tag{2.35}$$

Since the angular momentum can also be expressed as

$$h^2 = a\left(1-e^2\right) \tag{2.36}$$

where a is the semi-major axis and e is the eccentricity of the spacecraft about P_1, then

$$X\dot{Y} - Y\dot{X} = \sqrt{a\left(1-e^2\right)}\cos i . \tag{2.37}$$

Assuming that $r_1 \approx r$, the Jacobi Constant is approximated as

$$J \approx -2\mu\left(\frac{1}{r} - \frac{1}{r_2}\right) + 2\sqrt{a\left(1-e^2\right)}\cos i + \frac{1}{a} . \tag{2.38}$$

To complete the derivation of the Tisserand Constant, assume that μ, r, and r_2 are small. Then the Tisserand Constant is

$$TC = 2\sqrt{a\left(1-e^2\right)}\cos i + \frac{1}{a} . \tag{2.39}$$

The Jacobi and Tisserand Constants provide insight into the characteristics of a given spacecraft trajectory.

2.1.5. Equilibrium Solutions

While the equations of motion in the CR3BP cannot be solved analytically, they do possess various particular solutions. For example, five equilibrium solutions exist in the CR3BP, frequently labeled as the libration points. These consist of the three collinear points (L_1, L_2, and L_3) and two equilateral points (L_4 and L_5). At each of these points, the velocity and acceleration of the spacecraft relative to the rotating frame are equal to zero; the combined gravitational acceleration of P_1 and P_2 offset the centripetal acceleration due to the rotation of the frame. To solve for the equilibrium states, the partials of the pseudopotential are set equal to zero,

$$\frac{\partial U^*}{\partial x} = \frac{\partial U^*}{\partial y} = \frac{\partial U^*}{\partial z} = 0 \tag{2.40}$$

to yield

$$\begin{aligned}
&x - \frac{(1-\mu)(x+\mu)}{\left[(x+\mu)^2 + y^2 + z^2\right]^{3/2}} - \frac{\mu\left(x-(1-\mu)\right)}{\left[\left(x-(1-\mu)\right)^2 + y^2 + z^2\right]^{3/2}} = 0 \\
&y - \frac{(1-\mu)y}{\left[(x+\mu)^2 + y^2 + z^2\right]^{3/2}} - \frac{\mu y}{\left[\left(x-(1-\mu)\right)^2 + y^2 + z^2\right]^{3/2}} = 0 \\
&\frac{(1-\mu)z}{\left[(x+\mu)^2 + y^2 + z^2\right]^{3/2}} - \frac{\mu z}{\left[\left(x-(1-\mu)\right)^2 + y^2 + z^2\right]^{3/2}} = 0.
\end{aligned} \tag{2.41}$$

From inspection of the z equation in Eq. (2.41), it is clear that to achieve equilibrium, $z = 0$, and consequently, all of the equilibrium solutions lie in the P_1-P_2 orbital plane. A closer inspection of the y equation in Eq. (2.41) yields

$$y\left[1 - \frac{(1-\mu)}{\left[(x+\mu)^2 + y^2\right]^{3/2}} - \frac{\mu}{\left[\left(x-(1-\mu)\right)^2 + y^2\right]^{3/2}}\right] = 0. \tag{2.42}$$

Clearly, $y = 0$ is a solution of Eq. (2.42). If indeed $y = 0$, the x equation from Eq. (2.41) becomes a set of three quintic equations that are numerically solved for the three equilibrium points on the x-axis, i.e., the collinear points. The two equilateral points possess a nonzero y-component; Eq. (2.42) is analytically solvable for the equilateral points by setting

$$\frac{(1-\mu)}{\left[(x+\mu)^2+y^2\right]^{3/2}}+\frac{\mu}{\left[(x-(1-\mu))^2+y^2\right]^{3/2}}=1. \tag{2.43}$$

Next, assuming that

$$(x+\mu)^2+y^2=(x-(1-\mu))^2+y^2=1 \tag{2.44}$$

then Eq. (2.43) yields

$$L_{4,5}=\left(\frac{1}{2}-\mu,\frac{\pm\sqrt{3}}{2}\right). \tag{2.45}$$

The locations of the five libration points appear in a schematic in Figure 2.2. In the CR3BP, the distances between the second primary, P_2, and the two libration points L_1 and L_2 are defined as x_{L1} and x_{L2}. These values are not equal; however, they are similar.

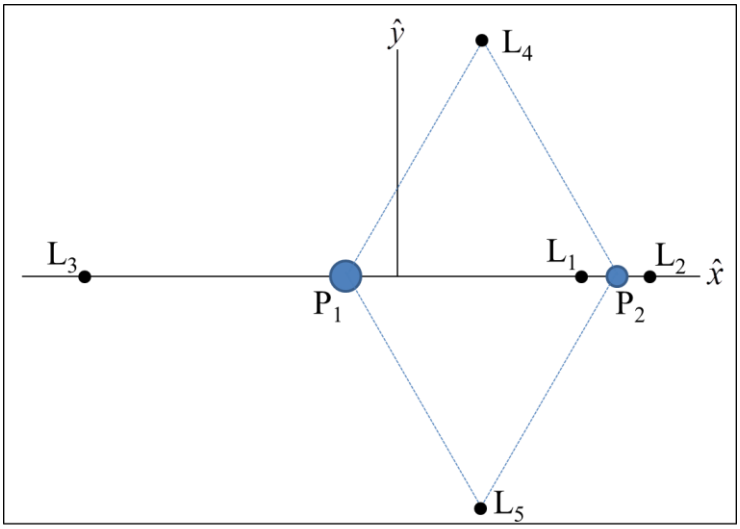

Figure 2.2 The five libration points in the CR3BP.

2.1.6. Hill's Restricted 3-Body Problem

In the limit $\mu\rightarrow 0$, and assuming that the spacecraft remains close to P_2, the CR3BP equations of motion can be approximated by the P_2-centered equations of motion from the Hill Restricted 3-Body Problem (HR3BP). From the CR3BP equations of motion in Eq. (2.18), assume $\mu << 1$ so that

$$\begin{aligned} 1-\mu &\approx 1 \\ x+\mu &\approx x \end{aligned} \tag{2.46}$$

and translate to a P_2-centered set of axes

$$\begin{aligned} x &\to x+1 \\ r_2 &\to r \\ r_1^2 &\approx 1+2x. \end{aligned} \tag{2.47}$$

Equation (2.18) then becomes

$$\begin{aligned} \ddot{x}-2\dot{y} &= (x+1)-\frac{(x+1)}{(1+2x)^{3/2}}-\frac{\mu x}{r^3} \\ \ddot{y}+2\dot{x} &= y-\frac{y}{(1+2x)^{3/2}}-\frac{\mu y}{r^3} \\ \ddot{z} &= \frac{-z}{(1+2x)^{3/2}}-\frac{\mu z}{r^3}. \end{aligned} \tag{2.48}$$

Since the spacecraft remains close to P_2, x is small, and the red term in Eq. (2.48) is expanded in a Taylor series about $x = 0$ such that

$$\frac{(x+1)}{(1+2x)^{3/2}} \approx 1-2x. \tag{2.49}$$

Similarly, the two blue terms in Eq. (2.48) are expanded assuming that x and y remain small, and

$$\begin{aligned} \frac{y}{(1+2x)^{3/2}} &\approx y \\ \frac{z}{(1+2x)^{3/2}} &\approx z. \end{aligned} \tag{2.50}$$

Substituting Eqs. (2.49) and (2.50) into Eq. (2.48) yields the HR3BP equations of motion,

$$\begin{aligned} \ddot{x}-2\dot{y} &= 3x-\frac{\mu x}{r^3} \\ \ddot{y}+2\dot{x} &= -\frac{\mu y}{r^3} \\ \ddot{z} &= -\frac{\mu z}{r^3}. \end{aligned} \tag{2.51}$$

In the HR3BP, the collinear libration points L_1 and L_2 are located at an equal distance from P_2; this distance, known as the Hill radius, is equal to

$$r_H = \left(\frac{\mu}{3}\right)^{1/3}. \tag{2.52}$$

It is also approximately equal to the distance of the libration points L_1 and L_2 from the smaller primary in the CR3BP. This quantity is sometimes used as an approximation of the sphere of influence,[25, 54] and is employed as a unit of distance for visualization of trajectories in the vicinity of P_2.

2.1.7. Zero Velocity Curves

The expression for the Jacobi Constant in Eq. (2.31) clearly demonstrates that the motion of the spacecraft is restricted to regions in space where $v^2 \geq 0$; these regions are bounded by surfaces of zero velocity. The zero velocity surfaces are defined by the relationship

$$x^2 + y^2 + \frac{2(1-\mu)}{r_1} + \frac{2\mu}{r_2} - J = 0. \tag{2.53}$$

The physical laws for vehicle motion prevent the crossing of these surfaces by the spacecraft. In fact, the surfaces enclose a forbidden region where the required velocity is imaginary to satisfy Eq. (2.53). In the planar problem, the surfaces reduce to the zero velocity curves (ZVCs), which represent the intersection of the zero velocity surfaces with the plane defined by $z = 0$. For values of the Jacobi Integral that are greater than that associated with the L_1 libration point, the ZVCs form closed regions around the two primaries. As the energy of the spacecraft is increased, the value of the Jacobi Constant decreases until, at the L_1 value, the ZVCs open at the L_1 libration point and the spacecraft is free to move between the two primaries. Similarly, when the value of the Jacobi Integral decreases to the value associated with L_2, the ZVCs open at L_2 and the spacecraft may escape entirely from the vicinity of the primaries. At a still lower value of J, the ZVCs open at L_3, forming curves that enclose the equilateral libration points. Finally, at the value of J associated with L_4 and L_5, the zero velocity surfaces leave the plane entirely and planar motion is unrestricted in the CR3BP. The evolution of the ZVCs in the Earth-Moon system appears in Figure 2.3.

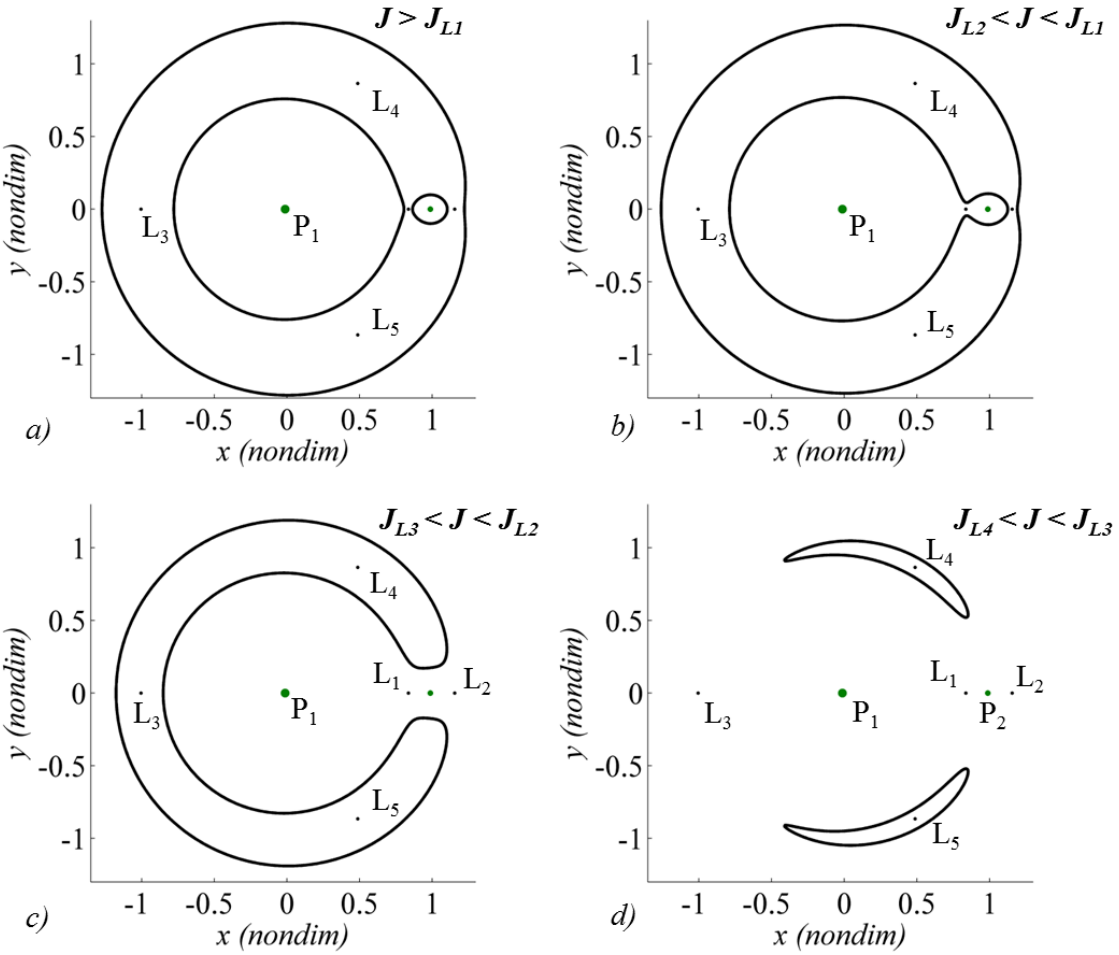

Figure 2.3 Zero velocity curves for four values of *J* in the Earth-Moon system.

2.1.8. Planar Periodic Motion near the Libration Points

In addition to the equilibrium points, particular solutions in the CR3BP include periodic orbits. Various families of periodic orbits in the vicinity of the libration points exist; planar periodic trajectories near the collinear libration points are known as Lyapunov orbits. A family of Lyapunov orbits is associated with each of the three collinear points. Characterized by symmetry across the *x*-axis, the smallest of the Lyapunov orbits are nearly elliptical and are well approximated by a linear path relative to L_i.[56] As the size of the orbits grows, the shape evolves to resemble a "kidney-bean", although periodicity is retained and the intersection with the *x*-axis is perpendicular with a zero component of velocity in the *x*-direction. A portion of each Lyapunov family at L_1, L_2, and L_3 appears in Figure 2.4. Note that the L_3 family is comprised of

relatively larger orbits, in general, than the L_1 and L_2 Lyapunov families. For physical comparison, the Earth-Moon distance is 384,400 km. The Hill radius associated with the Earth-Moon system is r_H = 61,279 km, and the distance from the Moon to the L_1 and L_2 libration points is x_{L1} = 58,024 km and x_{L2} = 64,521 km.

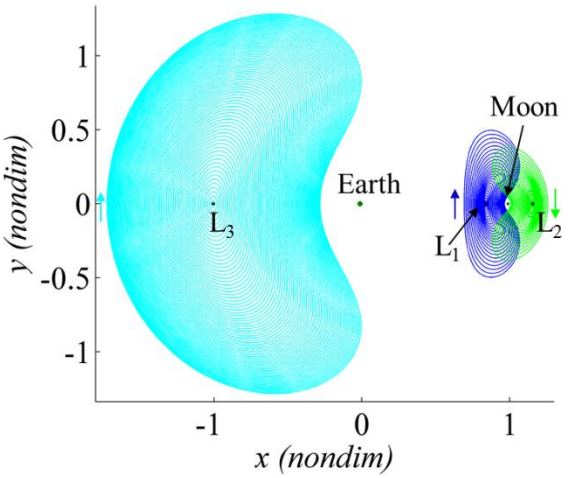

Figure 2.4 Lyapunov orbit families around the collinear libration points.

Each Lyapunov orbit within a family is characterized by a particular Jacobi Constant, and J changes as the size of the orbits in each family evolves. For a given value of J, a Lyapunov orbit may exist near each of the collinear libration points. For example, for J = 3.1672 in the Earth-Moon system, a value such that $J_{L1} < J < J_{L2}$, the corresponding L_1 and L_2 Lyapunov orbits appear with the ZVC in Figure 2.5. At this Jacobi Constant, the ZVCs remain closed at L_3, and no L_3 Lyapunov orbit exists.

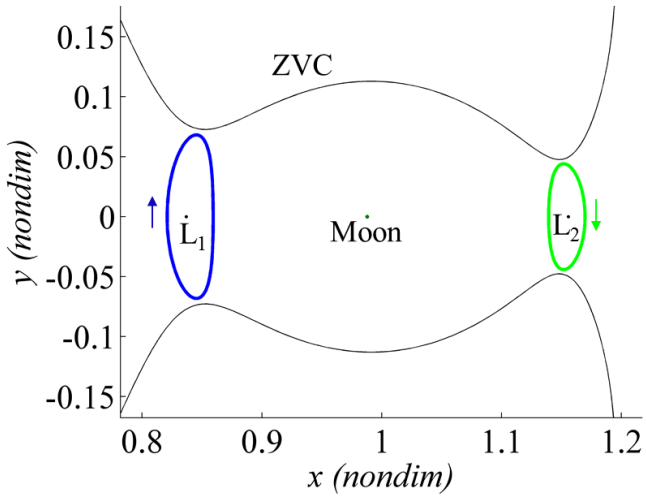

Figure 2.5 L_1 and L_2 Lyapunov orbits with J = 3.1672 in the Earth-Moon system.

2.1.9. The State Transition Matrix and Differential Corrections

The Lyapunov families are commonly computed by using a differential corrections process to target the required perpendicular crossings of the *x*-axis. The equations of motion are linearized relative to a nearby reference path, and the solution of the linearized equations results in the development of the State Transition Matrix (STM).[57] The STM relates variations in the initial state to changes in some final state downstream. This final state is specified, for example, in terms of some physical geometry, in terms of a parameter value, or other options. This relationship is used to determine the changes in the initial conditions that are required to yield the desired final path.

The derivation of the STM begins with the CR3BP equations of motion. The nonlinear equations of motion are of the form

$$\bar{r}(\tau) = \bar{F}(\bar{r}_0) \tag{2.54}$$

where $\bar{r}(\tau) = \begin{bmatrix} x(\tau) & y(\tau) & z(\tau) & \dot{x}(\tau) & \dot{y}(\tau) & \dot{z}(\tau) \end{bmatrix}^T$ and τ is nondimensional time. Given a particular reference solution, the variation in the state relative to the reference trajectory is

$$\delta\bar{r}(\tau) = \bar{r}(\tau) - \bar{r}_{ref}(\tau)\,. \tag{2.55}$$

Using a first-order Taylor series expansion, the linear variational equations of motion are then written

$$\delta\dot{\bar{r}}(\tau) = A(\tau)\delta\bar{r}(\tau) \tag{2.56}$$

where the time varying matrix $A(\tau)$ is

$$A(\tau)=\begin{bmatrix} 0 & 0 & 0 & 1 & 0 & 0 \\ 0 & 0 & 0 & 0 & 1 & 0 \\ 0 & 0 & 0 & 0 & 0 & 1 \\ U^*_{xx} & U^*_{xy} & U^*_{xz} & 0 & 2 & 0 \\ U^*_{yx} & U^*_{yy} & U^*_{yz} & -2 & 0 & 0 \\ U^*_{zx} & U^*_{zy} & U^*_{zz} & 0 & 0 & 0 \end{bmatrix}. \tag{2.57}$$

The pseudopotential $U^*(\tau)$ is defined in Eq. (2.27), and the double subscripts denote the second partial derivatives so that

$$U^*_{ij}=\frac{\partial^2 U^*(\tau)}{\partial i \partial j} \tag{2.58}$$

where $U^*_{ij}=U^*_{ji}$. The solution to the variational equations of motion in Eq. (2.56) is then written

$$\delta\bar{r}(\tau)=\Psi(\tau,\tau_0)\delta\bar{r}(\tau_0)\,. \tag{2.59}$$

The matrix $\Psi(\tau,\tau_0)$ is the STM; it represents the sensitivity of the state at time τ to variations in the state at time τ_0. It is governed by the matrix differential equation

$$\dot{\Psi}(\tau,\tau_0)=A(\tau)\Psi(\tau,\tau_0) \tag{2.60}$$

with the initial condition

$$\Psi(\tau_0,\tau_0)=I_{6x6} \tag{2.61}$$

where I_{6x6} is the 6x6 identity matrix. Equation (2.60) therefore represents a set of 36 scalar, first-order differential equations. The differential equations are numerically integrated simultaneously with the 6 scalar, first-order equations of motion represented in Eq. (2.18).

Since the change in the final state as a function of variations in the initial state as described in Eq. (2.59) is a first-order approximation, a series of iterations allows convergence on the actual initial conditions that yield the desired final reference trajectory. The process of iterating using the linear variational equations is frequently denoted as differential corrections. This process is used to target a perpendicular crossing of the *x*-axis to calculate the Lyapunov orbits as well as other periodic orbits; differential corrections can be implemented using a variety of computational techniques. A differential corrections process is also employed for other applications, for example, to target a particular flyby of a moon in a planet-moon system. The process is not

restricted to use in the CR3BP; differential corrections are also applicable to targeting problems using other formulations of the equations of motion; for example, the relative equations of motion in an inertial frame of reference.

2.1.10. The Monodromy Matrix and Stable and Unstable Manifolds

The STM of a periodic orbit evaluated after one full period, $\Psi(T,0)$, is known as the monodromy matrix. The monodromy matrix relates variations in the state at time $\tau = 0$ to the variations in the state after one period; the STM represents a stroboscopic map that reduces the continuous system to a discrete-time system. Any point along a periodic trajectory, for example a Lyapunov orbit, is a fixed point on the stroboscopic map represented by the monodromy matrix. The eigenvalues of the monodromy matrix reveal information about the stability of the periodic orbit, and its eigenvectors are key to the computation of the invariant manifolds associated with the orbit.[58, 59]

Consider the monodromy matrix associated with a point on a Lyapunov orbit. The eigenvalues of the monodromy matrix are labeled λ_i, and the corresponding eigenvectors are denoted $\bar{e}_i$. Two of the eigenvalues are equal to one; these eigenvalues correspond to the center subspace. If $|\lambda_i| < 1$ for all remaining eigenvectors, then a small perturbation to the state on the Lyapunov orbit tends to zero as $\tau \to \infty$ and the orbit is considered linearly stable. If $|\lambda_i| > 1$ for any *i*, then any perturbation to the initial state grows as time passes, and the orbit is considered unstable. Many Lyapunov orbits possess both stable and unstable eigenvalues, λ_s and λ_u. If a Lyapunov orbit possesses both stable and unstable eigenvalues, perturbations in a particular direction asymptotically approach the orbit while others asymptotically depart the vicinity of the orbit. The corresponding trajectories lie on these manifolds that are associated with the Lyapunov orbit. The set of trajectories that asymptotically approach the orbit comprise the stable manifold, while the trajectories that asymptotically depart the Lyapunov orbit are located on the unstable manifold.[58, 59] In the immediate vicinity of the fixed point corresponding to the orbit, the local stable and unstable manifolds defined on the map are tangent to the eigenvectors, $\bar{e}_s$ and $\bar{e}_u$, associated with λ_s and λ_u. By applying an offset to the Lypunov orbit in the direction of the unstable eigenvector and numerically integrating the state forward in time, a trajectory along the unstable manifold is numerically computed. The unstable manifold trajectory asymptotically

departs the Lyapunov orbit. Likewise, by propagating a state offset from the Lyapunov orbit in the direction of the stable orbit backwards in time, the numerical representation of a trajectory associated with the stable manifold results. A spacecraft or particle that is precisely specified in both position and velocity to be on the stable manifold trajectory asymptotically approaches the Lyapunov orbit. Repeating the procedure for a series of fixed points along the Lyapunov orbit, and projecting the higher-dimensional manifolds onto configuration space, forms a set of stable and unstable manifold tubes that aid in visualizing the flow along the stable and unstable manifolds. For example, a set of stable and unstable manifold tubes associated with the Lyapunov orbits from Figure 2.5 appear in Figure 2.6. The stable manifold trajectories appear in green, the unstable in red.

As discussed by Conley[60] and Gomez et al.,[38] the four-dimensional stable manifold tubes associated with the L_1 and L_2 Lyapunov orbits, at a given value of the Jacobi Integral, act as separatrices between trajectories that escape the vicinity of P_2 and trajectories that remain captured within the P_2 region. Trajectories near P_2 located inside the stable manifold tube associated with the L_1 or L_2 Lyapunov orbit will escape out the respective gateway, while a trajectory that lies outside the tubes remains trapped in the P_2 vicinity.

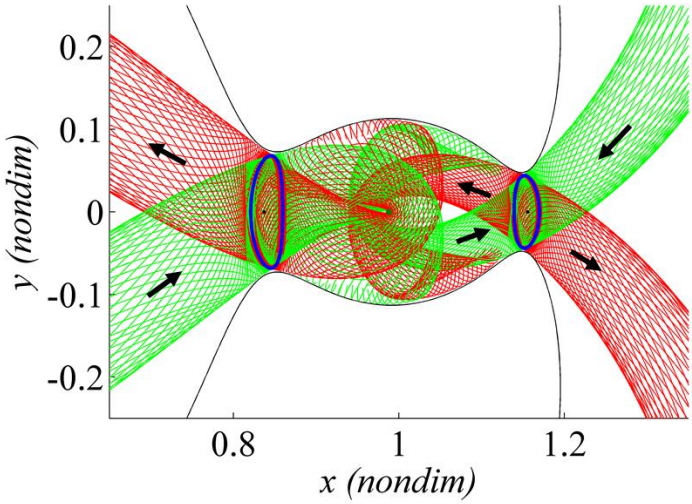

Figure 2.6 Stable (green) and unstable (red) manifolds associated with L_1 and L_2 Lyapunov orbits for J = 3.1672 in the Earth-Moon system.

2.2. Poincaré Maps

The monodromy matrix is an example of a stroboscopic map: a map that results from sampling the flow of a system at periodic intervals. Another fundamental type of map is the Poincaré map, or first return map. The Poincaré map is commonly used to interpret the behavior of groups of trajectories, relating the states at one point in time to a set of future states forward along the path. One of the advantages of the Poincaré map lies in its power as a visualization tool. Such a map reduces the order of the problem, condensing quantities of information into a lower-dimensional image. Poincaré maps reveal, at a glance, various characteristics of individual trajectories or groups of trajectories, whose features are otherwise difficult to isolate within the vast quantity of available information. The following discussion summarizes information that is available in greater detail in Parker and Chua[58] as well as Guckenheimer and Holmes.[59]

A Poincaré map is applied to a nonlinear system of equations. Consider an autonomous system defined in *m*-dimensional phase space as

$$\dot{\bar{x}} = \bar{f}\left(\bar{x}\right). \tag{2.62}$$

A flow, $\bar{\phi}\left(\bar{x},t\right)$, is generated by the vector field $\bar{f}\left(\bar{x}\right)$. An (*m*-1)-dimensional hyperplane, or surface of section, Σ, is defined in the system. While not necessarily planar in physical space, Σ must be transverse to the flow. That is, $\bar{f}\left(\bar{x}\right)\bullet\bar{\eta}\left(\bar{x}\right)\neq 0$ for all $\bar{x}\in\Sigma$, where $\bar{\eta}$ is the unit normal to Σ. A trajectory associated with the flow $\bar{\phi}\left(\bar{x},t\right)$ crosses the hyperplane Σ at a point *x*. Assume that the trajectory repeatedly crosses through Σ, as seen in Figure 2.7, crossing from Σ^- to Σ^+ and back again to Σ^-. Then, the first return of the trajectory to the hyperplane defines a nonlinear map $P:\Sigma\rightarrow\Sigma$, such that

$$P(\bar{x}_0)=\bar{x}\left(\bar{x}_0\right). \tag{2.63}$$

The sequence $\{x_1, x_3, x_5, \ldots\}$ lies on the one-sided Poincaré map P^+, while $\{x_2, x_4, \ldots\}$ is a set of points on P^-. The complete set of points, $\{x_1, x_2, x_3, x_4, x_5, \ldots\}$ belongs to the two-sided map, $P^{\pm}$. The crossing x_3 represents the first return to Σ^+, while x_4 is the first return to the surface Σ^-. Subsequent points on each of the maps represent multiple intersections of a trajectory with a single surface of section.

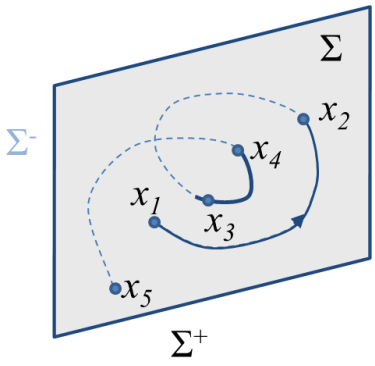

Figure 2.7 Multiple crossings of Σ by a single trajectory.

Consider a simply periodic orbit Γ with initial state $\bar{x}_0 = \bar{x}^*$. The periodic orbit always returns to the map in the same location, so $P : \Sigma \to \Sigma$ repeatedly maps $\bar{x}^*$ onto itself and

$$P(\bar{x}^*) = \bar{x}^*. \tag{2.64}$$

The state $\bar{x}^*$ is therefore known as a fixed point on the map; a sample periodic orbit crossing the surface of section Σ appears in Figure 2.8. A nearby point, $\bar{x}$, maps to $P(\bar{x}) \neq \bar{x}$.

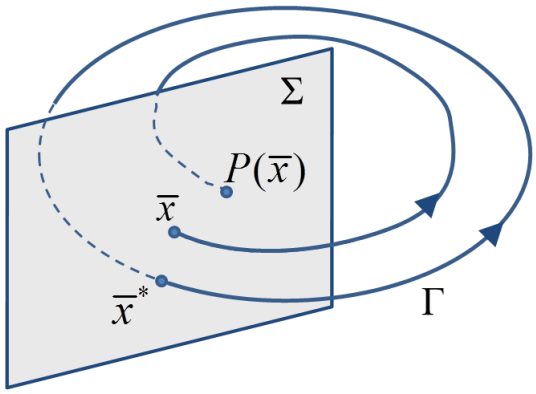

Figure 2.8 A periodic trajectory returns to the Poincaré map at $\bar{x}^*$; a nearby point $\bar{x}$ maps to $\bar{P}(\bar{x}) \neq \bar{x}$.

Note that the sampling of the Poincaré map reduces the dimension of a trajectory by one: a periodic trajectory becomes a point on the map, while a non-periodic trajectory is represented by a set of points. When a Poincaré map is exploited in the CR3BP, the Jacobi Constant is typically

fixed, again reducing the dimension by one. In the planar CR3BP, therefore, a 4-dimensional trajectory is reduced to 2 dimensions. When the map is, thus, projected onto a plane, the resulting image represents the entire state space, revealing considerable information about the mapped trajectory.

2.2.1. Selection of the Surface of Section

The appearance of the Poincaré map changes significantly depending on the selection of the surface of section as well as the plane of projection. Traditionally, a surface of section in the CR3BP is chosen as a plane in position space, for example, the plane represented by $y = 0$. The map is then typically visualized in terms of the coordinates x and $\dot{x}$. As an example, consider the Lyapunov manifold trajectories appearing in Figure 2.6 for $J = 3.1762$ in the Earth-Moon system. A two-sided map is created for this set of trajectories by recording the x position and velocity at every x-axis crossing. The map, which focuses on the region between the L_1 and L_2 libration points, appears in Figure 2.9. The ordinate represents the velocity in the x-direction, while the abscissa corresponds to the x-coordinate of the position. The y-coordinate of the position vector is equal to zero by definition, and the magnitude of the y-velocity is constrained by the Jacobi Constant. At this particular value of J, exactly two Lyapunov trajectories exist, one near L_1 and one near L_2. The two libration points are represented by the black points on the map, and the location of the Moon is marked in blue. Any path that crosses the surface of section, $y = 0$, will appear on the map. On this particular map, only the stable and unstable Lyapunov manifold trajectories are represented. The green points represent crossings of the L_1 and L_2 stable manifold trajectories while red points correspond to the unstable manifold trajectories.

Because the map reduces the dimensionality of the system by two, the map represents the full dynamics of this set of planar prograde trajectories. While a given trajectory may cross the map multiple times, any single point on the map is produced by the crossing of the surface of section by one unique trajectory. Therefore, a point on the Poincaré map where the red curve representing the unstable manifold exactly intersects the green curve of the stable manifold represents a single path that departs a Lyapunov orbit on a red unstable trajectory and subsequently approaches a Lyapunov orbit on a green stable trajectory. This type of map can therefore be used, for example, to find natural transitions from the L_1 Lyapunov orbit to the L_2 Lyapunov orbit.[61] One such intersection point is circled on the map in Figure 2.9.

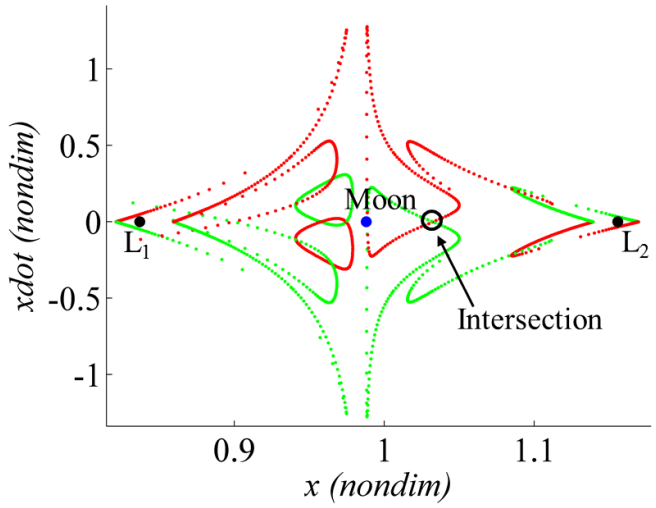

Figure 2.9 Two-sided Poincaré map representing the L_1 and L_2 stable (green) and unstable (red) manifold trajectories for $J = 3.1672$ in the Earth-Moon system.

The same information is available in different forms. For example, an alternative map might represent y versus $\dot{y}$ at x-axis crossings. A third option, however, employs a different type of surface of section. Instead of a plane in configuration space (such as $y = 0$ or $x = 0$), the hyperplane is defined as the plane of periapse passages. Such a map is identified as a periapsis Poincaré map.

In the multi-body problem, periapsis is defined as a point along the trajectory where the magnitude of the primary-centered position vector is at a local minimum. To meet this requirement, two conditions must be satisfied: the first derivative of the position vector is equal to zero, and the second derivative is positive.[62] Consider a P_2-centered position vector. Then, a periapsis point is specified by

$$\begin{aligned} &\bar{r}_2 \bullet \bar{v} = 0 \\ &D \equiv v^2 + \bar{r}_2 \bullet \ddot{\bar{r}}_2 > 0. \end{aligned} \tag{2.65}$$

The second relationship in Eq. (2.65) effectively determines a boundary. Thus, $D = 0$ defines a contour that specifically forms a boundary between regions where periapses exist and regions where $\bar{r}_2 \bullet \bar{v} = 0$ but instead corresponds to apoapses. This contour appears in Figure 2.10. Set in configuration space, Figure 2.10 is centered at P_2 and labeled in units of Hill radii, r_H. The ZVCs bound the forbidden region, colored in grey. The contour corresponding to $D = 0$ separates two

regions. Within the green region, $D < 0$, and $\bar{r}_2 \bullet \bar{v} = 0$ defines trajectory apoapses. In the white region and within the Hill sphere, $D > 0$, and $\bar{r}_2 \bullet \bar{v} = 0$ corresponds instead to periapses.

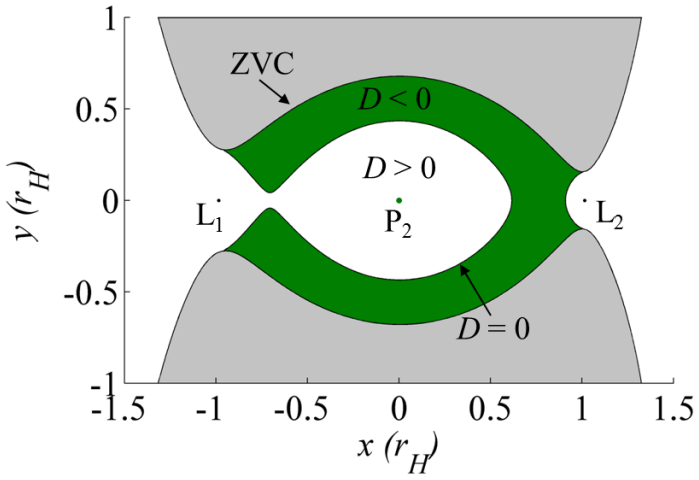

Figure 2.10 A contour is defined by $D = 0$. The contour divides the region within the Hill sphere where $\bar{r}_2 \bullet \bar{v} = 0$ defines periapses (white) from the region where the relationship instead defines apoapses (green).

With a surface of section defined as the plane of periapse passage with respect to P_2, a Poincaré map is plotted in position space. The first-return map corresponding to the L_1 and L_2 Lyapunov manifold trajectories from Figure 2.6 appears in Figure 2.11. The trajectories are included in the figure for reference; the first periapsis along each trajectory is plotted as a point in red (unstable manifold trajectories) or green (stable manifold trajectories). These periapse crossings comprise a first-return periapsis Poincaré map. This type of map is employed by Villac and Scheeres[43, 45] as well as Paskowitz and Scheeres.[44] One advantage of the periapsis Poincaré map is that the representation is in position space, y versus x. Hence, the map is simple to relate visually to the trajectories represented. The choice of other coordinates, for example, periapse radius r_p and angle ω_r, reveals additional information, particularly in long-term maps representing multiple crossings of the surface of section.

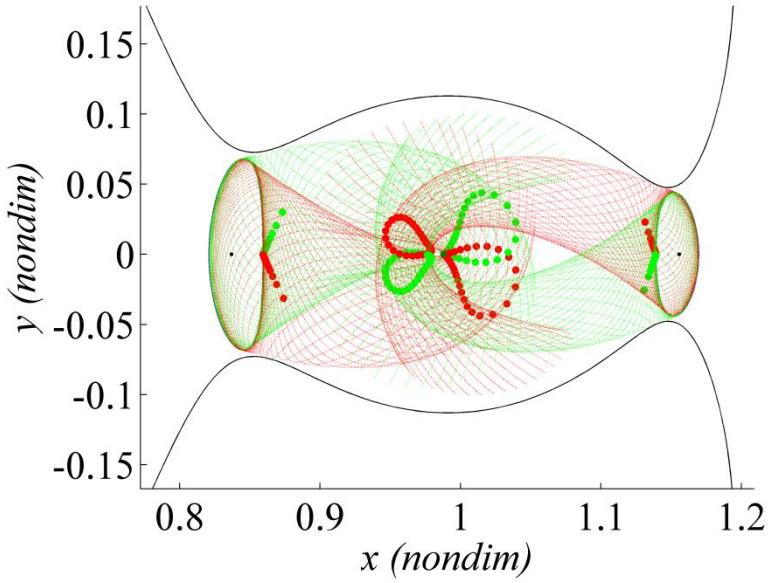

Figure 2.11 Periapsis Poincaré map of the L_1 and L_2 Lyapunov manifold trajectories for $J = 3.1672$ in the Earth-Moon system.

2.3. Models and Constants

Examples in this analysis are based mainly in the Sun-Saturn-Titan system, although other Sun-planet and planet-moon systems are also investigated. Several different numerical integration schemes are employed. Relevant details are included below.

2.3.1. The Saturnian System, the Cassini Mission, and Representative Constants

One motivating problem for this investigation was the search for end-of-life options in support of the extended mission for the Cassini spacecraft. The Cassini-Huygens spacecraft[63] was launched in October 1997 and entered Saturn orbit on July 1, 2004. The primary mission included 74 revolutions of Saturn, the release of the Huygens probe into a trajectory that delivered a vehicle onto the surface of Titan, and multiple flybys of various Saturnian moons. The primary mission ended on May 28, 2008, with the 43rd Titan flyby. The Cassini Equinox Mission extended the life of the spacecraft through September 2010, adding 60 orbits of Saturn, 26 additional Titan flybys, as well as 7 Enceladus flybys. The subsequent Cassini Solstice Mission again extended the spacecraft flight plan through May 2017. The Solstice Mission is

scheduled to include 155 additional revolutions around Saturn, 54 Titan flybys, and 11 close approaches to Enceladus.

The Saturnian system includes a large family of moons in addition to the planetary rings. Currently, 53 named moons orbit Saturn, the largest by far being Titan. Titan orbits Saturn approximately once every 16 days, following a nearly circular path with eccentricity $e = 0.0288$. Its orbit is inclined 0.35º to the equatorial ring plane, which itself is tilted 26.73º from the Sun-Saturn orbital plane. The second-largest moon in the known solar system, Titan is sufficiently massive to be an effective gravity assist body, and flybys of the large moon are used to modify the path of the Cassini spacecraft. The most distant moon of significant size is Phoebe, which completes a revolution of Saturn every 1.5 years. An irregular satellite, Phoebe's retrograde orbit is inclined 151.78º to Saturn's ring plane.

While the methods developed and used in this investigation are not specific to a given system, the Sun-Saturn and Saturn-Titan systems are employed for most of the analysis. Constant parameters that reflect the two systems appear in Table 2.1. Note the similarity between the Sun-Saturn and Saturn-Titan system mass parameters. For comparison, simulations are also completed in several other Sun-planet and planet-moon systems; constants used for these examples appear in Table 2.2 and Table 2.3.

Table 2.1 Constants for the Sun-Saturn and Saturn-Titan systems

	Sun-Saturn	**Saturn-Titan**
μ	2.8580427×10^{-4}	2.3658052×10^{-4}
l^*	1.4334494×10^{9} km	1.2218700×10^{6} km
t^*	1.4895519×10^{9} s	2.1924711×10^{5} s
T	29.6776 years	15.9441 days
r_H	6.54683×10^{7} km	5.23975×10^{4} km
r_{P2}	6.02680×10^{4} km	2.57600×10^{3} km

Table 2.2 Constants for Sun-planet systems

	Sun-Earth	**Sun-Neptune**	**Sun-Jupiter**
μ	3.00272×10^{-6}	5.14982×10^{-5}	9.53684×10^{-4}
l^*	1.49598×10^{8} km	4.49825×10^{9} km	7.78412×10^{8} km
r_H	1.49643×10^{6} km	1.16038×10^{8} km	5.31256×10^{7} km
r_{P2}	6.378×10^{3} km	2.4764×10^{4} km	7.1492×10^{4} km

Table 2.3 Constants for planet-moon systems

	Jupiter-Europa	**Earth-Moon**	**Pluto-Charon**
μ	2.52802×10^{-5}	1.21536×10^{-2}	1.09653×10^{-1}
l^*	6.71100×10^{5} km	3.84400×10^{5} km	1.75360×10^{4} km
r_H	1.36565×10^{4} km	6.12790×10^{4} km	5.81966×10^{3} km
r_{P2}	1.5608×10^{3} km	1.7375×10^{3} km	6.0300×10^{2} km

2.3.2. Numerical Integration

Numerical integrations in this investigation are performed using a Runge-Kutta (4,5) integrator in MATLAB with relative and absolute tolerances equal to 1×10^{-12} or a Runge-Kutta-Verner (8,9) integrator in Fortran with a tolerance of 1×10^{-12}. The CR3BP equations of motion, with constants from Tables 2.1-2.3, are used for the majority of the analysis. However, a significant example in the Cassini end-of-life analysis is completed using the relative equations of motion in the inertial frame, as specified in Eq. (2.1). This force model includes the effects of the Sun and Saturn, as well as Titan when specified. The orbital elements of the primaries in this model are obtained from the JPL de405 ephemeris.

3. UNDERSTANDING THE TIDALLY-INFLUENCED ENVIRONMENT: INDIVIDUAL TRAJECTORIES

Recall that a spacecraft in orbit about a primary is always subject to perturbations, but the perturbations are not always small. The influence of an additional gravity field may be large, and quantifying the impact of the additional force is necessary for understanding the behavior of spacecraft moving under the influences of the various forces. A spacecraft in the vicinity of the smaller primary in the CR3BP is affected by the tidal acceleration originating from the distant larger primary. A vital step towards a methodical design strategy for trajectories in a tidally-influenced environment is the development of a better understanding of the underlying dynamical structure of the region near the smaller primary, P_2. The first step is an investigation of the behavior of individual trajectories over one and several revolutions. Changes in a given orbit are generally predictable based on the trajectory's size and orientation relative to the two primaries.

3.1. Tidal Acceleration by Quadrants

The direction of the net perturbing acceleration due to the gravity of P_1 on a spacecraft in an orbit about P_2 depends on the orientation of the spacecraft orbit relative to the two bodies. To facilitate the investigation of the solar gravitational influence, four quadrants centered at P_2 are defined in the rotating frame and appear in Figure 3.1. The quadrants are defined in a counterclockwise fashion, with quadrant I on the far side of the primary and leading P_2 in its orbit. When the spacecraft orbit is viewed in this rotating frame, its orientation is defined by the quadrant that contains the apoapsis on a given revolution. The quadrant angle Φ is the angle between the positive *x*-axis and apoapsis, as depicted in Figure 3.1.

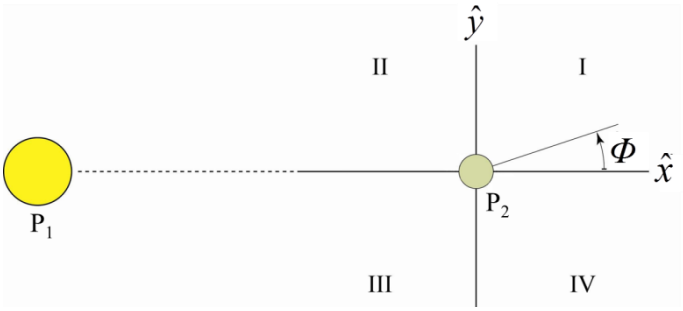

Figure 3.1 Quadrants and quadrant angle Φ, as defined in the rotating frame.

The direction of the tidal acceleration in the vicinity of P_2 appears in Figure 3.2. For a value of μ = 0.01, and with the *y*-component exaggerated to clarify the detail, the pattern of the tidal acceleration appears in Figure 3.2(*a*). The tidal acceleration for the Sun-Saturn system appears to scale in Figure 3.2(*b*), with distance measured in units of Saturn radii (1 R_S = 60,269 km). Clearly, in this region, the tidal acceleration is dominated by the *x*-component and is always directed outwards from P_2. The effects of the tidal acceleration on a P_2-centered orbit are greatest near apoapsis. In quadrants I and III, the perturbations generally oppose the direction of motion in a prograde orbit. In quadrants II and IV, on the other hand, the net perturbing acceleration at apoapsis is in the same direction as the motion along a prograde orbit. As a result, the tidal effects on an orbit are similar in diagonal quadrants. For example, solar gravity perturbations tend to circularize prograde orbits lying in quadrants II and IV and to elongate prograde orbits with apoapsis in either quadrant I or quadrant III.

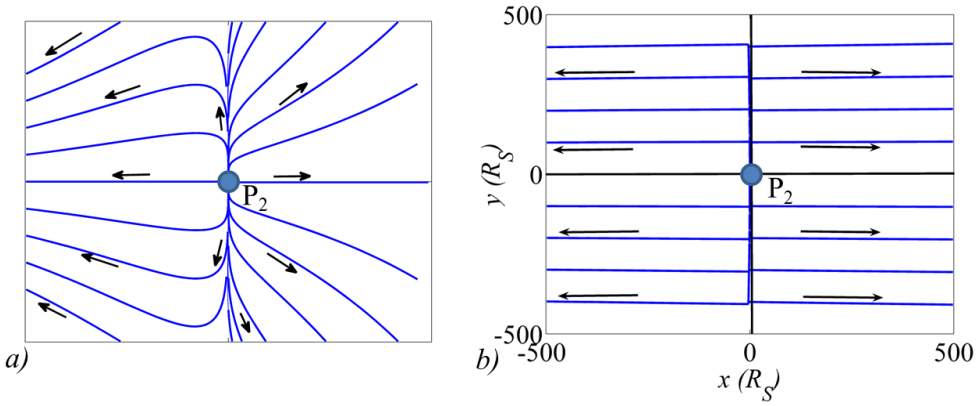

Figure 3.2 Direction of tidal acceleration with an exaggerated *y*-component (*a*) and for the Sun-Saturn system (*b*).

The effects of tidal acceleration on the orbital elements of a trajectory centered at P_2 depend on the orientation of apoapsis within the quadrants, as well as on the size, shape, and inclination of the orbit.[33, 64] By comparing the osculating orbital elements measured at two subsequent periapse passages, these effects are quantized. Consider an eccentric prograde orbit sufficiently large to be impacted significantly by the gravity of P_2 but the impact is such that the perturbations do not cause the orbit to become retrograde or to escape the vicinity of P_2. If apoapsis lies in quadrant I or III, tidal acceleration lowers periapse radius, decreases semi-major axis, and increases eccentricity. Tidal acceleration acting on an orbit oriented in quadrant I or III also increases the V_∞ of the spacecraft with respect to a flyby body, for encounters of the type described in Chapter 6. Conversely, if apoapsis instead lies in quadrant II or IV, tidal acceleration raises periapse radius, increases semi-major axis, and decreases eccentricity, and decreases the V_∞ of the spacecraft with respect to a flyby body, for the type of close encounters specified in Chapter 6. These results are summarized in Table 3.1. The gravitational perturbations due to P_1 are greatest when the orbit lies in the ecliptic plane. Also, within each quadrant, effects on a, e, and r_p are at a maximum when apoapsis lies at approximately 45° from the P_1-P_2 line. Note that the effects of tidal acceleration on argument of periapsis are out of phase with the other orbital elements—the maximum change in ω lies approximately along the P_1-P_2 line (largest increase in ω) and at 90º from the P_1-P_2 line (maximum decrease in ω), where changes in the other orbital elements are at a minimum. Of course, the precise value of the quadrant angle corresponding to the maximum change in orbital elements is orbit-dependent.

Table 3.1 Effects of tidal acceleration on a trajectory relative to the previous periapse passage

	Quadrants I and III	**Quadrants II and IV**
$\boldsymbol{a}$	decreases	increases
$\boldsymbol{r_p}$	decreases	increases
$\boldsymbol{e}$	increases	decreases
$\mathbf{V}_\infty$	increases	decreases

Consider a set of planar Saturn-centered trajectories with initial semi-major axis $a_0 = 202\ R_S$ (corresponding to a Keplerian period of 500 days) and initial eccentricity $e_0 = 0.78$. The initial periapse radius of this set of orbits is 44.3 R_S. Each orbit is propagated forwards to its subsequent periapsis, and the changes in orbital elements (a, r_p, e, and ω) due to tidal acceleration are recorded for quadrant angles $-180^\circ < \Phi < 180^\circ$. The results appear in Figure 3.3. As the quadrant

angles range through the rotating frame, the changes in orbital elements follow a sinusoidal pattern. This pattern is representative of smaller orbits; however, the amplitude and phase of the curve will change for different initial conditions. In addition, for long-period orbits—when the time from one periapse passage to the next is a significant percentage of the orbital period of the primaries—the sinusoidal nature of the curve is disturbed. This is due to the rotation of the primaries relative to the trajectory as P_3 moves from periapsis to apoapsis. For example, consider a second set of Saturn-centered trajectories with initial semi-major axis a_0 = 400 R_S (corresponding to a Keplerian period of 1,400 days) and initial eccentricity e_0 = 0.78. These parameters correspond to an initial periapse radius r_{p0} = 88 R_S. For quadrant angles -180º < Φ < 180º, the orbital element changes from one periapse passage to the next appear in Figure 3.4. Clearly, the curve is no longer sinusoidal in appearance, and quadrant angles corresponding to the maximum magnitude changes in a, r_p, and e are no longer at 45º from the Sun-Saturn line. The Keplerian period of this trajectory is approximately 13% of the orbital period of Saturn about the Sun. During one spacecraft revolution about the planet, Saturn has therefore shifted about 46º in its course around the Sun, and the spacecraft trajectory can spend time in multiple quadrants during a single revolution. The neat sinusoidal pattern of orbital element changes is therefore disrupted. Note also that the decrease in periapse radius is limited by the initial r_{p0} associated with the trajectory set—the greatest decrease in periapse radius results in impact with Saturn. It is also noted that it is necessary to precisely define the quadrant angle Φ – in this application, the quadrant angle is computed as the angle between the P_2-P_3 line and the positive x-axis at the moment of apoapse passage.

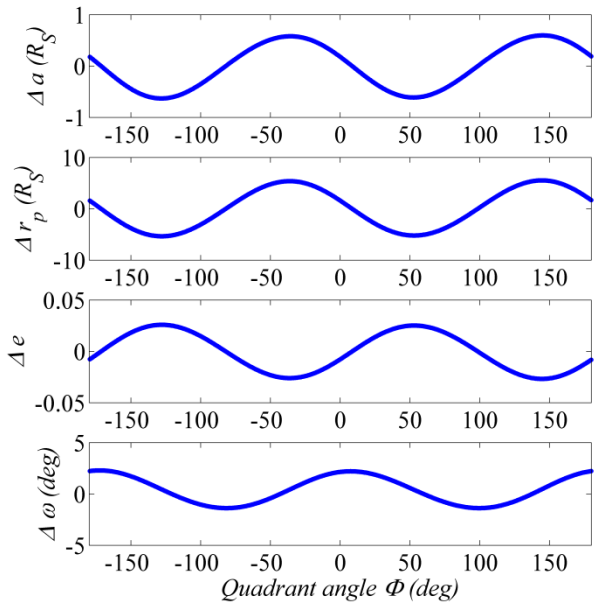

Figure 3.3 Changes in orbital elements from one periapsis to the next as a function of quadrant angle Φ: Saturn-centered orbit, a_0 = 202 R_S, e_0 = 0.78.

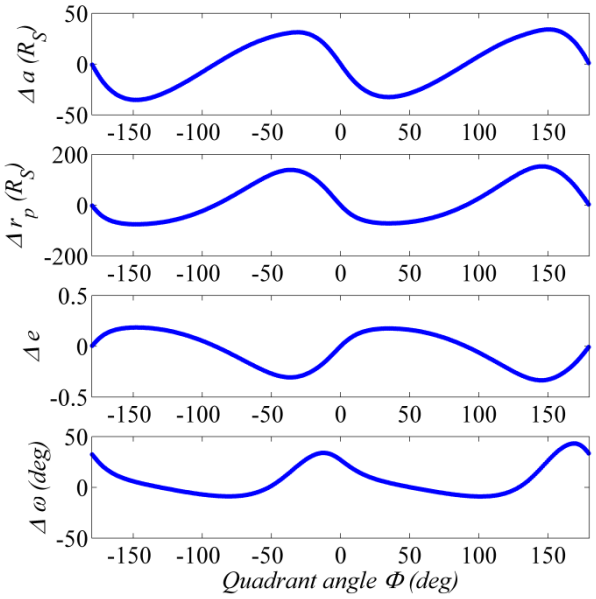

Figure 3.4 Changes in orbital elements from one periapsis to the next as a function of quadrant angle Φ: Saturn-centered orbit, a_0 = 400 R_S, e_0 = 0.78.

The eccentricity of the orbit also significantly affects the orbital element changes over one revolution. Adjusting the value of the initial eccentricity changes the magnitude (but not the

direction) of the curves associated with Δe, Δr_p, and $\Delta\omega$. Increasing eccentricity increases Δe and Δr_p up to about e = 0.7, and then the amplitude of the curves falls as eccentricity is increased further. Increasing eccentricity, on the other hand, decreases the amplitude of the $\Delta\omega$ curve: the maximum changes in the argument of periapsis occur for the most circular orbits. However, both the sign and the phase shift in the Δa curve as eccentricity changes. As eccentricity is decreased below about 0.3, the changes in semimajor axis in Quadrants I and III flip from negative to positive, and in Quadrants II and IV, Δa becomes negative. These effects are clearly visible in Figure 3.5. For a set of orbits with an initial conic period of 500 days, the eccentricity is varied from 0.1 to 0.9, and the resulting changes in the orbital elements from one periapse passage to the next are plotted as a function of quadrant angle.

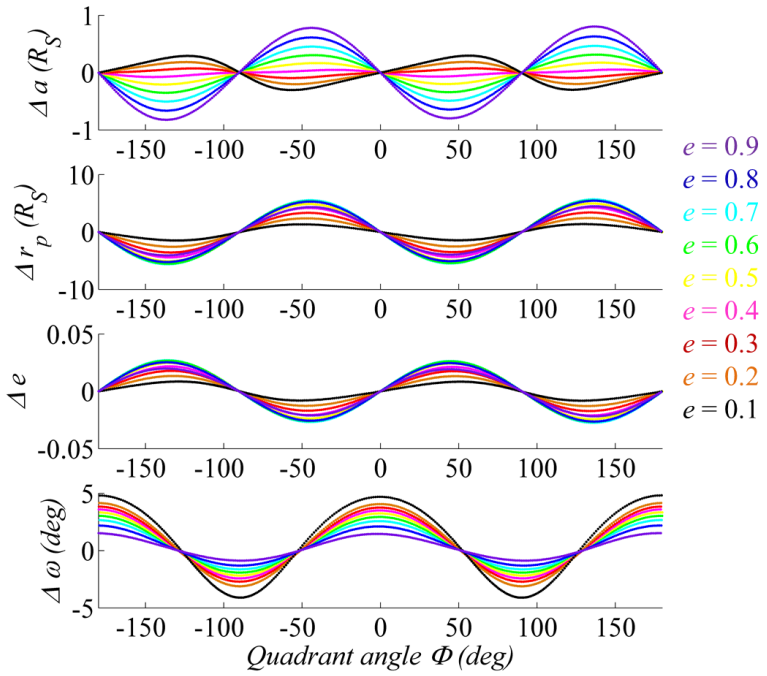

Figure 3.5 Change in orbital elements over one revolution as eccentricity changes. Saturn-centered orbit, a_0 = 202 R_S.

For out-of-plane trajectories, the tidal effects on semi-major axis, periapse radius, and eccentricity decrease as the inclination of the orbit increases. The change in inclination due to tidal acceleration, on the other hand, increases with increasing inclination, since the gravity of P_2 works to pull the orbit back into the ecliptic plane. As initial inclination increases, therefore, the

change in inclination over one revolution becomes more negative. These effects are clearly evident for a Quadrant IV orbit (Φ = -45º) with longitude of the ascending node set to zero, propagated for a single revolution such that initial inclinations vary from 0 to 90º. The changes in the orbital elements appear in Figure 3.6.

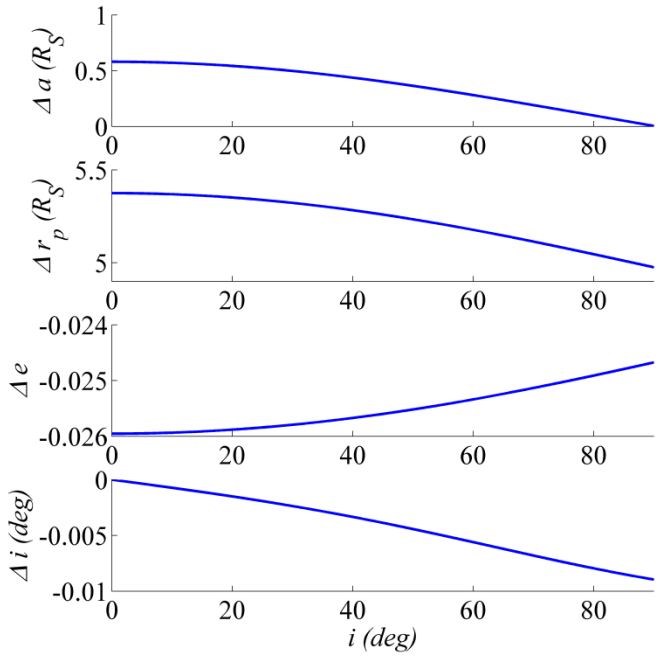

Figure 3.6 Changes in orbital elements from one periapsis to the next as a function of inclination: Saturn-centered orbit, a_0 = 202 R_S, e_0 = 0.78.

As demonstrated, the magnitudes of the changes in the orbital elements due to tidal acceleration depend on initial orbital parameters. For a given quadrant angle and semi-major axis, the effects of solar gravity increase with increasing eccentricity and decrease with increasing inclination. For certain orbits, the influence of tidal acceleration can be dramatic. An initially-prograde orbit may remain on a prograde path about P_2 or it may escape the vicinity of P_2. If the physical radius of the smaller primary is considered, a trajectory's periapsis may be lowered sufficiently to result in impact with P_2. Three sample orbits appear in Figure 3.7 and Figure 3.8. On the left, a quadrant IV trajectory is initially prograde in its orbit about Saturn, and although solar gravity visibly alters its characteristics, significantly raising r_p, it remains in orbit after one revolution. In the center, a similar trajectory escapes the vicinity of Saturn prior to passing through its second periapsis. On the right, a quadrant III trajectory impacts Saturn upon reaching

its subsequent periapsis. The three trajectories appear in the Sun-Saturn rotating frame in Figure 3.7 and in an inertial frame in Figure 3.8.

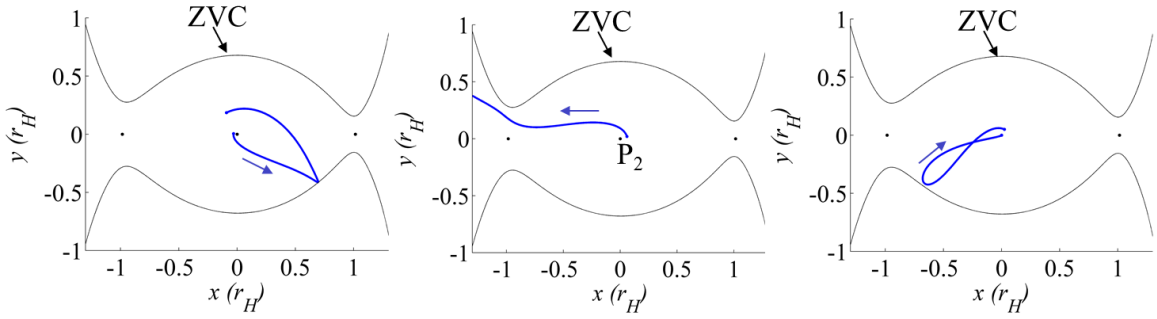

Figure 3.7 Three Saturn-centered trajectories affected by solar gravity: rotating view.

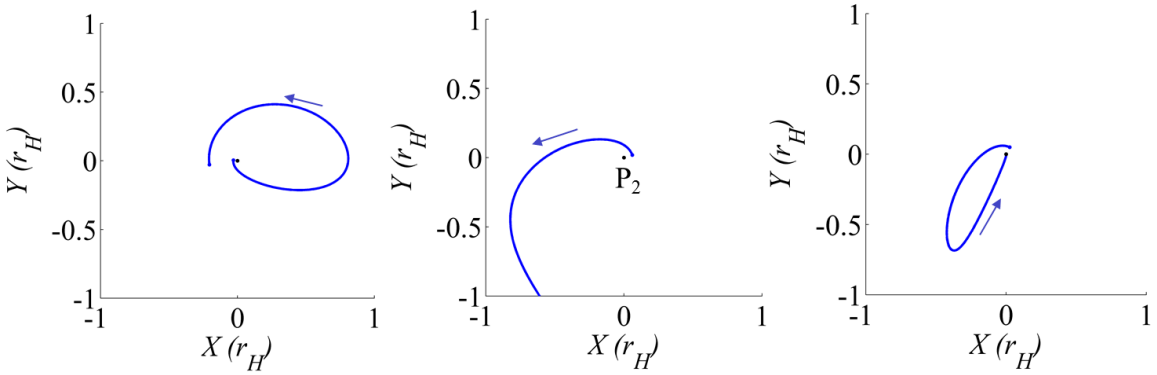

Figure 3.8 Three Saturn-centered trajectories affected by solar gravity: inertial view.

3.1.1. Coriolis Acceleration and the Stability of Retrograde Orbits

As noted by Hamilton and Burns[25] as well as Hamilton and Krivov,[26] the direction of the Coriolis acceleration affects the stability of retrograde orbits as compared with prograde trajectories. While not considered part of the tidal acceleration, it is nevertheless an important component of the total net acceleration acting on a spacecraft to produce a trajectory, and it is illuminating to consider its effects on orbit stability.

The direct acceleration due to P_2 is attractive and opposite the radial vector, of course, for all trajectories. The tidal acceleration is directed away from the *y*-axis as depicted in Figure 3.2. In contrast, the Coriolis acceleration is a function of the velocity of P_3. For prograde trajectories, this acceleration is directed outwards, away from P_2; for retrograde trajectories, it is directed inwards,

towards P_2. It is therefore tends to produce a stabilizing effect on retrograde trajectories, while encouraging instability in prograde trajectories.

As an example, consider the initial conditions resulting in the trajectories that appear in Figure 3.8. If the same initial position and velocity magnitude are applied (and, hence, the same value of Jacobi Constant), but the velocity direction is selected such that the trajectories are retrograde as opposed to prograde, significantly different characteristics are evident in the subsequent orbits. In Figure 3.9, each trajectory is propagated for one period of the primaries, or about 29.7 years. Each trajectory remains far from the boundary representing the ZVCs, a typical characteristic of retrograde trajectories, and each appears well-ordered. Despite the open ZVCs, none of the three trajectories threatens to escape the vicinity of P_2.

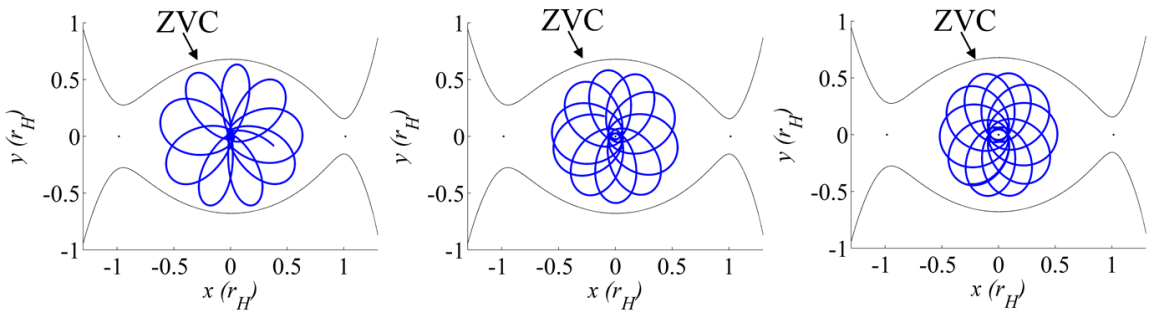

Figure 3.9 Three Saturn-centered retrograde trajectories affected by solar gravity: rotating view.

3.2. The Tidal Kick Function

One effective method for estimating the effects of tidal acceleration on the orbital elements over one revolution involves the application of the tidal kick function, as described by Villac and Scheeres.[6] The approach summarized here uses the P_2-centered equations of motion from the HR3BP. The derivation of the tidal kick function employs Picard's method of successive approximations[7] to first order and estimates the changes in energy and angular momentum due to tidal acceleration, and in turn, the corresponding changes in osculating semi-major axis, inclination, and eccentricity.

The derivation of the tidal kick function is performed in terms of the HR3BP. Hill's equations of motion, presented in Eq. (2.51), can be written in terms of a perturbation potential,

$$R = \frac{1}{2} N^2 \left(3x^2 - r \right) \tag{3.1}$$

such that

$$\begin{aligned}\ddot{x}-2N\dot{y}+\frac{\mu x}{r^3}-N^2x&=\frac{\partial R}{\partial x}\\ \ddot{y}+2N\dot{x}+\frac{\mu y}{r^3}-N^2y&=\frac{\partial R}{\partial y}\\ \ddot{z}+\frac{\mu z}{r^3}&=\frac{\partial R}{\partial z}\end{aligned} \tag{3.2}$$

where N is angular velocity of the smaller primary. The potential R is rewritten in terms of osculating orbital elements,

$$R=\frac{1}{4}N^2r^2\left[\begin{array}{l}1+3\cos^4(i/2)\left\{\begin{array}{l}\cos 2(\omega+\Omega)\cos 2(\theta^*-N(t-t_0))\\ -\sin 2(\omega+\Omega)\sin 2(\theta^*-N(t-t_0))\end{array}\right\}\\ +3\sin^4(i/2)\left\{\begin{array}{l}\cos 2(\omega-\Omega)\cos 2(\theta^*+N(t-t_0))\\ -\sin 2(\omega-\Omega)\sin 2(\theta^*+N(t-t_0))\end{array}\right\}\\ +\frac{3}{2}\sin^2 i\left\{\begin{array}{l}\cos 2\Omega\cos 2N(t-t_0)+\sin 2\Omega\sin 2N(t-t_0)\\ +\cos 2\omega\cos 2\theta^*-\sin 2\omega\sin 2\theta^*-1\end{array}\right\}\end{array}\right]. \tag{3.3}$$

Three variables, C (Keplerian energy), L (the magnitude of the orbital angular momentum vector), and H (scalar angular momentum component projected onto the z-axis) are defined in terms of a, e, and i,

$$C=\frac{-GM_2}{2a} \tag{3.4}$$

$$L=\sqrt{GM_2a\left(1-e^2\right)}, \tag{3.5}$$

$$H=L\cos i \tag{3.6}$$

where GM_2 is the gravitational parameter of P_2. The Lagrange Planetary Equations[57] then yield the change in these variables over time, via

$$\dot{C}=\frac{\partial R}{\partial t} \tag{3.7}$$

$$\dot{L}=\frac{\partial R}{\partial \omega} \tag{3.8}$$

$$\dot{H}=\frac{\partial R}{\partial \Omega}. \tag{3.9}$$

These equations are used to determine the changes in *a*, *e*, and *i* over one period, where a period is defined in the conic sense, $T = 2\pi\sqrt{a^3 / GM_2}$. (Caution is urged when comparing the results obtained from this analysis to results that emerge from a numerical simulation. The tidal perturbations on certain orbits can result in a periapse passage that occurs after a significantly different duration than the time defined by the conic period. Disparities are observed when the estimate for the period, i.e., the time corresponding to one revolution, is poor.)

Given the assumption concerning the period, to compute the changes in *C*, *L*, and *H* (and hence *a*, *e*, and *i*) over one revolution, the first iteration of Picard's method of successive approximations is applied. Consider a system of differential equations defined as

$$\begin{aligned} \dot{X} &= F(X,t) \\ X\left(t_0\right) &= X_0. \end{aligned} \tag{3.10}$$

Picard's method of successive approximations defines the first *k* iterations as

$$\begin{aligned} X_{(0)}\left(t\right) &= X_0 \\ X_{(1)}\left(t\right) &= X_0 + \int_{t_0}^{t} F\left(X_{(0)}, t\right)dt \\ &\vdots \\ X_{(k)}\left(t\right) &= X_0 + \int_{t_0}^{t} F\left(X_{(k-1)}, t\right)dt. \end{aligned} \tag{3.11}$$

Using only the first iteration, the change in the quantity *X* over the period *T* is then written

$$\Delta X_{(1)} = X_{(1)}\left(t_0 + T/2\right) - X_{(1)}\left(t_0 - T/2\right) = \int_{t_0 - T/2}^{t_0 + T/2} F\left(X_0, t\right)dt\,. \tag{3.12}$$

In this application, the initial time, t_0, is defined as the moment of apoapse passage, since the tidal perturbations are strongest at this point, and the method therefore yields the most accurate results when the orbital elements are defined at apoapsis. The method assumes coincidence of the rotating and inertial reference frames at the moment of apoapse passage to yield estimates for the changes in *C*, *L*, and *H* over one period. Using non-dimensional quantities (denoted with tildes),

$$\Delta\tilde{C} = -\frac{3}{2}\tilde{p}^{\frac{7}{2}}\left[\begin{array}{l} \cos^4\left(i/2\right)\sin 2\left(\omega+\Omega\right)\left(I_2^{-4} - I\right) \\ -\sin^4\left(i/2\right)\sin 2\left(\omega-\Omega\right)\left(I_{-2}^{-4} - I\right) \\ +\dfrac{1}{2}\sin^2 i \sin 2\Omega\left(I_0^{-4} - I\right) \end{array}\right] \tag{3.13}$$

$$\Delta\tilde{L} = -\frac{3}{2}\tilde{p}^{\frac{7}{2}}\left[\begin{array}{l}\cos^4(i/2)\sin 2(\omega+\Omega)I_2^{-4} \\ -\sin^4(i/2)\sin 2(\omega-\Omega)I_{-2}^{-4} \\ +\dfrac{5\pi}{2}\sin^2 i\sin 2\omega\dfrac{e^2}{\left(1-e^2\right)^{7/2}}\end{array}\right] \tag{3.14}$$

$$\Delta\tilde{H} = -\frac{3}{2}\tilde{p}^{\frac{7}{2}}\left[\begin{array}{l}\cos^4(i/2)\sin 2(\omega+\Omega)I_2^{-4} \\ -\sin^4(i/2)\sin 2(\omega-\Omega)I_{-2}^{-4} \\ +\dfrac{1}{2}\sin^2 i\sin 2\Omega I_0^{-4}\end{array}\right] \tag{3.15}$$

where $\Delta\tilde{C} = \dfrac{\Delta C}{N^2 r_s^2}$, $\Delta\tilde{L} = \dfrac{\Delta L}{N r_s^2}$, and $\Delta\tilde{H} = \dfrac{\Delta H}{N r_s^2}$. The nondimensional unit of time is 1/*N*, and the nondimensional unit of length is defined as $r_s = \left(\dfrac{GM_2}{N^2}\right)^{1/3}$, with $\tilde{a} = \dfrac{a}{r_s}$ and $\tilde{p} = \tilde{a}\left(1-e^2\right)$. Note that this form of nondimensionalization is unique, different from the standard quantities used when nondimensionalizing in the CR3BP. The integrals *I* and I_k^l appearing in Eqs. (3.12)-(3.14) are defined as

$$I = \frac{\sin\left(2\pi\tilde{a}^{3/2}\right)}{\tilde{p}^{3/2}\left(1+e\right)^2} \tag{3.16}$$

and

$$I_k^l = 2\int_0^{\pi}\left(1+e\cos\theta^*\right)^l\cos\left[k\theta^* - 2\tilde{a}^{3/2}\left(M-\pi\right)\right]d\theta^*. \tag{3.17}$$

These quantities arise after a change in integration variables from time to true anomaly; again the analysis assumes that a full 360º has been traversed by the true anomaly from one periapse passage to the next. When the tidal effects are large, this assumption can break down and, in reality, the interval from one periapsis to the next may be more or less than 360º. The changes in orbital elements are now computed, using

$$\frac{\Delta a}{a} = -\frac{\Delta C}{C}$$
$$\frac{\Delta e}{e} = -\frac{1-e^2}{e^2}\left[\frac{1}{2}\frac{\Delta C}{C} + \frac{\Delta L}{L}\right] \tag{3.18}$$
$$\Delta i = \left(\cot i\right)\left[\frac{\Delta L}{L} - \frac{\Delta H}{H}\right].$$

The accuracy of these predictions is investigated for varying initial values of *a*, *e*, and *i*. Not surprisingly, orbits characterized by smaller values of *a* are more accurately approximated by the tidal kick function, and predictions for orbits with higher eccentricity are more accurate than those for more circular orbits. For example, consider a set of orbits with initial conic period equal to 1,000 days, corresponding to a_0 = 320 R_S. For an initial eccentricity e_0 = 0.78 and quadrant angle -180º < Φ < 180º, the changes in orbital elements are calculated using two approaches: (*i*) using integration in the CR3BP and (*ii*) by the tidal kick function approximation. The output from the two methods is then compared. Recall that in the expression for the tidal kick function, the orbital elements are defined at orbit apoapsis. Therefore, for comparison, in this set of CR3BP simulations, the initial conditions are specified at apoapsis. Each trajectory is integrated forward to its next periapsis and backwards to its previous periapsis, and the osculating elements are computed at the two periapses and subtracted to yield the change from one periapsis to the next. The results appear in Figure 3.10. For this set of orbits, the kick function is a good approximation to the integrated case. The change in semi-major axis is estimated to within 0.48 R_S, which is 0.1% of the initial semi-major axis; the percent difference between the two methods remains below 2%, except for quadrant angles corresponding to Δa near zero. The estimate for Δr_p is accurate to within 1.61 R_S, and the percent difference between the integration and the kick estimate remains below 5% for most quadrant angles. Finally, the kick function approximates Δe to within 0.006, with a percent difference between the methods usually remaining below 7%. However, as the initial semi-major axis increases or as the initial eccentricity decreases, the accuracy of the estimates from the tidal kick function decreases. For example, for a larger orbit with an initial conic period of 2,000 days (a_0 = 320 R_S), the difference between the integrated results and the kick function estimate for Δa is up to 24 R_S, with a percent difference of 20-40% for most values of the quadrant angle. The difference between the estimate for Δr_p and the integrated result is up to 64 R_S, with a percent difference between 5-10% for most quadrant angles, and the percent difference in Δe ranges from 15-30% for most quadrant angles, with a difference between the two methods of up to 0.16.

Recall that since tidal acceleration impacts not only a, e, and i, but also the argument of periapsis, ω, one revolution from periapsis to periapsis does not necessarily complete 360°. The estimates for orbital element changes are derived for a full 360° revolution, and as a result, they more accurately reflect the changes after an integration through 360° rather than a periapsis-to-periapsis propagation. This is particularly true for more circular trajectories, which yield larger variations in argument of periapsis over one revolution. It is also noted that the change in argument of periapsis over one revolution is highly sensitive to initial conditions, and the methods used to derive estimates in the other orbital elements are less effective when applied to developing estimates for $\Delta\omega$.

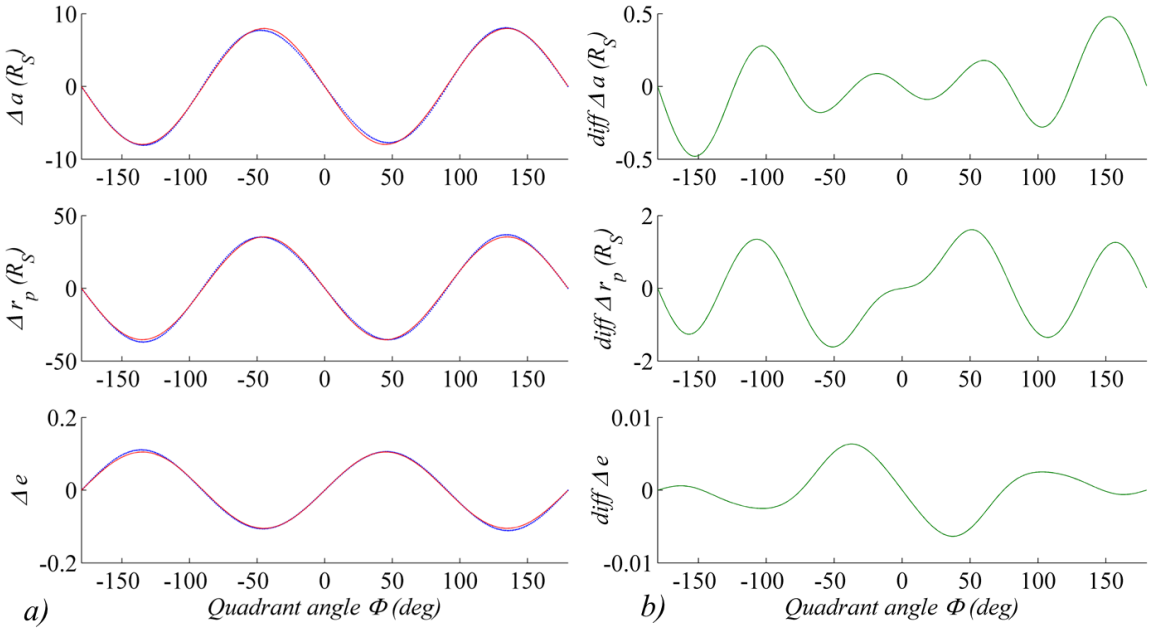

Figure 3.10 Change in orbital elements as a function of quadrant angle Φ (a) from simulations in the CR3BP (blue) as well as the tidal kick function approximation (red). Differences between the integrated results and the tidal kick function approximations (b) appear in green. Saturn-centered orbit, a_0 = 320 R_S, e_0 = 0.78.

3.3. Orbital Element Changes Over Time

For orbits that remain bounded at Saturn for multiple revolutions, apoapsis rotates through the quadrants as the trajectory evolves. The orbital elements, therefore, also evolve over time, moving through cycles of increasing and decreasing values. For example, consider the trajectory appearing in Figure 3.7 on the left: the trajectory that begins in quadrant IV and whose periapsis

is therefore raised after the first revolution. This trajectory is propagated for a longer timeframe so that the evolution of the orbital elements can be assessed. The trajectory appears in rotating and inertial views in Figure 3.11. Clearly, this is not a near-conic trajectory—the solar gravity has significantly affected the orbit. The osculating orbital elements over time appear in Figure 3.12. For approximately the first 90 years (about 3 periods of the primaries), the semimajor axis oscillates around 500 R_S as the trajectory rotates in a clockwise fashion through the quadrants. The periapse radius varies from about 32 R_S to about 230 R_S, and the eccentricity varies from around 0.5 to about 0.9. However, after this point, the variations (especially in eccentricity) begin to increase, and after approximately 122 years (about 4 periods of the primaries), this trajectory escapes the vicinity of Saturn through the L_2 gateway. Certain frequencies are apparent in the evolution of the orbital elements. Especially towards the beginning of the propagation, it requires just one period of the primaries for the trajectory to cycle through the four quadrants. This ~29-year period is visible in the oscillations. In addition, the orbital period associated with the trajectory, as defined by the time from one periapse passage to the next, ranges from about 2.5 years to about 4.5 years. This short period also appears in the oscillations, especially in eccentricity and periapse radius.

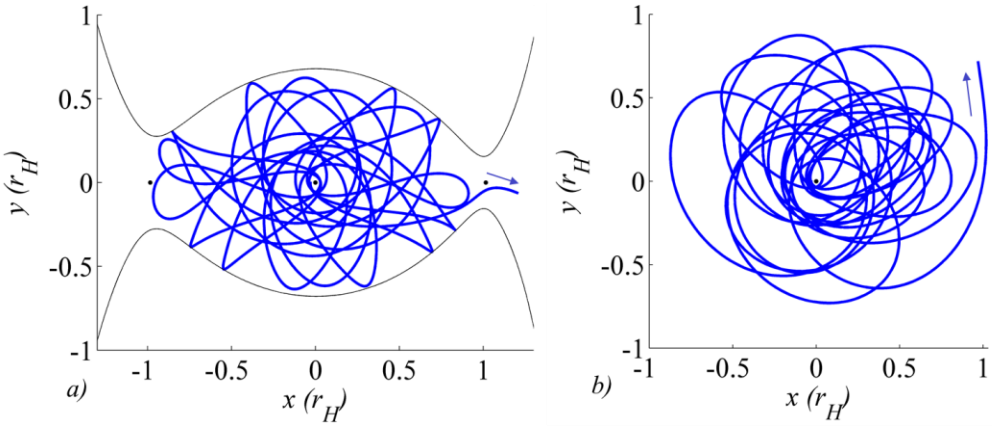

Figure 3.11 Saturn-centered trajectory propagated for 122 years in rotating (*a*) and inertial views (*b*). $J = J_1 = 3.0173046596239$ ($J < J_{L2}$).

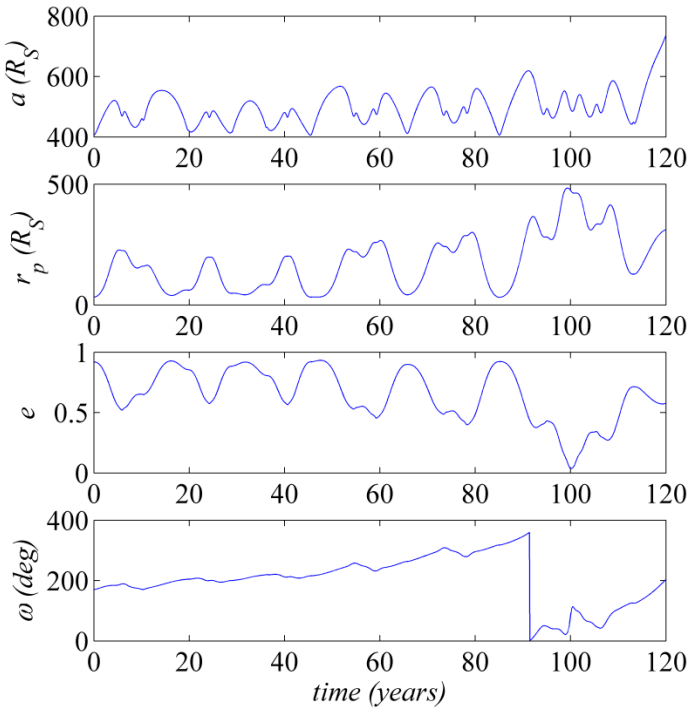

Figure 3.12 Osculating orbital elements over time for the trajectory appearing in Figure 3.11.

One significant goal in this investigation is the prediction of the eventual fate of a given trajectory, that is, if the path will remain in the vicinity of the smaller primary indefinitely or if the vehicle eventually escapes the region. A clue is revealed by plotting the eccentricity of the trajectory as it evolves over time against the osculating semimajor axis. Consider the trajectory appearing in Figure 3.11, which escapes after about 122 years. A similar trajectory at the same Jacobi Constant, $J = J_1 = 3.0173046596239$ ($J < J_{L2}$), remains in orbit about Saturn indefinitely. While it is not periodic or quasi-periodic, and although the ZVCs are open at this level of Jacobi Constant, the trajectory does not escape after a 2,000-year propagation. Little difference is evident between the two trajectories over a 120-year propagation, viewed in the rotating frame in Figure 3.13. The escaping trajectory appears in blue, the non-escaping trajectory appears in red. However, it is clear in the *e-a* plot (Figure 3.14) that there are significantly more variations in both eccentricity and semi-major axis in the escaping trajectory (blue) than in the non-escaping trajectory (red), even well before the escape occurs.

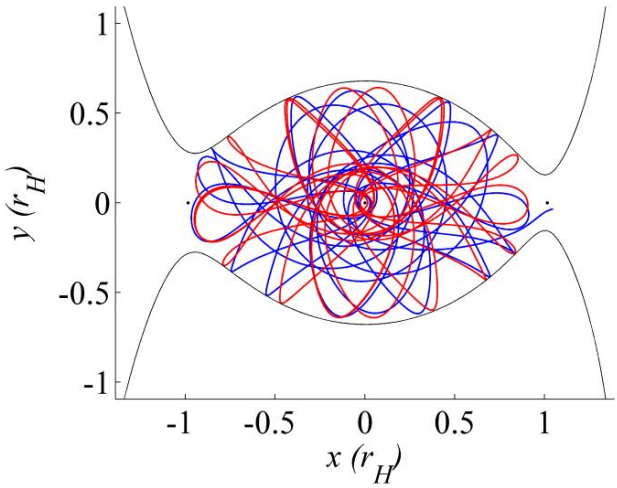

Figure 3.13 Escaping (blue) and non-escaping (red) trajectories propagated for 120 years. $J = J_1$.

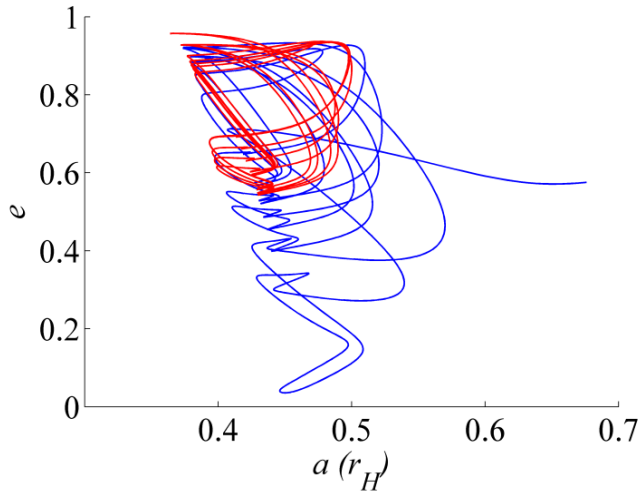

Figure 3.14 Eccentricity plotted against semi-major axis for escaping (blue) and non-escaping (red) trajectories propagated for 120 years.

4. UNDERSTANDING THE TIDALLY-INFLUENCED ENVIRONMENT: PERIAPSIS POINCARÉ MAPS

The analysis of the effects of tidal acceleration on individual trajectories in Chapter 3 provides insight into the dynamics of spacecraft and natural bodies in space. However, when designing a trajectory to satisfy given mission requirements, or attempting to understand the behavior of groups of natural bodies such as comets, the vast scale of the available design space calls for the introduction of additional tools. In particular, the periapsis Poincaré map is used to condense large quantities of information into a manageable and insightful format.

4.1. Short-Term Trajectory Behavior

After considering the effects of tidal acceleration on individual trajectories, it is useful to generalize the results. An investigation of short-term orbit behavior is based on the construction of periapsis Poincaré maps. Recall that in this type of map, the surface of section is the plane of periapsis passage, defined by the conditions $\dot{r}_2 = 0$ and $\ddot{r}_2 > 0$. For a given Jacobi Integral, or Jacobi value, a region on the surface of section is isolated within the zero-acceleration contour that forms the boundary between periapses and apoapses.[19] A set of initial periapse conditions is then defined within the contour. Each point within the region corresponds to the initial condition associated with a specific prograde planar trajectory about P_2; each trajectory is propagated forward in time to its subsequent periapsis. Four possible outcomes of this propagation exist: the spacecraft impacts P_2; the spacecraft escapes out the L_1 gateway; the spacecraft escapes through the L_2 gateway; or, the spacecraft remains captured near P_2, that is, it continues to evolve within the ZVCs. As an example, consider a spacecraft in the vicinity of Saturn in the Sun-Saturn system. For a Jacobi value $J = J_1 = 3.0173046596239$ ($J < J_{L2}$), each initial condition within the contour is propagated forward to its next periapsis; the integration is terminated early if the state reaches escape or impact. The resulting map, which displays approximately 60,000 periapsis points, appears in Figure 4.1. Each point within the contour is colored consistent with the outcome of the propagation: black corresponds to impact, blue reflects escape out L_1, red indicates escape through L_2, and grey signifies an orbit that remains captured. Note that well-

defined lobes exist in the map that identify the escaping trajectories. These lobes are analogous to the lobes defined for the HR3BP in Villac and Scheeres[43] and Paskowitz and Scheeres.[44] These lobes represent regions in which a periapsis occurs just prior to direct escape from the vicinity of Saturn; any trajectory with a periapsis in one of these lobes escapes prior to reaching its next periapsis. Conversely, a trajectory with periapsis lying outside a lobe does not escape before its next periapse passage. These lobes can, therefore, be considered gateways to escape: all escaping trajectories pass through one of these regions at the final periapse passage prior to escape. (While some trajectories pass through an additional periapse state near the L_1 or L_2 gateways, the final periapse passage close to the smaller primary occurs within the red or blue lobe. Of course, a Lyapunov orbit exists around both L_1 and L_2 at this value of J, but the focus of the investigation is on P_2-centered trajectories and transits through the gateways.) Similarly, the black regions represent initial conditions associated with orbits that impact Saturn prior to the next periapse passage.

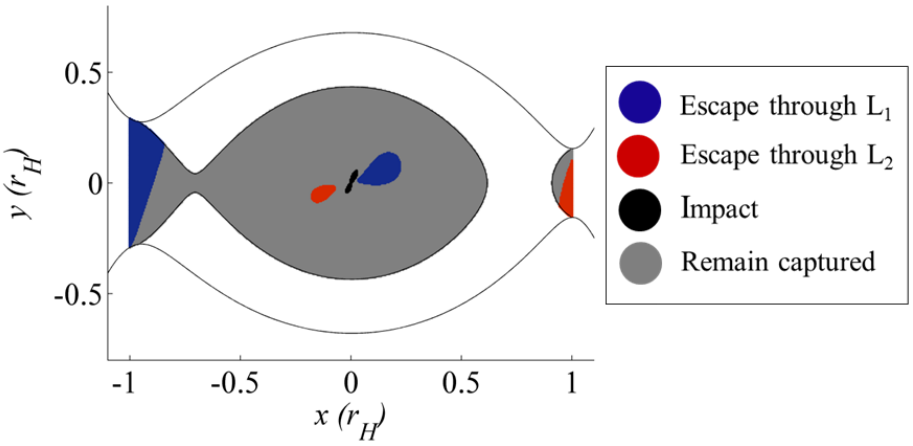

Figure 4.1 Initial condition map for one revolution, Sun-Saturn system, $J = J_1 < J_{L2}$.

If the initial conditions are propagated for a longer span of time, a similar initial condition map is created. Figure 4.2 represents an initial condition map that results when each trajectory is propagated for up to 6 revolutions. Again, integration is terminated if the trajectory escapes or impacts Saturn; if the path reaches its 6th periapse passage without impacting or escaping, it remains classified as captured. As before, the colors represent the fate of each trajectory. As expected, during the longer propagations, more trajectories escape or impact Saturn. The lobes from Figure 4.1 remain; they are joined by additional regions of escape and impact. Similar lobes

are defined for up to 4 periapse passages in the HR3BP by Paskowitz and Scheeres.[44] Note the near-symmetry that exists between the L_1 and L_2 escapes in Figure 4.1 and Figure 4.2. In the Hill 3-body problem, symmetry is exact, while in the CR3BP the symmetry properties slowly diminish for increasing values of μ.

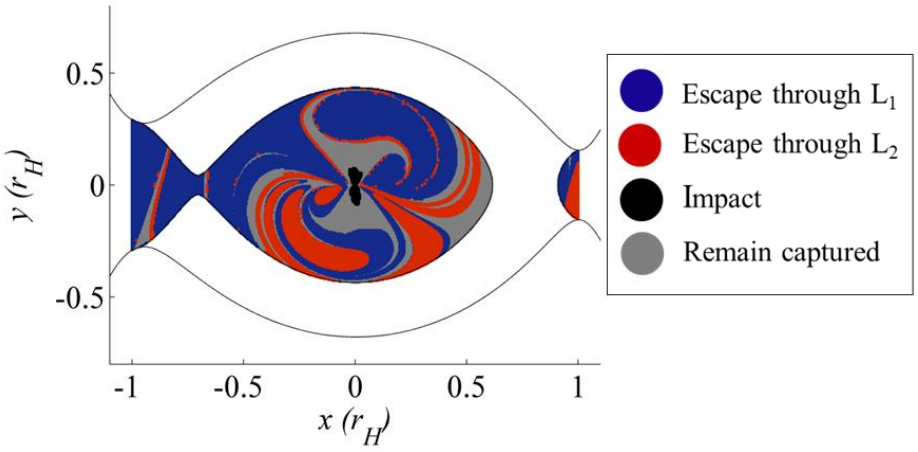

Figure 4.2 Initial condition map for six revolutions, Sun-Saturn system, $J = J_1 < J_{L2}$.

4.1.1. Interpretation in Terms of Quadrants

Due to tidal acceleration, the periapse radius of a trajectory that follows an apoapsis in quadrant I or III decreases over the course of one revolution and the eccentricity of the orbit increases. Therefore, trajectories oriented such that their apoapses lie in quadrants I and III possess the potential to either impact upon reaching periapsis (if the decrease in r_p results in a periapsis below the surface of P_2) or to escape (due to the increase in eccentricity). In general, a periapsis located in quadrant I is followed (or preceded) by an apoapsis in quadrant III, and vice versa. The locations of the escape and impact trajectories in Figure 4.1 and Figure 4.2 can therefore be understood in terms of quadrants. For the set of initial conditions defined above, the final periapse and apoapse locations associated with each trajectory appear in Figure 4.3. If the periapsis/apoapsis pair precedes impact, it is colored black. If it occurs just before an escape through L_1 (L_2), it is colored blue (red). Note that the escaping and captured trajectories are mainly characterized by apoapses in quadrants I and III, as expected. The exceptions are associated with escape trajectories that either achieve apoapsis conditions on their way out the gateway (see the green orbit in Figure 4.3), or with trajectories that enter the P_2 system and depart through the same gateway after several revolutions. Four sample trajectories appear in Figure

4.3. With an apoapsis in quadrant I, the red trajectory passes through the L_2 escape lobe at periapsis before departing out the L_2 gateway. Similarly, the blue trajectory moves from apoapsis in quadrant III through the lobe associated with L_1 escapes at periapsis; it subsequently escapes through L_1. The black orbit begins from a periapsis located in a black impact lobe. This trajectory passes through apoapsis in quadrant III, and its subsequent periapse radius is lowered sufficiently to result in an impact with Saturn. The green trajectory is an example of an orbit that achieves an additional apoapsis and periapsis near L_1 on its way out of the gateway. Note that it still passes through the L_1 direct escape lobe.

In summary, for the lobes associated with immediate escape in Figure 4.1, the trajectory is oriented in quadrant I or III such that the increase in eccentricity due to the tidal acceleration results in escape prior to another periapsis near Saturn. For the immediate impacts in Figure 4.1, the tidal acceleration does not result in escape, but the periapsis is lowered sufficiently that the radius falls below the surface of P_2.

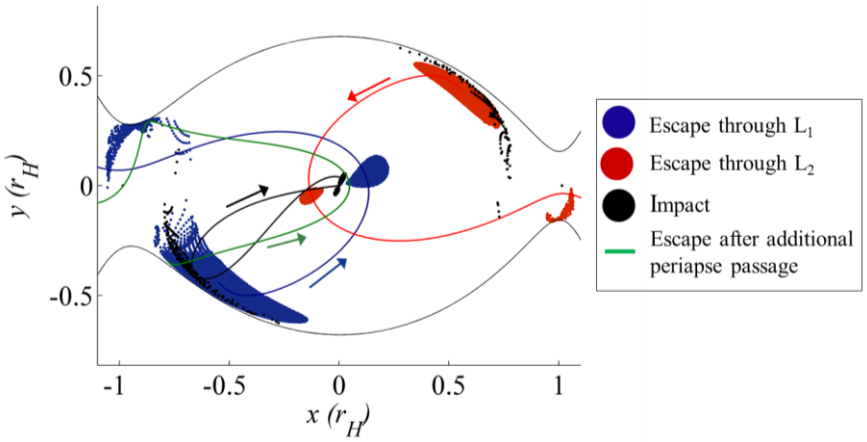

Figure 4.3 Periapse and apoapse locations immediately prior to escape/impact, and four sample trajectories. Sun-Saturn system, $J = J_1 < J_{L2}$.

4.1.2. Periapse Passages Prior to Escape

The regions defining initial conditions that result in escaping trajectories — the red and blue regions in Figure 4.2 — may be categorized by the number of periapse passages the spacecraft completes before escaping the vicinity of P_2. These maps appear in Figure 4.4, with each lobe numbered according to periapse passages prior to escape. The zones labeled "1" correspond to immediate escape; trajectories originating in zones labeled "2" pass through one additional

periapsis before escaping the vicinity of Saturn; and so on. A trajectory that remains in the vicinity of P_2 after the 6th periapse passage is classified as captured. Analogous regions are defined for up to three revolutions in the Hill problem by Paskowitz and Scheeres.[44] Figure 4.4 therefore maps each region forward: for example, an initial state in region 3 will, when it reaches its first subsequent periapsis, lie in region 2; on its second passage it will lie in region 1, and it will escape on the following revolution. As noted in Paskowitz and Scheeres,[44] some trajectories reach periapse conditions near L_1 or L_2 just prior to escape (see the green trajectory in Figure 4.3). This phenomenon is responsible for the overlap in the regions, for example, the lighter points bordering the otherwise darker immediate escape lobe. Regardless, the final periapse passage near P_2 for every escaping trajectory lies in one of the lobes corresponding to immediate escape. If these figures are flipped across the *x*-axis, they represent regions of entrance into the system rather than escape. That is, a trajectory will enter the vicinity of Saturn through one of the two gateways, and pass its first periapsis in the "1" lobe, its second periapsis in the "2" lobe, etc. The predictable nature of the locations of periapse passages over time is exploited in trajectory design applications.

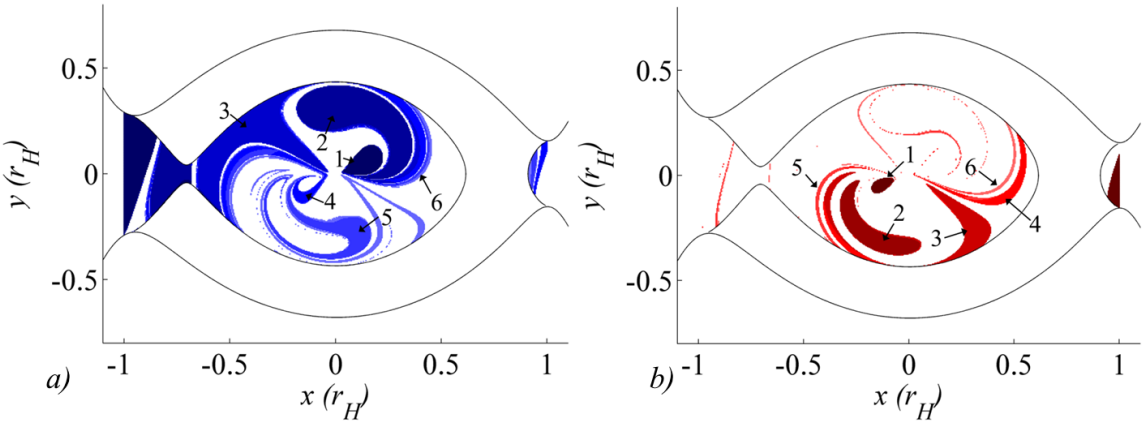

Figure 4.4 Escapes out L_1 (*a*) and L_2 (*b*). Numbered by periapse passages prior to escape. Sun-Saturn system, $J = J_1 < J_{L2}$.

4.1.3. Manifold Trajectories Associated with L_1 and L_2 Lyapunov Orbits

Recall that the invariant stable manifold tubes associated with the L_1 and L_2 Lyapunov orbits, at a given value of the Jacobi Integral, act as separatrices between escaping and captured trajectories in the vicinity of P_2.[60, 61] In a traditional Poincaré map created with a surface of

section defined, for example, as the plane $y = 0$, escaping trajectories correspond to points on the map that lie within the curve formed by a stable manifold tube; non-escaping trajectories lie outside the curves on the map that correspond to the manifold tubes. Similarly, in the periapsis Poincaré maps, regions of escape are delineated by the stable manifolds associated with the L_1 and L_2 Lyapunov orbits. The periapses of the stable manifold trajectories associated with the L_1 Lyapunov orbit appear overlaid in blue on the initial condition map in Figure 4.5(*a*). Note that the periapses of the manifold trajectories neatly outline the first several regions of escape through L_1. Similarly, the periapses of the trajectories lying on the stable manifold corresponding to the L_2 Lyapunov orbit appear in red in Figure 4.5(*b*). Again, these periapses outline the lobes of initial conditions escaping through L_2.

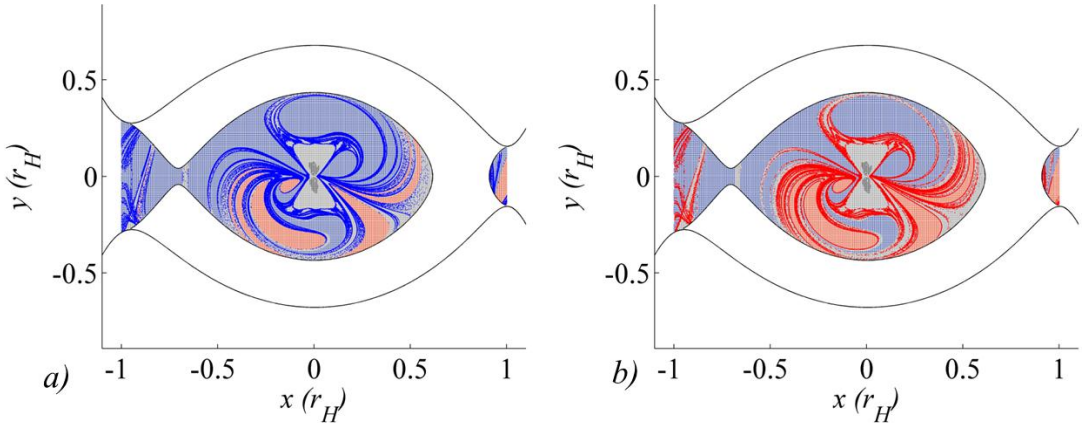

Figure 4.5 Peripses along L_1 (*a*) and L_2 (*b*) stable manifolds trajectories overlaid on the initial condition map, Sun-Saturn system, $J = J_1 < J_{L2}$.

The unstable manifold tubes corresponding to the L_1 and L_2 Lyapunov orbits delineate regions in the periapsis maps that correspond to trajectories that enter the vicinity of P_2 through the L_1 or L_2 gateways. The periapses of the unstable manifold trajectories are the mirror image (reflected across the *x*-axis) of the stable manifold apses. A trajectory that lies both within a stable L_1 tube and an unstable L_2 tube can represent a 'transit' trajectory, i.e., a trajectory that transits through both gateways. Such a trajectory enters the P_2 vicinity through L_2 and subsequently escapes, after an unspecified number of revolutions about P_2, through L_1.[38] Similarly, a transit trajectory may enter through the L_1 gateway and depart through L_2. A sample transit trajectory ($L_2 \rightarrow L_1$) appears in Figure 4.6. The first two lobes representing periapses within the L_2 unstable manifold appears in red; the first two lobes associated with the L_1 stable manifold appear in the figure in blue. A periapse state is selected that lies within both of the

tubes; it appears as a black dot. Note that it is located in an L_2 unstable lobe: the "2" lobe in Figure 4.4 (*b*), mirrored across the *x*-axis, which corresponds to the second periapsis after entering the vicinity of Saturn. The same initial state also lies in an L_1 escape lobe [the "2" lobe in Figure 4.4 (*a*)] and in a forward propagation, will pass through one more periapsis [in the "1" direct escape lobe in Figure 4.4 (*a*)] before escaping through L_1. The result is a transit trajectory that enters the vicinity of Saturn through L_2 and completes three periapse passages before escaping through the L_1 gateway, passing through three periapse lobes in sequence that highlight its passage. Such a transit trajectory can also be selected consistent with the number of periapse passages, between entering the P_2 vicinity and escaping, by employing the maps in Figure 4.4 along with their reflections across the *x*-axis. One advantage of the periapsis Poincaré map for trajectory design applications is that the maps exist in configuration space, allowing the selection of initial conditions based on the physical location of periapsis. Haapala and Howell[65] explore the use of periapsis Poincaré maps as a transit trajectory design tool.

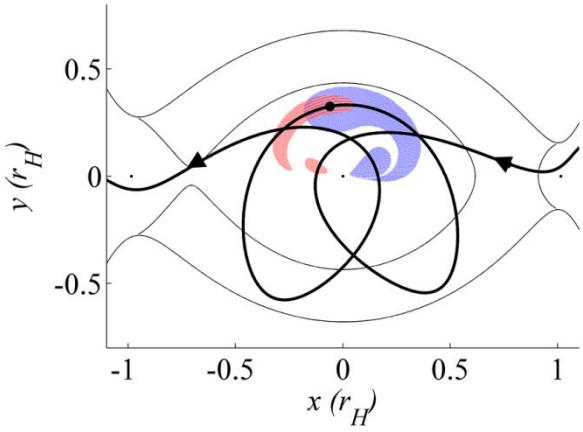

Figure 4.6 Initial condition map representing two periapse passages within the L_2 unstable (red) and L_1 stable (blue) manifold tubes; transit trajectory overlaid in black; $J = J_1 < J_{L2}$.

4.1.4. Initial Condition Maps for Changing Parameters

As each initial condition map is created, the mass parameter of the system, μ, and the Jacobi Constant, *J*, are held steady. That is, each map is representative of one P_1-P_2 system at a single energy level. Thus far, the initial condition maps apply to a single energy level, $J = J_1$, in the Sun-Saturn system. As either of these parameters is changed, the characteristics in the corresponding map also shift. Figure 4.7 and Figure 4.8 display a series of maps at varying energy levels in the Sun-Saturn system. Consistent with previous such maps, blue regions

represent initial states that escape through the L_1 gateway; red regions correspond to initial conditions that escape through L_2; trajectories originating in black regions impact the planet; and, initial conditions colored grey remain captured in orbit around Saturn for at least six revolutions without escaping or impacting the planet. Originating at a lower value of energy, such that the ZVCs are only slightly open at L_1, the energy is increased by increments until the ZVCs are wide open at both L_1 and L_2. Clearly, higher energies correspond to more escapes and impacts. In Figure 4.7(*a*) and (*b*), the ZVCs are closed at L_2, and therefore the only escaping trajectories depart the vicinity of P_2 through the L_1 gateway. That is, no red-colored initial conditions appear in the maps. As the energy is increased, the ZVCs open at L_2, and escapes through that gateway emerge in Figure 4.7(*c)*. As the energy of the spacecraft continues to increase and the value of Jacobi Constant decreases, the corresponding maps evolve: the regions of impact and escape expand, and the regions representing trajectories that remain captured contract. Note in particular the incremental increase in the size of the lobes corresponding to immediate escape (i.e., escape prior to reaching the first subsequent periapsis) as the value of energy grows. At high energies, the trajectories escape quickly, after few periapse passages. Higher energy maps appear in Figure 4.8. It is clear from these maps that for $J < J_{L2} - 0.0009$, trajectories that remain captured after 6 revolutions are nearly absent, and the majority of trajectories escape within three or fewer revolutions. For example, consider the initial condition map appearing in Figure 4.8(*d)*; this map corresponds to $J = J_{L2} - 0.0018$. If the L_1 and L_2 escapes are numbered according to the number of periapse passages prior to escape, it is clear that the majority of the trajectories at this energy level escape the vicinity of P_2 before three revolutions are completed, as illustrated in Figure 4.9. Note the well-defined lobes (labeled "1") corresponding to immediate escape. These lobes are analogous to the immediate escape lobes appearing in Figure 4.1. At higher energies, the blue and red regions, corresponding to escapes through L_1 and L_2 respectively, become nearly symmetric.

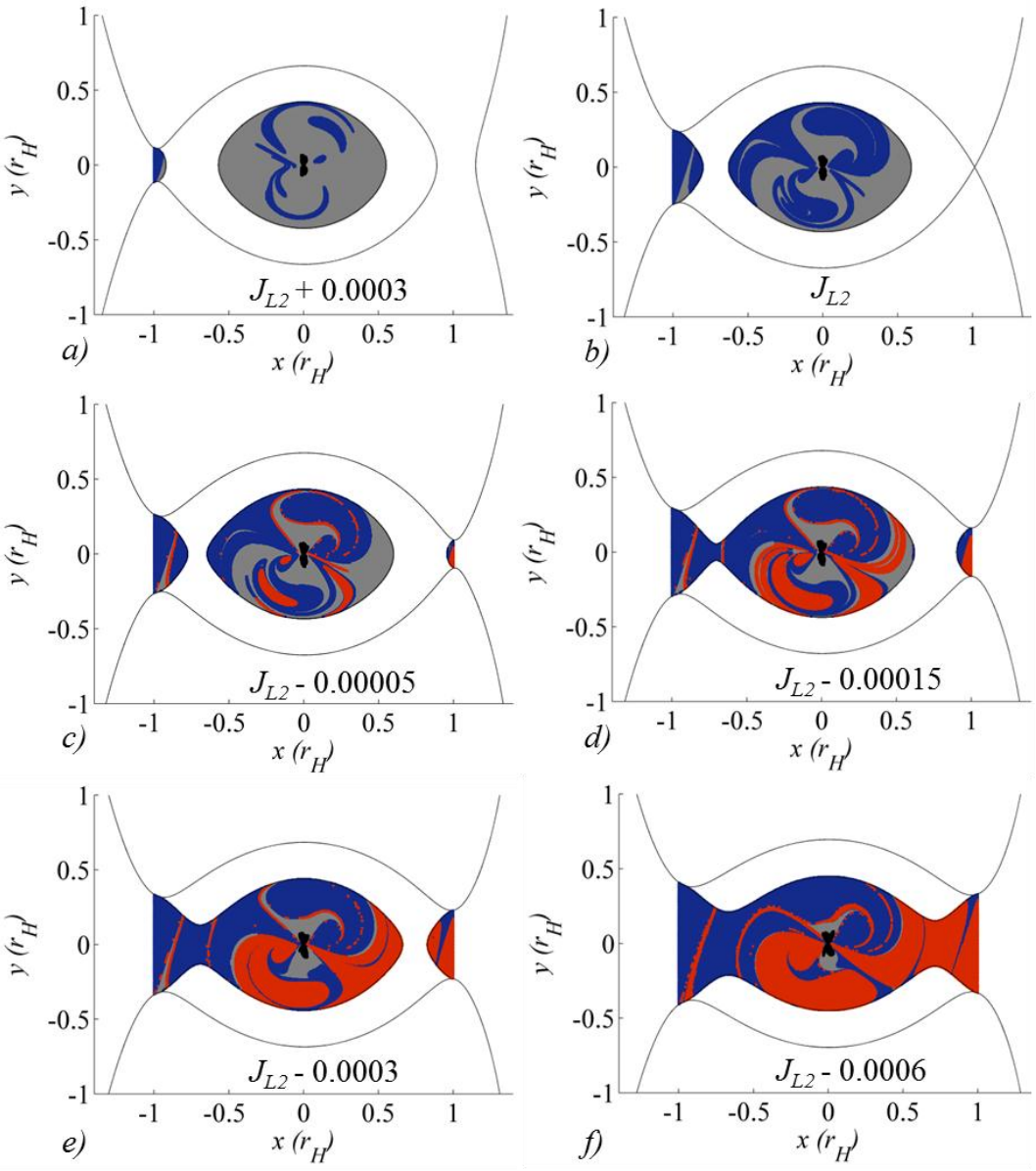

Figure 4.7 Initial condition maps for decreasing values of Jacobi Constant in the Sun-Saturn system.

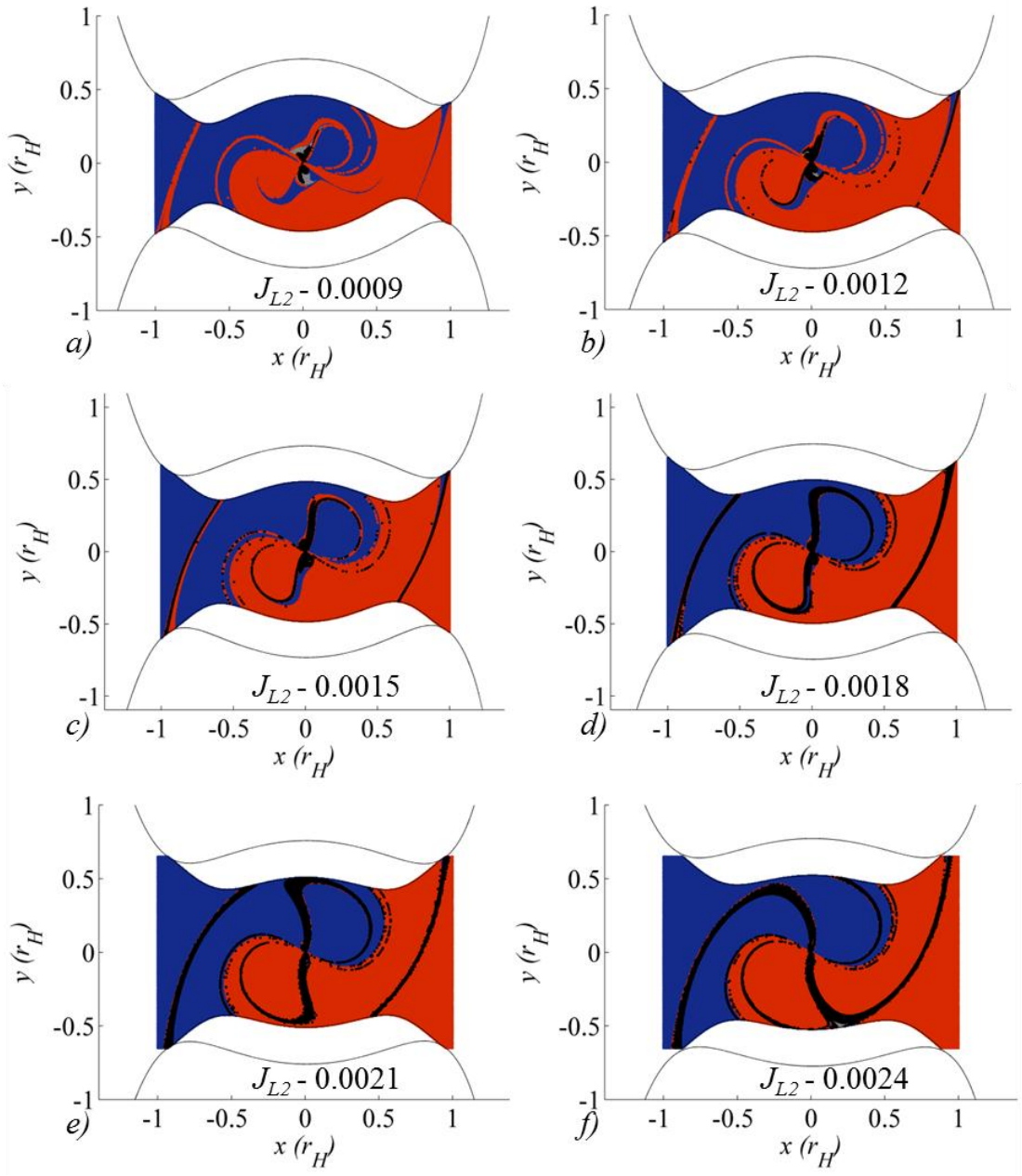

Figure 4.8 Initial condition maps for decreasing values of Jacobi Constant in the Sun-Saturn system.

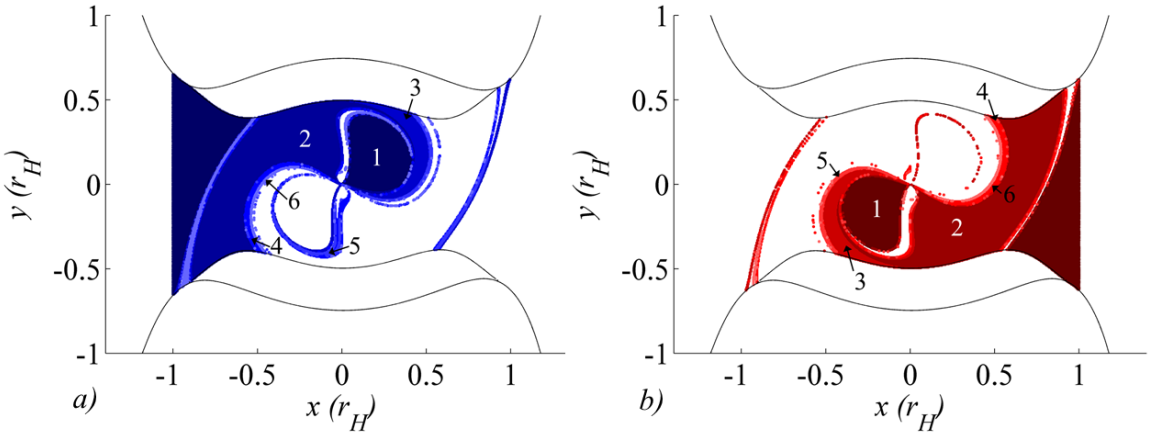

Figure 4.9 Escapes out L_1 (*a*) and L_2 (*b*). Numbered by periapse passages prior to escape; Sun-Saturn system, $J = J_{L2} - 0.0018$.

Thus far, each initial condition map has applied to the Sun-Saturn system. However, the maps are equally applicable to other P_1-P_2 systems. Initial condition maps for eight Sun-planet and planet-moon systems appear in Figure 4.10. To establish an equivalent standard for comparison, in each case the value of the Jacobi Integral is equal to the value associated with L_2. For μ approximately equal to 0, the ZVCs open at L_1 and L_2 simultaneously, so at an energy level such that $J = J_{L1} = J_{L2}$, no trajectories escape from the vicinity of P_2. As μ increases, the percentage of initial conditions corresponding to trajectories that escape through L_1 also increases. For example, in the Sun-Earth system, the L_1 gateway is only narrowly open when $J = J_{L2}$, so relatively few trajectories escape the P_2 vicinity after six revolutions. For P_1-P_2 systems with larger values of μ, on the other hand, the L_1 gateway is open wider when $J = J_{L2}$. For example, the larger value of μ associated with the Sun-Jupiter system leads to more L_1 escapes at this energy level, a fact that is clearly visible in the maps. Of course, the physical radius of P_2 significantly affects the number of initial points that result in impact trajectories. This effect leads to many more impact trajectories (colored black) in the planet-moon systems than in the Sun-planet systems appearing in Figure 4.10. In particular, few planar trajectories in the Jupiter-Europa system avoid impact with Europa. So, for a spacecraft arriving at Europa with an energy such that J is just below J_{L2}, nearly every trajectory will impact prior to completing 6 revolutions. This represents an inherent challenge in the design of a Europa Orbiter mission. Similarly, in the Earth-Moon, system, the majority of planar trajectories at this energy level impact the surface of the Moon or escape from its vicinity. Such initial condition maps are useful for the selection of

trajectories that escape from a smaller primary, such as a moon in a planet-moon system, or by exploiting symmetries in the system, for selecting trajectories captured by the smaller primary.[44] At a given energy level, an initial condition map for a particular P_1-P_2 system provides a visual tool that allows the selection of an initial periapsis state that automatically leads to escape through the desired gateway or impact into the surface of P_2. Also of interest are capture regions that continue to exist after multiple apoapse passages. These regions represent sets of initial conditions that neither impact nor escape from P_2 — initial conditions that represent potential long-term orbits about P_2.

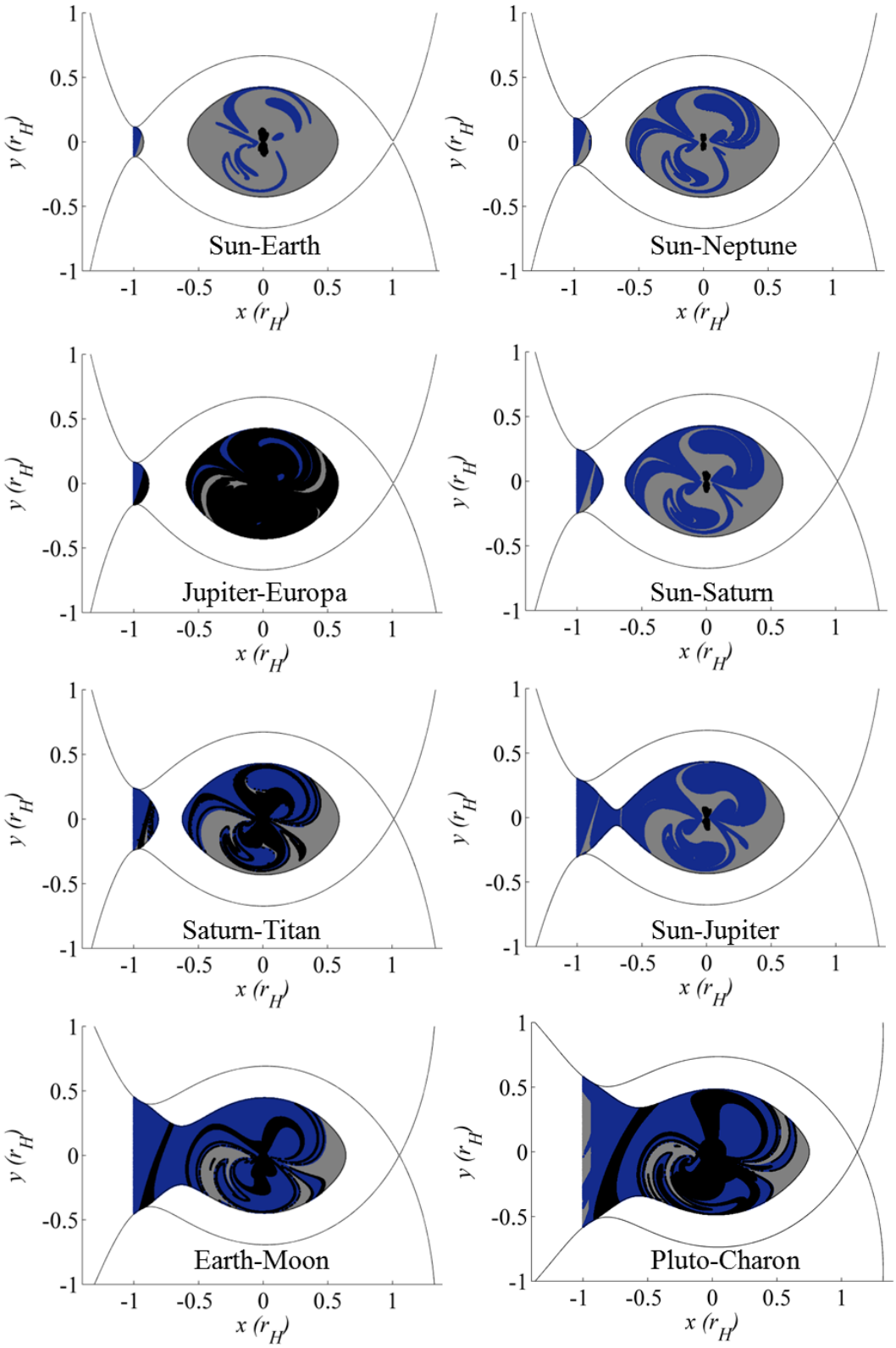

Figure 4.10 Initial condition maps for $J = J_{L2}$ for increasing values of μ.

Of particular interest here is a comparison between several Sun-Saturn and Saturn-Titan maps. The mass parameter associated with the Saturn-Titan system, $\mu = 2.3658\times10^{-4}$, is similar in value to that of the Sun-Saturn system, $\mu = 2.8580\times10^{-4}$. Thus, for an equivalent energy level, the regions of escape are similar in appearance between the two systems. However, in units of Hill radii, Titan's radius ($r_T = 4.916\times10^{-2}\ r_H$) is much larger than that of Saturn ($r_S = 9.206\times10^{-4}\ r_H$) and, consequently, many more initial states lead to impact in the Saturn-Titan system as compared to the Sun-Saturn system. A comparison of initial condition maps appears in Figure 4.11 for one revolution for the two systems. In each case, $J = J_1 = J_{L2} - 1.38\times10^{-4}$. While the lobes corresponding to immediate escape through both the L_1 and L_2 gateways appear nearly identical, the black region, corresponding to impact at the subsequent periapsis, in the Saturn-Titan map is far more prominent than in the Sun-Saturn map. Similarly, a comparison of the same two sets of initial conditions propagated for up to 6 revolutions appears in Figure 4.12. Again, impacting trajectories comprise a significantly larger percentage of the Saturn-Titan map as compared to the Sun-Saturn map. In fact, it is clear from Figure 4.12(*b*) that few trajectories at this energy level remain in orbit about Titan after 6 revolutions. Nearly all have either escaped Titan's vicinity or impacted its surface.

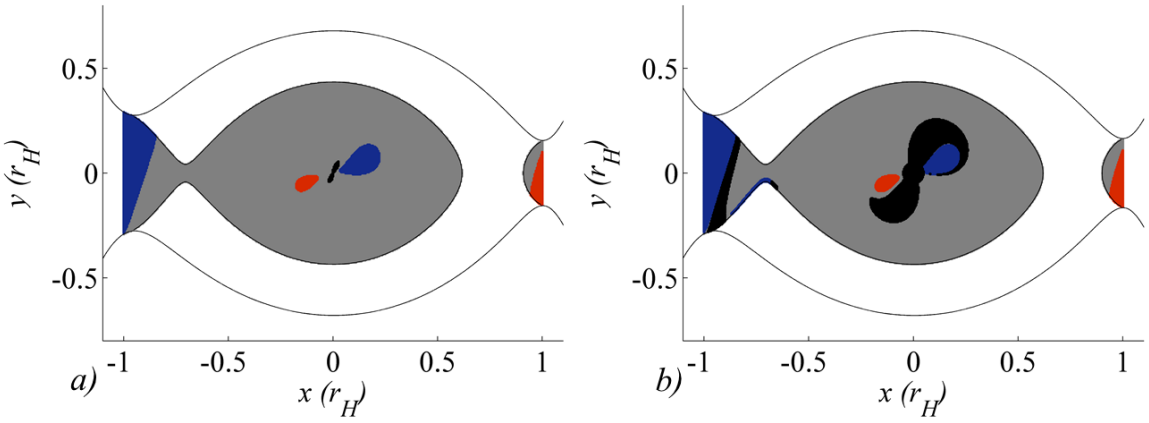

Figure 4.11 Initial condition maps for one revolution, Sun-Saturn system (*a*) and Saturn-Titan system (*b*).

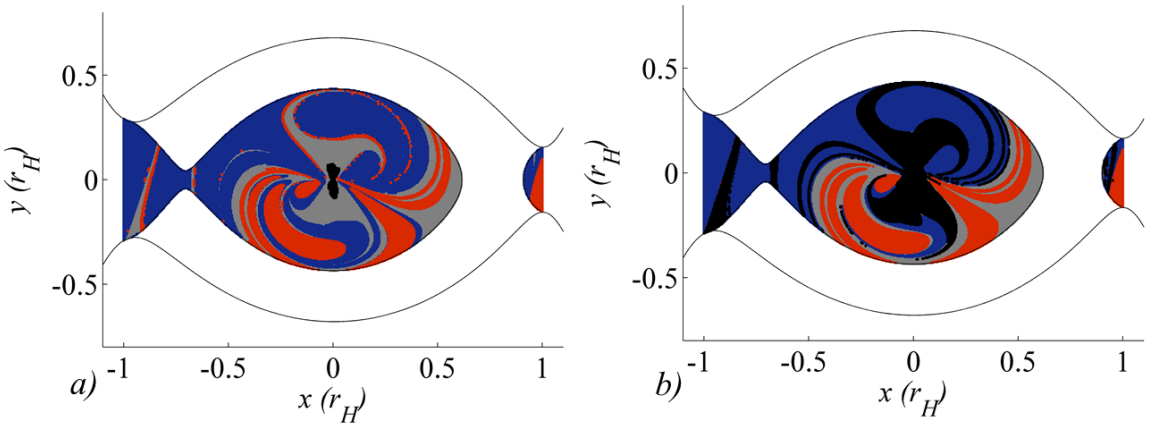

Figure 4.12 Initial condition maps for six revolutions, Sun-Saturn system (*a*) and Saturn-Titan system (*b*).

4.1.5. Change in r_p Over One Revolution

The examination of initial condition maps has, thus far, focused on characterizing the design space in terms of the sets of initial conditions that lead to escape or impact. However, periapsis Poincaré maps are also a valuable design tool for describing the effects of tidal acceleration on trajectories that remain in orbit about P_2 for one or more revolutions. In Chapter 3, the tidal influence on orbital elements was investigated for individual trajectories. By applying periapsis Poincaré maps, this information can be condensed for large groups of orbits, yielding a visual tool that supplies a broad understanding of the design space.

This investigation begins with a closer examination of trajectories that remain in orbit about the smaller primary after a single revolution. That is, the initial focus is on the trajectories resulting from initial conditions colored grey in Figure 4.1. Each orbit is considered in terms of the effect of tidal acceleration on periapse radius, and the resulting information is displayed in a periapsis Poincaré map. Consider again an energy level such that $J = J_1$. In Figure 4.13, each initial state in the Sun-Saturn system that remains in orbit after a single revolution is colored according to the change in periapse radius from one periapsis to the next. Solar gravity results in a rise in the periapse distance in trajectories represented in red. Initial states colored blue experience a decrease in periapse radius over one revolution. It is clear that trajectories oriented in quadrants I and III generally experience a decrease in periapse radius over one revolution, while trajectories in quadrants II and IV tend to undergo an increase in periapse radius during a

single orbit. Note that the lobes associated with immediate escape appear in white; these lobes are oriented in quadrants I and III.

In Chapter 3, it is noted that for smaller trajectories, the tidal effects are smaller, and the associated changes in orbital elements follow neat patterns. By inspecting a periapsis Poincaré map for a lower-energy set of trajectories, these neat patterns are apparent in Δr_p. Consider a set of trajectories with $J = J_{L2} + 0.01$. At this energy level, the ZVCs are completely closed. The values of Δr_p are an order of magnitude smaller than in the previous, higher-energy case, and it is clear that the maximum change in r_p is associated with quadrant angles approximately 45° from the Sun-Saturn line. Recall that quadrant angles are defined in terms of the angle at apoapsis, while this map displays the location of periapsis. The locations of the regions of maximum Δr_p are offset from 45° due to the rotation of the primaries relative to the spacecraft trajectory in the time between initial periapsis and apoapsis.

This broad look at the design space is consistent with the analysis of solar gravity by quadrants detailed in Chapter 3. However, rather than looking at the effects of tidal gravity on a small subset of the design space at a time, the periapsis Poincaré map allows a quick look at the tidal effects on every trajectory at a given energy level.

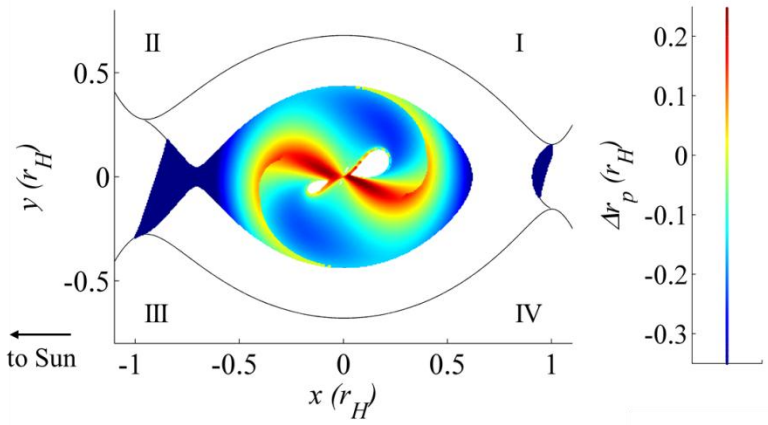

Figure 4.13 Change in r_p over one revolution for captured trajectories in the Sun-Saturn system, $J = J_1$.

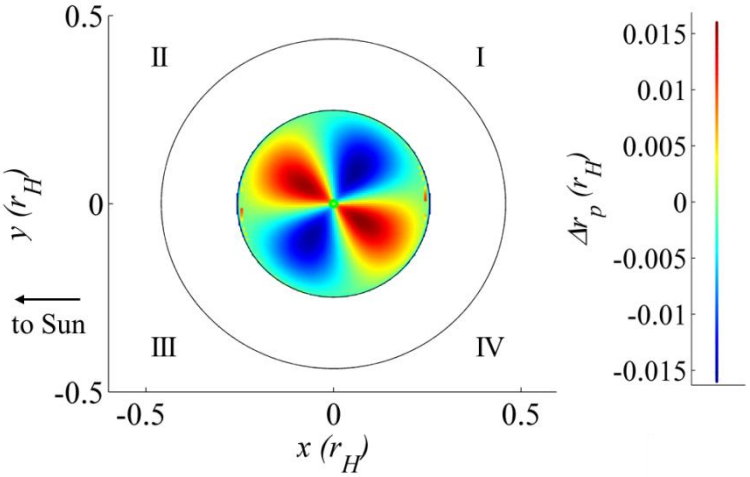

Figure 4.14 Change in r_p over one revolution for captured trajectories in the Sun-Saturn system, $J = J_{L2}+0.01$.

4.1.6. Retrograde Behavior

Thus far, only prograde trajectories have been examined. However, periapsis Poincaré maps also reveal information about retrograde trajectories in orbit around the smaller primary. As discussed in Chapter 3, retrograde orbits tend to be more stable than prograde trajectories; that is, at a given energy level, fewer retrograde trajectories escape the vicinity of the smaller primary as compared to prograde trajectories at the same value of Jacobi Constant. In fact, the initial condition maps for retrograde trajectories in the Sun-Saturn system at $J = J_1$ are entirely grey — no trajectories either escape or impact P_2. For a higher energy, escapes and impacts do appear on retrograde initial condition maps. Consider an energy level such that $J = 3.008864$, halfway between the values associated with L_2 and L_3. The associated initial condition map for a single revolution appears in Figure 4.15. The small regions of escaping and impacting trajectories near Saturn remain far from the ZVCs. Sample escaping and impacting trajectories, originating from the points marked in Figure 4.15, appear in Figure 4.16(*a*). A sample trajectory that remains captured appears in Figure 4.16(*b*), propagated for one period of the primaries, about 29 years. Note the elongation of this retrograde trajectory along the *y*-axis. This *y*-direction elongation is typical of retrograde trajectories. In contrast, prograde trajectories tend to be elongated along the rotating *x*-axis.

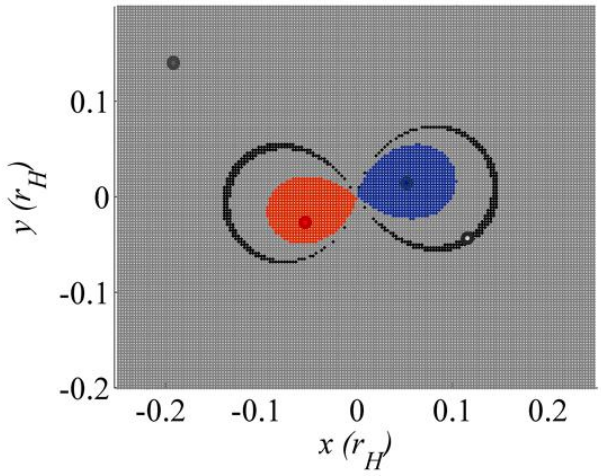

Figure 4.15 Initial condition map for retrograde trajectories in the Sun-Saturn system, $J = 3.008864$.

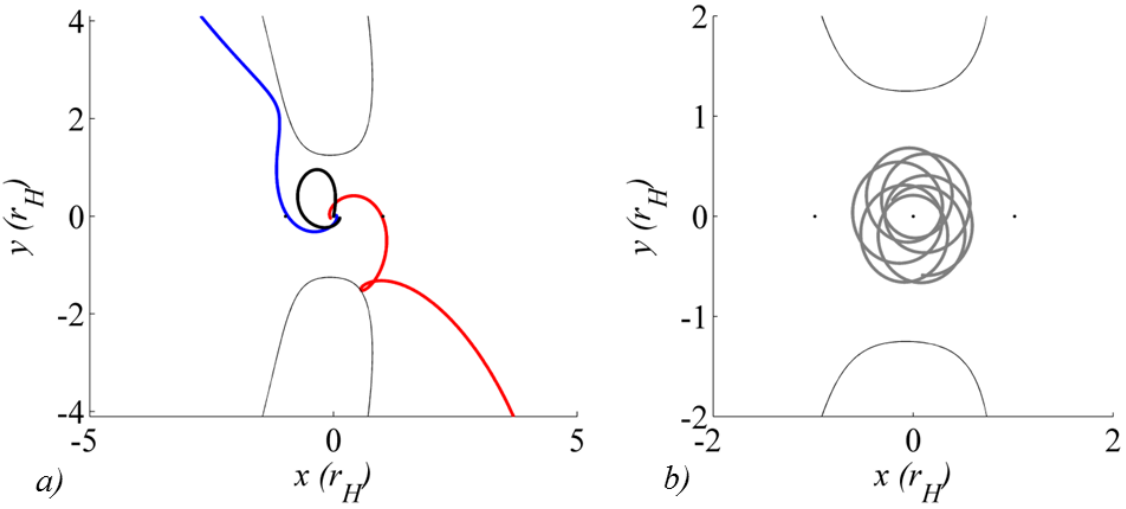

Figure 4.16 Four retrograde trajectories in the Sun-Saturn system with $J = 3.008864$. Initial conditions from the marked periapses in Figure 4.15.

4.1.7. Out-of Plane Behavior

The initial condition maps that appear in Figure 4.1-Figure 4.13 represent prograde planar trajectories; these maps are now generalized to explore out-of-plane trajectories. In 3D space, the ZVCs and the contours that separate periapses from apoapses become surfaces. However, adding a *z*-component to the position and velocity along a trajectory complicates the visualization of the solution space. In the planar case, for each (*x*, *y*) position coordinate, the velocity magnitude is specified by the Jacobi Constant, and the velocity direction is specified by the apse condition, which requires that the velocity be perpendicular to the position vector. Hence the position coordinate defines a single prograde trajectory (or one retrograde trajectory). In 3D space, however, the velocity direction is no longer completely constrained by the (*x*, *y*, *z*) position coordinate; the apse condition only restricts the velocity to a plane normal to the position vector. To manage this complication, a plane is defined at r_{p0} such that the position vector is normal to the plane. Then, a velocity angle is introduced in this plane to isolate the velocity direction. Consider a trajectory characterized by a periapsis located at a particular position in space denoted by (*x*, *y*, *z*). The velocity angle ϕ is defined as the angle between the *x*-*y* plane and the velocity vector, as depicted in Figure 4.17.

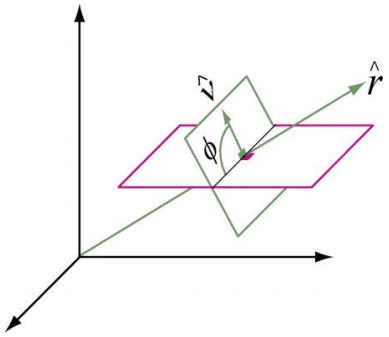

Figure 4.17 Velocity angle ϕ between the *x*-*y* plane and the velocity vector.

In this analysis, the space inside the 3D periapsis contour is populated with initial conditions possessing a given Jacobi Constant and velocity angle. Each initial state is propagated forward in time until arrival at a subsequent periapsis occurs or until the trajectory impacts P_2 or escapes through the L_1 or L_2 gateways. Three-dimensional lobes, analogous to the planar lobes in Figure 4.1, are produced. Consider a velocity angle $\phi = 0°$, which corresponds to an initial velocity vector parallel to the *x*-*y* plane for each periapse location in (*x*, *y*, *z*) space. The corresponding initial condition map appears in Figure 4.18 for $J = J_1$ in *x*-*y* (*a*) and *x*-*z* (*b*) projections. As

before, blue signifies trajectories that escape out L_1, red denotes trajectories that escape out L_2, and black corresponds to impact trajectories. As the velocity angle ϕ increases, the corresponding lobes representing escape and impact shrink. For example, the 3D lobes appear in Figure 4.19 for two larger values of ϕ. For ϕ = 11.5º in Figure 4.19(*a*), both the L_1 and L_2 lobes have decreased in size compared to the lobes for ϕ = 0º. At a higher velocity angle, ϕ = 22.9º in Figure 4.19(*b*), the L_1 lobe is still smaller, and the L_2 lobe has disappeared entirely. At this and larger velocity angles, no trajectories escape through the L_2 gateway even though the zero-velocity surfaces are open at L_2. This decrease in lobe size is consistent with the fact, noted above, that the influence of the tidal acceleration is at a maximum for planar trajectories.

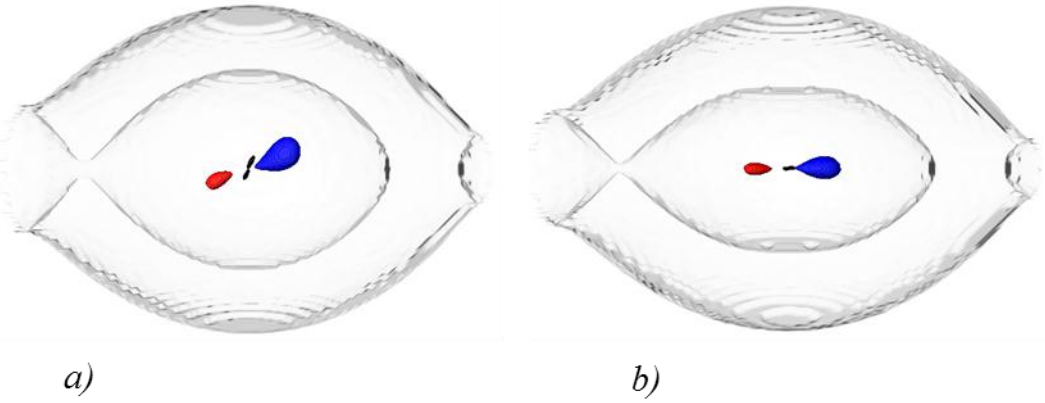

Figure 4.18 Three-dimensional initial condition maps for one revolution. *x-y* view (*a*) and *x-z* view (*b*). Sun-Saturn system, velocity angle ϕ = 0º, $J = J_1$.

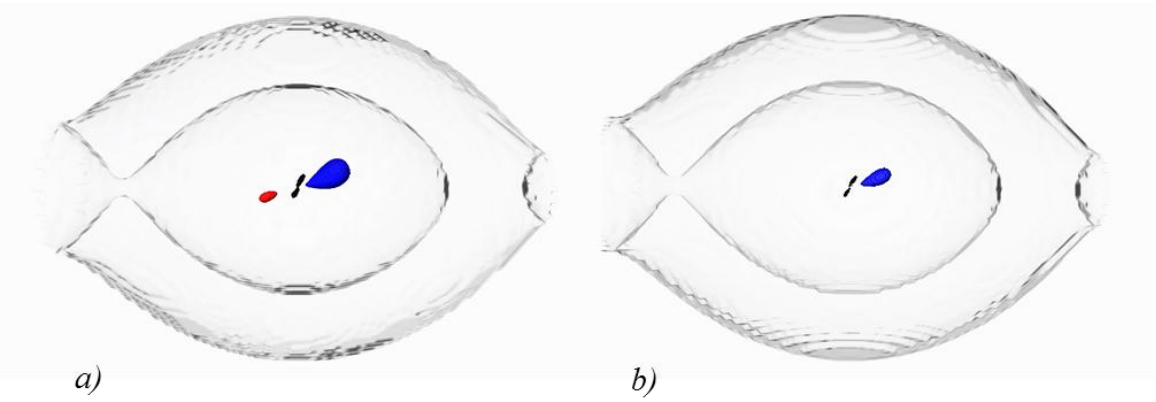

Figure 4.19 Three-dimensional initial condition maps for one revolution. x-y views, Sun-Saturn system, $J = J_1$, velocity angle ϕ = 11.5º (*a*), ϕ = 22.9º (*b*).

As in the planar case, varying the Jacobi Constant changes the size and shape of the 3D escape lobes. For example, consider a higher-energy case with $J = J_1 - 0.001 = 3.0163$. At this energy level, the zero-velocity surfaces are open much wider at both the L_1 and L_2 gateways. The corresponding 3D escape lobes are also larger: more trajectories escape the vicinity of P_2 at this higher energy. The 3D initial condition map for one revolution for velocity angle $\phi = 0^o$ appears in Figure 4.20 in an *x*-*y* view (*a*) and *x*-*z* view (*b*).

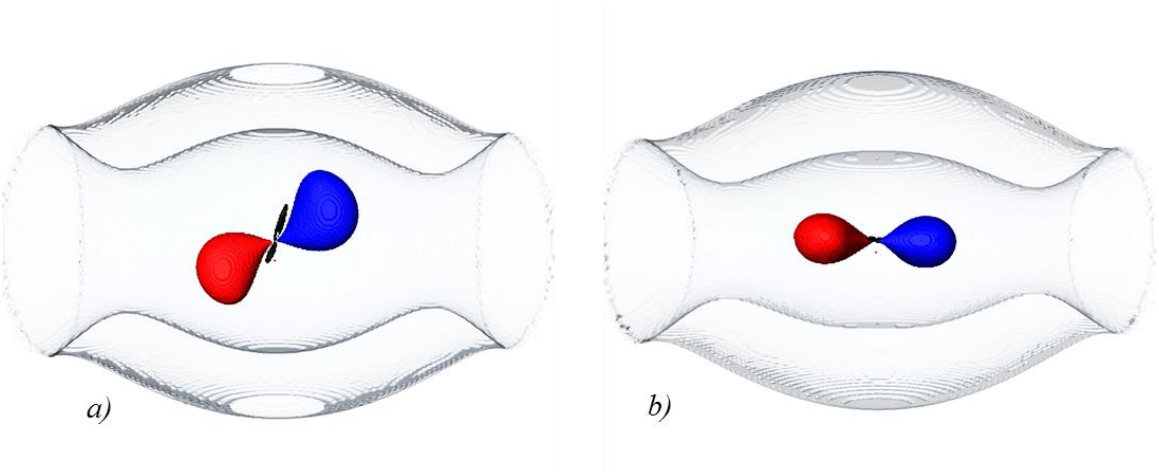

Figure 4.20 Three-dimensional initial condition maps for one revolution. *x*-*y* view (*a*) and *x*-*z* view (*b*). Sun-Saturn system, velocity angle $\phi = 0^o$, $J = J_1$-0.001.

When each initial periapsis is propagated for up to 6 revolutions, the 3D case again mirrors the planar case, and lobes are produced that represent the placement of periapses prior to escape. Such a map appears in Figure 4.21. This map corresponds to escape trajectories for initial periapses with four velocity angles: $\phi = 0°$, 11.5°, 17.2°, and 22.9°. Escapes through L_1 are plotted in shades of blue and L_2 escapes in red, with darker colors signifying fewer periapse passages remaining until escape. The patterns in the out-of-plane maps correspond to the planar maps appearing in Figure 4.9.

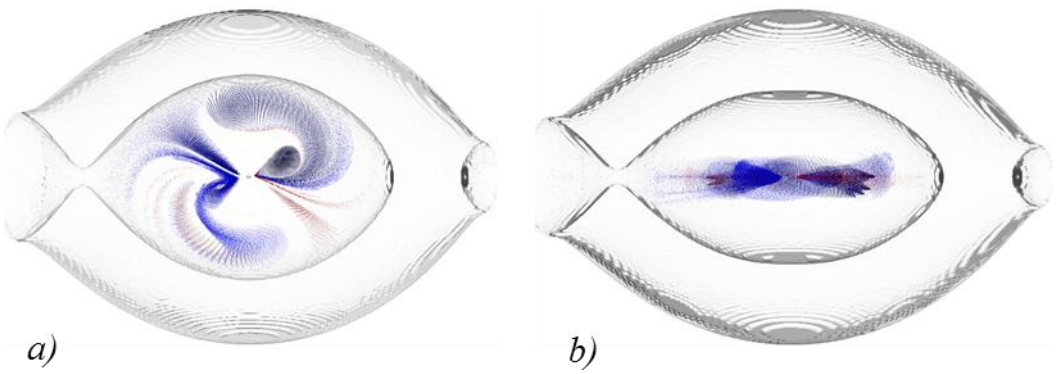

Figure 4.21 Initial condition map for up to 6 revolutions; velocity angles ϕ = 0°, 11.5°, 17.2°, and 22.9°, *x*-*y* view (*a*) and *x*-*z* view (*b*), Sun-Saturn system, $J = J_1$.

4.1.8. Relationship to Weak Stability Boundary Theory

Weak Stability Boundary (WSB) Theory was proposed by Belbruno[31] in 1987 as a method for the design of Earth-Moon ballistic transfers. The WSB is described as "a region in the phase space where the perturbative effects of the Earth-Moon-Sun acting on the spacecraft tend to balance"[32] or "a transition region between the gravitational capture and escape from the Moon in the phase space."[66] The theory serves as one approach to identify the boundary between stable and unstable trajectories in the vicinity of the Moon in the Earth-Moon system. The WSB is defined in terms of the Keplerian energy of the spacecraft, h_K, where

$$h_K = \frac{\mu}{2a}. \tag{4.1}$$

Consider a P_2-centered trajectory with initial conditions defined at periapsis and with negative Keplerian energy, i.e., an instantaneously elliptical orbit. The periapse angle and radius are represented by ω_{r0} and r_{p0} respectively. Then, in terms of osculating elements, the Keplerian energy at periapsis is evaluated

$$h_K = \frac{\mu}{2}\frac{e-1}{r_{p0}}. \tag{4.2}$$

From WSB definitions,[67] the trajectory is considered *stable* if, after leaving its initial periapsis, it completes a full revolution around P_2 without orbiting P_1 and passes through the angle ω_{r0} with negative Keplerian energy. The orbit is labeled *unstable* if either of these two conditions is not met.

Recent examinations of WSB theory include those by García and Gómez[67] as well as Sousa Silva and Terra.[68, 69] Both groups create initial condition maps similar to the planar maps in Section 4.1 of the present work. However, the initial condition maps in the WSB studies are created with constant initial osculating eccentricity, in contrast to the initial condition maps in the current investigation, where Jacobi Constant is maintained at a steady value across each map. Additionally, rather than defining the concept of stability in terms of Keplerian energy, the current investigation focuses simply on the distinction between orbits that escape (passing beyond L_1 and L_2) or remain captured in the P_2 vicinity. The structure of the maps with eccentricity held constant is relatively complex, with an unclear boundary between stable and unstable orbits.[i] For prograde trajectories at high eccentricities, Sousa Silva and Terra[69] note that the measurement of the Keplerian energy loses meaning as an indicator of stability in light of the heavy influence of Earth gravity on the trajectories. By contrast, when the constant parameter across each map is the value of Jacobi Constant rather than osculating eccentricity, and the trajectories are categorized according to escape/non-escape rather than WSB-type stability, the map structure remains relatively simple. In the planar problem, the stable manifolds of the associated Lyapunov orbits then define the clear boundary between escaping and non-escaping orbits, and the initial condition maps become simple to interpret and use for preliminary mission design. The WSB theory has successfully been used to design Earth-Moon ballistic transfers in the Sun-Earth-Moon system.[32] However, to predict the behavior of large groups of trajectories in a regime where the gravitational influence of the distant larger primary is significant, conic quantities are sometimes difficult to interpret and additional indicators of trajectory characteristics are also useful.

4.2. Long-Term Trajectory Behavior

The initial condition maps relate initial periapses to the fate of the trajectory after a given propagation time, revealing information about the short-term behavior of the full set of trajectories. Another type of periapsis Poincaré map is useful for the investigation of the long-term evolution of trajectories in the vicinity of P_2 in the CR3BP. Long-term periapsis Poincaré maps are created with a surface of section at periapsis; the state corresponding to each periapsis

[i] Sousa Silva and Terra[69] note that the original definition of stability as defined in WSB theory is restricted by the validity of the two-body approximation; the WSB definition of stability "is not always consistent with the highly nonlinear behavior of the trajectories."

as the trajectory evolves is recorded over a long-term propagation. Particular attention is focused on the grey regions of the initial condition map appearing in Figure 4.2, that is, trajectories that remain captured about the smaller primary for multiple revolutions.

4.2.1. Periapse Profiles

An initial step towards understanding the long-term behavior of a collection of trajectories involves the examination of a single trajectory. When a single initial periapsis, selected from the captured region in the short-term initial condition map, is propagated for an extended span of time, a pattern emerges in the subsequent periapse locations relative to P_2. This pattern is a signpost that reveals information about the trajectory's characteristics. If the ZVCs are open, trajectories characterized by periapses that form chaotic patterns tend to escape the vicinity of P_2, while trajectories that remain captured for extended intervals of time possess periapses that form neat patterns in the rotating frame. At a given energy level, and for a particular P_1-P_2 system, a specific set of periapse profiles exist for non-escaping trajectories. For example, consider a set of trajectories in the Sun-Saturn system characterized by a Jacobi value $J = J_1$ such that the ZVCs are open at both L_1 and L_2. The ordered periapse profiles created by trajectories that remain captured fall into several types. For $J = J_1$, the profiles fall into six categories that are illustrated by the trajectories in Figure 4.22 in the rotating frame and Figure 4.23 in an inertial reference frame. Each trajectory is propagated for ~33 periods of the primaries, or 1,000 years in the Sun-Saturn system, and is colored with its periapse locations plotted in black. Note the differing shapes of each set of black periapse points; this shape defines the periapse profile. The first example, appearing in Figure 4.22(*a*), is a 'figure 8' shape, generated in this case with an initial periapsis defined by $r_{p0} = 0.125 r_H$ and $\omega_{r0} = 91.67°$. Trajectories generating figure 8-shaped periapse profiles tend to fill out the ZVCs near $x = 0$ but remain distant from the libration points. In addition, the argument of periapsis in the inertial frame for figure 8-type trajectories can move quite slowly; the figure 8-type trajectory represented in Figure 4.22*(a)* and Figure 4.23(*a*) is quasi-frozen in the inertial frame, where the term quasi-frozen denotes an orbit with limited variation in the argument of periapsis, ω_i. The second periapse profile is an 'hourglass' shape. An example of this profile is represented by the black periapse points in Figure 4.22(*b*); this example results from an initial periapsis with $r_{p0} = 0.125 r_H$ and $\omega_{r0} = 48.70°$. Such trajectories tend to remain clear of the ZVCs near $x = 0$ and extend further towards the libration points than do figure 8-type trajectories. The arguments of periapsis in the inertial frame for hourglass-type

of trajectories tend to rotate more quickly than for figure 8-type orbits. Another group of hourglass-type trajectories, characterized by slightly larger values of r_{p0}, exhibit quasi-periodic behavior. An example of a quasi-periodic hourglass-type trajectory appears in Figure 4.22*(c)*. This trajectory results from initial conditions $r_{p0} = 0.213 r_H$ and $\omega_{r0} = 126.16°$. A fourth type of periapse profile is a hybrid of the hourglass- and figure 8-type profiles. The periapses along these trajectories form lobes. Two examples of lobe-type profiles appear in Figure 4.22(*d*) and Figure 4.22(*e*), identified by $r_{p0} = 0.125 r_H$ and initial angles $\omega_{r0} = 127.8°$ and $\omega_{r0} = 118.6°$, respectively. Note in Figure 4.22(*d*) that the trajectory includes revolutions that reach the ZVCs near $x = 0$, as is typical of figure 8-type profiles; the trajectory also possesses revolutions that remain far from the ZVCs near $x = 0$, as do the hourglass-type profiles. The quasi-periodic lobe-type trajectory in Figure 4.22(*e*) shares the same characteristics. Certainly, the characteristics in the inertial views of the figure 8- and hourglass-type trajectories in Figure 4.23(*a*) and Figure 4.23(*b*) are both represented in the lobe-type trajectories in Figure 4.23(*d*) and Figure 4.23(*e*). A fifth type of profile exists at this Jacobi value, comprised of trajectories with periapses always near $\omega_r = 180°$. These trajectories are quasi-periodic with apoapses near L_2; an example appears in Figure 4.22(*f*). The periapses of this trajectory are nearly identically located; in an expanded view, the periapses form an 'arrowhead' shape. The orbit is also clearly quasi-periodic in the inertial frame, as apparent in Figure 4.23(*f*). The 'arrowhead' type trajectories are associated with a well-known family of stable periodic trajectories, the 'g-family' of periodic orbits.[56]

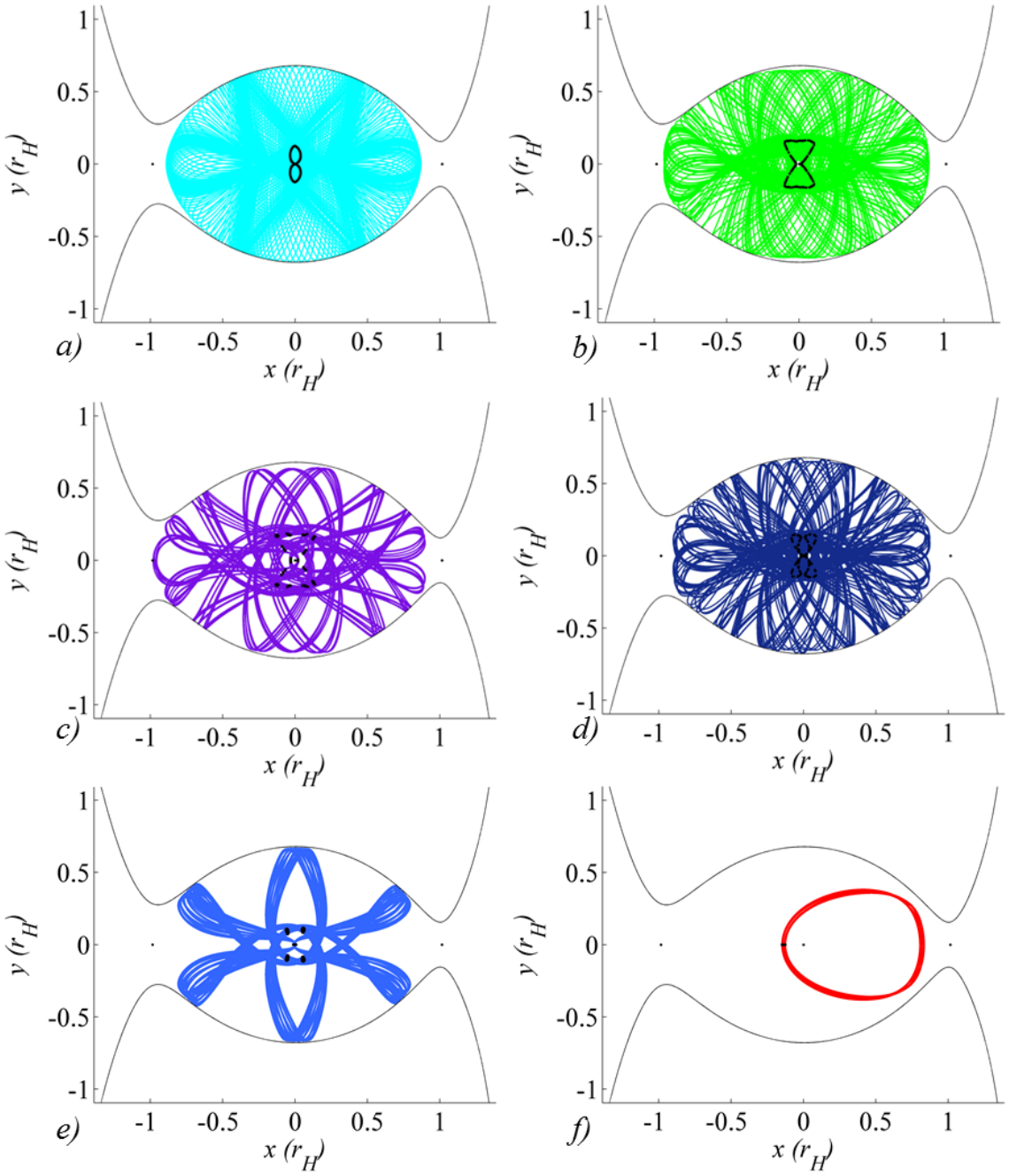

Figure 4.22 Periapsis profiles viewed in the rotating frame for six trajectories in the Sun-Saturn system, $J = J_1$.

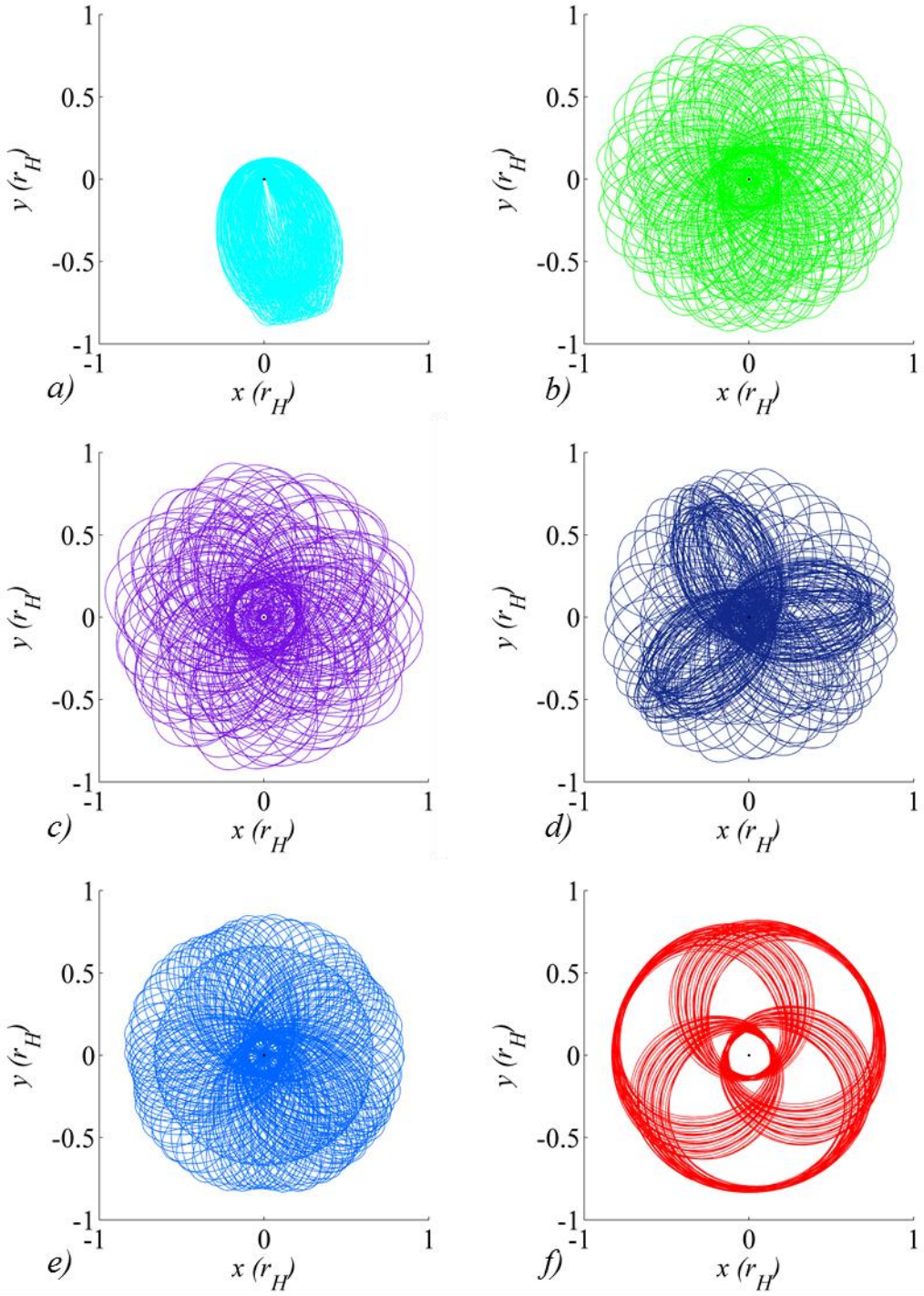

Figure 4.23 The six trajectories from Figure 4.22 viewed in an inertial frame of reference.

The trajectories appearing in Figure 4.22 are representative of the types of captured trajectories that exist at this value of Jacobi Constant, $J = J_1$. The periapse profile of a given captured trajectory is correlated with the change in periapse angle from one periapse passage to the next during the evolution of the trajectory. At this value of Jacobi Constant, the periapse angle shifts by approximately 60º from one periapsis to the next for the majority of the captured trajectories. Define a *cycle* as the number of revolutions required to approximately return to the same periapse angle; at this Jacobi value, $J = J_1$, a cycle consists of a set of six periapses. (At different values of J, a cycle will be defined by a different number of periapse passages. For example, at $J = J_{L1} + 0.01$, the periapse angle of most captured trajectories changes by about 20º per revolution, and a cycle is defined as 18 periapses.) The periapse angle ω_0 occurs at the initial time, t_0; after six revolutions, the angle at time t_6 is ω_6. Thus, define the change in periapse angle after one cycle,

$$\Delta\omega_r = \omega_6 - \omega_0 . \tag{4.3}$$

Note that after one cycle, the locations of periapsis (and apoapsis) have returned nearly to their original positions along the quasi-periodic trajectory in Figure 4.22(*e*). In figure 8-type trajectories, the change in the periapse angle after one cycle is always positive; the line of apsides defined in the rotating frame moves in a counter-clockwise direction from one cycle to the next, and $\Delta\omega_r > 0$. In hourglass-type trajectories, the line of apsides in the rotating frame moves in a clockwise direction from one cycle to the next, corresponding to a negative change in the periapse angle after each cycle: $\Delta\omega_r < 0$. In lobe-type trajectories, the direction of motion of the line of apsides in the rotating frame over a cycle oscillates, and $\Delta\omega_r$ moves between positive and negative values. The change in periapse angle over a cycle, $\Delta\omega_r$, is visualized in Figure 4.24 for five of the six trajectories from Figure 4.22 and Figure 4.23. Note that the green curve, representing $\Delta\omega_r$ along the hourglass-type trajectory, remains negative; the light blue curve, which corresponds to $\Delta\omega_r$ along the figure 8-type trajectory, is always positive. The blue and purple curves, associated with the lobe-type trajectories, oscillate between positive and negative values. The red curve, which represents the arrowhead-type orbits, also oscillates but always remains near 180º. A sixth trajectory, periodic with a 6:1 resonance, is represented by the black curve. Note that over a cycle, $\Delta\omega_r$ is always zero for this trajectory; this curve consists of six points.

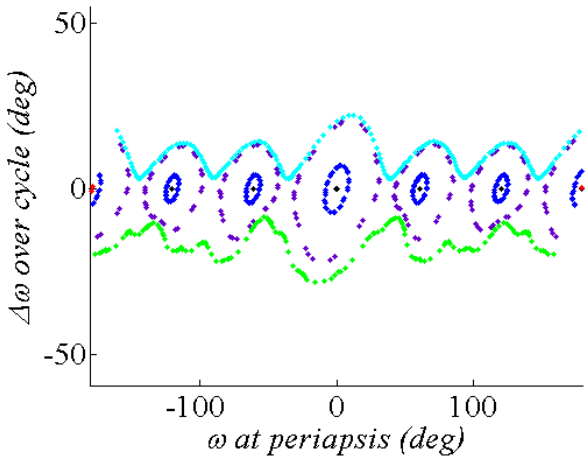

Figure 4.24 Change in periapsis angle ω_r over cycles of six periapses for each of six trajectories.

The trajectories appearing in Figure 4.22 share a common energy level, $J = J_1$. However, as J changes, other patterns emerge in the shape of the locus of trajectory periapses. For example, consider a value of Jacobi Constant such that the ZVCs are closed at the libration points, $J = J_{L1}$. At this energy level, all trajectories remain captured for the full propagation time. Figure 8- and arrowhead-type trajectories are present, while hourglass and lobe-type trajectories are not seen. However, several other profiles appear, some of which are pictured in Figure 4.25. Note, in particular, the presence of a profile without a defined pattern. This type of apparently chaotic trajectory seems to exist only at lower energies; when the ZVCs are open, trajectories that do not follow a defined pattern tend to escape from the vicinity of Saturn over long propagation times. An example of a chaotic profile appears in Figure 4.25(*a*). The trajectory appearing in Figure 4.25(*b*) is an example of a trajectory type described by Russell[19] as an "egg-shaped trajectory". Its periapses lie always near $\omega = 0^o$. A third type of profile existing at this energy level, pictured in Figure 4.25(*c*), is similar to the arrowhead-type trajectories, in that it possesses periapses near $\omega = 180^o$, but a second grouping of periapse points lies in a nearly vertical line centered at $\omega = 0^o$. At this energy level, two sets of quasi-periodic figure 8-type trajectories also exist. One example appears in Figure 4.25(*d*).

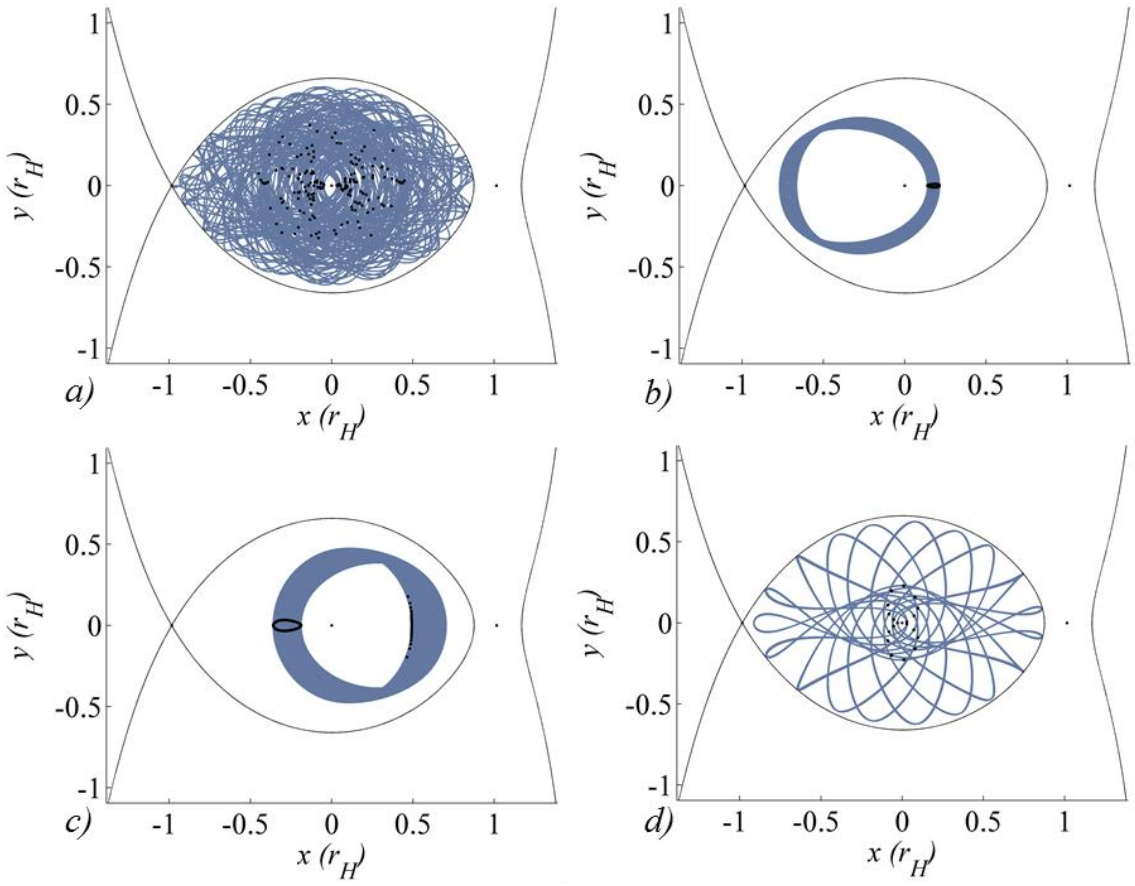

Figure 4.25 Four samples of periapse profiles at a lower energy: $J = J_{L1}$.

4.2.2. Long-Term Periapsis Poincaré Maps

Many researchers have investigated the behavior of trajectories in the vicinity of P_2.[10-21] By characterizing each trajectory according to its periapse profile, however, information regarding its long-term behavior is immediately available. In fact, the location of a single periapsis point at a given value of Jacobi Integral reveals information about the long-term behavior of the trajectory. This fact is made clear when the periapse locations of many trajectories are plotted together in a long-term periapsis Poincaré map.

The trajectories and periapse profiles for six pairs of initial conditions appear in Figure 4.22. Consider a larger set of trajectories in the planar Sun-Saturn system characterized by a Jacobi value $J = J_1$ such that the ZVCs are open at both L_1 and L_2. For initial periapse radius values selected such that $0.07r_H < r_{p0} < 0.25r_H$, values of ω_{r0} ranging from 0 to π are selected. Each

initial state is propagated for approximately 33 revolutions of the primaries: equivalent to 1,000 years in the Sun-Saturn system. Some of the trajectories escape from the vicinity of Saturn during the course of the propagation; others remain captured over the full time span. As each trajectory evolves, the spacecraft state is recorded at each periapse passage. The coordinates y_p versus x_p, relative to the rotating frame, are plotted on a map as the trajectories evolve over ~33 periods of the primaries. For $J = J_1$, the map appears in Figure 4.26(*a*). The points corresponding to each trajectory are colored consistent with their initial condition ω_{r0}; the color scheme appears in Figure 4.26(*b*). The Saturn-centered view focuses on the trajectories that remain captured for the duration of the propagation. The map consists of two main regions. First, an hourglass-shaped region is comprised of points corresponding to several types of captured trajectories. Trajectories associated with four of the periapse profile types combine to create this region — figure 8-type trajectories, lobe-type trajectories, hourglass-type trajectories, and quasi-periodic hourglass-type trajectories. A second (red) region exists to the left of the hourglass, centered about $y_p = 0$; it is composed of periapse points belonging to arrowhead-type trajectories. Surrounding these two regions is a large zone corresponding to trajectories that eventually escape.

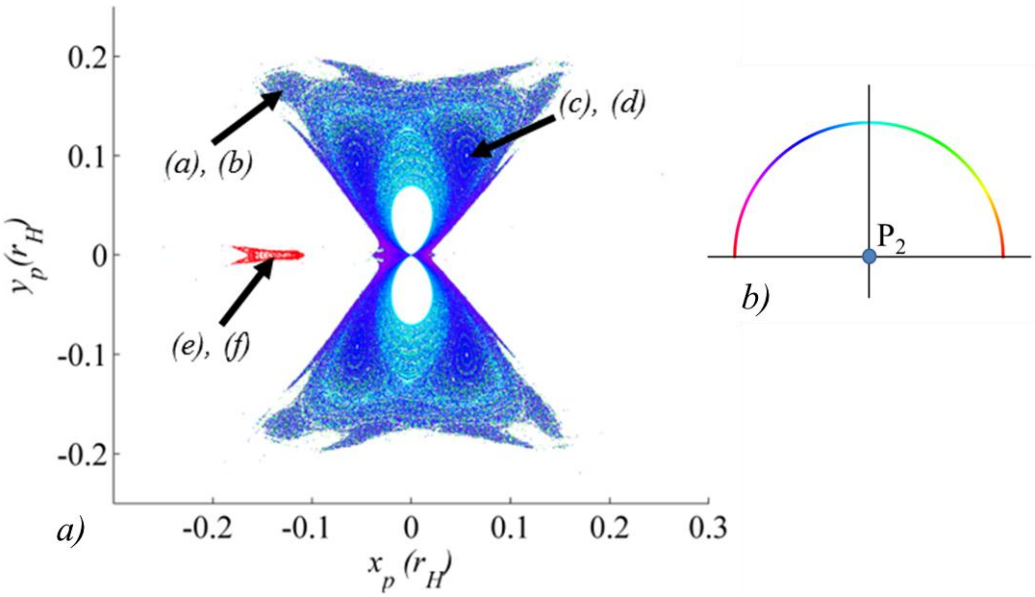

Figure 4.26 Periapsis Poincaré map displaying y_p vs. x_p over 1,000 years for captured trajectories in the Sun-Saturn system with $J = J_1$, $0.07r_H < r_{p0} < 0.25r_H$, $0 < \omega_{r0} < \pi$ (*a*). Three islands associated with periodic trajectories are marked with arrows. Each point is colored according to the initial condition ω_{r0}, following the scheme shown in the legend (*b*).

Islands associated with periodic trajectories exist within the periapsis Poincaré map. Three islands are marked by arrows in Figure 4.26, and their associated periodic trajectories appear in Figure 4.27. On the left, Figure 4.27*(a)*, *(c)*, and *(e)*, the trajectories are plotted relative to the rotating frame; the corresponding inertial views appear in Figure 4.27*(b)*, *(d)*, and *(f)*. Note that these three periodic orbits are computed by simply propagating the initial conditions located from the map — no corrections procedure is employed. The complex structure of this region of the dynamical space is clearly apparent from the map — in addition to the periodic trajectories lying at the center of the lobes, many other island structures representing resonant trajectories appear. The stable manifold trajectories associated with the L_1 and L_2 Lyapunov orbits at this value of Jacobi Integral are represented by the red points in Figure 4.28, with the periapses corresponding to 1,000-year propagations of 11,182 initial conditions in black. Note how the regions of captured trajectories are neatly outlined by the stable manifold tubes.

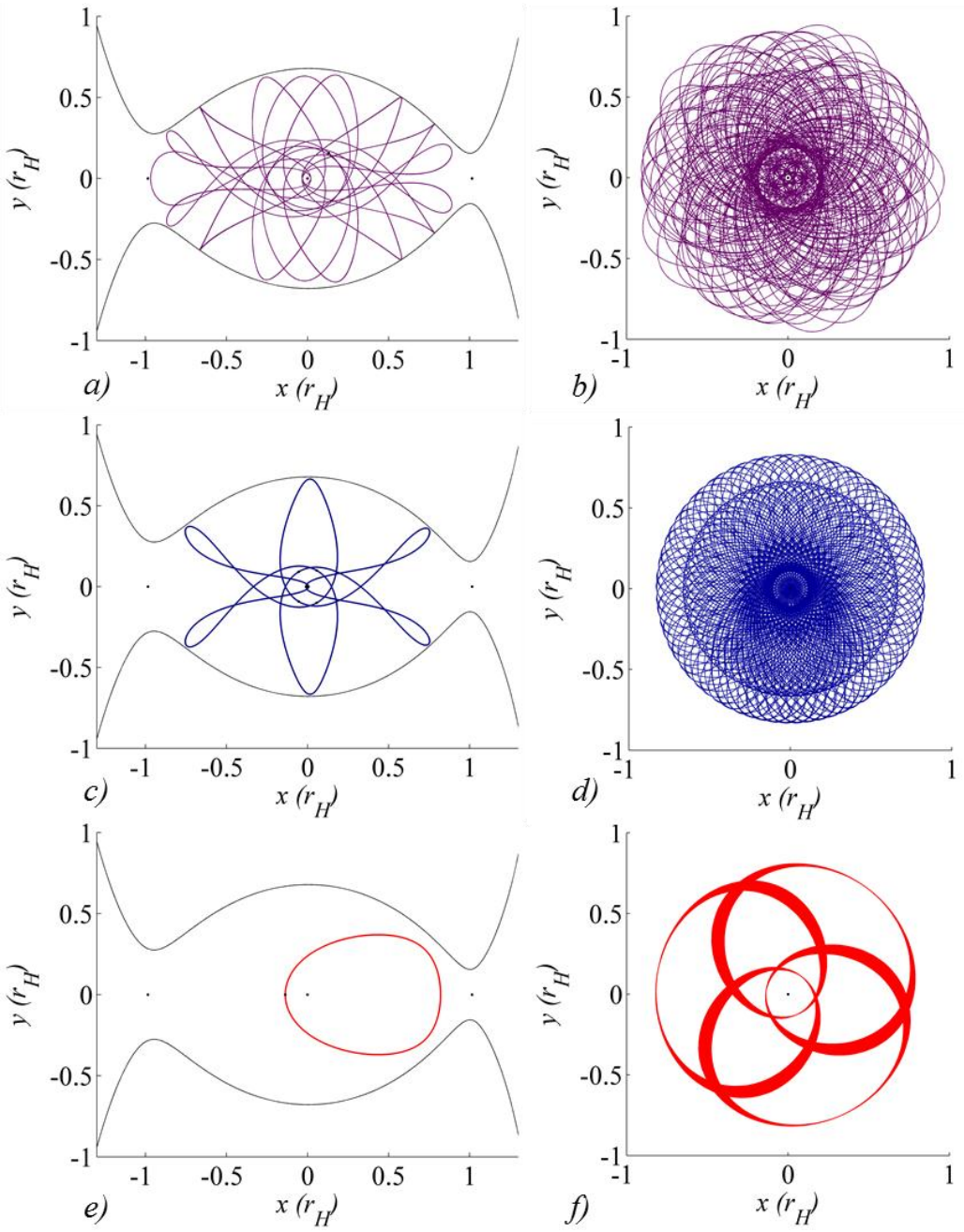

Figure 4.27 Periodic trajectories corresponding to the points marked by arrows in Fig. 10. Rotating views appear on the left, inertial views on the right. Lobe-type trajectory (*top*), hourglass-type trajectory (*center*), and arrowhead-type trajectory (*bottom*).

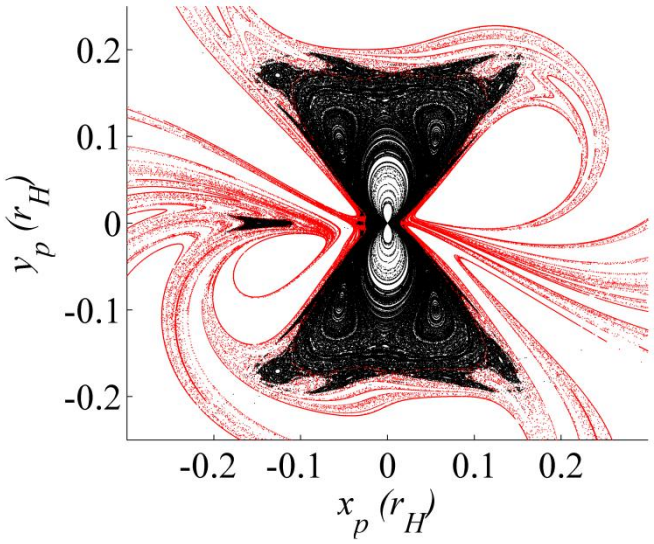

Figure 4.28 Periapsis Poincaré map of captured trajectories for 11,182 initial conditions (black) and L_1 and L_2 stable manifolds (red); $J = J_1$.

Recall that by employing the short-term initial condition maps discussed above, the location of an initial periapsis reveals the fate of the trajectory over one to six revolutions. In the same way, the location of periapsis in *x*-*y* space defines the periapse profile and therefore the behavior of a planar trajectory over a long-term propagation. A schematic appears in Figure 4.29 for $J = J_1$ in the Sun-Saturn system. Each colored zone represents a periapse profile type. If a trajectory possesses a periapsis located in one of the colored zones, every periapsis over a long-term propagation will also lie within the same colored zone. For example, if a trajectory with $J = J_1$ in the Sun-Saturn system possesses an initial periapsis state within the light blue region, the trajectory is characterized as a figure 8-type trajectory, and each periapsis over a long-term propagation will remain within the light blue region. Similarly, any trajectory originating from a periapse location within the black region will eventually impact Saturn. A periapsis lying within the dark blue region corresponds to a lobe-type trajectory, and within the green region, to an hourglass-type trajectory. Periapses located in the purple regions also belong to hourglass-type trajectories; however, the periapses along these paths remain within discrete regions, yielding quasi-periodic trajectories. The red zone is comprised of periapses from arrowhead-type trajectories, and any trajectory with an initial periapsis within the white region will escape from the vicinity of Saturn over a long-term propagation. This schematic may be used in a design process; simply by placing an initial periapsis within one of the colored regions at the specified value of Jacobi Integral, a designer is certain to achieve a trajectory with particular characteristics. Note, however, that the boundaries between the regions are imprecise. Close to

the edges of the regions, trajectories may exhibit characteristics of both types of trajectories, or they may flip from one type of trajectory to another. The schematic provides a quick, methodical way to identify trajectories with certain types of behaviors.

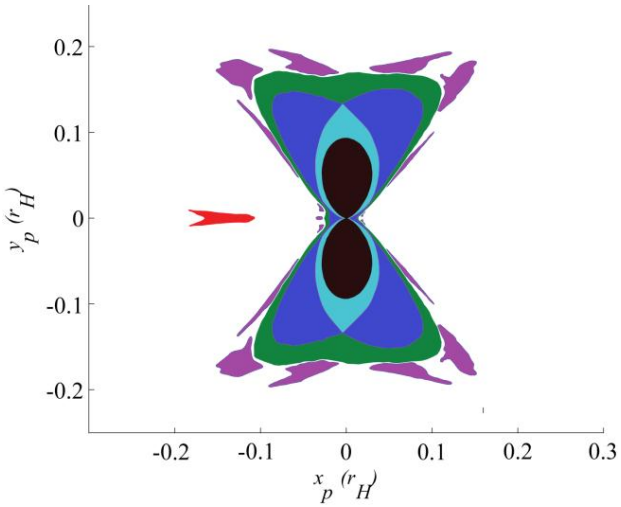

Figure 4.29 Periapsis profile schematic for $J = J_1$ in the Sun-Saturn system. Black corresponds to impact trajectories, light blue to figure 8-type trajectories, dark blue to lobe-type trajectories, green to hourglass-type trajectories, purple to quasi-periodic hourglass-type trajectories, red to arrowhead-type trajectories, and white to escaping trajectories.

The map in Figure 4.26 and the schematic in Figure 4.29 are specific to the mass parameter and Jacobi Constant associated with this set of trajectories; changing either of these parameters will alter the characteristics in the figures. In Figure 4.30, periapsis Poincaré maps appear for the Sun-Saturn system at a series of increasing energy levels. As before, each point is colored consistent with its initial periapse angle, according to the legend in Figure 4.26. The lowest energy value in this set, in Figure 4.30(*a*), corresponds to $J = J_{L1} + 5\times10^{-4}$. At this low energy, the ZVCs are completely closed, and the majority of trajectories possess ordered periapse profiles. Many islands exist in the map, corresponding to quasi-periodic and periodic trajectories. Three sample quasi-periodic trajectories appear in Figure 4.31; the map facilitates the identification of both low-order resonance and high-order resonance quasi-periodic trajectories. A fourth orbit, corresponding to a very large figure 8-type profile, appears in Figure 4.31(*d*). These large figure 8-type profiles are apparent in dark blue in the map in Figure 4.30(*a*). As the energy of P_3 increases, the maps begin to lose their well-ordered characteristics, and more chaotic trajectories appear. The long-term map corresponding to $J = J_{L1}$ appears in Figure 4.30(*b*). One

sample chaotic trajectory at this energy level appears in Figure 4.25(*a*). As the energy is increased further, the ZVCs open, and the chaotic trajectories begin to escape the vicinity of P_2. At $J = J_{L1} - 1\times10^{-4}$, vacant zones are visible in Figure 4.30(*c*) that correspond to the first several lobes of escaping trajectories seen in the initial condition maps. Clearly, figure 8-type trajectories, egg-type trajectories, and arrowhead-type trajectories, among others, exist at this energy level. At a still higher energy, $J = J_{L1} - 4\times10^{-4}$, egg-type trajectories have disappeared, and lobe-type trajectories are prevalent, as are trajectories with figure 8-type and arrowhead-type profiles. Note that the scale has been adjusted in Figure 4.30(*d*). With an increase in energy to $J = J_{L1} - 5\times10^{-4}$, hourglass-type profiles have appeared, and arrowhead-type profiles are nearly gone. Above this energy level, fewer and fewer trajectories remain captured for long-term propagations, as seen in Figure 4.30(*e*). At $J = J_{L1} - 5\times10^{-4}$, figure 8-type trajectories are now absent and lobe-type trajectories are disappearing. Some hourglass and quasi-periodic hourglass-type profiles remain captured in the vicinity of P_2. This map appears in Figure 4.30(*f*).

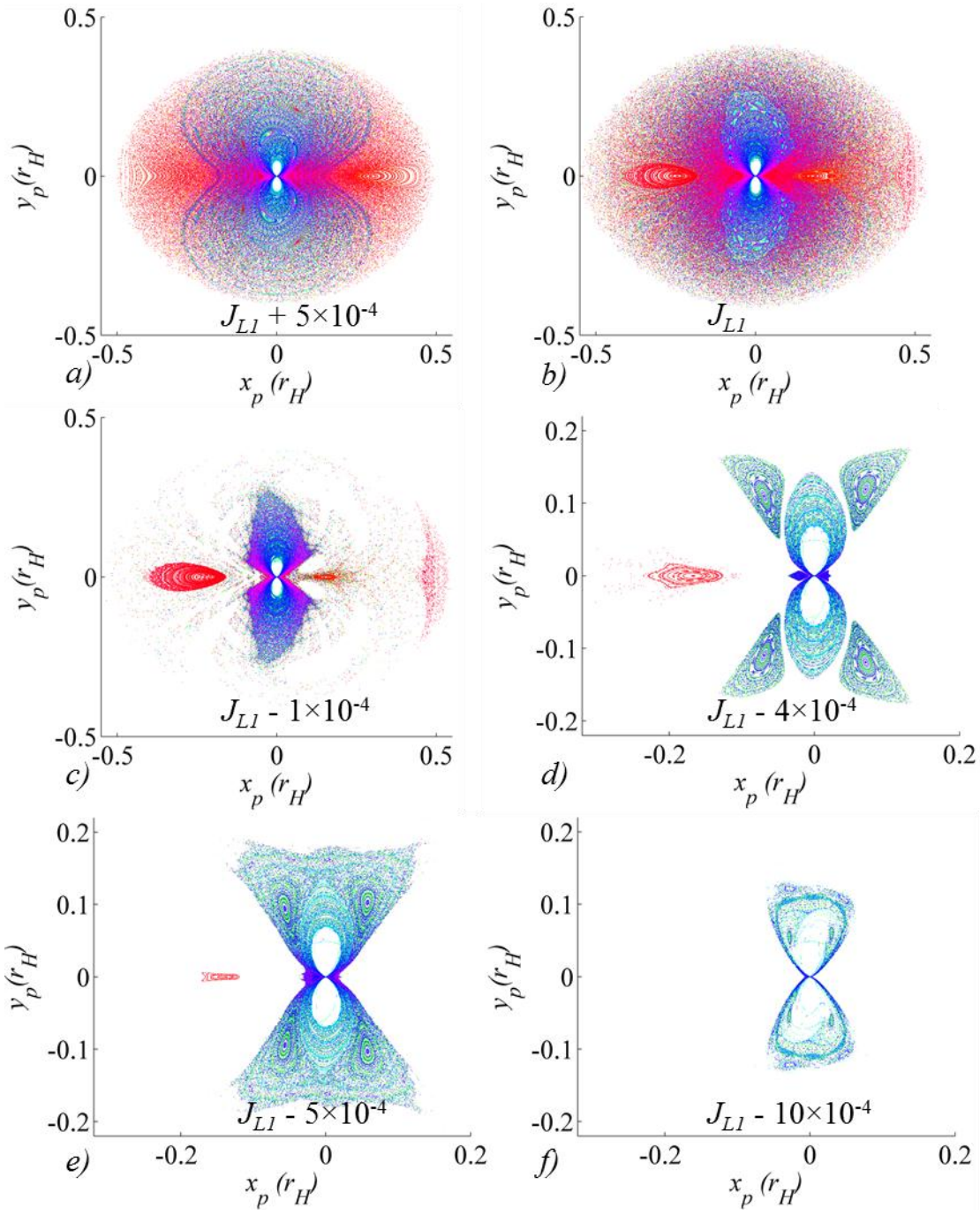

Figure 4.30 Periapsis Poincaré maps for varying values of *J* in the Sun-Saturn system.

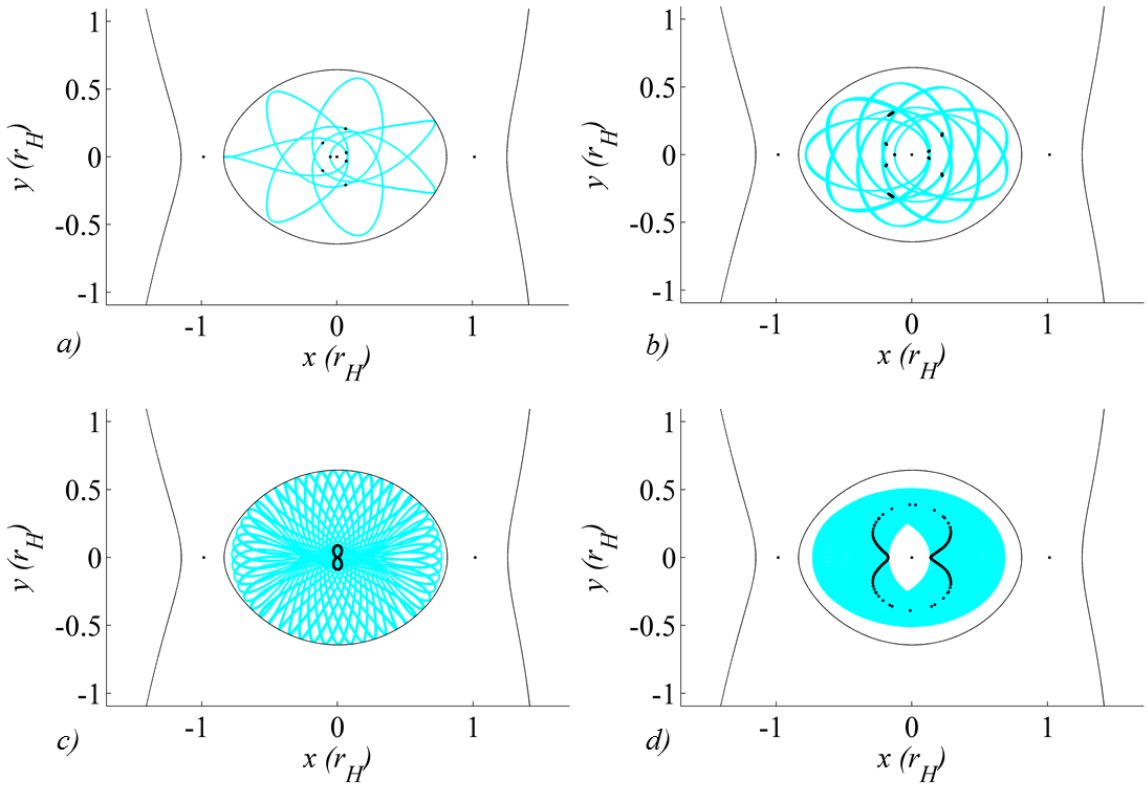

Figure 4.31 Four ordered orbits in the Sun-Saturn system with $J = J_{L1} + 5\times10^{-4}$.

The long-term periapsis Poincaré maps appearing thus far have been limited to the Sun-Saturn system. However, the maps also evolve as the mass parameter changes. In Figure 4.32, four long-term maps appear for the Earth-Moon system, which is characterized by a significantly larger mass parameter than the Sun-Saturn system. Again, the periapses are colored consistent with the initial periapse angle as described in the legend in Figure 4.26. At a relatively low energy, $J = J_{L1}$, all trajectories remain captured for the full propagation time. This map appears in Figure 4.32(*a*), and it is evident that chaotic trajectories fill much of the space. Several distinct differences exist in comparison to the Sun-Saturn map at $J = J_{L1}$ (seen in Figure 4.30(*b*)). In the Earth-Moon map, arrowhead-type trajectories are not apparent, in contrast to the Sun-Saturn map. Figure 8- and egg-type orbits exist in both systems; however, the Earth-Moon map possesses lobe- and hourglass-type trajectories at $J = J_{L1}$, neither of which exists in the Sun-Saturn system at this energy level. The lack of symmetry across the *y*-axis, a result of the large value of μ in the Earth-Moon system, is clearly apparent in the Earth-Moon map. At a higher energy, $J = J_{L1} - 1.95\times10^{-3}$, the ZVCs are open, and the chaotic trajectories have escaped the vicinity of P2,

apparent in Figure 4.32(*b*). Figure 8-, lobe-, hourglass-, and egg-type trajectories still appear at this energy level. However, as the energy level is further increased, egg-type trajectories disappear, as do the hourglass- and lobe-type trajectories. Arrowhead-type trajectories appear in the Earth-Moon system at an energy value approximately $J = J_{L1} - 6\times10^{-3}$, apparent in Figure 4.32(*c*). As the Jacobi Constant is decreased further to $J = J_{L1} - 10\times10^{-3}$, the presence of arrowhead-type trajectories expands, lobe-type trajectories reappear, and the region of figure-8 type trajectories begins to disappear. The lack of symmetry across the *y*-axis due to the large mass parameter remains apparent at all energy levels.

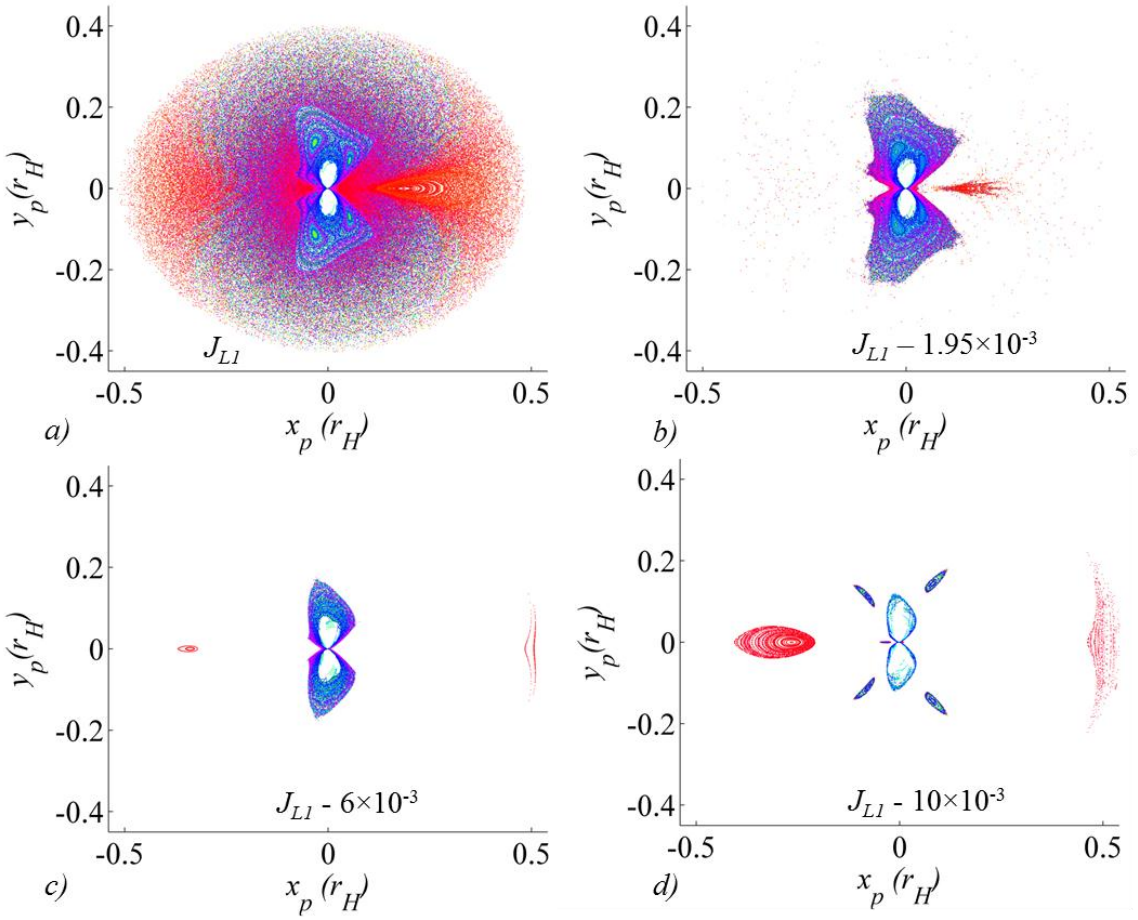

Figure 4.32 Periapsis Poincaré maps for varying values of *J* in the Earth-Moon system.

4.2.3. Periapsis Poincaré Maps for Specific Values of r_{p0}

While the maps in Figure 4.26 and Figure 4.28 offer an extensive picture of the design space at $J = J_1$ in the Sun-Saturn system, visualizing smaller subsets of the space reveals additional details. Consider a set of initial conditions with a single initial periapse radius r_{p0}, and values of ω_0 ranging from 0 to 180º. This set forms a semicircle of initial states, which is overlaid on the initial condition map for 6 revolutions in Figure 4.33. Of course, those trajectories originating in red or blue areas in Figure 4.33 will escape; each trajectory that remains captured for a long-term propagation begins in the grey zone. However, not every trajectory that remains captured in the shorter-term propagation will also remain captured for the long-term propagation. As before, each initial state is propagated for 1,000 years, about 33 revolutions of the primaries. Examples of the corresponding Poincaré maps for three sets of initial conditions appear in Figure 4.34. The semicircle of initial states is plotted in black over each colored map. For a given initial periapse radius, a corresponding set of trajectories is produced, which depends on the periapse profiles available at that specific value of r_{p0}. For example, for $r_{p0} = 0.09r_H$, the initial semicircle passes through regions corresponding to figure 8-type trajectories, lobe-type trajectories, and hourglass- as well as quasi-periodic hourglass-type trajectories. However, arrowhead-type trajectories only exist for $0.108r_H < r_{p0} < 0.181r_H$ at this energy level. Therefore, a set of trajectories with initial periapse radius either smaller or larger than this range will produce no arrowhead-type trajectories, and for $r_{p0} = 0.09r_H$, arrowhead-type trajectories are absent, apparent from the corresponding map in Figure 4.34(*a*). At this relatively small radius, a number of propagated arcs originating from a group of initial conditions centered at 90º lead to impact trajectories. While these trajectories are propagated for the full ~33 periods of the primaries, despite the impact conditions, the corresponding points on the map are colored black. Impact trajectories exist only for $r_{p0} \leq 0.10r_H$. For a larger initial periapse radius, $r_{p0} = 0.16r_H$, the map characteristics are altered; it appears in Figure 4.34(*b*). As expected, impact trajectories are absent, while arrowhead-type trajectories are apparent. Figure 8-type trajectories have disappeared at this radius. At a still larger value of r_{p0}, for example, $r_{p0} = 0.21r_H$ in Figure 4.34(*c*), only hourglass- and quasi-periodic hourglass-type trajectories remain. Note in particular the vacant zones in each of the maps in Figure 4.34, and the tangency of the semicircle of initial conditions to the vacant zones. These vacant zones appear simply because none of the initial states result in trajectories with periapse profiles within these regions. Since each captured trajectory corresponds to a single, well-ordered profile, none of the initial conditions used to create each map produce any periapses within the corresponding vacant zones.

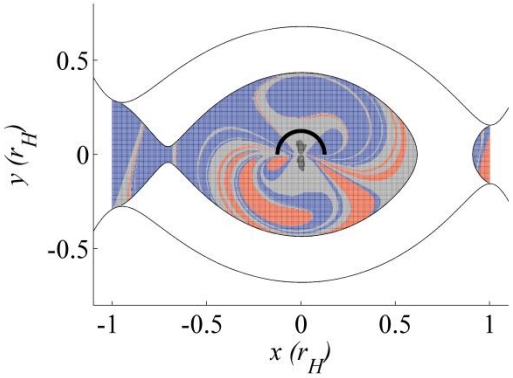

Figure 4.33 One set of initial conditions for a long-term propagation; $r_{p0} = 0.125 r_H$.

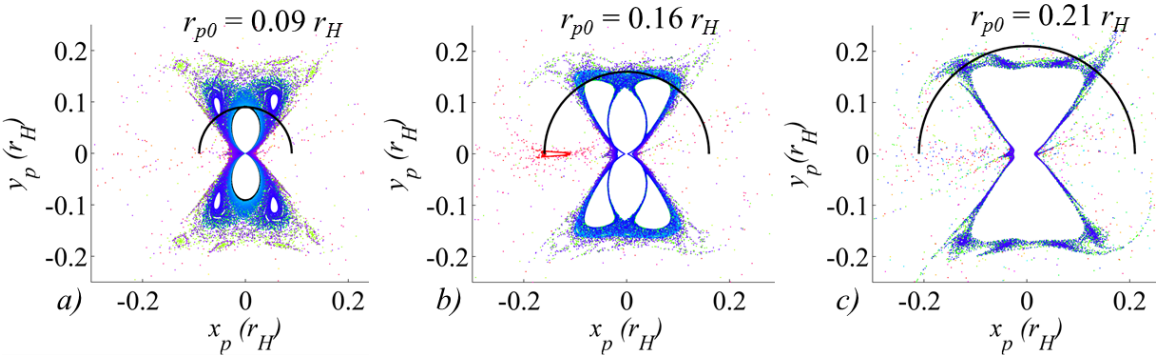

Figure 4.34 Long-term periapsis Poincaré maps for three values of r_{p0}.

4.2.4. Out-of-plane Long-Term Trajectory Evolution

By characterizing the velocity direction in terms of the angle ϕ as described in Figure 4.17, the planar long-term analysis is extended into three dimensions. Out-of-plane periapsis Poincaré maps are produced for the Sun-Saturn system. For an initial periapse radius $r_{p0} = 0.12\ r_H$, maps of y_p versus x_p appear in Figure 4.35 for four selected velocity angles: ϕ = 17.2°, ϕ = 68.8°, ϕ = 91.7°, and ϕ = 137.5°. In each case, the initial *z*-height is set to zero, and the Jacobi Constant $J = J_1$. As in the planar case, the points are colored according to initial periapse angle ω_{r0}, which ranges from 0° to 180°. The hourglass shape of the captured periapses, familiar from the planar examples, persists from ϕ = 0° to approximately ϕ = 20°. When the velocity vector is oriented such that ϕ is a larger angle, the figure 8 shape is prominent in the shape of the periapses. For

angles larger than $\phi \approx 40°$, all of the initial conditions result in trajectories that remain captured for the duration of the 1,000-year propagation: no trajectory escapes through either the L_1 or L_2 gateways, even though the zero velocity surfaces remain open at this value of J. As discussed in Hamilton and Krivov,[26] retrograde trajectories about P_2 are more stable than similar prograde trajectories, due in part to the direction of the Coriolis acceleration, which is directed inward towards P_2 in the retrograde case but radially, away from P_2, in the prograde case. The periapsis Poincaré maps support this conjecture, becoming tightly ordered as the velocity angle increases towards $\phi = 180°$, representing planar retrograde trajectories. The long-term periapsis Poincaré map for planar retrograde trajectories (or, velocity angle $\phi = 180°$) appears in Figure 4.36. Compare this map to the corresponding map for planar prograde trajectories in Figure 4.26; clearly, the retrograde map is far more ordered. No retrograde trajectories escape at this energy level.

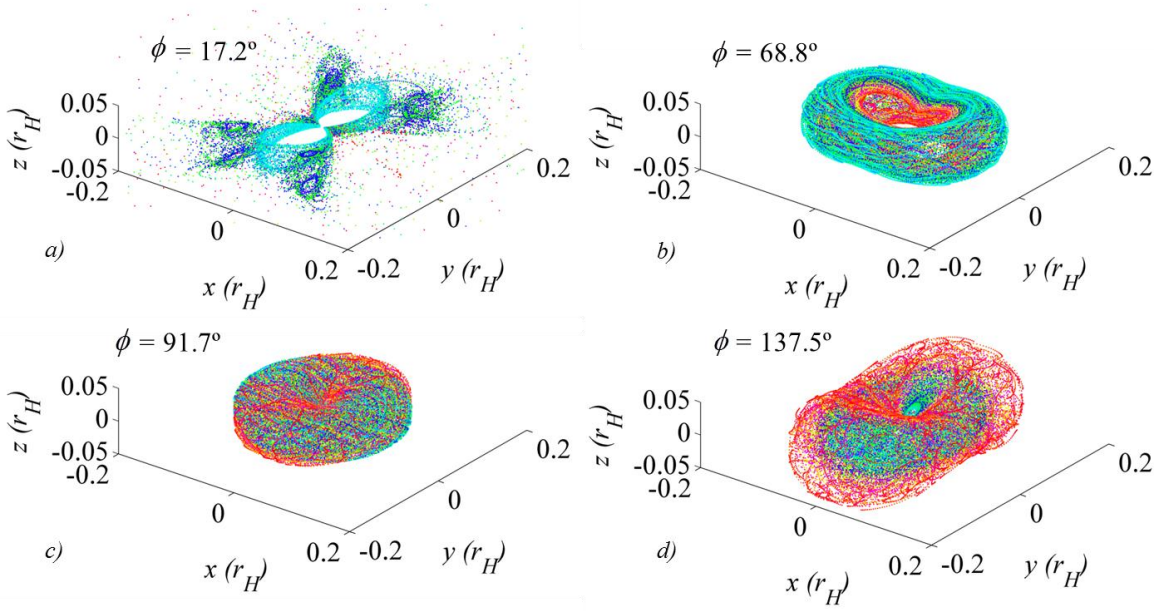

Figure 4.35 Periapsis Poincaré maps representing trajectories with velocity angles $\phi = 17.2°$, $\phi = 68.8°$, $\phi = 91.7°$, and $\phi = 137.5°$. Sun-Saturn system, $J = J_1$, $r_{p0} = 0.12\ r_H$.

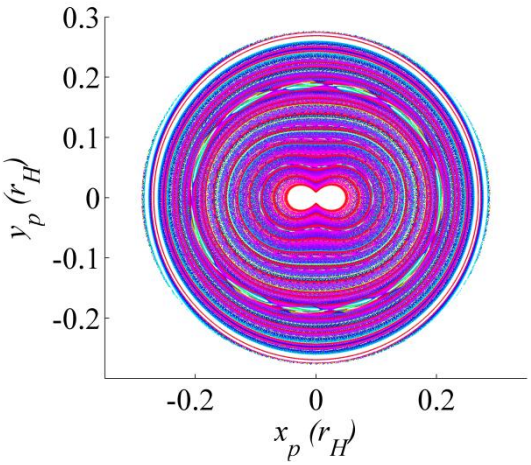

Figure 4.36 Long-term periapsis Poincaré map for retrograde trajectories in the Sun-Saturn system, $J = J_1$.

5. DESIGNING TRAJECTORIES IN A TIDALLY-INFLUENCED ENVIRONMENT

By applying an expanded understanding of the trajectory behavior in the vicinity of P_2, orbits with various desired characteristics can be selected to fulfill mission objectives. The first examples introduced below, both Cassini end-of-life trajectory options, were originally designed without the benefit of periapsis Poincaré maps. Previously, several point solutions were painstakingly computed with extensive trial-and-error processes. After the introduction of the maps, families of similar solutions emerge and are easily produced in a methodical manner. The same principles are applied to other design applications.

5.1. Mission Design for Cassini End-of-Life: Point Solutions

After an impressive tour of Saturn, and as the Cassini mission winds down, safe disposal of the spacecraft is necessary. Because Cassini is already in orbit about Saturn, and because the design of the extended phase is close to completion, the initial conditions for any final end-of-life stage of the mission are constrained. In addition, the available ΔV is always limited by the amount of propellant remaining on the spacecraft. Working within this framework, in 2007 a preliminary Cassini end-of-life design study was completed.[70] As a part of this study, one strategy developed for the final phase of the Cassini mission as envisioned in 2007 combines solar perturbations with Titan encounters and small maneuvers to enable the spacecraft to reach various end-of-mission orbits.

5.1.1. Saturn Impact Example

The first example, a set of three point solutions, involves a trajectory originating in quadrant III such that the solar gravity acts to lower periapsis. With a sufficiently large orbit oriented and inclined appropriately, the spacecraft can impact Saturn with low ΔV or without a maneuver at apoapsis. Analysis for the long-period impact originates with initial conditions from STOUR for an outbound Titan flyby on April 8, 2011, after a series of 7 flybys that serve to pump up and

reorient the orbit (see Yam et al.[71], Yam[72]), and is completed in the Saturn-centered ephemeris model described in Section 2.3. The penultimate orbit is assumed to be in a 5:1 resonance with Titan, which is associated with a period of 80 days. It is inclined at 25.8º with respect to Saturn's equator, corresponding to a 0.9º inclination with respect to Saturn's ecliptic plane. The periapse radius prior to the Titan flyby is 5.58×10^5 km, or 9.26 R_S. The final flyby conditions are adjusted to yield post-flyby orbits of different Keplerian periods. If solar gravity is not modeled, the periapse radius of each of the post-flyby orbits is approximately 12 R_S. However, solar gravity significantly affects the orbits, resulting in naturally reduced periapse radii.

Three candidate post-flyby orbits are characterized by Keplerian periods of 877 days, 957 days and 1116 days. The inclination of these post-flyby trajectories relative to Saturn's ecliptic plane is approximately 2º. The quadrant angles range from $\Phi = 217^\circ$ for the largest orbit to $\Phi = 222^\circ$ for the smallest orbit. Although no ΔV is applied, solar gravity slows the spacecraft and decreases the periapse radius of each orbit. The periapse radius of the 1116-day orbit is lowered to 0.2 R_S, and the spacecraft impacts Saturn without a maneuver. The subsequent periapse radius of the 957-day orbit, on the other hand, is 1.82 R_S, still above the surface of Saturn. A maneuver may be implemented at apoapsis to further lower the periapsis and achieve impact. With a ΔV of 21 m/s applied at apoapsis, the periapse radius of the 957-day orbit becomes 0.99 R_S, and the spacecraft impacts Saturn. Similarly, with a ΔV of 47 m/s applied at apoapsis, a spacecraft following the 877-day trajectory impacts Saturn. While specific trajectory characteristics will change with different post-flyby conditions, these particular examples may serve as a guide in relating orbit size and apoapse ΔV requirements for Saturn impact. Titan encounters can be used to deliver the spacecraft to orbits of different periods and orientations as desired. Minor adjustments to orientation and inclination (via the final Titan encounter) can alter the impact conditions. The Saturn approach of each trajectory appears in Figure 5.1. Table 5.1 summarizes the subsequent periapse radii and the ΔV required for Saturn impact.

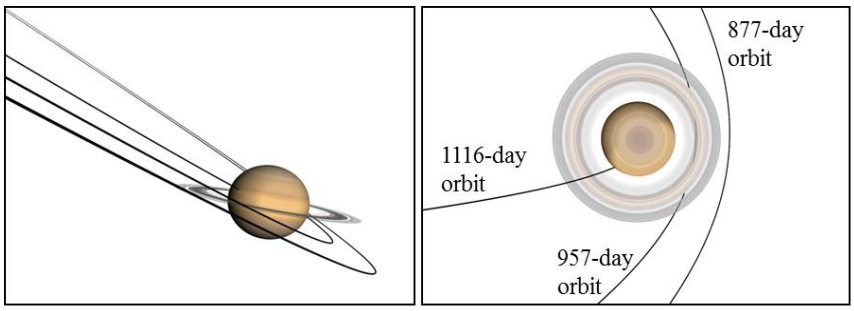

Figure 5.1 Three Saturn-centered trajectories with no ΔV applied: 1116-day, 957-day, and 877-day orbits.

Table 5.1 ΔV at apoapsis and subsequent periapse radii

Period	ΔV, m/s	Post-maneuver r_p, R_S
877 days	0	3.02
877 days	47	0.97
957 days	0	1.82
957 days	21	0.99
1116 days	0	0.20

The patched-conic STOUR approach and 1116-day post-flyby orbit were incorporated as a first guess for an end-to-end trajectory optimized in CATO[73]; see Yam et al.[71] for further details. The end-to-end impact appears in Figure 5.2. A total deterministic ΔV of 14.6 m/s is used to target the desired sequence of Titan flybys. After the final Titan flyby, with no additional ΔV required, solar gravity decreases periapse radius to 0.22 Rs, and the spacecraft impacts Saturn on May 2, 2014. The total time of flight from the initial conditions to Saturn impact is 1446 days, with a total of 7 Titan flybys.

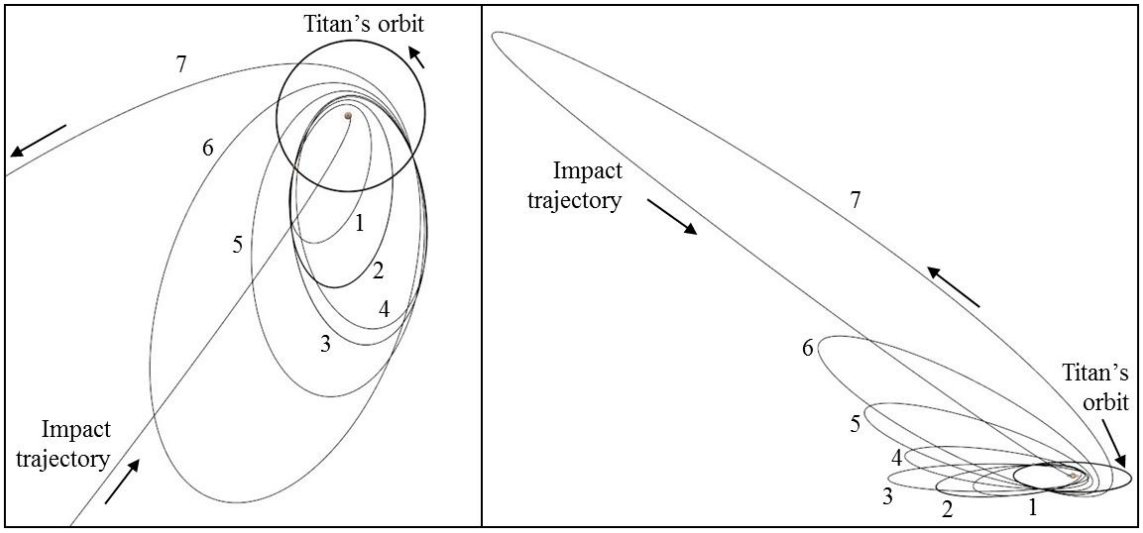

Figure 5.2 Saturn impact trajectory, plotted in an inertial frame.

5.1.2. Long-Term Orbit Beyond Phoebe

A second end-of-life mission option for the Cassini spacecraft involves entering a large, quasi-circular orbit beyond the irregular, retrograde orbit of Phoebe. Phoebe's semi-major axis is 214 R_S, which corresponds to a period of 1.5 years, and its orbit is inclined at ~173° with respect to

Saturn's ecliptic plane. A transfer from some likely spacecraft trajectory at end-of-mission into a long-term trajectory beyond the orbit of Phoebe cannot be accomplished solely with Titan encounters and ΔV, since the required maneuvers are prohibitively large. Instead, solar perturbations are employed to reduce the required ΔV.

Assume that a series of Titan encounters delivers the spacecraft into a quadrant II orbit with a Keplerian period of 1478 days and an initial periapse radius of 9.23 R_S. With an initial state near Titan's orbit, the spacecraft subsequently passes through apoapsis after about 3.2 years. Although there is no ΔV applied, the characteristics of the orbit noticeably change due to solar perturbations along the trajectory, and the next periapsis is raised significantly. At periapsis, a ΔV is applied to the trajectory to lower apoapsis and achieve a quasi-circular orbit. Two examples of such trajectories appear in Figure 5.3, each propagated for 500 years. In each case, the maneuver occurs about 8.25 years after the final Titan flyby at a new periapse radius of 391 R_S. In Figure 5.3(a), a 172 m/s maneuver is applied at this periapsis; this value corresponds to the ΔV that is required to circularize the orbit in a Keplerian model. The resulting near-circular orbit has a period of approximately 3.7 years and a semi-major axis of $a \sim 0.36\ r_H$. Over 500 years, the radius remains fairly tightly bounded. In Figure 5.3(*b*), a lower ΔV of 120 m/s is applied at periapsis. An approximate resonance is achieved between the motion of the line of apsides in the spacecraft orbit about Saturn and Saturn's orbital period. This relationship results in a quasi-periodic spacecraft orbit that appears 'locked' in a 13:2 near commensurability with Saturn's orbit about the Sun. This particular trajectory does descend below the orbit of Phoebe, but the closest approach to Phoebe in the 500-year time frame is 12.7 R_S. The same trajectories appear in Figure 5.4 in the rotating frame. Note the elongation along the *x*-axis in the rotating view, as is typical of prograde trajectories.

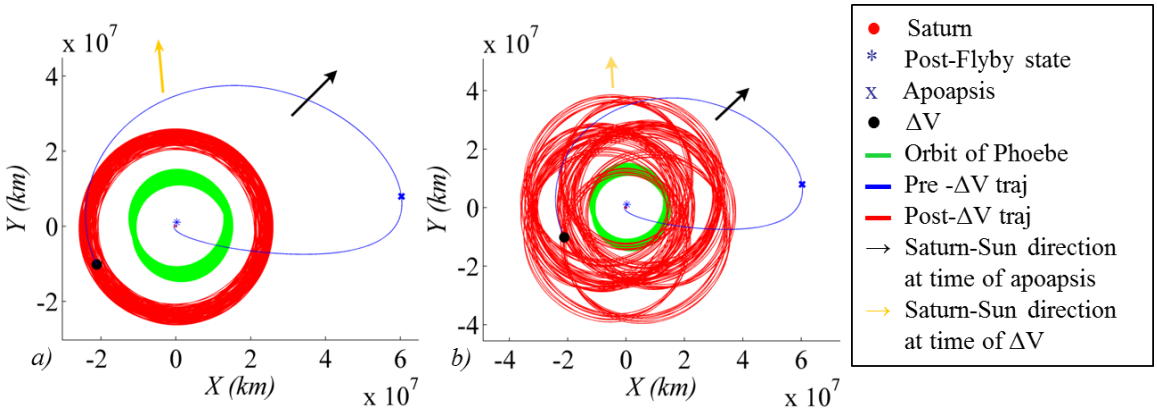

Figure 5.3 Long-term Cassini end-of-life trajectories: inertial view.

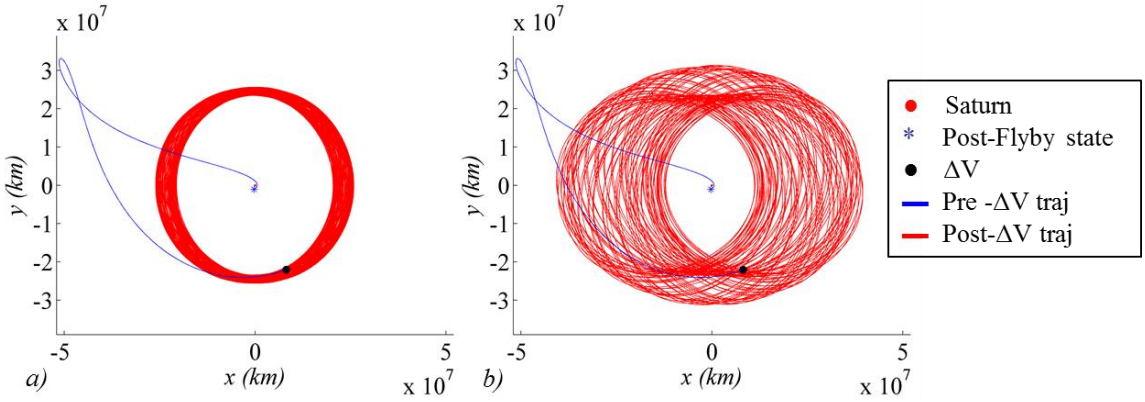

Figure 5.4 Long-term Cassini end-of-life trajectories: rotating view.

5.1.3. Cassini Escape Trajectories

A third proposed Cassini end-of-life option involves escape from the vicinity of Saturn, with another of the outer planets as a destination.[74] By adjusting the initial condition of the post-flyby trajectory, a series of escaping trajectories was produced during the 2007 study.[70] By no means a complete survey of the design space, trajectories were designed that escape towards both the inner and outer solar system, and after many revolutions of Saturn or after a short span of time. The first example departs relatively quickly through the L_2 gateway towards the outer solar system. The post-flyby trajectory is identical to that used to produce the trajectories in Figure 5.3; however, in this case, no maneuver is applied. After approximately 20 years in a large orbit about Saturn, the spacecraft departs the neighborhood of the planet. Inertial and rotating views of this trajectory appear in Figure 5.5. By changing the quadrant angle of the post-flyby trajectory by just 1.5°, however, the spacecraft remains in orbit about Saturn for just over 65 years, escaping through the L_1 gateway in the direction of the inner solar system. Trajectories in this regime are clearly extremely sensitive to initial conditions; a trial-and-error method is inefficient for the design of escaping trajectories, as well as in the search for quasi-periodic or other trajectories that remain in the vicinity of Saturn. The use of periapsis Poincaré maps allows a simple identification and selection of desired trajectories.

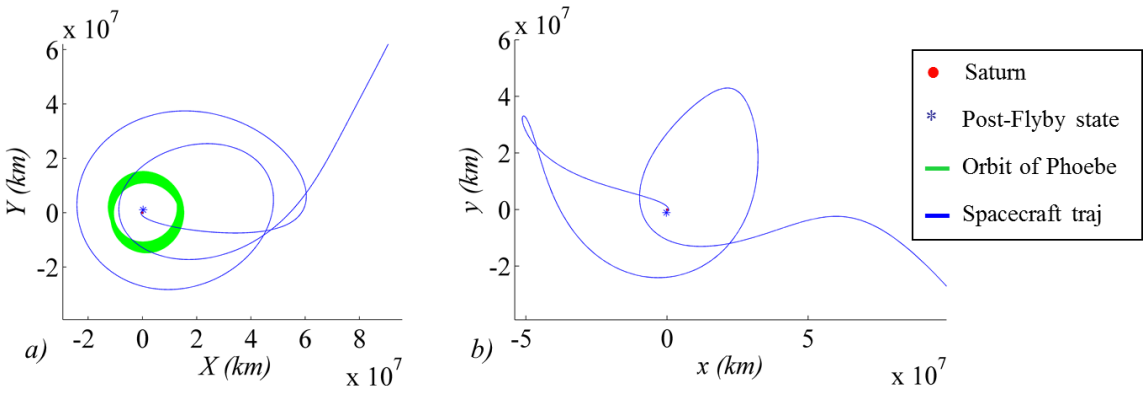

Figure 5.5 Cassini end-of-life escape trajectory in the inertial (*a*) and rotating (*b*) frames.

5.2. Long-Term Maps: Identifying Particular Trajectories

After completing the painstaking design of the point-solution trajectories for the Cassini end-of-life analysis, some limitations were noted. In summary:

1. The trajectories in this regime are highly sensitive to initial conditions
2. Testing every potential trajectory individually is prohibitively time-consuming
3. Manually locating a trajectory with a particular set of characteristics is challenging

It is clear that a more methodical technique would be valuable for future applications. With this motivation, periapsis Poincaré maps are employed to organize the design space and allow easy identification of trajectories that satisfy various mission objectives.

The periapsis Poincaré maps featured thus far have been limited to state-space visualizations — y versus x at periapsis. However, other types of periapsis maps can also be produced, and several of these maps are particularly useful for various applications. One such map displays periapse radii over time as a function of initial periapse angle: r_p versus ω_{r0}. Consider the set of initial conditions appearing in Figure 4.33, corresponding to the initial radius value $r_{p0} = 0.125 r_H$ and $J = J_1$. The first map is produced when the periapse radii of each trajectory as it evolves over time are plotted as a function of initial periapse angle $\omega_{r0.}$ This map of r_p versus ω_{r0} appears in Figure 5.6; it reveals much information concerning the associated trajectories. In Figure 5.6(*a*), the full view differentiates between trajectories that remain captured for the duration of the propagation and trajectories that escape through L_1 and L_2. Trajectories that escape from the vicinity of Saturn evolve to possess larger periapse radii, a distinction that is clear from the map. Escapes through L_2 result in still larger radii, and may therefore be distinguished from the L_1

escapes. With this knowledge, it is therefore clear from the map that captured trajectories possess initial periapse angles between ~ 47 deg and ~132 deg. In Figure 5.6(*b*), a zoomed view decomposes the captured trajectories into regions corresponding to the four periapsis profiles. Trajectories comprising the region of figure 8-type profiles are centered about 90º and possess the smallest maximum values of r_p. The lobe-type trajectories are characterized by small values of r_p near the *x*-axis and larger values of r_p off the axes (see Figure 4.22(*e*), for example); the corresponding r_p values are discontinuous, and the lobe-type trajectories consequently produce discontinuous regions in the r_p versus ω_{r0} map. In contrast, the hourglass-type trajectories are characterized by a continuous range of periapse radii with relatively large minimum r_p values. The arrowhead-type trajectories are centered about ω_{r0} = 180º, and they possess r_p values over a narrow range. This information is also available from the schematic in Figure 4.29, but the r_p versus ω_{r0} map yields precise angles for a particular initial periapse radius.

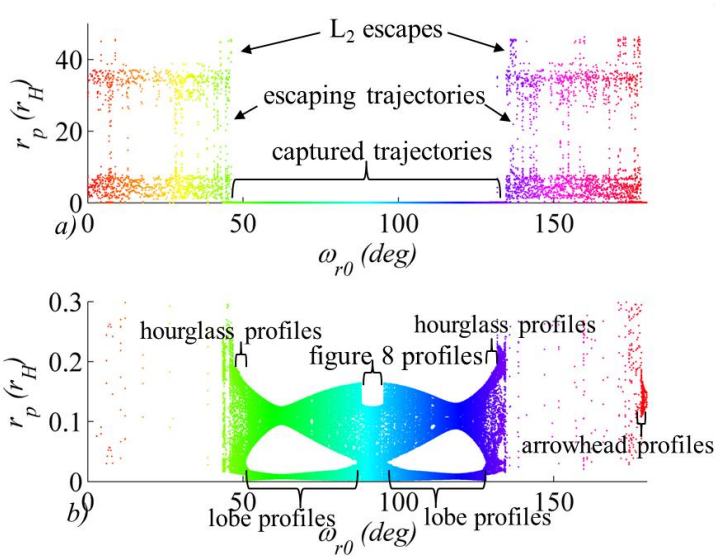

Figure 5.6 Periapse radii over time, r_p, plotted against initial periapse angles ω_{r0} for initial conditions corresponding to periapses with $J = J_1$, $r_{po} = 0.125 r_H$, $0 < \omega_{r0} < 180º$.

Another type of map is particularly useful for locating quasi-periodic trajectories at a given r_{p0}. While a non-periodic trajectory produces continuous values of ω over time, a quasi-periodic trajectory produces only discrete, repeating values of periapse angle as the trajectory evolves over time. Therefore, by plotting periapse angles over time as a function of initial periapse angle, quasi-periodic trajectories can be located by identifying regions of the map where only discrete

values of ω_r exist. An example of a ω_r vs. ω_{r0} map appears in Figure 5.7(*a*) for $r_{po} = 0.125 r_H$ and $0 < \omega_{r0} < 180^o$. The lobe-type trajectories are immediately apparent from the large gaps they form in the map in the green and blue regions. A zoomed view of the map appears in Figure 5.7(*b*). Two examples of quasi-periodic trajectories are marked with arrows on the map, though other quasi-periodic orbits are also apparent. The corresponding values of ω_{r0} produce quasi-periodic orbits in the rotating frame; these two quasi-periodic trajectories identified from the ω_r vs. ω_{r0} map appear in Figure 5.8. The trajectory that corresponds to an intial periapse angle $\omega_{r0} = 92.53^o$ appears in Figure 5.8(*a*); the trajectory in Figure 5.8(*b*) is produced from $\omega_{r0} = 133.5^o$. Each is propagated for ~33 periods of the primaries, or 1,000 years.

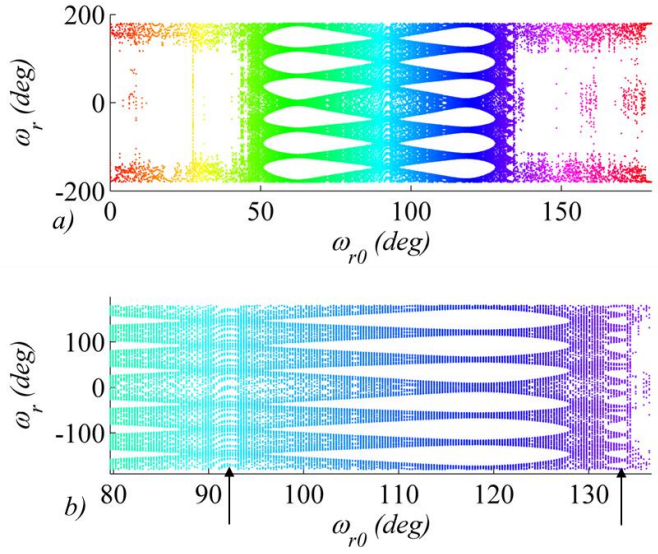

Figure 5.7 Periapse angles over time, ω_r, plotted against initial periapse angles ω_{r0}. Two sample quasi-periodic orbits are marked with arrows.

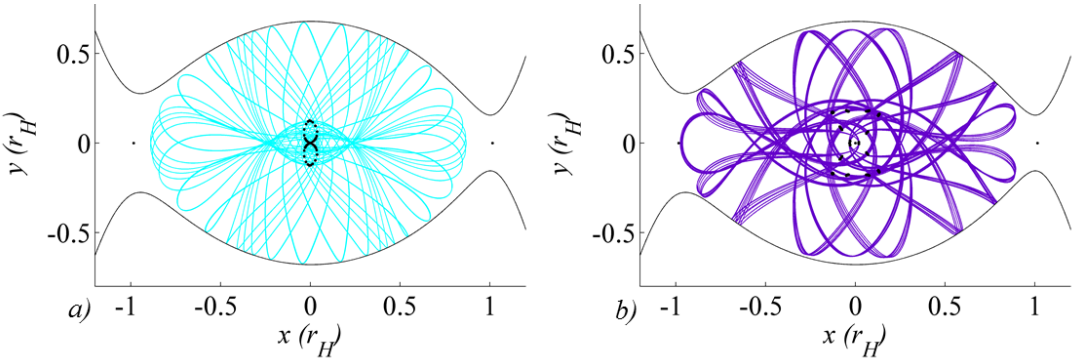

Figure 5.8 Two quasi-periodic trajectories in the Sun-Saturn system identified from the ω_r vs. ω_{r0} map in Figure 5.7.

The map in Figure 5.7 relating periapse angles over time to initial periapse angle reveals characteristics of particular trajectories as viewed in the rotating frame. A similar map locates trajectories with particular characteristics in an inertial reference frame. A map correlating the argument of periapsis in the inertial frame, denoted ω_i, to an initial periapse angle in the rotating frame, ω_{r0}, appears in Fig. 21 for $r_{po} = 0.125 r_H$ and $0 < \omega_{r0} < 180^o$. Inspection of this map immediately reveals quasi-frozen orbits around $\omega_{r0} = 90°$; these trajectories possess a finite range of inertial arguments of periapsis over the propagation time of ~33 revolutions of the primaries. An example of a quasi-frozen trajectory appears in Figure 4.23(*a*). Note that the existence of planar frozen orbits is not predicted by perturbation methods employing the Lagrange planetary equations;[1,3] the third-body effects are sufficiently large in this regime that they are not easily modeled as a perturbation. The map of ω_i versus ω_{r0} also reveals trajectories that are quasi-periodic in the inertial frame: these trajectories possess arguments of periapsis in fixed ranges, rather than continuously over the range 0 to 2π. One such trajectory is characterized by an initial periapse angle of 180º; it appears in Figure 4.23(*f*).

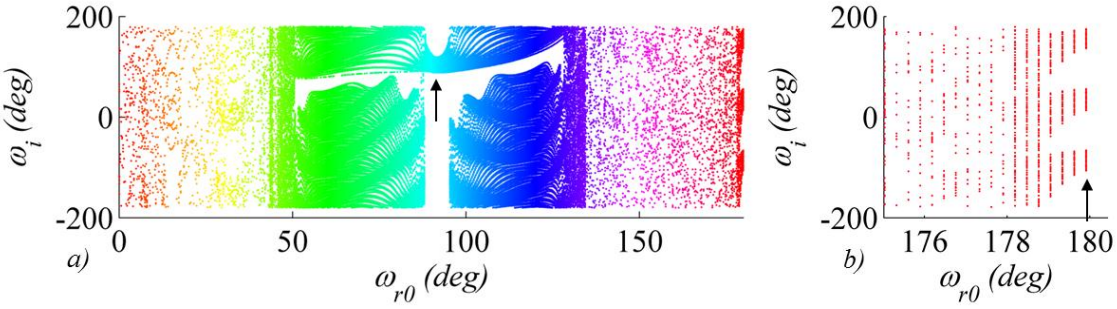

Figure 5.9 Inertial arguments of periapsis over time, ω_i, plotted against ω_{r0} for initial conditions $J = J_1$, $r_{po} = 0.125 r_H$, and $0 < \omega_{r0} < 180^o$. Quasi-frozen (in terms of a limited range for ω_i) and quasi-periodic trajectories are marked with arrows.

In a similar way, maps representing periapse angles over time versus initial periapse angle are used to select particular 3-dimensional trajectories in both the rotating and inertial frames. An example of a map of ω_r vs. ω_{r0} appears in Figure 5.10 for initial *z*-height equal to zero, a velocity angle $\varphi = 68.8°$, and $r_{po} = 0.12 r_H$. By locating initial periapse angles ω_{r0} that result in repeating periapse angles over time from the map of ω_r versus ω_{r0}, quasi-periodic trajectories are easily selected; two examples appear in Figure 5.11(*a*) and (*b*), viewed in the Sun-Saturn rotating frame. A map of ω_i versus ω_{r0} for the same set of initial conditions reveals the existence of trajectories

that are quasi-frozen in the inertial frame; an example appears in Figure 5.11(*c*). Note that no correction process is required to generate these 3D trajectories; the plots in Figure 5.11 are propagated directly from initial states identified from the maps.

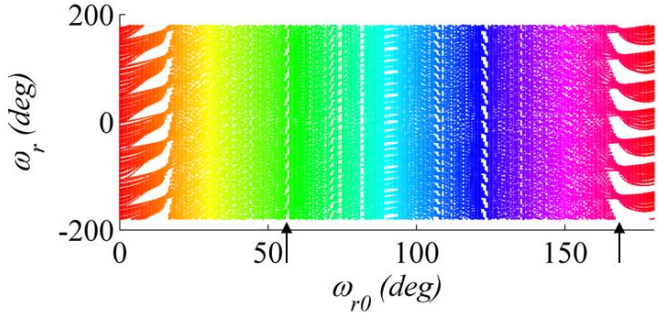

Figure 5.10 Periapse angles over time, ω_r, plotted against initial periapse angles ω_{r0}. Sun-Saturn system, $J = J_1$, $r_{p0} = 0.12r_H$, and $\varphi = 68.8°$. Quasi-periodic orbits result in discrete values of ω_r over time; two such orbits are marked with arrows.

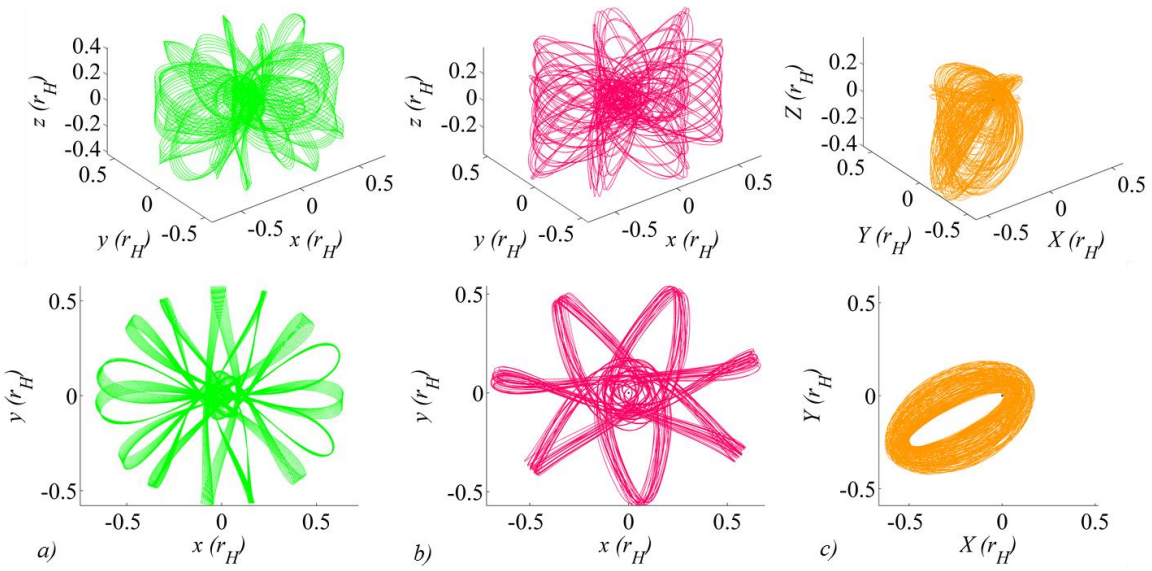

Figure 5.11 Two 3D quasi-periodic orbits viewed in the rotating frame (*a*, *b*) and a 3D quasi-frozen trajectory viewed in the inertial frame (*c*), with *x*-*y* projections (bottom) for $r_{p0} = 0.12r_H$, $z_0 = 0$, and $\varphi = 68.8°$.

In summary, trajectories that would otherwise be quite difficult to locate are easily selected off the periapsis Poincaré maps described above. For example, the two trajectories selected for the Cassini end-of-life analysis, and many other similar candidate trajectories, were originally determined through a painstaking trial-and-error process. By instead employing sets of maps,

similar trajectories are immediately located for analysis. The maps presented thus far are useful in gaining an understanding of the dynamics of the design space: determining the types of trajectories that exist at a certain energy level and predicting the behavior of a spacecraft or natural body in various scenarios. The maps are also directly applicable to specific mission design problems.

5.3. Transitioning CR3BP trajectories to the Ephemeris Model

The time-invariant nature of the CR3BP provides a valuable environment for investigating the design space in a multi-body environment. Preliminary trajectory design is commonly performed in the CR3BP, and selected trajectories are then transitioned into an ephemeris model specific to the particular mission design application.[37, 75, 76] Periodic trajectories in the vicinity of P_2, like many other types of trajectories, are suitable for this process.

The Generator suite of programs developed at Purdue provides a valuable tool for the transition of trajectories from the CR3BP to an ephemeris model. Generator employs a two-level differential corrections scheme as described in Howell and Pernicka.[77] The trajectory is first discretized into a series of patch points, consisting of the time, position, and velocity of the spacecraft along the trajectory. Propagating forwards or backwards in time from each patch point results in a discontinuous path in the ephemeris force model. After implementing the corrector in an iterative manner, a continuous trajectory is produced. A periodic orbit in the CR3BP becomes a quasi-periodic orbit in the ephemeris model.

Two examples appear below. First, the periodic arrowhead-type trajectory from Figure 4.27(*e*) is corrected by Generator to become a continuous quasi-periodic orbit in the ephemeris model. Four patch points are defined along each revolution of the trajectory, as marked in black in Figure 5.12. Six revolutions of the periodic trajectory then define 24 patch points in time and space. These 24 patch points are entered into the Generator differential corrector. A quasi-periodic trajectory, continuous in both position and velocity, results from the corrections process. This corrected trajectory resembles a similar quasi-periodic trajectory that exists in the CR3BP. The quasi-periodic CR3BP orbit appears in red in Figure 5.13(*a*), and the corrected ephemeris orbit appears in blue in Figure 5.13(*b*). Of course, ZVCs do not exist in the ephemeris model, but they serve as a reference for comparison in Figure 5.13. Inertial views of the same two trajectories appear in Figure 5.14. The six revolutions of Saturn are completed in approximately 60 years.

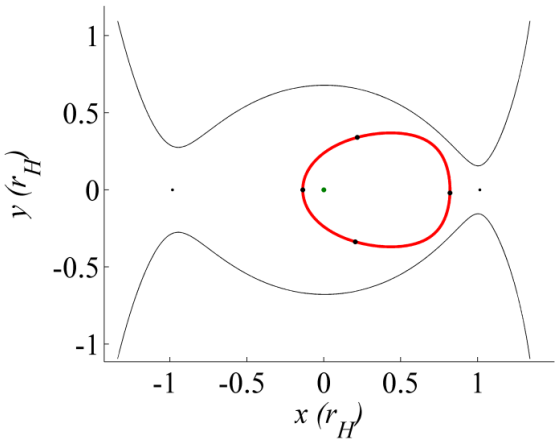

Figure 5.12 Periodic arrowhead-type trajectory with 4 patch points in the CR3BP.

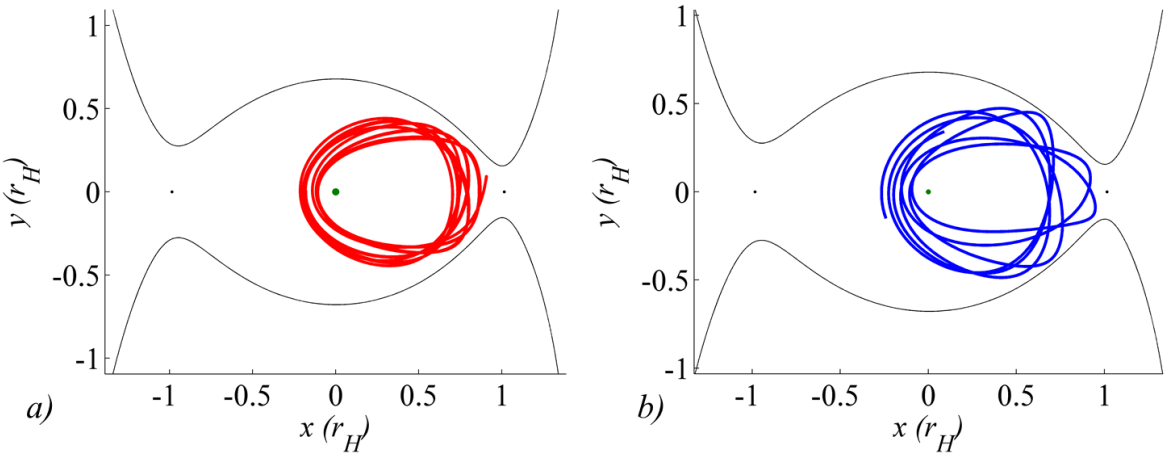

Figure 5.13 Quasi-periodic trajectory in the CR3BP (*a*), and the corrected quasi-periodic trajectory in the ephemeris model (*b*), viewed in the Saturn-centered rotating frame.

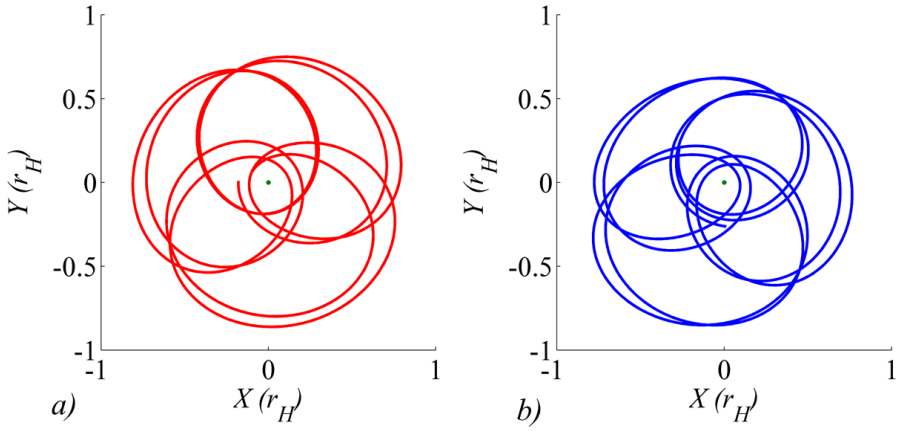

Figure 5.14 Quasi-periodic trajectory in the CR3BP (*a*), and the corrected quasi-periodic trajectory in the ephemeris model (*b*), viewed in the Saturn-centered inertial frame.

In a second example, the periodic figure 8-type trajectory from Figure 4.27(*c*) is corrected in Generator to become a quasi-periodic orbit in the ephemeris model. One full period of the resonant trajectory in the rotating frame consists of 6 revolutions of the spacecraft around Saturn, as is apparent in Figure 5.15. Four patch points are defined along each revolution, so that 24 patch points occur on one period of the resonant trajectory. The patch points are marked in black in Figure 5.15. Three full periods of the resonant trajectory thus contain 72 patch points. When corrected in Generator, the trajectory becomes a quasi-periodic orbit in the ephemeris model, completing 18 revolutions of Saturn in approximately 90 years. The converged solution appears in Figure 5.16 in the Sun-Saturn rotating frame. The inertial views of the quasi-periodic solution in the ephemeris model and the original periodic orbit in the CR3BP appear in Figure 5.17. These two examples demonstrate that periodic trajectories centered at P_2 in the CR3BP can be transitioned into quasi-periodic orbits in the ephemeris model. That is, P_2-centered trajectories initially designed in the CR3BP remain applicable in higher-fidelity models.

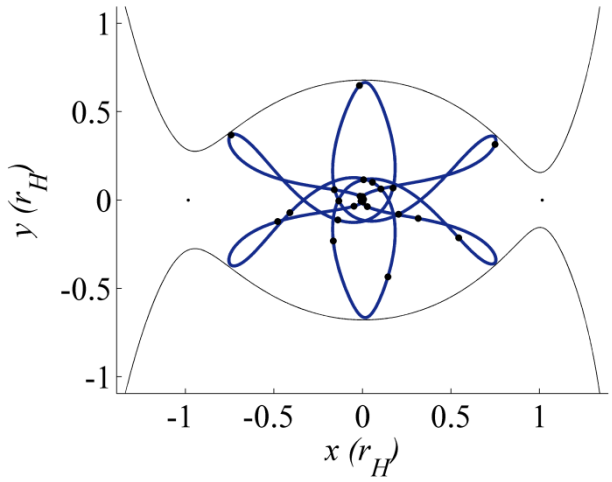

Figure 5.15 Twenty-four patch points along a periodic figure 8-type trajectory in the CR3BP.

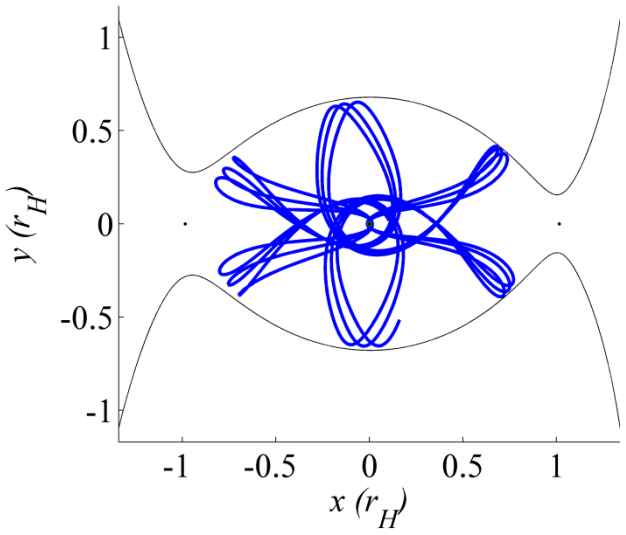

Figure 5.16 Corrected quasi-periodic trajectory in the ephemeris model, viewed in the Saturn-centered rotating frame.

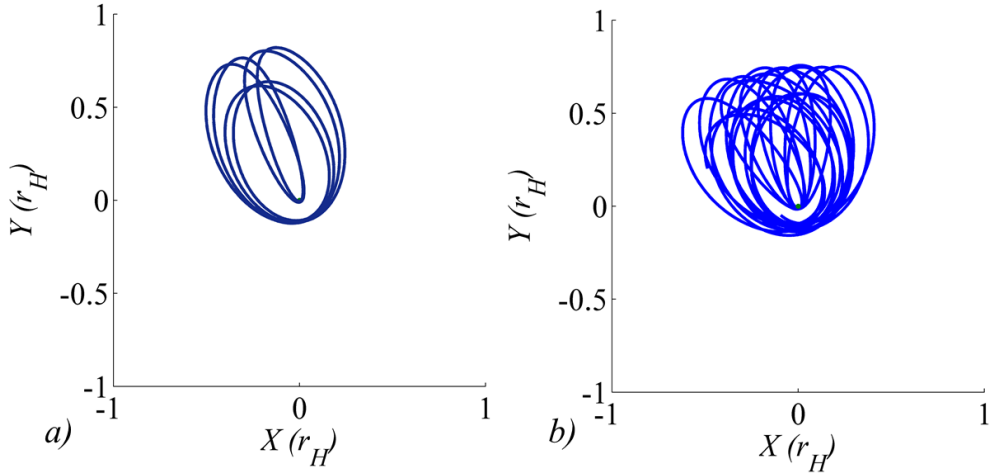

Figure 5.17 The original periodic trajectory in the CR3BP (*a*), and the corrected quasi-periodic trajectory in the ephemeris model (*b*), viewed in the Saturn-centered inertial frame.

5.4. Mission Design for Cassini End-of-Life Using Periapsis Poincaré Maps

Periapsis Poincaré maps are applied to specific mission design applications, demonstrating their effectiveness at simplifying the preliminary trajectory design process. Instead of proceeding with a time-consuming and tedious trial and error procedure, the maps allow trajectories with specific desired characteristics to be visually selected in a quick and easy process.

5.4.1. Example 1: Impact and Escape Trajectories

As a first example, consider again the Cassini end-of-life problem. Spacecraft disposal options include escape from Saturn as well as impact into the planet. As discussed above, Titan flybys can deliver the Cassini spacecraft to a desired orbit, which is characterized by a particular value of Sun-Saturn Jacobi Constant. The initial condition map corresponding to the Jacobi Constant of one post-flyby trajectory option, J = 3.106, appears in Figure 5.18. At this energy level, it is apparent that, depending on the location of periapsis, the trajectory can either impact Saturn, escape through the L_1 or L_2 gateways, or remain in orbit about Saturn. In the Sun-Saturn frame, given r_p, the periapsis of the orbit can lie anywhere on a Saturn-centered ring, its periapse angle depending on the relative orientation of the three bodies at the time of the flyby. For the scenario described above, this ring appears in yellow in Figure 5.18(*b*), overlaid on a zoomed view of the initial conditions map. From this figure, the appropriate orientation of periapsis is immediately apparent to achieve either escape through L_1 or L_2 (place periapsis in the blue and red regions respectively) or impact into Saturn (place periapsis in a black region). Three sample orbits, originating from the three white markers in Figure 5.18(*b*), are plotted in Figure 5.19. Clearly, the selection of the initial periapse angle results in the desired outcome in each case. This method is a significant improvement over the technique used in the tidal acceleration investigation in the original Cassini end-of-life analysis;[64] instead of using a trial-and-error procedure to determine the correct energy level and orientation required to achieve an impact or escape trajectory, the desired orbit is methodically selected from the map in a simple process that requires just minutes to complete.

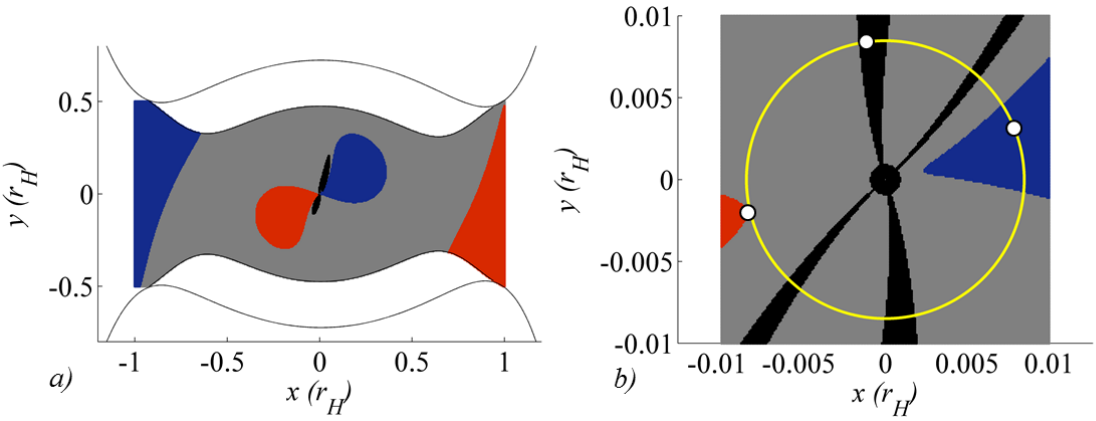

Figure 5.18 Initial condition maps for a post-flyby Cassini end-of-life trajectory. Full view (*a*) and zoomed view (*b*). Initial conditions for three sample trajectories marked on the map.

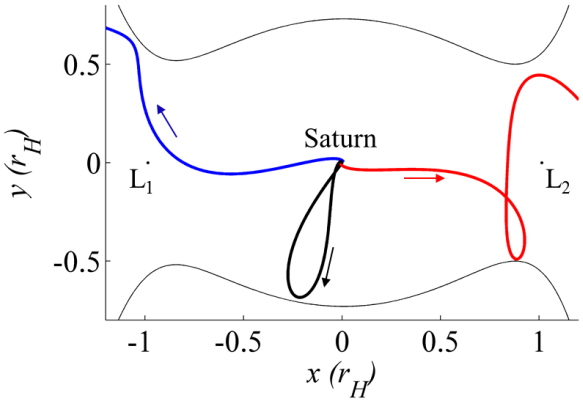

Figure 5.19 Sample impact and escape trajectories originating from periapses marked in Figure 5.18(*b*).

5.4.2. Example 2: Long-term Orbit Beyond Phoebe

In a second application, a design strategy combines an initial condition map with a long-term periapsis Poincaré map to achieve a potential Cassini end-of-life orbit beyond the irregular, retrograde orbit of Phoebe. The goal in this example is to employ the Sun's gravity to raise periapsis significantly, at which point a maneuver is applied to circularize the trajectory. The focus is therefore on post-flyby trajectories that remain captured in the system after one revolution, that is, the grey regions in Figure 5.18. Since the goal is to raise the second periapse radius, the map from Figure 5.18(*b*) is re-plotted in Figure 5.20 for the same Jacobi Constant, J = 3.016; the colors now reflect new information. As in Figure 4.13, each initial periapsis (represented by a point on the map) is now colored consistent with the change in periapse radius after one revolution. The blue regions indicate a decrease in r_p (note that the impact zones exist in the midst of the deepest blue, indicating the largest decrease in r_p) and the red regions correspond to the greatest increase in periapse distance. By orienting the post-flyby periapsis in a region of sufficiently increased r_p, periapsis is raised above Phoebe's orbit. The selected post-flyby trajectory appears in Figure 5.21.

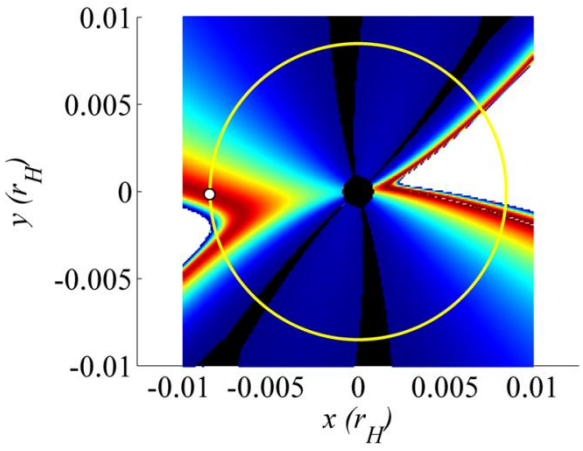

Figure 5.20 Initial condition map colored according to Δr_p over one revolution. The selected initial condition lies in a deep red zone, corresponding to an increase in periapse radius.

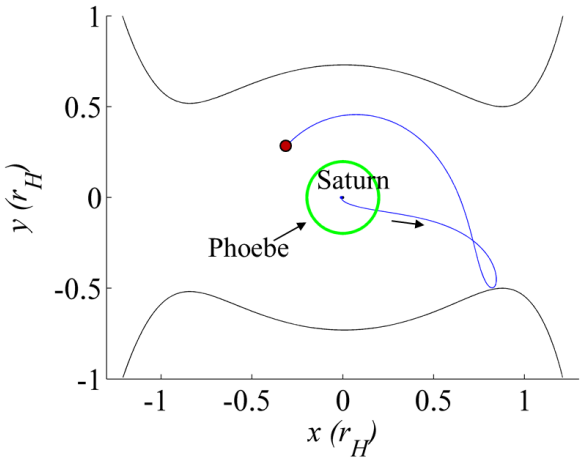

Figure 5.21 Trajectory corresponding to the selected initial condition from Figure 5.20. Maneuver location at the second periapsis is marked in red.

It is now necessary to implement a maneuver at the second periapsis (marked in red in Figure 5.21) to achieve a long-term orbit that neither impacts nor escapes for at least 500 years, as specified by the Cassini end-of-life requirements. The maneuver is assumed to be tangent to the spacecraft velocity. To facilitate the selection of the ΔV magnitude, a long-term periapsis Poincaré map is produced to examine the possible post-maneuver trajectories. A set of potential trajectories is created by varying the magnitude of the maneuver from 0 m/s to 250 m/s. Each trajectory is propagated for 500 years, and the periapse radii over time are recorded and plotted against ΔV magnitude in a map appearing in Figure 4.36. Marked on the map are lines that

highlight the ΔV required to close the L_1 gateway as well as the orbital radius of Phoebe. From this map, it is straightforward to select the minimum value of ΔV that is required to guarantee that a trajectory will not escape or that the periapsis will remain above the orbit of Phoebe for the 500-year propagation time. Also apparent are quasi-periodic trajectories; a similar map of ω_i versus ΔV allows selection of trajectories that display quasi-periodic behavior in the inertial frame. One particular solution requires a ΔV = 105.6 m/s. This orbit remains beyond the orbit of Phoebe and displays quasi-periodic behavior in both the rotating and inertial frames. It appears in Figure 5.23. Note the similarity of this trajectory with the long-term trajectories designed in the initial Cassini end-of-life study appearing in Figure 5.3 and Figure 5.4.

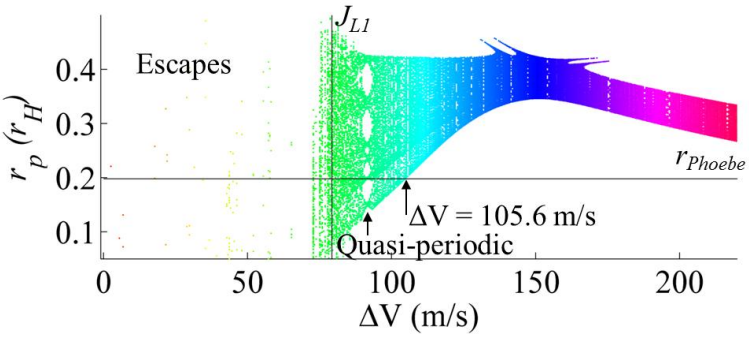

Figure 5.22 Periapse radius versus ΔV for potential long-term end-of-life orbits. Selected trajectory, with ΔV = 105.6 m/s, is marked with an arrow.

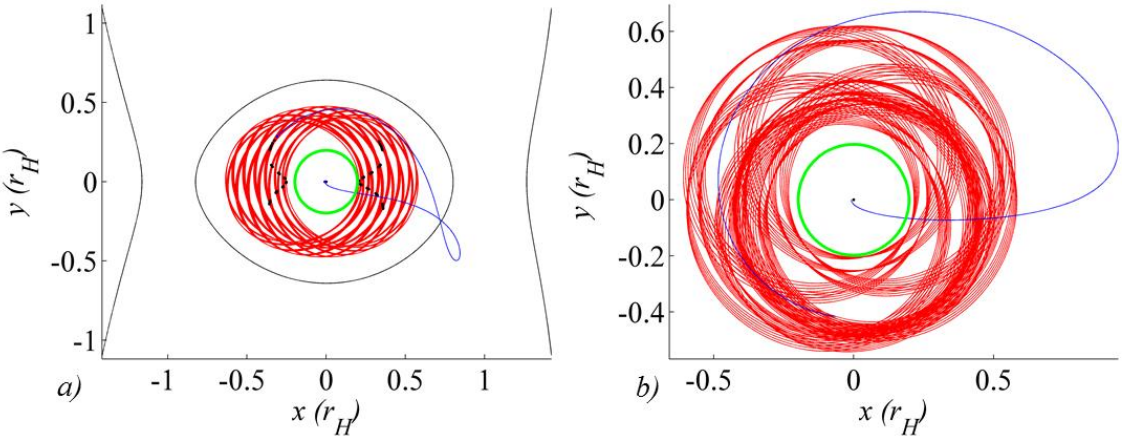

Figure 5.23 Post-flyby Cassini trajectory for long-term end-of-life option in rotating (*left*) and inertial (*right*) views. Phoebe's orbital radius is marked in green, the post-flyby trajectory is blue, and the post-ΔV trajectory is red.

In Figure 5.23, a single post-flyby orientation angle is selected, resulting in a trajectory oriented in Quadrant IV. However, the method is also easily applied to other post-flyby trajectories. By selecting an initial condition lying in a different dark-red area along the yellow circle in Figure 5.20, the characteristics of the resulting r_p vs. ΔV map changes, and different long-term trajectory options are available. For example, three additional post-flyby periapses are marked on the map in Figure 5.24. A corresponding long-term trajectory is selected for each case; these three sample trajectories appear in Figure 5.25. Each remains beyond Phoebe's orbital radius for the full propagation. One post-flyby trajectory, in Figure 5.25(*a*), lies in Quadrant IV; it requires a ΔV of 107.9 m/s. The other two sample orbits proceed from post-flyby trajectories in Quadrant II. The orbit appearing in Figure 5.25(*b*) requires 99.0 m/s, while the trajectory in Figure 5.25(*a*) is produced with a ΔV of only 97.1 m/s.

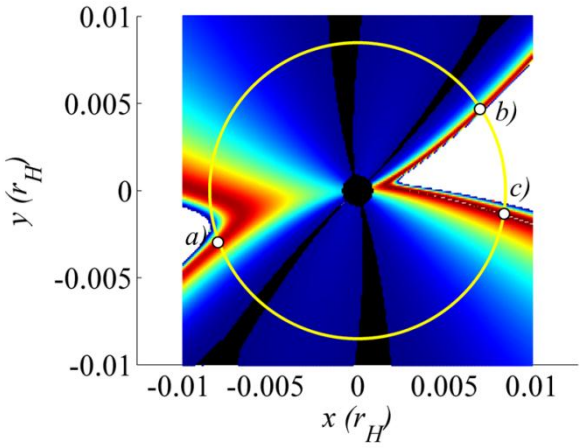

Figure 5.24 Post-flyby initial condition map, with three initial conditions marked.

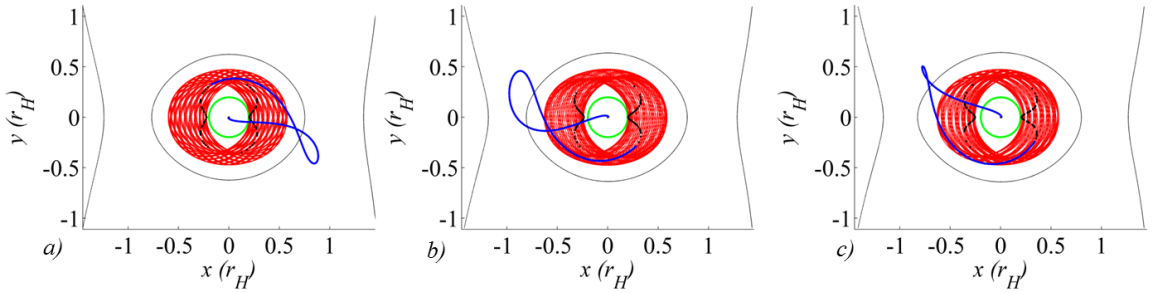

Figure 5.25 Three sample long-term Cassini end-of-life trajectories, originating from post-flyby states in Figure 5.24.

It is again noted that, during the tidal acceleration analysis in support of the Cassini end-of-life study in 2007, each trajectory computed was a point solution, and each was located through manual iterations. No tool was available at the time to allow selection of trajectories with the desired characteristics in a methodical way. The initial condition maps and long-term periapsis Poincaré maps allow easy selection of orbits for preliminary trajectory design. These maps also lend insight into the characteristics of the design space.

5.5. Mission Design for Titan Capture

Potential applications are not limited to the Sun-Saturn system. In this example, periapsis Poincaré maps are also used to design a capture into a periodic orbit about Titan. Consider a spacecraft in the Saturn-Titan system with an energy level such that the ZVCs are open at L_1 and L_2 ($J = 3.015311017945150 < J_{L2}$). Recall that the initial condition map in Figure 4.12(*b*) represents regions of escape from Titan's vicinity after up to 6 revolutions of the spacecraft. If this map is reflected across the *x*-axis, time is reversed; that is, the reflected map corresponds to regions of entrance into the region near Titan through the gateways at L_1 and L_2. This reflected map appears in Figure 5.26. In this map, the blue regions correspond to periapses of trajectories entering through L_1 to shift into orbit about Titan, while the red lobes are comprised of periapses of orbits entering the vicinity of Titan through L_2.

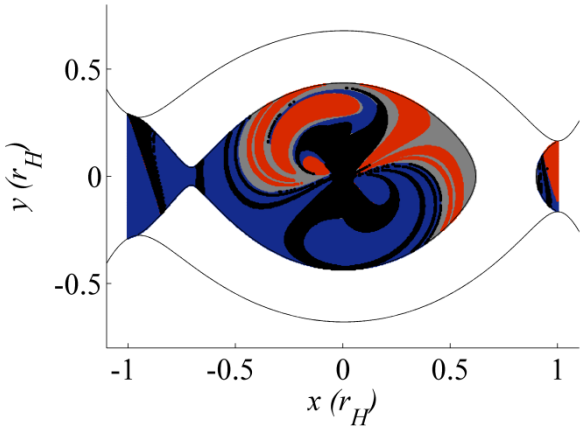

Figure 5.26 Saturn-Titan initial condition map for $J = J_1$, reflected across the *x*-axis; corresponds to regions of entrance into the vicinity of Titan.

By applying a ΔV at a selected periapsis corresponding to one of these entering trajectories, the energy level of that trajectory is reduced, with the goal of reaching a quasi-periodic orbit about Titan. To achieve this objective, however, the particular trajectory must be carefully selected. To ensure that the orbit remains captured at Titan, the energy level is selected to just close off the L_1 gateway, that is, $J = J_{L1}$. A long-term periapsis Poincaré map is created by propagating 2,844 trajectories for 33 periods of the primaries. In the Saturn-Titan system, this corresponds to approximately 1.44 years. Initial conditions correspond to regions of the design space such that $0.049\ r_H < r_{p0} < 0.4\ r_H$ and $0 < \omega_0 < \pi$. The map of y_p versus x_p over time appears in Figure 5.27. The periapses of each trajectory are colored according to the orbit's initial periapse angle, ω_0. From this map, it is clear that regions of quasi-periodic trajectories exist centered at $\omega_0 = 0$ and $\omega_0 = \pi$. Three periodic trajectories are located at the center of these sets of islands. They correspond to approximately $r_{p0} = 0.163\ r_H$ and $r_{p0} = 0.231\ r_H$ at $\omega_0 = 0$, and $r_{p0} = 0.225\ r_H$ at $\omega_0 = \pi$.

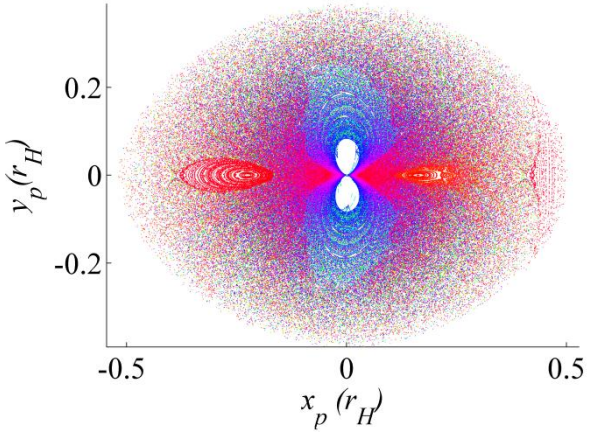

Figure 5.27 Periapsis Poincaré map for 2,844 trajectories in the Saturn-Titan system, each propagated for 1.44 years, $J = J_{L1}$.

By overlaying the long-term map in Figure 5.27 on the initial condition map from Figure 5.26, it is simple to determine which long-term orbits with $J = J_{L1}$ can be achieved by applying a ΔV at periapsis soon after entering the vicinity of Titan at an energy level corresponding to $J = J_1$. A zoomed view of the overlaid maps appears in Figure 5.28. Consider the periodic orbit with $J = J_{L1}$ and with periapsis located at $r_{p0} = 0.231\ r_H$ and $\omega_0 = 0$. This coordinate is marked in green in Figure 5.28. The corresponding trajectory is located in the lobe associated with the second periapsis after L_1 capture. That is, the trajectory enters through the L_1 gateway and reaches the desired location at its second periapsis passage in the vicinity of Titan, as in Figure 5.29(*a*).

When the trajectory passes through this periapsis, a ΔV of 7.4 m/s is applied to lower the energy so that $J = J_{L1}$. The resulting periodic trajectory appears in Figure 5.29(*b*). It is propagated for 1.44 years, equivalent to 33 periods of the primaries. The same trajectories appear in a Saturn-centered inertial view in Figure 5.30. The path commences from a Saturn-centered trajectory, shown in blue, that is slightly smaller than Titan's orbit. The spacecraft enters the vicinity of Titan near $x = 0$, and a ΔV approximately a quarter of a revolution later places the spacecraft onto the green periodic trajectory about Titan.

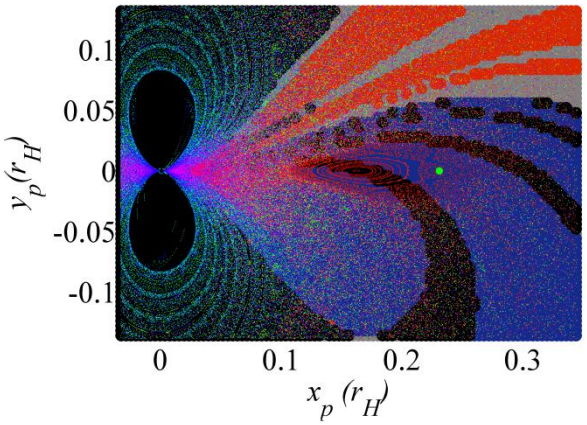

Figure 5.28 Long-term map at $J = J_{L1}$ overlaid on initial condition map at $J = J_1$; periodic trajectory marked in green lies in the lobe corresponding to the second periapsis after entrance into the vicinity of Titan through L_1.

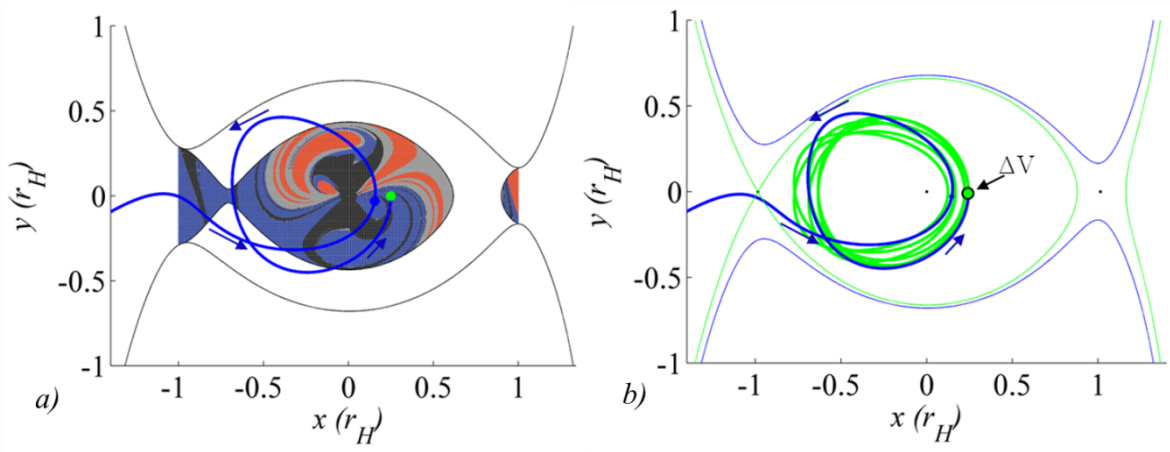

Figure 5.29 Pre-ΔV trajectory overlaid on Saturn-Titan initial condition map (*a*); ΔV applied at second periapsis (marked in green) results in the green periodic Titan-centered trajectory (*b*).

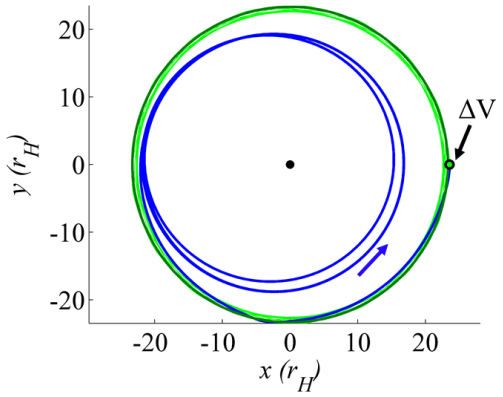

Figure 5.30 Saturn-centered inertial view of the pre-ΔV trajectory (blue) and the post-ΔV orbit (green).

In a similar way, a combination of long-term and short-term maps facilitates the design of a Titan capture trajectory for a spacecraft on a Saturn-centered path but further from Saturn than Titan's orbit. In this case, the spacecraft enters the vicinity of Titan through the L_2 gateway. The same set of maps is employed; in this case, an initial condition is selected that lies in the red lobe corresponding to the second periapsis after entrance through L_2 for $J = J_1$, as marked in green in Figure 5.31. This periapsis, located at $r_{p0} = 0.233\ r_H$ and $\omega_0 = 174.9^{\circ}$, also corresponds to a quasi-periodic Titan-centered trajectory at $J = J_{L1}$. By applying a $\Delta V = 7.2$ m/s at this point, the energy is lowered from $J = J_1$ to $J = J_{L1}$, and the spacecraft enters the quasi-periodic orbit about Titan. The resulting trajectory appears in Figure 5.32. The spacecraft enters the vicinity of Titan through L_2 on the red trajectory and reaches its second periapsis in the L_2 lobe as marked in Figure 5.32(*a*). After the maneuver, the spacecraft moves in the green quasi-periodic orbit around Titan, as is apparent (in green) in Figure 5.32(*b*). The same pair of trajectories appears in a Saturn-centered inertial view in Figure 5.33. The pre-ΔV orbit lies beyond Titan; after the spacecraft enters the vicinity of Titan, the maneuver captures the spacecraft into the quasi-periodic Titan-centered trajectory. By combining initial condition maps corresponding to entrance into the vicinity of Titan with a long-term periapsis Poincaré map, a capture into a quasi-periodic orbit about Titan is methodically designed.

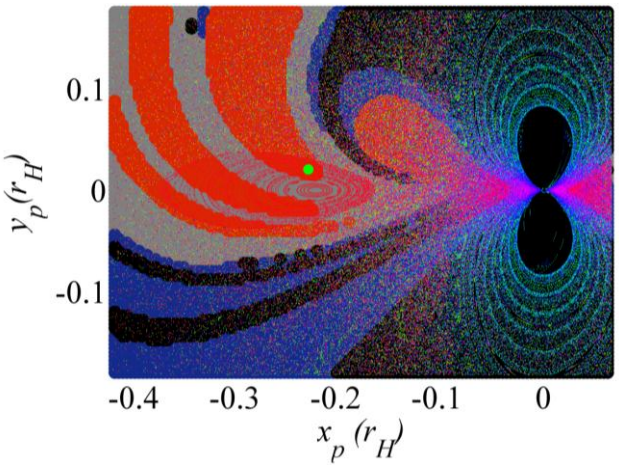

Figure 5.31 Long-term map at $J = J_{L1}$ overlaid on initial condition map at $J = J_1$; quasi-periodic trajectory marked in green lies in the lobe corresponding to the second periapsis after entrance into the vicinity of Titan through L_2.

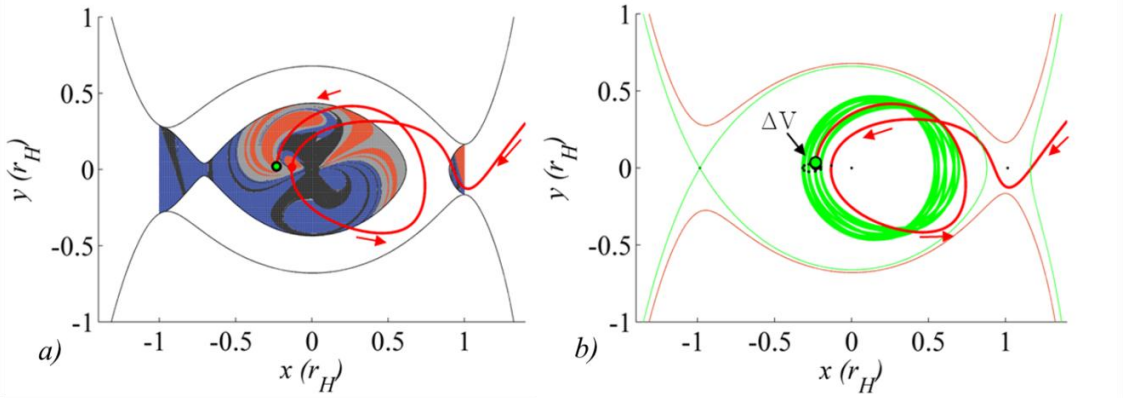

Figure 5.32 Pre-ΔV trajectory overlaid on Saturn-Titan initial condition map (*a*); ΔV applied at second periapsis (marked in green) results in the green periodic Titan-centered trajectory (*b*).

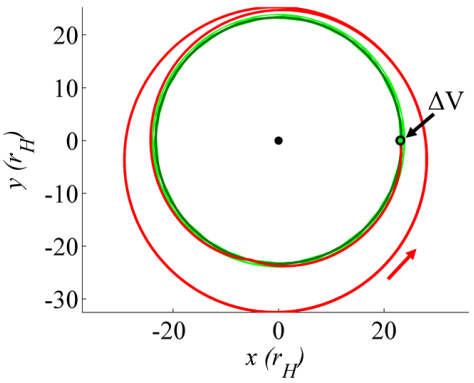

Figure 5.33 Saturn-centered inertial view of the pre-ΔV trajectory (red) and the post-ΔV orbit (green).

5.6. Mission Design for Earth-Moon Transfer

Periapsis Poincaré maps are also applied to the problem of designing a low-energy ballistic lunar transfer from low Earth orbit. A well-researched problem,[31, 32, 35, 40] a ballistic lunar transfer utilizes the gravity of the Sun to naturally raise the periapsis of an Earth-centered trajectory, lowering the ΔV required to reach the orbital radius of the Moon as compared to a Hohmann transfer. Initial condition maps simplify the problem of determining both the ΔV and the orientation in the Sun-Earth frame that yield the appropriate periapse raise.

Consider a spacecraft in a 167 km circular parking orbit centered at Earth. At this energy level, the ZVCs are completely closed and the Sun has little effect on the orbit. A maneuver applied at an appropriate location in the parking orbit decreases Jacobi Constant and shifts the spacecraft to periapsis of a large Earth-centered orbit. This larger orbit is affected significantly by the Sun, and the subsequent periapsis is raised to the radius of the lunar orbit. To reach the Moon's orbital radius, the periapse must be raised from R_E + 167 km to 384,400 km, corresponding to Δr_p = 377,855 km = 0.2525 r_H, in terms of the Sun-Earth Hill radius. To determine the required ΔV, initial condition maps are created for a series of post-ΔV Jacobi values. For each value of ΔV, a Δr_p map (similar to those in Figure 5.24 or Figure 5.36) is created. These maps allow a quick visualization of the orientation that produces the largest increase in periapse radius for each ΔV. The ZVCs and the trajectories corresponding to approximately the largest periapse increase for a set of 8 values of ΔV appear in Figure 5.34. For ΔV < 3.199 km/s, the ZVCs constrain the apoapsis to a radius too small to allow solar gravity to raise periapsis sufficiently. For ΔV ≥ 3.2 km/s, however, the ZVCs are sufficiently open (that is, the Jacobi Constant is low enough) to result in a periapse raise sufficiently large to reach the lunar orbit. This value agrees well with a theoretical minimum ΔV determined by Sweetser[78] as 3.099 km/s for transfer from a 167 km parking orbit at Earth, as well as with optimized Earth Moon transfer ΔV values calculated by Parker,[79] who finds ΔV ≈ 3.2 km/s for a transfer from a 185 km parking orbit in a Sun-Earth-Moon gravity model.

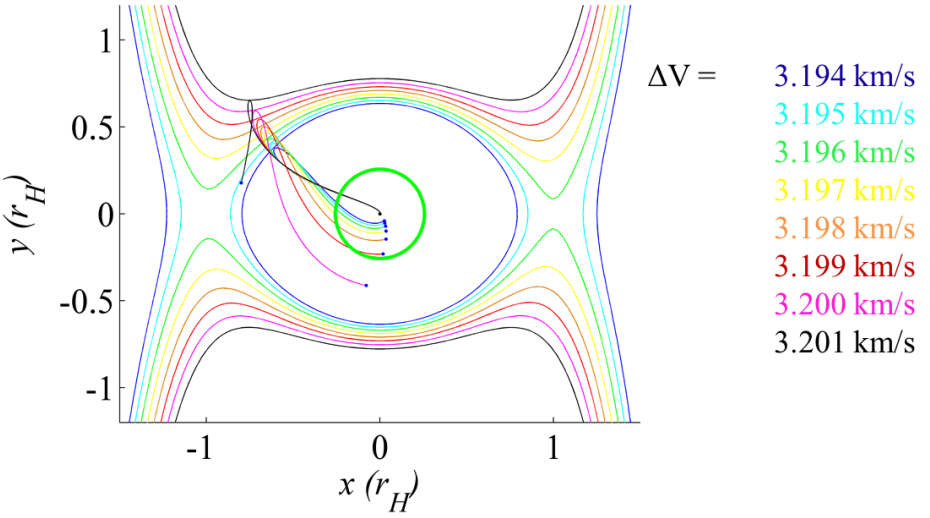

Figure 5.34 Trajectories at a series of ΔV values, each oriented for the largest periapse raise. Lunar orbital radius marked in green.

A maneuver of 3.2 km/s changes the value of Jacobi Constant from J = 3.068621, the value of J corresponding to the low-Earth orbit, to J = 3.000785 in the Sun-Saturn system, the value of J associated with the transfer orbit. The post-maneuver initial condition map corresponding to ΔV = 3.2 km/s, or J = 3.000785, appears in Figure 5.35 in a full view (*a*) and a zoomed view (*b*); both are in the Sun-Earth rotating frame. The 167-km parking orbit is marked in green. Clearly, at this Jacobi Constant, J = 3.00078518, depending on the location of the post- ΔV periapsis along the parking orbit, the spacecraft can impact Earth or escape the vicinity of the Earth entirely. However, in this application, the focus is on trajectories that remain in Earth orbit for at least one revolution, with a significant raise in radius at the second periapsis. To locate the orientation for the appropriate periapse raise, a Δr_p map is produced. As before, each periapsis corresponding to a trajectory that remains captured is colored according to Δr_p over one revolution. The Δr_p map appears in Figure 5.36(*a*). The 167-km parking orbit is again marked in green on the map. Four bands of initial periapse angles exist that correspond to $\Delta r_p = 0.2525\ r_H$: two bands producing apoapses in Quadrant II, two in Quadrant IV. These bands are marked by purple rays. By selecting an initial periapsis at the intersection of a purple ray with the green parking orbit, the orientation is determined that will result in the desired raise in periapsis. Four such trajectories appear in Figure 5.37 corresponding to the four initial conditions marked on the map in Figure 5.36(*a*). Clearly, each trajectory originates from the 167 km parking orbit; after a 3.2 km/s ΔV, it reaches apoapsis well beyond the radius of the Moon's orbit. The next periapsis

along each orbit is precisely at the radius of the Moon's orbit. Note that these trajectories have previously been designed without incorporating the gravity of the Moon, the Moon's inclination with respect to the ecliptic, or the problem of Sun-Earth-Moon phasing. However, the maps provide a fast, easy method for preliminary design.

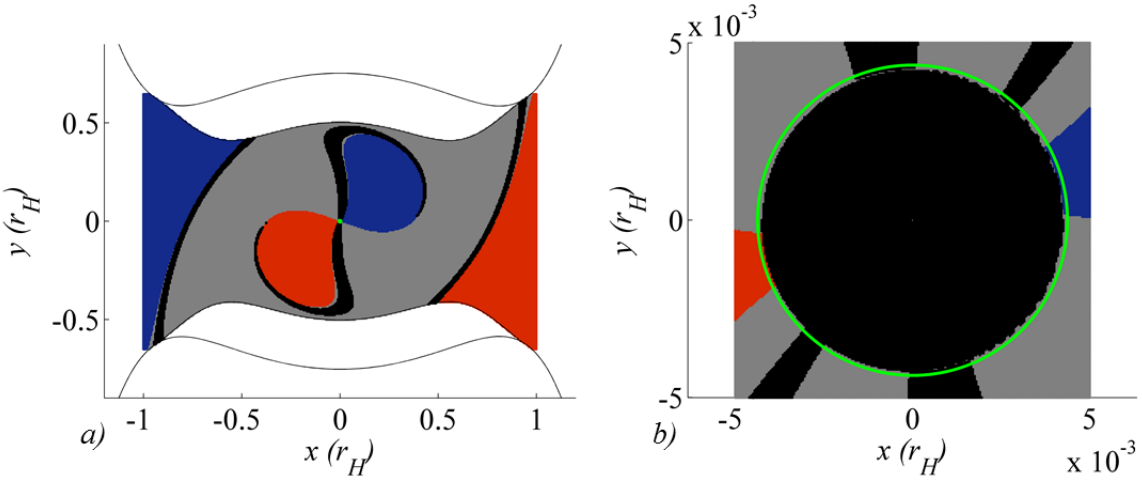

Figure 5.35 Sun-Earth initial condition maps corresponding to ΔV = 3.2 km/s, or J = 3.000785; 167 km parking orbit marked in green.

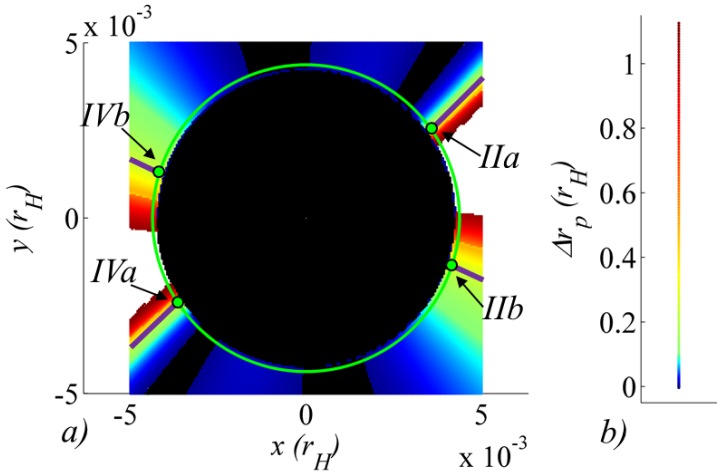

Figure 5.36 Initial condition map visualizing Δr_p over one revolution for ΔV = 3.2 km/s, or J = 3.000785. Desired Δr_p for Earth-Moon transfer denoted by purple rays; four selected ICs marked.

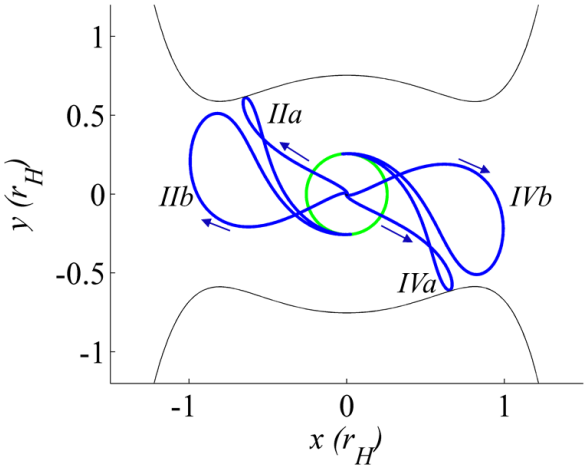

Figure 5.37 Four Earth-Moon transfer trajectories corresponding to the initial conditions marked in Figure 5.36.

6. INCLUDING THE INFLUENCE OF AN ADDITIONAL SMALLER PRIMARY

Traditionally, patched-conic analysis has dominated preliminary design approaches for missions that include satellite tours such as Galileo and Cassini. However, incorporating multiple gravity fields in the dynamical model, early in the tour design process, can expand the design options. Of course, gravity assists have been investigated and exploited very successfully for decades. Nevertheless, incorporating the gravity of the encounter body explicitly during the early design process more accurately reflects the flyby characteristics and might add trajectory options. This is particularly important in certain regimes where the gravity fields of multiple bodies impact the spacecraft behavior to a similar degree and must be simultaneously considered. One recent example is the design of the end-game trajectory for a Europa orbiter mission. In this design problem, considering the gravitational influences of Jupiter and its moons simultaneously can significantly lower the ΔV required to achieve orbit around Europa.[49, 80, 81] Therefore, an examination of flybys from a multi-body perspective is insightful. Before adding the influence of a gravity assist body to the larger problem, the flyby itself must be understood. Then, the flyby design can be combined with a tidally-influenced orbit to produce a trajectory that fully exploits its multi-body environment. For example, a close encounter with Titan is investigated in terms of the Saturn-Titan CR3BP, and later, the tidal effects due to solar gravity are added to the analysis.

Consider a system with three large gravitational bodies: P_1, P_2, and the flyby body; for example, the Sun-Saturn-Titan system. A spacecraft in orbit about P_2 (Saturn) approaches periapsis and encounters the flyby body (Titan). The encounter may occur prior to periapse passage and, thus, is denoted an inbound flyby. An example of an inbound flyby appears in inertial and rotating views in Figure 6.1. An outbound flyby, on the other hand, occurs after periapse passage, as the spacecraft is departing the vicinity of P_2. A sample outbound flyby appears in inertial and rotating views in Figure 6.2. A first goal is to predict the change in orbital elements, such as semi-major axis a or periapse radius r_p, due to the flyby. Instead of using a patched-conic approach, the CR3BP is the basis for this analysis. Note that periapse radius r_p refers to periapsis with respect to P_2 (Saturn, in this example), while flyby altitude refers to the altitude of closest approach relative to the flyby body (Titan).

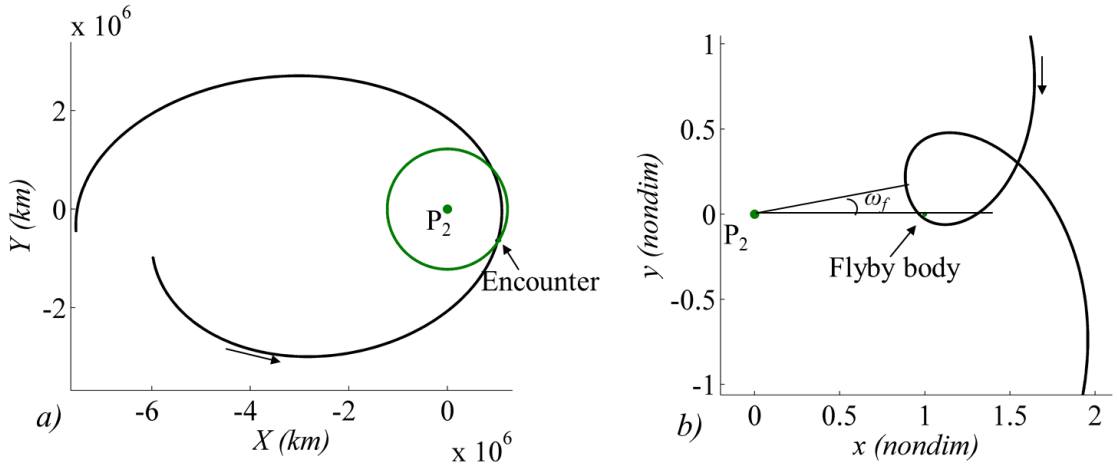

Figure 6.1 Inertial and rotating views of an inbound (prior to periapsis) flyby in the Saturn-Titan system.

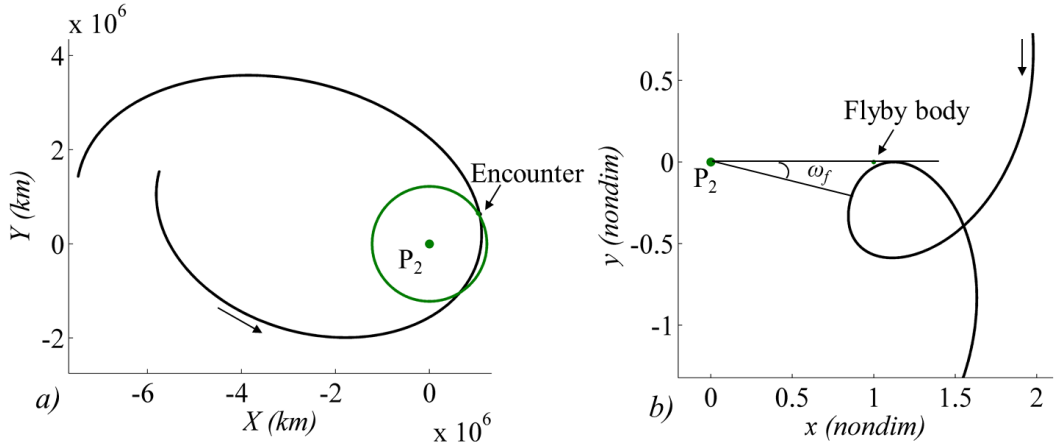

Figure 6.2 Inertial and rotating views of an outbound (post-periapsis) flyby in the Saturn-Titan system.

6.1. The Flyby Kick Function

The complexity involved with flyby analysis in the P_2-flyby body CR3BP is reduced by employing a kick function, which estimates changes in some of the orbital elements due to the flyby. Several previous investigations of orbits in multi-body regimes, including comets and other solar system particles, as well as spacecraft, employ the kick function to lend insight to the problem.[51-54] A major advantage from employing the kick function is a quick method for estimating the flyby angle, or the angle with respect to the P_2-flyby body rotating *x*-axis

associated with the periapsis immediately prior to/following the flyby, ω_f, that yields a particular change in an osculating element, such as semi-major axis, *a*. Without requiring transformations between the conic model and the CR3BP, or between the rotating and inertial reference frames, the kick function supplies an estimate of certain orbit parameters that yield desired effects on the trajectory due to the flyby. The accuracy of the estimate depends on the specific assumptions associated with a given application; however, in the regime where the Lagrange Planetary Equations are applicable, the flyby kick function provides accurate approximations of the effects of a flyby on a spacecraft trajectory. In this application, the gravity of P_1 is not considered; the kick function approximates the gravitational influences in the P_2-flyby body CR3BP.

Consider a spacecraft initially located at apoapsis. If the spacecraft encounters the flyby body on its next approach to periapsis, the gravity assist from the flyby alters the spacecraft orbital parameters, including the osculating semi-major axis. This change in semi-major axis *a* is related to the angle between periapsis and the rotating *x*-axis, ω_f, by the flyby kick function. This approximation is derived from the CR3BP equations of motion (see Zhou et al.[52]) or from the expression for the Jacobi Integral, as demonstrated in Ross and Scheeres.[54] Assuming that $m_2 << m_1$, for a planar orbit, this expression is approximated as follows

$$\begin{aligned} J \approx & \underbrace{-2\mu\left(\frac{1}{r}-\frac{1}{r_2}\right)}+\underbrace{2\sqrt{a(1-e^2)}}+\frac{1}{a} \\ = & \quad -2\mu R \qquad\quad -2\Lambda \qquad -2K \end{aligned} \tag{6.1}$$

if it is evaluated in terms of osculating orbital elements. Recall that for small values of μ, or for large values of r_1 and r_2, the Jacobi Constant reduces to the Tisserand Constant,

$$TC = 2\sqrt{a(1-e^2)}+\frac{1}{a}. \tag{6.2}$$

Of course, in the CR3BP, the Tisserand Constant is an approximation and therefore is not, in fact, constant. In the more complete expression in Eq. (6.1), the component $K = -a/2$ can be considered the Keplerian contribution due to P_2, and $\Lambda = \sqrt{a(1-e^2)}$ is the angular momentum of the spacecraft. The component of the Jacobi Constant expression in Eq. (6.1) that is contributed by the smaller primary is *R*, approximated as

$$R \approx -\frac{1}{\sqrt{1+r^2-2r\cos\theta}}+\frac{\cos\theta}{r^2}+\frac{1}{r} \tag{6.3}$$

to first order in μ. The angle between the spacecraft state vector $\bar{r}$ and the rotating *x*-axis is

$$\theta = \omega_i + \theta^* - nt = \omega_i + \theta^* - t = \omega_f + \theta^* \tag{6.4}$$

where ω_i is the spacecraft's inertial argument of periapsis, θ^* is the true anomaly, nt is the angle between the inertial and rotating axes, and ω_f is the angle of periapsis immediately before/after the flyby in the rotating coordinate frame, as illustrated in Figure 6.3. Recall that the nondimensional mean motion of the primaries, n = 1, and, thus, $nt = t$. Assume that, at the moment of periapsis, the inertial and rotating frames are coincident so that $t = \theta^* = 0$ and $\omega_i = \omega_f$. The ultimate goal in this section is the blending the flyby analysis with the tidal effects of a distant

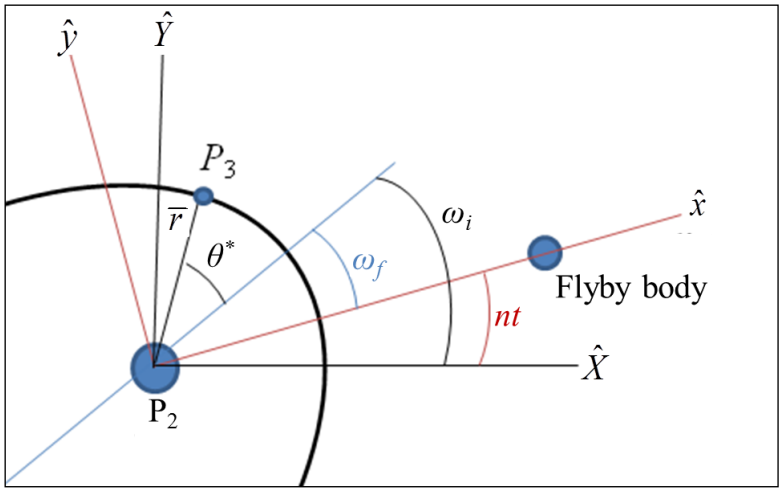

Figure 6.3 The relationships between the angles ω_i, ω_f, θ^*, and nt, where $\hat{X}$ and $\hat{Y}$ are the inertial axes and $\hat{x}$ and $\hat{y}$ rotate with the P_2- Flyby body frame.

larger primary, for example in a Sun-planet-moon system. Therefore, the Sun is denoted as P_1, the planet is defined as P_2, and the moon is termed the flyby body. The component R is considered a perturbing function, and the Lagrange Planetary Equations[14] are employed to relate R and Λ such that

$$\frac{d\Lambda}{dt} = -\mu \frac{\partial R}{\partial \omega_i} = -\mu \left(\frac{r}{r_2^3} \sin(\omega_i + \theta^* - t) - \frac{1}{r^2} \sin(\omega_i + \theta^* - t) \right). \tag{6.5}$$

Using the Picard method of successive approximations to first order[13],

$$\begin{aligned}\Delta\Lambda &= -\mu \int_{-T/2}^{T/2} \frac{\partial R}{\partial \omega_i}\, dt \\ &= -\mu \int_{-T/2}^{T/2} \left[\frac{r}{r_2^3}\sin(\omega_i + \theta^* - t) - \frac{1}{r^2}\sin(\omega_i + \theta^* - t) \right] dt \\ &= -\frac{\mu}{\sqrt{p}} \int_{-\pi}^{\pi} \left[\left(\frac{r}{r_2} \right)^3 \sin(\omega_f + \theta^*) - \sin(\omega_f + \theta^*) \right] d\theta^*.\end{aligned} \tag{6.6}$$

Since the Jacobi Constant does not vary over the trajectory, $\Delta J = 0$, and from Eq. (6.1)

$$\mu\Delta R + \Delta\Lambda + \Delta K = 0. \tag{6.7}$$

Over the range of trajectories for the application investigated here, the value of $\mu\Delta R$ is four orders of magnitude smaller than $\Delta\Lambda$ and can be neglected. Therefore, the Keplerian contribution is approximated, $\Delta K \approx -\Delta\Lambda$. Since $K = -a/2$,

$$\Delta a = \frac{2a^2\Delta\Lambda}{1 - 2a\Delta\Lambda}. \tag{6.8}$$

The definite integral in the expression for $\Delta\Lambda$ is evaluated by quadratures, rendering a relationship between Δa and ω_f, labeled a kick function.

An alternative method for computing Δa is used by Zhou et al.[52] This approach originates with the planar equations of motion in the CR3BP, written in inertial coordinates,

$$\begin{aligned}\ddot{X} &= \frac{(1-\mu)(X_{P1} - X)}{r_1^3} + \frac{\mu(X_{P2} - X)}{r_2^3} \\ \ddot{Y} &= \frac{(1-\mu)(Y_{P1} - Y)}{r_1^3} + \frac{\mu(Y_{P2} - Y)}{r_2^3}\end{aligned} \tag{6.9}$$

where the x and y coordinates of the two primaries are

$$\begin{aligned} X_{P1} &= -\mu\cos(t) & X_{P2} &= (1-\mu)\cos(t) \\ Y_{P1} &= -\mu\sin(t) & Y_{P2} &= (1-\mu)\sin(t). \end{aligned} \tag{6.10}$$

Expanding to first order in μ, the equations of motion become

$$\begin{aligned}\ddot{X} &= \frac{-X}{r^3} + \mu A(X, Y, t) + O(\mu^2) \\ \ddot{Y} &= \frac{-Y}{r^3} + \mu B(X, Y, t) + O(\mu^2)\end{aligned} \tag{6.11}$$

where

$$A(X,Y,t) = \frac{X - \cos(t)}{r^3} + \frac{3X[X\cos(t) + Y\sin(t)]}{r^5} + \frac{\cos(t) - X}{([X - \cos(t)]^2 + [Y - \sin(t)]^2)^{3/2}}$$

$$B(X,Y,t) = \frac{Y - \cos(t)}{r^3} + \frac{3Y[X\cos(t) + Y\sin(t)]}{r^5} + \frac{\cos(t) - Y}{([X - \cos(t)]^2 + [Y - \sin(t)]^2)^{3/2}}. \quad (6.12)$$

Again, it is assumed that $t = \theta^* = 0$ at the moment of periapsis passage. Note that the spacecraft state is a function of the inertial argument of periapsis, ω_i, which is equal to ω_r when the spacecraft passes through periapsis, due to the coincidence of the coordinate frames at this moment. Define the Keplerian energy as above, i.e.,

$$K = -\frac{1}{2a} = \frac{\dot{X}^2 + \dot{Y}^2}{2} - \frac{1}{r} \quad (6.13)$$

and the change in K over time is

$$\frac{dK}{dt} = \mu[\dot{X}(t)A(X(t),Y(t),t) + \dot{Y}(t)B(x(t),Y(t),t)]. \quad (6.14)$$

From one apoapsis passage to the next, the change in K is, therefore,

$$\Delta K = \mu \int_{-T/2}^{T/2} [\dot{X}(t)A(t) + \dot{Y}(t)B(t)]dt = \frac{\mu r^2}{\sqrt{p}} \int_{-\pi}^{\pi} [\dot{X}(\theta^*)A(\theta^*) + \dot{Y}(\theta^*)B(\theta^*)]d\theta^*. \quad (6.15)$$

The expression in Eq. (6.15) can, again, be integrated by quadratures such that,

$$\Delta a = \frac{2a^2\Delta K}{1 - 2a\Delta K}. \quad (6.16)$$

The two approaches for calculating Δa yield equivalent results. The second approach is somewhat more straightforward to derive; however, it requires a calculation of the spacecraft state during each integration step and, therefore, requires a longer computation time.

Consider a spacecraft in orbit about Saturn (P_2); it is initially located at apoapsis. (The gravity of the Sun (P_1) is not considered.) If the spacecraft encounters Titan (the flyby body) on its next approach to periapsis, the gravity assist from the Titan flyby changes the spacecraft

orbital parameters, including the osculating semi-major axis. This change in semi-major axis a is related to the angle between periapsis and the rotating x-axis, ω_f, by the kick function, via the relationships in Eq. (6.6) and Eq. (6.8). This parameter ω_f is selected a priori to achieve a desired value of Δa from the Titan flyby.

The kick function appears in Figure 6.4 for two sets of sample trajectories, each possessing a single value of osculating a and e but varying values of ω_f. Employing the characteristic length, l^*, associated with the Saturn-Titan system, the first set of sample trajectories originates from an orbit with parameters $a = 4$ nondimensional units and $e = 0.73$. This first set of trajectories is characterized by periapses above the orbital radius of the flyby body, resulting in relatively distant flybys and a single peak in the kick function. In this case, the maximum change in a is limited. The second set of trajectories is generated from an orbit defined by $a = 4$ and $e = 0.78$. In this case, the periapse radius is smaller in magnitude than the distance between P_2 and the flyby body, as in Figure 6.2, which theoretically allows arbitrarily close flybys and results in a double peak in the kick function. The magnitude of Δa is unlimited in this case; as the flyby distance approaches zero, the change in semi-major axis approaches infinity. Consistent with Figure 6.1 and Figure 6.2, negative values of ω_f correspond to outbound flybys, positive values to inbound flybys. For both inbound and outbound encounters, a flyby that leads Titan results in a decreased semi-major axis, while a trailing flyby increases the semi-major axis of the trajectory (or causes escape from the vicinity of Saturn). A leading flyby is, thus, labeled an energy-decreasing flyby, while a trailing flyby is denoted an energy-increasing flyby. In all cases, a value of $\omega_f = 0$ results in zero net change in the semi-major axis from apoapsis to apoapsis, that is, targeting a perpendicular crossing of the rotating x-axis with a value of semi-major axis that corresponds to a period commensurate with the rotation of the primary system results in a resonant orbit with the second primary and incorporates both gravity fields. Two examples of such orbits, each with a flyby angle $\omega_f = 0$, appear in Figure 6.5.

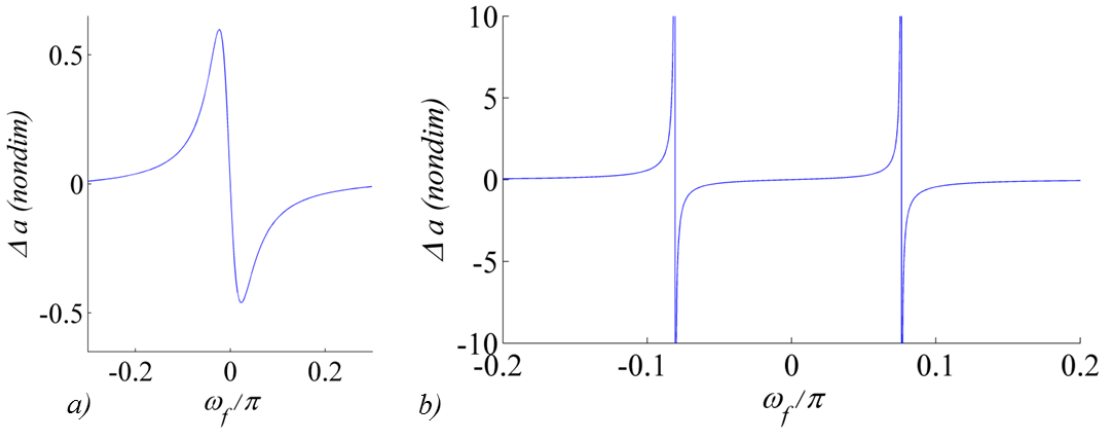

Figure 6.4 The relationship between Δa and ω_f for two sets of trajectories with $a = 4$ nondimensional units and l^* defined in the Saturn-Titan frame. On the left, $e = 0.73$ and periapsis remains above the radius of P_2, on the right, $e = 0.78$ and periapsis dips below the radius of P_2.

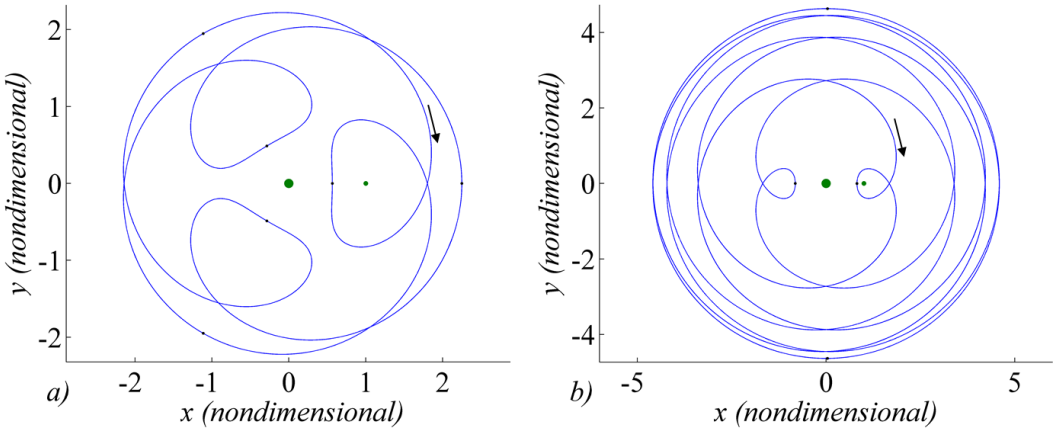

Figure 6.5 Two resonant orbits generated by targeting $\omega_f = 0$; Titan-spacecraft resonances of 3:5 (*a*) and 2:9 (*b*).

It is clear from the slopes of the functions in Figure 6.4 that, in a close flyby, the change in semi-major axis is highly sensitive to the flyby angle ω_f. Because the kick function is an approximation of the equations of motion, the change in semi-major axis resulting from an encounter at a particular angle ω_f can be quite different when computed from the approximation in contrast to an integrated result. For comparison, the kick function is also generated by propagating a series of initial states in the CR3BP. Originating from the same initial parameters, that is, $a = 4$ and $e = 0.78$, with varying values of flyby angle ω_f, each trajectory is integrated

forwards and backwards from periapsis to the first apoapsis, and the change in semimajor axis is computed over the complete revolution. Thus, Δa is calculated for each value of ω_f, producing a curve similar to that in Figure 6.4. A comparison between the kick function estimate (in blue) and the results from the series of CR3BP integrations (in red) of Δa as a function of flyby angle appears in Figure 6.6 and Figure 6.7 given initial parameter values $a = 4$, $e = 0.78$. Clearly, the two curves lie nearly on top of each other in Figure 6.6 — the kick function supplies a good estimate for the periapse angle that yields a given change in semi-major axis. However, when the two curves are subtracted in Figure 6.7, the difference between the kick function estimates and the integrated results grows asymptotically as the flyby distance nears zero. It is also observed that the approximation requires coincidence between the rotating and inertial frames of reference at the moment of periapse passage. If this is not the case, an offset associated with the angle between the frames at periapsis is applied to correct the estimate.[61] However, the kick function supplies a valuable initial guess of the periapse angle required to yield a desired Δa in the CR3BP.

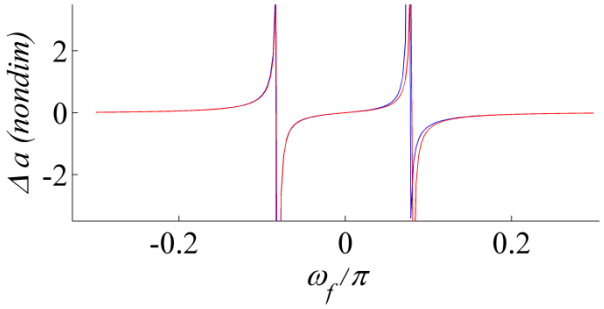

Figure 6.6 Change in semi-major axis as a function of periapse angle as calculated from the flyby kick function (blue) and by a series of CR3BP integrations (red); the magnitude of Δa approaches infinity as the flyby distance approaches zero.

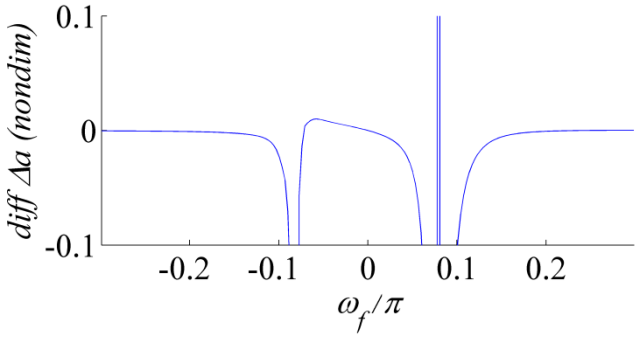

Figure 6.7 Difference between the two curves in Figure 6.6.

A closer look at the integrated function in Figure 6.6 reveals detail that illuminates the behavior of trajectories at very close flyby radii. The peak in the function associated with outbound flybys is located at $\omega_f \approx -0.0805\pi$, and a second, narrower asymptote is visible at slightly higher flyby angles, with $\omega_f \approx -0.0785\pi$. The curve appears in a zoomed view in Figure 6.8. Recall that the magnitude of Δa is unlimited when the orbit periapsis lies below the orbital radius of the flyby body. Due to a higher resolution in the scale of ω_f, the limits on Δa are larger in Figure 6.8 than in Figure 6.6. Consider the main peak centered at $\omega_f \approx -0.0805\pi$. To the left of the asymptote, $\Delta a > 0$, and the flyby results in an increased semi-major axis: each flyby increases the Keplerian energy of the trajectory. Recall that the pre-flyby orbit is characterized by $a = 4$ nondimensional units. The green marker represents a flyby angle $\omega_f = -0.0807\pi$ and a change in semi-major axis $\Delta a = +68.1$. The semi-major axis of the post-flyby orbit is therefore $a = 72.1$ nondimensional units, representing a significant increase in the size of the orbit. As ω_f grows and the flyby radius decreases, the semi-major axis of the post-flyby orbit is further increased until, at the asymptote, the trajectory escapes the vicinity of P_2. At this point, the orbit is hyperbolic with respect to P_2, and the semi-major axis of the post-flyby orbit is negative. For example, at the blue marker, the flyby results in a semi-major axis change of $\Delta a = -66.3$ nondimensional units. With a pre-flyby value of $a = 4$ nondimensional units, the semi-major axis of the hyperbolic post-flyby orbit is $a = -62.3$ nondimensional units. As the flyby angle ω_f is further increased, the flyby radius continues to decrease, and the post-flyby orbits remain hyperbolic: each encounter is an energy-increasing flyby.

Consider now the smaller asymptote centered at $\omega_f \approx -0.0785\pi$. This asymptote represents an arbitrarily close approach to the center of the flyby body. At the black marker, the encounter is, again, an energy-increasing flyby: with $\Delta a = -13.9$, the semi-major axis of the hyperbolic post-flyby orbit is $a = -9.9$ nondimensional units. To the right of the smaller asymptote, on the other hand, the trajectory has moved to the opposite side of the flyby body: each encounter is now an energy-decreasing flyby. The change in semi-major axis is still negative, but the magnitude is smaller than that of the pre-flyby value of a, and the post-flyby orbit possesses a smaller, positive value of a. At the red marker, for example, $\Delta a = -2.0$ and the final semi-major axis is $a = 2.0$ nondimensional units — the orbit remains captured at a smaller value of a. The orbits signified by the black and red markers have negative flyby altitudes — these two trajectories pass below the surface of Titan. Note that the value of Δa predicted by the kick function is unlimited: the value of semi-major axis approaches infinity as the trajectory transitions from an ellipse to a hyperbola, and again when flyby distance approaches zero. The limits on the ordinate in Figure

6.6 and Figure 6.8 are selected for clarity of the curves; however, the value of Δa in each figure is unlimited.

The details associated with the four Titan flyby orbits are summarized in Table 6.1, including the flyby angles, the shifts in semi-major axis, and other details relating to each orbit; the trajectories are plotted in an inertial view in Figure 6.9. Note that the green and red orbits both remain captured at Saturn, although the green orbit is characterized by a very large semi-major axis value. Both the blue and black trajectories are hyperbolic and escape. The same trajectories are also plotted in the Saturn-Titan rotating frame in Figure 6.10, in a wide view (*a*) and a zoomed view (*b*). The trajectories approach Titan on nearly identical paths; after the flyby, the orbits diverge. Note in Figure 6.10 (*b*) that the flyby distances of the red and black trajectories are very tight. Also, the red trajectory flies by Titan on the opposite side of the moon as compared to the first three orbits. The green, blue, and black trajectories all represent energy-increasing flybys, while the red flyby decreases the energy.

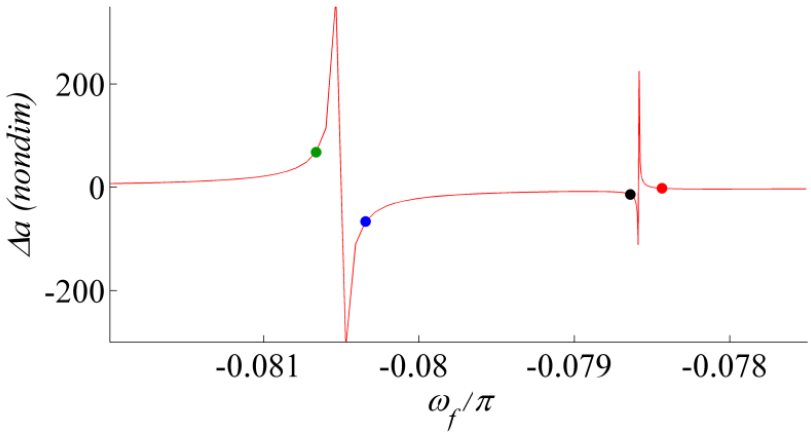

Figure 6.8 Zoomed view of the integrated function; four sample trajectories marked in color appear in Figure 6.9 and Figure 6.10.

Table 6.1 Trajectory details of four Titan flyby orbits

	Green	**Blue**	**Black**	**Red**
ω_f/π	-0.08066	-0.08034	-0.07864	-0.07844
Δa (nondim)	68.08	-66.30	-13.95	-2.00
a_{final} (nondim)	72.11	-62.29	-10.03	2.00
flyby distance (km)	6884.3	5821.3	490.2	102.6
flyby altitude(km)	4308.3	3245.3	-2085.8	-2473.4

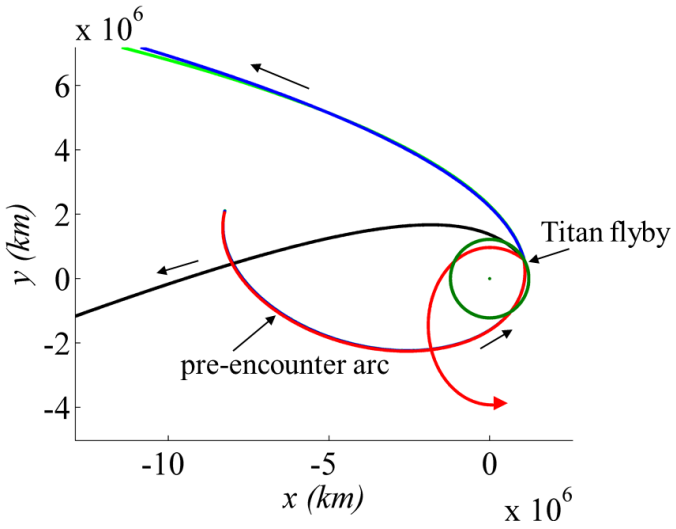

Figure 6.9 Four Titan flyby trajectories, inertial view.

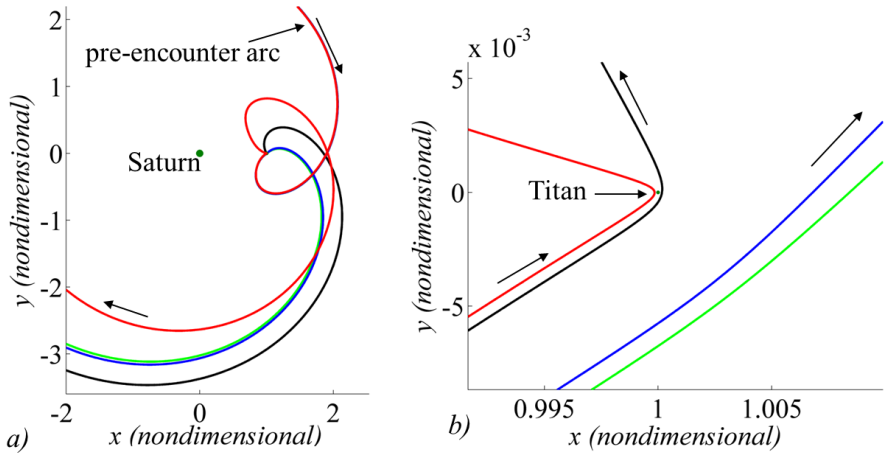

Figure 6.10 Four flyby trajectories in the Saturn-Titan rotating frame. Wide view (*a*) and zoomed view (*b*).

In Zhou et al.[52] and Pan and Sari,[53] as well as Ross and Scheeres,[54] the kick function is derived for use with nearly circular orbits characterized by periapses remaining beyond the orbit of the flyby body which, therefore, result in relatively distant flybys. In such scenarios, the closest approach occurs at spacecraft periapsis, in accordance with the modeling of the flyby as an energy kick at spacecraft periapsis. In addition, under these conditions, the assumption that one revolution from one periapsis to the next encompasses 360º is relatively accurate. For the orbits investigated in this study, however, the periapses of the eccentric orbits can also be lower (closer

to P_2) than the orbit of the flyby body. These types of encounters allow close flybys that do not occur at spacecraft periapsis. Note that previous studies have focused on the analytical kick function itself; the current research employs the kick function as a part of a numerical tool for preliminary trajectory design. It supplies an effective initial guess, for example, for the design of a series of resonant flybys in the Jupiter system. By employing the kick function to estimate the flyby angle required to achieve the appropriate Δa to "hop" from one resonant orbit to the next, a series of flybys can be designed to achieve a particular goal.

6.2. Inbound versus Outbound Flybys in the CR3BP

A further investigation of flybys in the CR3BP reveals differences between the effects of inbound and outbound flybys for certain scenarios in the P_2-flyby body CR3BP. The analysis focuses on the Saturn-Titan system. The spacecraft is assumed to be initially in resonance with Titan; for example, a spacecraft in a 3:1 resonance with Titan completes one full revolution of Saturn for every three Titan revolutions. For the pre-flyby orbits, the resonance is computed in a conic sense. That is, the osculating semi-major axis prior to the flyby is specified such that the Keplerian period of the spacecraft is equal to an integer number of Titan periods. Five cases are investigated: 1:1, 2:1, 3:1, 4:1, and 5:1 pre-flyby resonances with Titan. Both energy-increasing and energy-decreasing flybys are investigated. Due to Titan's atmosphere, the flyby altitude is restricted to be higher than 1,000 km. In this analysis, the flyby altitude is held constant at 1,000 km. It is therefore necessary to determine, for each pre-flyby trajectory, the flyby angle that yields a 1,000 km flyby altitude.

Recall that the flyby angle, ω_f, is defined as the angle of periapsis with respect to the rotating x-axis, as noted in Figure 6.1(b) for inbound flybys and Figure 6.2(b) for outbound flybys. The flyby angle ω_f is equal to the osculating argument of periapsis ω_i at the moment of the flyby if the inertial and rotating frames are incident at that moment. Since the osculating argument of periapsis does not change significantly while the spacecraft remains far from Titan, the flyby angle as computed by the kick function supplies a good initial guess for the initial argument of periapsis that results in an outbound flyby.

The integration of each orbit commences from apoapsis. Semi-major axis a, periapse radius r_p, and the inertial argument of periapsis ω_i are also defined at apoapsis as osculating orbital elements. It is assumed that the rotating and inertial frames align at the moment of periapse

passage as computed in a Saturn-only conic model. For outbound flybys, the process is initialized and proceeds as follows for each set of resonances:

1. The spacecraft is placed at apoapsis (with respect to Saturn) prior to the flyby, and the semi-major axis that corresponds to the desired resonance is determined.
2. The kick function is then employed to compute a range of flyby angles that most likely span the 1,000 km flyby for a series of r_p values. This range of values supplies the initial guess for the osculating argument of periapsis at the pre-flyby apoapsis.
3. For each r_p, the corresponding orbits are integrated forward in the Saturn-Titan CR3BP, determining the exact initial osculating argument of periapsis that yields the 1,000 km flyby altitude.
4. A third-order polynomial relating the values of r_p and ω_i at the pre-flyby apoapsis for a 1,000 km flyby is fit to the data for each resonance.

The procedure is repeated for inbound flybys with a modification in step 2. Recall that the flyby angles for both inbound and outbound flybys that correspond to a given altitude are similar in magnitude but opposite in sign. Thus, the negative of the outbound argument of periapsis is computed for a given r_p and used as the initial guess for the value of argument of periapsis that best yields a 1,000 km inbound flyby.

The polynomials computed in step 4 of the above process provide an estimate for the initial argument of periapsis that results in the desired 1,000 km altitude flyby. The polynomials appear in Table 6.2 for energy-increasing outbound flybys and Table 6.3 for energy-increasing inbound flybys for the resonances investigated. These polynomials are used to approximate the necessary initial argument of periapsis for any r_p at a given resonance, using the relationship

$$\frac{\omega_i}{\pi} = P_3 r_p^3 + P_2 r_p^2 + P_1 r_p + P_0 \tag{6.17}$$

where r_p is measured in Saturn radii and computed at the pre-flyby apoapsis. The inertial argument of periapsis ω_i is defined at the pre-flyby apoapsis assuming the rotating and inertial frames align at the moment of periapse passage, where the time of periapse passage computed is in a Saturn-only conic model. The polynomials produce an estimate accurate to approximately 100 km; for more accuracy, linear interpolation between a pair of points straddling the desired altitude supplies a flyby within about 20 m of the desired 1,000 km altitude.

Table 6.2 Polynomials used to compute ω_i corresponding to a 1,000 km outbound energy-increasing flyby

	P_3	P_2	P_1	P_0
1:1	0.000074626847606	-0.00218813017111	0.05599942240696	-0.7470908612153
2:1	0.000089378704668	-0.00267885272835	0.06203044539256	-0.7506773701170
3:1	0.000093256903370	-0.00285759049609	0.06401926072110	-0.7510411101875
4:1	0.000095845755161	-0.00296407890050	0.06509231281859	-0.7511254120907
5:1	0.000097686528467	-0.00303542979185	0.06577536953350	-0.7511377047245

Table 6.3 Polynomials used to compute ω_i corresponding to a 1,000 km inbound energy-increasing flyby

	P_3	P_2	P_1	P_0
1:1	-0.000074787207596	0.002184480128695	-0.055954775952994	0.742700758018013
2:1	-0.000080992181544	0.002531533184169	-0.061192077940834	0.743977887070871
3:1	-0.000084787891128	0.002714119304813	-0.063291493050431	0.741007486136513
4:1	-0.000086672620321	0.002798839048599	-0.064103747409650	0.741442762464596
5:1	-0.000089191043466	0.002897914592467	-0.065142611573917	0.736370728790035

At a given pre-flyby resonance, the flyby angle (or argument of periapsis) that yields a 1,000 km altitude Titan encounter for either inbound or outbound encounters, is computed by selecting the appropriate set of polynomials. Two sample 1,000 km altitude flyby trajectories, one inbound (red) and one outbound (blue) are constructed; the trajectories are plotted in the rotating frame in Figure 6.11, and the view in Figure 6.12 is from the inertial frame. Each of these two sample trajectories originates from a 3:1 pre-flyby resonance with Titan with a pre-flyby periapsis at r_p = 3 R_S. The final Saturn-centered semi-major axis is 84.46 R_S in the outbound case and 83.60 R_S after the inbound flyby.

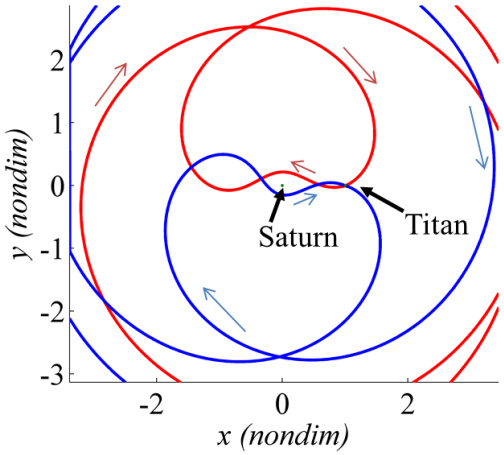

Figure 6.11 Inbound (red) and outbound (blue) flyby trajectories in the Saturn-Titan rotating frame.

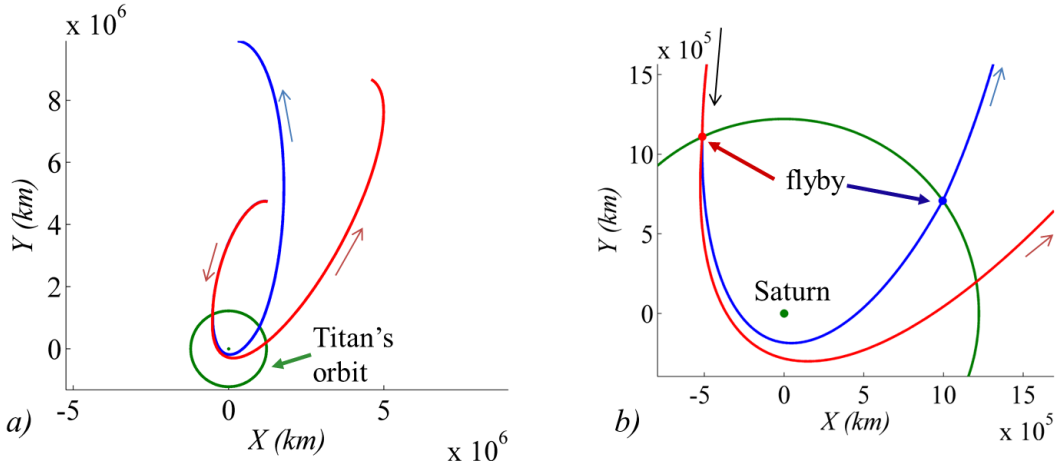

Figure 6.12 Inbound (red) and outbound (blue) flyby trajectories in a Saturn-centered inertial view. Full view (*a*) and zoomed view (*b*).

Inbound and outbound flybys at a given resonance share essentially the same value of Saturn-Titan Jacobi Constant as well as V_∞ with respect to Titan. A lower value of the Saturn-Titan Jacobi Constant corresponds to higher resonance orbits (that is, orbits with larger semi-major axes) as well as those with lower periapse radii (or higher eccentricity) prior to the flyby. The V_∞ with respect to Titan reflects the inverse relationship. The two sets of curves appear in Figure 6.13 for 3:1, 4:1, and 5:1 resonance pre-flyby obits. Since a lower V_∞ corresponds to a higher equivalent ΔV due to the flyby, greater changes in orbital elements are expected from pre-flyby

orbits corresponding to lower values of V_∞. The curves in Figure 6.13 apply to both inbound and outbound flybys.

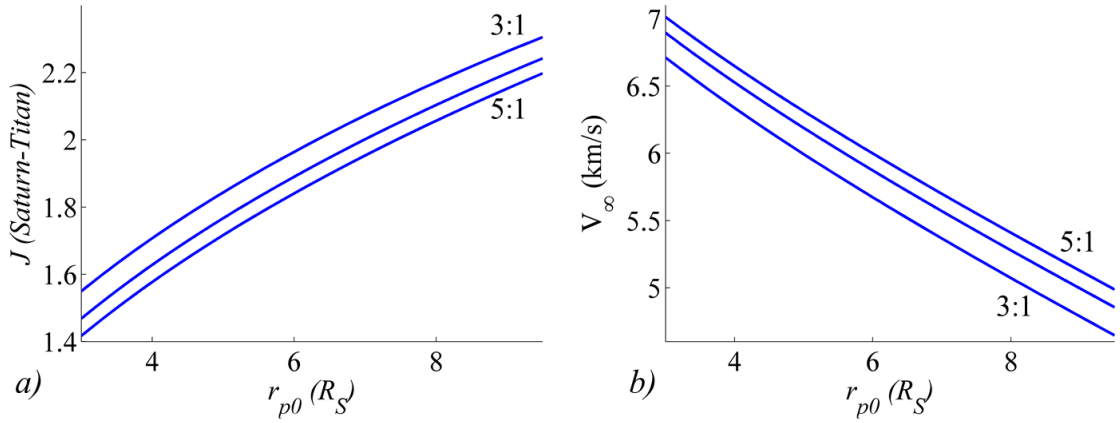

Figure 6.13 Saturn-Titan Jacobi Constant and V_∞ with respect to Titan as a function of pre-flyby periapse radius for 3:1, 4:1, and 5:1 resonance orbits prior to the encounter.

By computing the changes in orbital elements due to a flyby, the effects from 1,000 km altitude inbound and outbound flybys are compared for a specific range of pre-flyby trajectories. Given a 5:1 pre-flyby resonance with Titan, the changes in a and r_p due to a 1,000 km altitude energy-increasing Titan flyby are calculated for orbits with pre-flyby r_p values ranging from 3 R_S to 9.5 R_S. Both inbound and outbound cases are investigated. For both inbound and outbound encounters, the higher values of pre-flyby r_p correspond to larger changes in a and r_p due to the flyby, as expected, since V_∞ is, thus, lower for flybys at the same altitude. From the results in Figure 6.14(*a*), it is observed that, for this set of encounters, i.e., outbound flybys, represented by the blue curves, are more effective at increasing a as compared to inbound flybys, in red. Similar results are observed for 4:1 and 5:1 pre-flyby resonances, and the relative results are repeated in the corresponding curves depicting the changes in r_p. In the energy-decreasing encounters, however, the opposite trend is observed. A set of 1,000 km altitude energy-decreasing flybys are computed for a 5:1 pre-flyby resonance. The shifts in a are plotted as a function of initial periapse radius in Figure 6.14(*b*). Inbound flybys originating from these pre-flyby orbits in the CR3BP decrease both a and r_p more significantly than do outbound flybys at the same initial values of a and r_p.

While patched conics successfully predict the appropriate sign on the change in the argument of periapsis due to the encounter in this scenario, i.e., depending on whether the flyby occurs

before or after periapsis,[82] patched-conic analysis does not predict a difference in the change in a or r_p resulting from an inbound versus an outbound flyby. That is, patched conics results for Δa and Δr_p are identical for the two types of flybys. The patched conic predictions for the changes in a due to either an inbound or outbound flyby appear in green in Figure 6.14. The green curve passes approximately halfway between the curves that reflect the CR3BP simulation results in Δa for both energy-increasing and energy-decreasing flybys given the same sets of initial conditions.

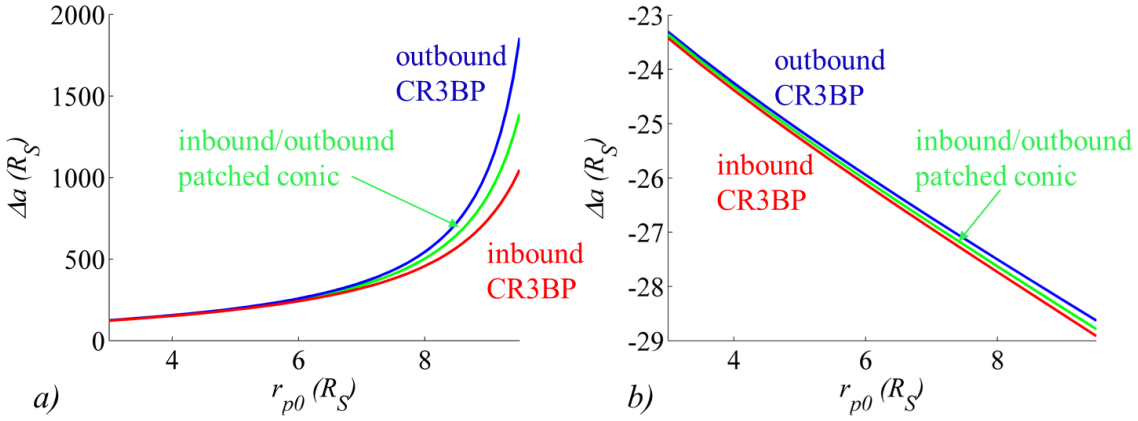

Figure 6.14 Changes in a for 1,000 km altitude energy-increasing (a) and energy-decreasing (b) inbound and outbound flybys originating from a 5:1 pre-flyby resonance with Titan; patched conic prediction in green.

An investigation of the differences in the effects of the inbound and outbound flybys from the perspective of the CR3BP reveals several notable patterns. First, it is important to recall that in a CR3BP propagation, the gravity of the flyby body affects the spacecraft trajectory continuously. Even distant encounters with the flyby body produce noticeable effects on the osculating elements. For this specific Titan flyby scenario, when the osculating semi-major axis of the trajectory is observed over time, two distinct patterns distinguish inbound flybys from outbound flybys. The first pattern appears in Figure 6.15. The osculating semi-major axis is plotted as a function of time from the apoapsis prior to the flyby for two sets of orbits. Each orbit originates from a 5:1 resonance with Titan; initial periapse radii range from 3 to 9.5 R_S. As before, inbound encounters appear in red while outbound encounters are colored blue. The semi-major axis oscillates in each case; however, it is noted that the outbound encounter approaches Titan with a steeper slope in the semi-major axis in this set of sample trajectories. The same pattern is noted in 1:1, 2:1, 3:1, 4:1, and 7:2 pre-flyby resonance cases. The steeper slope in a is a characteristic

of outbound encounters in both energy-increasing and energy-decreasing flybys under these specific conditions.

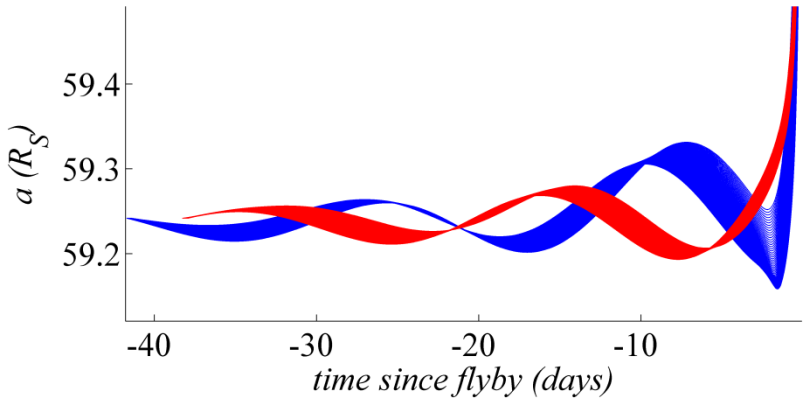

Figure 6.15 Osculating semi-major axis as a function of time approaching inbound (red) and outbound (blue) encounters; 5:1 pre-flyby resonance, $3R_S < r_{p0} < 9.5\ R_S$.

A second observation from this investigation also involves the osculating semi-major axis. This second pattern applies to all cases investigated: energy-increasing and energy-decreasing encounters at 1:1, 2:1, 3:1, 4:1, 5:1, and 7:2 resonances. It is observed that at the entrance to the Hill sphere (or the sphere of influence) surrounding Titan, the osculating semi-major axis corresponding to a trajectory arc that is approaching an outbound flyby is larger than the semi-major axis corresponding to the arc approaching the equivalent inbound flyby. That is, upon approaching an outbound Titan encounter, the trajectory arc already possesses a larger semi-major axis than an approach to the equivalent inbound encounter. The outbound flyby results in a larger final value of a as well, for the scenarios involved in this investigation.

Finally, it is observed that, for each initiating trajectory and encounter examined in this investigation, the more effective type of flyby occurs on the Saturn-side of Titan. That is, outbound energy-increasing flybys and inbound energy-decreasing flybys both occur between Saturn and Titan in the Saturn-Titan rotating frame. This fact is illustrated in Figure 6.16. Four sets of flybys are plotted. Each simulation is specified as a 3:1 pre-flyby resonance orbit and possesses an initial periapse radius between 3 and 9 R_S; the paths are plotted in the Saturn-Titan rotating frame. The position of the spacecraft at closest approach to Titan is marked in black for each orbit. Outbound flybys are colored blue, and inbound flybys appear in red. Energy-decreasing flybys lead Titan and therefore possess positive values of y at the moment of closest

approach. Conversely, energy-increasing flybys trail Titan and are characterized by negative *y*-values at closest approach. For the conditions in this example, it is clear from the figure that inbound energy-decreasing flybys, which are more effective than outbound flybys at lowering semi-major axis, are located to the left of Titan. Similarly, outbound energy-increasing flybys, which are more effective at raising semi-major axis, are also located on the Saturn-side of Titan. Conversely, the closest approach distances of outbound energy-decreasing flybys and inbound energy-increasing flybys lie to the right of Titan, on the anti-Saturn side.

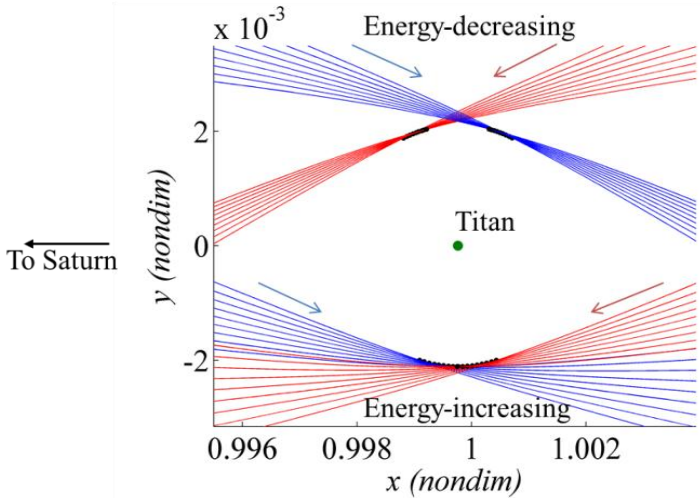

Figure 6.16 Four sets of flybys in the Saturn-Titan rotating frame.
Inbound flybys are colored red, outbound flybys are blue.

6.3. Flyby Periapsis Maps

Both inbound and outbound Titan flybys modify the orbital elements of a trajectory. During a post-flyby revolution, the orbital elements can be further modified by the tidal acceleration due to the Sun. The tidal effects depend, of course, on the size, shape, and orientation of the post-flyby orbit. By quantifying these changes, a trajectory may be designed in the Sun-Saturn-Titan system employing a strategy that combines a Titan flyby with the solar tidal acceleration to achieve a particular goal. As an example, consider again the Cassini end-of-life problem. Recall that a final energy-increasing Titan flyby boosts the spacecraft into a large orbit that is then affected by the Sun. The Saturn impact analysis is based on a final (inbound) flyby that occurs along an orbit that is in a 5:1 resonance with Titan. This point solution yields a Saturn impact orbit as desired. However, it is a single trajectory computed via a trial and error process. A more

methodical scheme for the design of the final Titan flyby is desirable. Toward that end, it is illuminating to examine the design space and determine the family of pre-flyby orbits that result in either Saturn impact or escape after the post-flyby revolution, as well as the pre-flyby orbits that yield particular changes in the trajectories that remain captured. While the Cassini end-of-life example employs inbound flybys, both inbound and outbound flybys are investigated in Section 6.3. The focus here is the *pre-flyby orbit*: the orbit just prior to the final flyby, or orbit #6 in the tour in Figure 6.17(*a*) and the schematic in Figure 6.17(*b*). The *post-flyby revolution*, or orbit #7 in Figure 6.17, is then affected by tidal acceleration. By incorporating solar gravity during the design of the final flyby, it may be possible to more methodically plan the flyby tour.

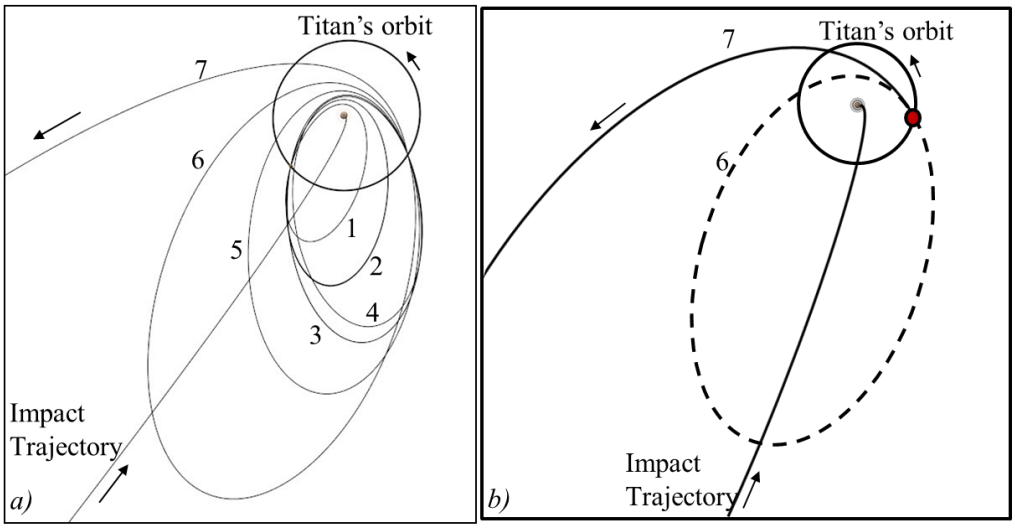

Figure 6.17 Flyby tour (*a*) and schematic (*b*) leading to Saturn impact. Flyby periapsis maps are created for facilitating the design of orbit #6.

6.3.1. Impact and Escape Trajectories

Consider the Sun-Saturn-Titan system, and assume that the three bodies are coplanar. Focusing on the orbit prior to the final Titan flyby, that is, orbit #6 in Figure 6.17, the goal is the determination of the possible pre-flyby orbits around Saturn that produce post-flyby trajectories that either impact Saturn or escape through L_1 or L_2 due to solar tidal acceleration. A set of flyby periapsis maps is created to visualize this information. The maps created in this section are tuned to the Cassini end-of-life example problem; however, the process and concept are applicable to

other types of mission design applications. The procedures used to create the maps apply to both inbound and outbound flybys.

To create a flyby periapsis map, it is necessary to combine the effects of the flyby with the influence of the Sun on the trajectory over one period. The maps are created by patching together the Sun-Saturn and Saturn-Titan CR3BPs. During computation of the flyby parameters, the spacecraft is in a relatively small resonant orbit, and it is located near periapsis with respect to Saturn. The solar gravity exerts little effect under these conditions, and the Saturn-Titan CR3BP is employed. During the post-flyby revolution, the spacecraft is far from Titan, and the Sun-Saturn CR3BP is used for propagation. The patching of the two problems occurs as follows, for either an inbound or outbound flyby:

1. The initial state is defined at apoapsis relative to Saturn prior to a 1,000 km altitude energy-increasing flyby. The spacecraft moves in a Titan-resonant orbit about Saturn. The trajectory is propagated from the initial apoapse state in the Saturn-Titan CR3BP through the flyby to the following apoapsis or for a time span equivalent to 10 Keplerian periods of the pre-flyby trajectory, as computed from the initial semi-major axis.
2. The final state from step 1 is rotated into a Saturn-centered inertial frame. A set of six osculating orbital elements is computed from the final state: semi-major axis, eccentricity, inclination, argument of periapsis, longitude of the ascending node, and true anomaly.
3. The Sun-Saturn propagation must commence well before apoapsis, however. Therefore, the post-flyby final state is artificially returned to periapsis with respect to Saturn for the Sun-Saturn propagation. Each of the orbital elements is fixed, with the exception of true anomaly, which is re-set to zero. The orbital elements are then used to compute the Saturn-centered inertial state in Cartesian coordinates using Saturn-centered conic relationships. This process returns a state at periapsis with respect to Saturn that has incorporated the full effects of the Titan flyby, for either an inbound or an outbound flyby.
4. The new post-flyby periapsis state is rotated into the Sun-Saturn rotating frame and propagated forward in the Sun-Saturn CR3BP. Integration is terminated if the spacecraft escapes through L_1 or L_2, if it impacts Saturn or, otherwise, when it reaches its subsequent periapsis.

The influence of the Sun depends on the pre-flyby semi-major axis and the periapse radius of the original orbit, as well as on the orbit orientation in the Sun-Saturn system. Therefore, in step 4,

each post-flyby trajectory is rotated into the Sun-Saturn system with a series of Sun-Saturn periapse angles ω_r ranging from 0° to 360°. A grid of trajectories is thus produced with varying values of r_p and ω_r. Three maps, corresponding to three different pre-flyby resonances, appear in Figure 6.18. Note that in this case, r_p refers to the pre-flyby periapse radius, while ω_r refers to the orientation of the post-flyby orbit. It is also noted that, in contrast to the maps in the previous chapters, this grid of points does not possess a single value of Jacobi Constant. Because the pre-flyby resonance with Titan (and therefore the pre-flyby semi-major axis) is held constant, the Jacobi Constant varies across the flyby map. For example, in the 5:1 map for outbound flybys, $3.003 < J < 3.036$.

Each initial condition in each map in Figure 6.18 is colored according to its fate after the Sun-Saturn propagation. As before, a blue initial condition produces a trajectory that escapes through the L_1 gateway prior to its subsequent periapsis, a red initial condition results in escape through L_2, a black initial condition yields an impact trajectory, and an orbit commencing from a grey initial condition remains in orbit about Saturn after a full revolution. Clearly, a 1,000 km flyby after a 3:1 resonance results only in captured Saturn-centered orbits after one revolution. From a 4:1 resonance, several outbound flyby trajectories originating with high values of r_p and oriented correctly in quadrants I and III achieve Saturn impact after one revolution. Pre-flyby trajectories in a 5:1 resonance with Saturn, however, possess the potential to either impact or escape from the vicinity of Saturn after a 1,000 km outbound Titan flyby. A mission designer searching for a trajectory that escapes through L_1, for example, can design a flyby tour resulting in a pre-flyby 5:1 resonance within a particular range of periapse radii and periapse angles (the blue region on the map) and be assured of the desired L_1 escape. The maps in Figure 6.18 apply to outbound flybys; similar maps also exist to visualize the design space corresponding to inbound flybys.

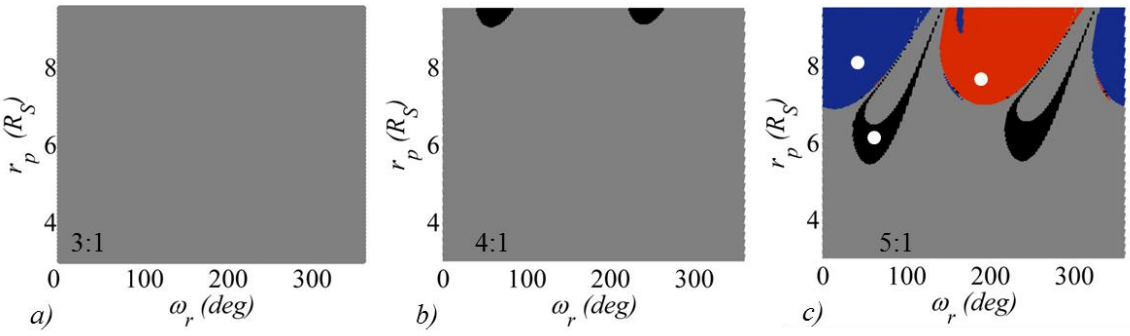

Figure 6.18 Pre-flyby periapse radius plotted against periapse angle for 3:1 (*a*), 4:1 (*b*), and 5:1 (*c*) resonant outbound flyby trajectories. Three sample initial conditions marked in white.

Three sample trajectories are selected from the flyby map in Figure 6.18(*c*); the initial states are marked in white in Figure 6.18(*c*), and the trajectories appear in Figure 6.19 and Figure 6.20. Each trajectory originates in a pre-flyby orbit about Saturn that is defined by a 5:1 resonance with Titan. The flyby angle ω_f is fixed in each case by the required pass distance of 1,000 km during the outbound encounter. By selecting the appropriate values of periapse radius and the Sun-Saturn periapse angle ω_r, the desired outcome is achieved. An initial orbit located in the blue region in the flyby map in Figure 6.18(*c*), with a pre-flyby radius r_p = 8 R_S paired with ω_r = 58º, results in a trajectory that escapes through the L_1 gateway; this trajectory arc is pictured in blue in Figure 6.19. An initial condition with r_p = 7.2 R_S and ω_r = 196º is located in the red zone in the flyby map; this trajectory escapes through L_2, as plotted in red in Figure 6.19. And, as expected, a trajectory originating from the black region in the flyby map, with coordinates r_p = 5.5 R_S and ω_r = 60º, impacts Saturn. The impacting revolution of this path appears in black in Figure 6.19. Note that the ZVCs are each colored to match the corresponding trajectory. Clearly, the Jacobi Constant varies significantly between these three orbits, which are each selected from the 5:1 flyby map. The flybys themselves are viewed in the Saturn-Titan rotating frame in Figure 6.20. Each trajectory passes Titan at 1,000 km altitude; each pre-flyby periapsis is marked. A zoomed view of the 1,000 km flybys appears in Figure 6.20(*b*). Finally, an inertial view of the three trajectories appears in Figure 6.21, each colored as above. Plainly visible is each 5:1 resonant pre-flyby trajectory, as well as the much-larger post-flyby paths that lead to escape from the vicinity of Saturn or impact into its surface. Note the similarity between the black impact trajectory in Figure 6.21 and the Cassini End-of-Life impact trajectory in Figure 6.17 that emerged as a point solution from the design process in 2007.

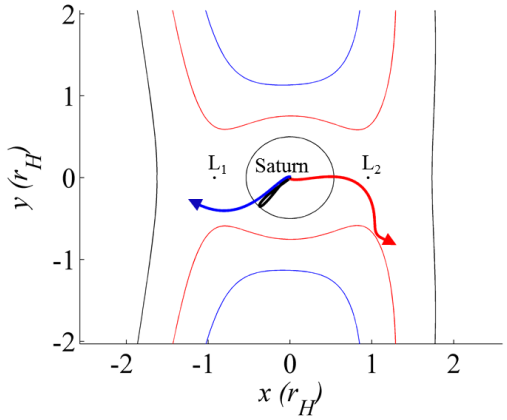

Figure 6.19 Escape and impact trajectories originating from trajectories in a 5:1 pre-flyby resonance with Titan. Sun-Saturn rotating view.

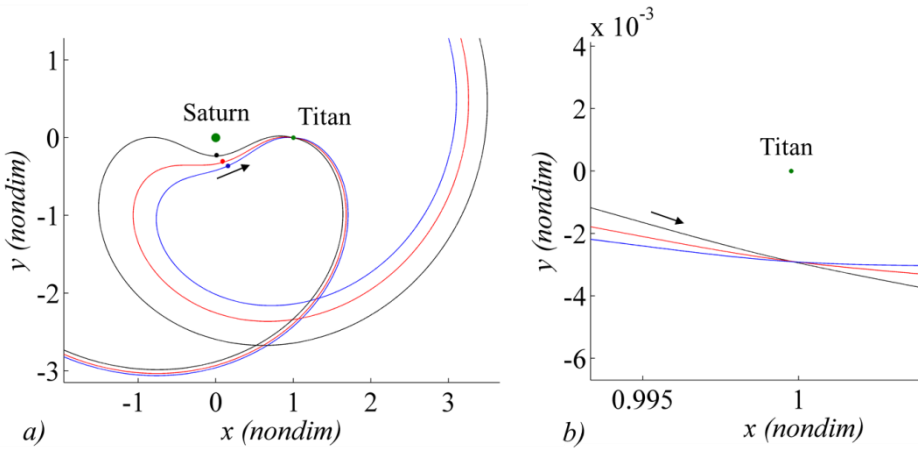

Figure 6.20 Views of the outbound flybys that result in the impact and escape trajectories in Figure 6.19. Saturn-Titan rotating view.

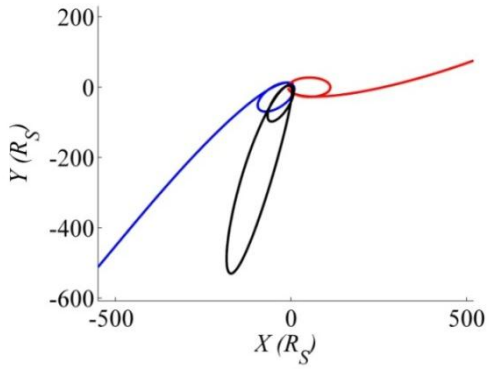

Figure 6.21 Inertial view of the 5:1 resonant pre-flyby trajectories and the post-flyby impact and escape trajectories.

Recall that the Jacobi Constant varies across each flyby periapsis map in this example. By examining the values of J featured in the maps in Figure 6.18, some of the characteristics of the flyby maps are clarified. The three initial condition maps for outbound flybys are plotted against their post-flyby Sun-Saturn Jacobi Constants in Figure 6.22(*a*). As expected, the 5:1 map possesses trajectories with the lowest values of J, corresponding to the highest energies, while the 3:1 map is characterized by higher Jacobi Constants. Interestingly, the 4:1 trajectories that impact Saturn possess the highest values of r_p found in the map. Due to their higher energy in the Sun-Saturn system, the gravitational influence of the Sun leads to Saturn impact in these trajectories despite the fact that each originates in an orbit with a large periapse radius relative to other trajectories represented in the map. Also marked by a black horizontal frame in Figure 6.22 is the Jacobi value associated with the Sun-Saturn libration point L_1. The absence of escaping

trajectories in the 3:1 and 4:1 maps is explained by noting that each trajectory possesses $J > J_{L1}$, which implies that the gateways are closed. Similarly, the escape lobes in the 5:1 map all exist below the value $J = J_{L1}$, as expected.

Earlier in the discussion of this particular Titan flyby scenario, it was noted that an inbound flyby increases the semi-major axis and the periapse radius less than an equivalent outbound flyby. Consequently, the Sun's tidal acceleration exerts less of an effect on any smaller orbit that results from an inbound flyby. The Sun-Saturn Jacobi Constant is slightly higher in the inbound case and, as a result, no inbound trajectories originating from a 4:1 pre-flyby resonance impact Saturn. In addition, the regions of escape and impact in a 5:1 inbound encounter are smaller than the equivalent regions in a 5:1 outbound flyby. These facts are visible in the inbound flyby maps in Figure 6.22(*b*). Note the higher values of J in the inbound maps. Also notice the absence of the black impact lobes in the 4:1 inbound map, and the smaller impact and escape lobes in the 5:1 inbound map, as compared to the outbound 4:1 and 5:1 maps.

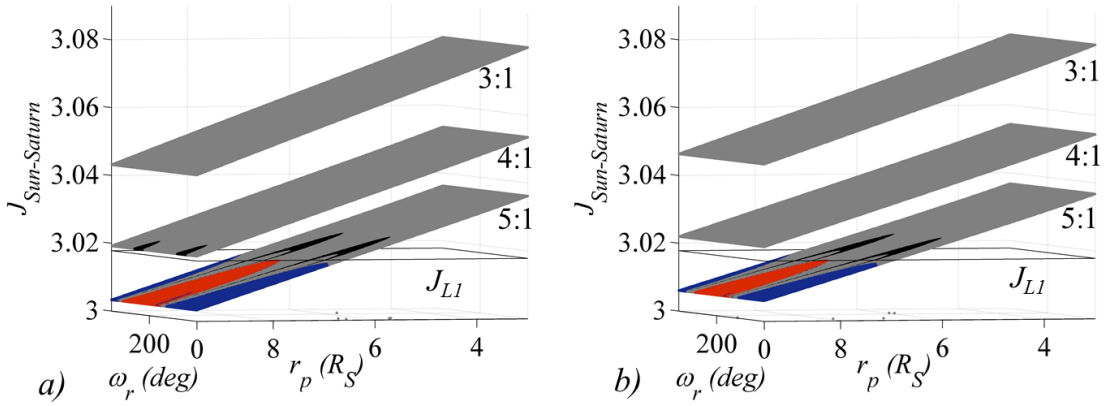

Figure 6.22 Initial condition maps plotted against Sun-Saturn Jacobi Constant for 3:1, 4:1, and 5:1 pre-flyby resonances for outbound (*a*) and inbound (*b*) flybys.

6.3.2. Orbital Changes after a Post-Flyby Revolution

The maps in Section 6.3.1 offer information concerning pre-flyby orbits that result in impact and escape trajectories. However, such maps do not yield information on the characteristics of trajectories that remain in orbit around Saturn beyond a post-flyby revolution. These trajectories are represented by grey points in the maps in Figure 6.18 and Figure 6.22. In this section, each grey point is instead colored consistent with the specific change in the instantaneous values of the orbital elements computed after the post-flyby revolution in comparison to the pre-flyby values.

Maps corresponding to Δr_p appear in Figure 6.23 for the outbound energy-increasing flybys in the example that is highlighted in Section 6.3.1 for 3:1, 4:1, and 5:1 resonances. Colorbars appear to the right in each map relating color to Δr_p. In each case, dark blue corresponds to the region in each map that produces the smallest increase (or largest decrease for the 4:1 and 5:1 resonance orbits) in periapse radius, while dark red corresponds to the largest increase in periapse radius; as noted, white reflects escapes. Clearly, in each of the three cases, the Sun-Saturn periapse angle ω_r significantly effects Δr_p. The largest increases in r_p lie in quadrants II and IV, the smallest in quadrants I and III, as expected. Logically, the black regions corresponding to impact in the 4:1 and 5:1 maps lie in the midst of the deepest blue: where periapsis is lowered all the way to impact. Also observe from the colorbar that all values of Δr_p are positive in the 3:1 case. This is consistent with the fact that there are no impact trajectories originating from a 3:1 pre-flyby resonance with Titan. Note that the change in r_p is calculated relative to the pre-flyby periapse radius; each flyby increases periapse radius, so although solar gravity acts to decrease periapse radius in quadrants I and III, the net change from the pre-flyby value is still positive for each trajectory in the 3:1 map.

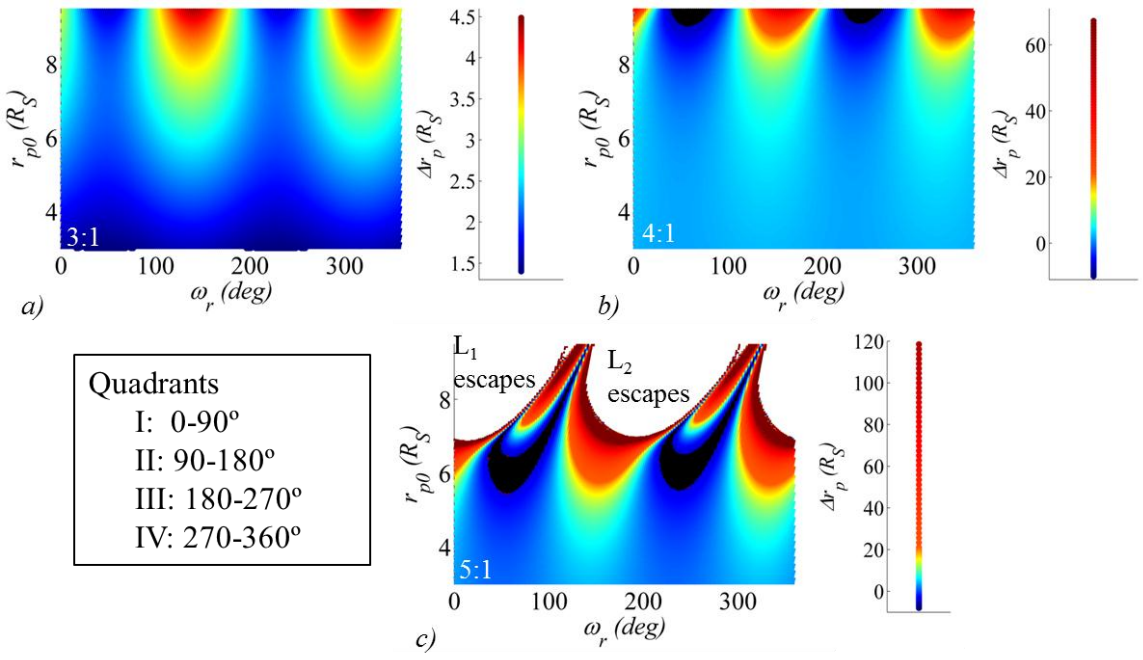

Figure 6.23 Flyby periapsis maps colored by Δr_p for outbound flybys with 3:1 (*a*), 4:1 (*b*), and 5:1 (*c*) pre-flyby resonances with Titan.

Two sample orbits from the 5:1 outbound flyby map appear in Figure 6.24. One corresponds to a periapse raise, one to a decrease in r_p. The post-flyby orbits appear in the Sun-Saturn rotating frame in Figure 6.24(*a*), and both the pre-flyby and post-flyby orbits appear in an inertial view in Figure 6.24(*b*). The red trajectory originates from a dark red region in the flyby map in Figure 6.23(*c*), corresponding to $r_p = 6.16\ R_S$ and $\omega_r = 342^o$. Its periapse radius is raised significantly, as expected. The blue trajectory corresponds to a state from a dark blue zone in the flyby map, with initial conditions $r_p = 4.46\ R_S$ and $\omega_r = 63^o$. Its periapsis is decreased, although it does not impact Saturn.

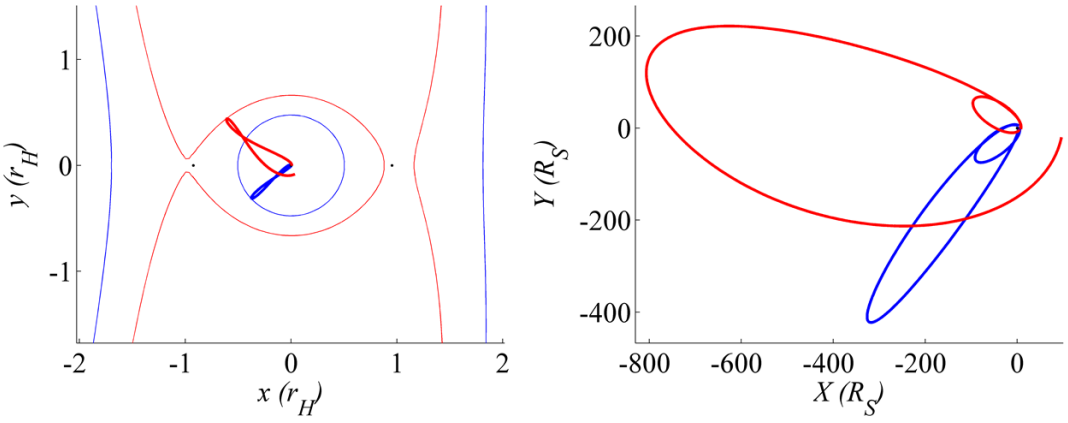

Figure 6.24 Two sample trajectories from the 5:1 Δr_p flyby map. Sun-Saturn rotating view of the post-flyby trajectories (*a*) and inertial view of the pre- and post-flyby orbits (*b*).

Similar maps are created for other orbital elements; for example, maps corresponding to Δa for energy-increasing outbound flybys appear in Figure 6.25. The change in a is positive for all initial conditions. Clearly, the dependence on Sun-Saturn orientation is less pronounced in the Δa maps as compared to the Δr_p maps; change in semi-major axis depends mainly on the initial periapse radius, especially in the 3:1 map. However, at higher initial periapse radii, the orientation dependence is visible in the 4:1 map, and for trajectories originating from a 5:1 resonance with Titan, the change in semi-major axis after a post-flyby revolution is highly dependent on the orientation in the Sun-Saturn frame. This is especially true for initial periapse radii greater than about 5.4 R_S where, with appropriate orientation, trajectories impact Saturn.

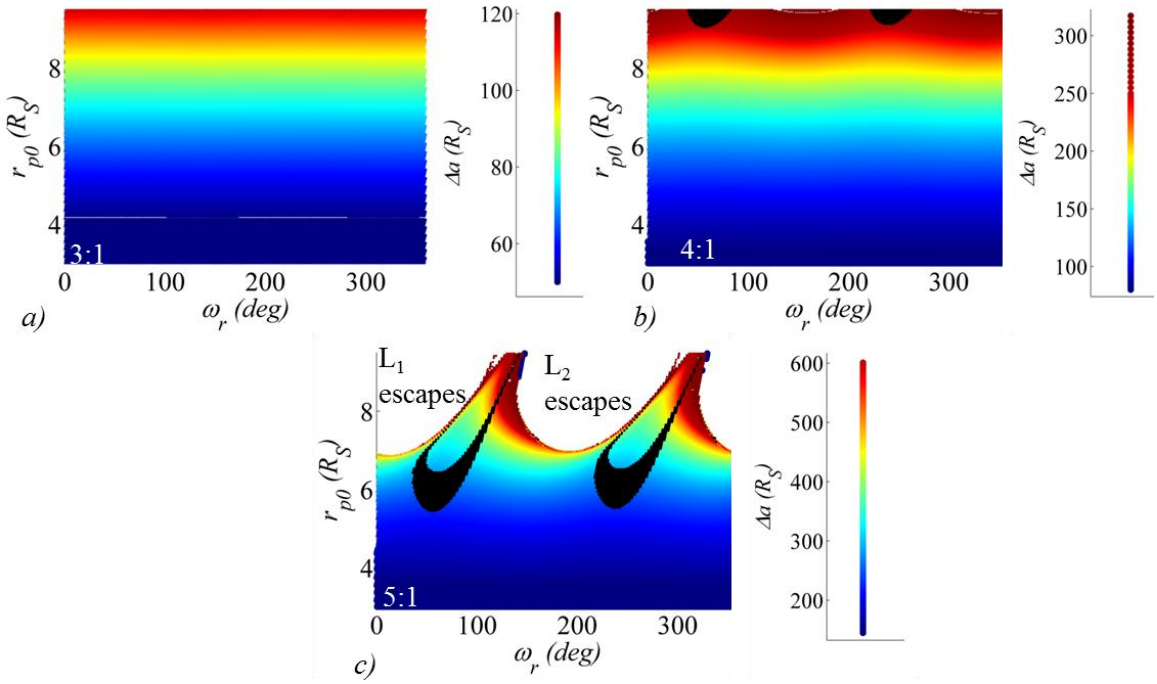

Figure 6.25 Flyby periapsis maps colored by Δ*a* for outbound 3:1 (*a*), 4:1 (*b*), and 5:1 (*c*) pre-flyby resonances with Titan.

6.3.3. Tidal acceleration for V_∞ leveraging

During any post-flyby revolution, the tidal acceleration perturbs the orbital elements, as demonstrated in the previous maps. In a similar way, tidal acceleration changes the V_∞ with respect to the flyby body. The V_∞, or hyperbolic excess velocity, is a measure of the relative velocity as the spacecraft approaches the flyby body. The effectiveness of the flyby at changing the orbital parameters depends on this value, with a lower V_∞ generally corresponding to greater changes in the trajectory due to the flyby. Therefore, it is of interest to mission designers to lower the V_∞ of the spacecraft relative arrival trajectory. This decrease in the hyperbolic excess velocity is typically accomplished using V_∞-leveraging maneuvers,[83, 84] however, tidal acceleration can augment or replace the ΔV maneuver to achieve the desired ΔV_∞.

Flyby periapsis maps are employed to estimate the change in V_∞ due to the tidal acceleration during the post-flyby revolution. Such maps allow visualization of V_∞ changes in large groups of trajectories. The computations are accomplished by expressing V_∞ in terms of osculating orbital elements, and a number of useful relationships emerge. The hyperbolic excess velocity vector,

$\mathbf{V}_\infty$, is defined as the difference between the velocity vector of the spacecraft and the velocity vector of the flyby body,

$$\mathbf{V}_\infty = \boldsymbol{v}_{s/c} - \boldsymbol{v}_{fb} \tag{6.18}$$

where the velocity of the spacecraft, $\boldsymbol{v}_{s/c}$, and the velocity of the flyby body, $\boldsymbol{v}_{fb}$, are measured relative to P_2 but from the perspective of an inertial observer. The flyby body is assumed to be moving in a circular path about P_2. In nondimensional units, the magnitude of the velocity of the flyby body is equal to one, since the flyby body travels a distance of $2\pi l^*$ (the circumference of the flyby body orbit about P_2) in time $2\pi t^*$ (period of the flyby body orbit about P_2), and the velocity is normalized by l^*/t^*. Then, the magnitude of the V_∞ is defined by[84, 85]

$$V_\infty^2 = 1 + {v_{s/c}}^2 - 2v_{s/c}\cos\gamma \tag{6.19}$$

where γ is the angle between the two velocity vectors. Since the flyby body is assumed to be in a circular orbit about P_2, γ is also the flight path angle of the spacecraft. The vis-viva equation and the expression for specific angular momentum then relate the V_∞ magnitude to osculating orbital elements. The vis-viva equation is

$${v_{s/c}}^2 = (1-\mu)\left(\frac{2}{r_{s/c}} - \frac{1}{a}\right) \tag{6.20}$$

where $\mu = \dfrac{m_{flyby\ body}}{m_{flyby\ body} + m_{P_2}}$ is the mass parameter of the P_2-flyby body CR3BP, $r_{s/c}$ is the spacecraft distance from P_2, and a is the semi-major axis of the spacecraft orbit relative to P_2. The magnitude of the specific angular momentum of the spacecraft in a conic orbit about P_2 is written,

$$h = \sqrt{(1-\mu)\,a\left(1-e^2\right)} = r_{s/c}v_{s/c}\cos\gamma. \tag{6.21}$$

To achieve a close encounter with the flyby body, the spacecraft periapsis with respect to P_2 must lie at or below the orbital radius of the flyby body, ensuring that the spacecraft trajectory crosses the orbit of the flyby body. At the point when the spacecraft trajectory crosses the orbit of the flyby body, $r_{s/c} = 1$ in nondimensional units, and for small values of μ, Eqs. (6.20) and (6.21) become, respectively,

$${v_{s/c}}^2 = 2 - \frac{1}{a} \tag{6.22}$$

and

$$v_{s/c}\cos\gamma = \sqrt{a\left(1-e^2\right)}. \tag{6.23}$$

Substituting Eqs. (6.22) and (6.23) into the Eq. (6.19) yields an expression for V_∞ in terms of orbital elements,

$$V_\infty^2 = 3 - \frac{1}{a} - 2\sqrt{a\left(1-e^2\right)}. \tag{6.24}$$

It is worth noting that a relationship exists between the Tisserand Constant and the V_∞. Recall that the Tisserand Constant, an approximation for the Jacobi Constant, is written

$$TC = \frac{1}{a} + 2\sqrt{a(1-e^2)} \tag{6.25}$$

for planar trajectories. Then, the magnitude of the V_∞ is related to the Tisserand Constant by

$$V_\infty^2 = 3 - TC. \tag{6.26}$$

The expression for V_∞ in Eq. (6.24) supplies a relationship between the osculating orbital elements of the spacecraft trajectory relative to P_2 and the V_∞ of the spacecraft with respect to the flyby body. Using this relationship, the V_∞ of the spacecraft with respect to the flyby body for each pre-flyby orbit is easily computed using osculating orbital elements. Similarly, the osculating *a* and *e* after the post-flyby revolution yield the new value of V_∞, which has been affected by tidal acceleration during the first revolution after the encounter. Note that the derivation depends on the computation of V_∞ occurring at the point where the spacecraft trajectory crosses the flyby body's orbital radius; in this investigation, the quantity is evaluated at spacecraft periapsis relative to P_2. In addition, phasing between the spacecraft and the flyby body is not yet addressed: there is no guarantee that a second close encounter with the flyby body occurs. As a result, each value of ΔV_∞ computed using Eq. (6.24) is an approximation for the actual ΔV_∞ between a set of two flybys. However, the resulting maps supply a useful estimate to isolate a set of pre-flyby orbits that results in a decreased V_∞ due to the tidal acceleration during the post-flyby revolution.

The expression for V_∞ in Eq. (6.24) is used to create a set of flyby periapsis Poincaré maps. The same sets of initial conditions used to create the maps appearing in Figure 6.18 and Figure 6.23 are again employed: for each map, the pre-flyby periapse radius r_p is bounded between 3 and 9.5 R_S, and the Sun-Saturn periapse angle ω_r ranges from 0 to 360º. Each point on the resulting maps represents a single initial condition pair r_p and ω_r, and each is now colored consistent with the estimated change in V_∞ due to solar gravity acting on the spacecraft during the

post-flyby revolution. Three maps, corresponding to the 3:1, 4:1, and 5:1 incoming Titan resonances, appear in Figure 6.26 for outbound, energy-increasing flybys. As before, black zones represent trajectories that impact Saturn. White regions identify trajectories that are infeasible for V_∞ leveraging due to escape (in the 5:1 case) or increase in periapse radius above the orbital radius of Titan (in both the 4:1 and 5:1 cases), which renders a second close flyby of Titan impossible. In the 3:1 resonant trajectory map, none of the trajectories impact or escape, and each trajectory returns to periapsis with a radius below the orbital radius of Titan. Red regions represent trajectories corresponding to values of V_∞ with respect to Titan that increase due to the gravity of the Sun during the post-flyby revolution. In contrast, blue regions correspond to trajectories affected by solar gravity such that the V_∞ decreases during the post-flyby revolution. These are potential candidate orbits for designing a second flyby at a lower value of V_∞. The ΔV_∞ flyby periapsis maps provide an easy estimate for the changes in the V_∞ of trajectories due to solar gravity during the post-flyby revolution.

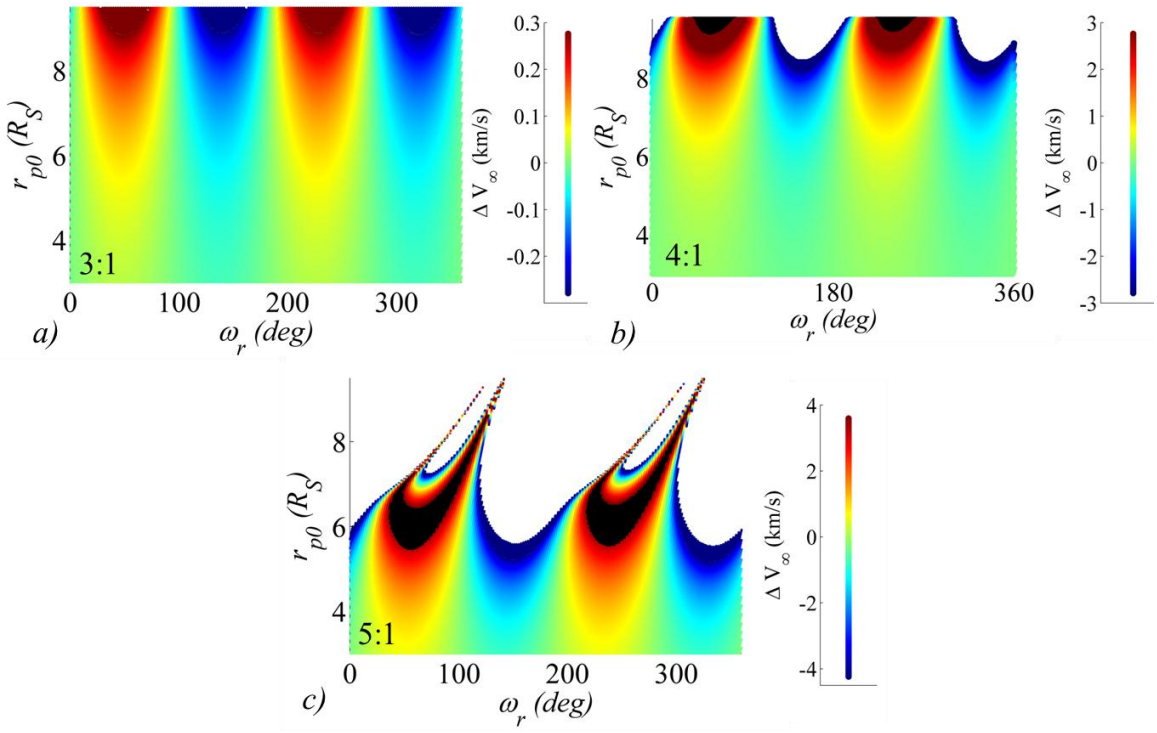

Figure 6.26 Flyby periapsis maps colored by ΔV_∞ for 3:1 (*a*), 4:1 (*b*), and 5:1 (*c*) pre-flyby resonances with Titan; outbound energy-increasing flybys.

6.3.4. Example: Designing a Second Titan Flyby at a Lower V_∞

By employing the ΔV_∞ flyby periapsis maps appearing in Figure 6.26, trajectories are selected that use the Sun's gravity to lower the estimated V_∞ with respect to Titan. For such a trajectory to be feasible, it must encounter Titan again, after the post-flyby revolution. For a preliminary design, it is useful to select the initial condition corresponding to the first flyby without requiring a numerical targeting algorithm. The ΔV_∞ flyby periapsis maps are augmented with additional information to offer an initial guess that effectively results in a second close flyby of Titan after the post-flyby revolution. The analysis in this section focuses on outbound, energy-increasing flybys.

As a first step towards assuring a second close flyby of Titan, a resonance with Titan during the post-flyby revolution is desired. Because solar gravity affects the trajectory significantly during the post-flyby revolution, calculating a resonance with Titan from the Keplerian period of the orbit just after the first flyby is insufficient. Instead, the time between periapse passages is measured, and trajectories that reach the subsequent periapsis within 1/64 day (22.5 minutes) of an integer number of Titan periods are marked in black on the flyby periapsis maps. Some of these "resonant" trajectories lie in red regions (corresponding to increasing V_∞) while others correspond to a decrease in V_∞ with respect to Titan. Because a decrease in V_∞ is desired, a resonant trajectory in a blue region is selected as an initial guess. For example, in the 3:1 resonance case, the flyby periapsis map appears in Figure 6.27, with resonant trajectories marked in black. A selected trajectory is marked by a white circle. It corresponds to a 3:1 pre-flyby resonance with Titan, an initial r_p = 9.3 R_S, and a Sun-Saturn periapse angle ω_r = 148.5º. The actual value of V_∞ with respect to Titan at the first flyby is 4.75 km/s – this value is the relative velocity between the spacecraft and Titan computed at the moment the spacecraft crosses the Hill radius on Titan approach. The initial state is propagated consistent with steps 1-4 from the algorithm in Section 6.3.1; an additional step is added at the end:

1. The initial state is defined at apoapsis relative to Saturn prior to a 1,000 km altitude energy-increasing flyby. The trajectory is propagated in the Saturn-Titan CR3BP through the flyby to the following apoapsis or for a time span equivalent to 10 conic periods of the pre-flyby trajectory.
2. The final state is rotated into a Saturn-centered inertial frame and a set of six osculating orbital elements is computed.
3. The post-flyby final state is artificially returned to periapsis for Sun-Saturn propagation. Each of the orbital elements is fixed, with the exception of true anomaly, which is re-set

to zero. The orbital elements are then used to compute the Saturn-centered inertial state in Cartesian coordinates using Saturn-centered conic relationships. This process returns a state at periapsis with respect to Saturn that incorporates the full effects of the Titan flyby.

4. The new post-flyby periapsis state is rotated into the Sun-Saturn rotating frame and propagated forward in the Sun-Saturn CR3BP. Integration is terminated if the spacecraft escapes through L_1 or L_2, if it impacts Saturn, or otherwise, when it reaches its subsequent periapsis.
5. The final periapsis state from Step 4 is rotated into the Saturn-Titan rotating frame; it is propagated in the Saturn-Titan CR3BP to apoapsis or for a time span equivalent to 10 conic periods of the pre-flyby trajectory.

The resulting trajectory appears in a Saturn-Titan rotating view in Figure 6.28(*a*) and a Saturn-centered inertial view in Figure 6.28(*b*). The 3:1 resonant pre-flyby trajectory appears in red; the post-flyby revolution appears in dark blue, and the subsequent revolution appears in light blue. The initial condition from the map is the periapsis marked in black. The trajectory approaches the first Titan flyby on the red trajectory and flies by at 1,000 km altitude. It then spirals out towards apoapsis on the dark blue path, and solar gravity affects the trajectory. The dark blue path returns to the vicinity of Saturn at its next periapsis, and then the second flyby occurs on the light blue path. The initial condition marked on the map does indeed result in a relatively close second flyby of Titan. The spacecraft flies by Titan at 51,176 km altitude.

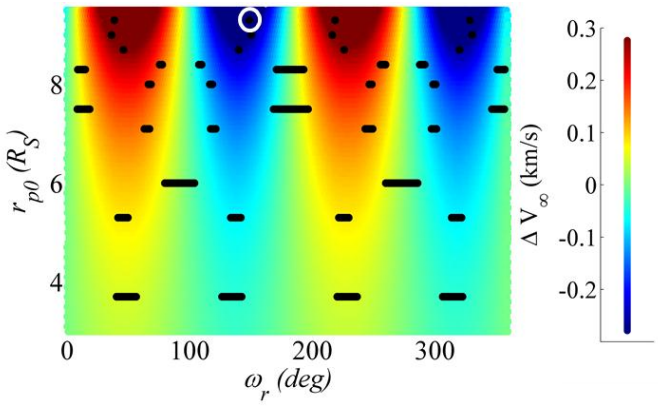

Figure 6.27 Flyby periapsis map for ΔV_∞ for a 3:1 pre-flyby resonance. Trajectories in near-resonance with Titan during the post-flyby revolution marked in black; initial guess marked in white.

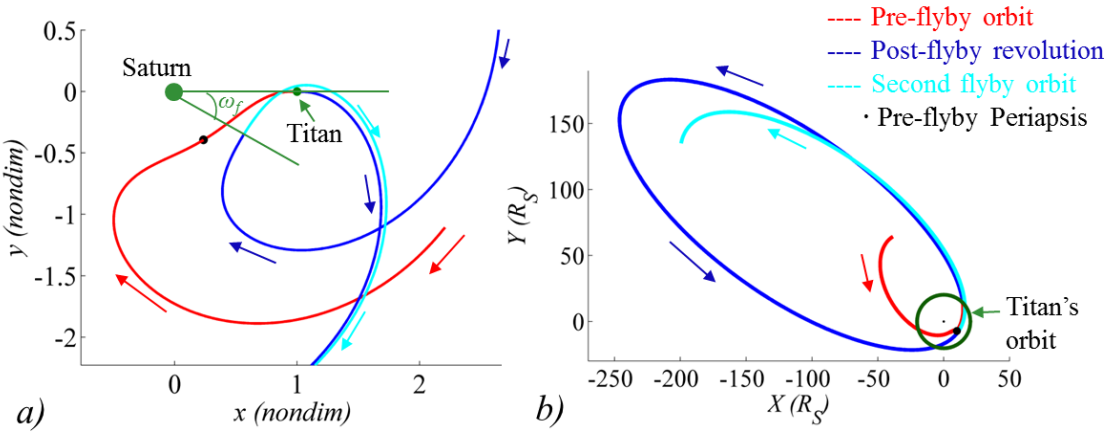

Figure 6.28 Trajectories in the Saturn-Titan rotating view (*a*) and the Saturn-centered inertial view (*b*).

To tune this second flyby, another type of flyby periapsis map is employed. Recall that the flyby angle, ω_f, is the angle of periapsis with respect to Saturn relative to the Saturn-Titan *x*-axis. A closer flyby of Titan may be achieved by decreasing (making more negative) the flyby angle of the second flyby, marked in green in Figure 6.28(*a*). In this example, the original value of flyby angle of the second flyby is ω_f = -31.84º; decreasing ω_f of the second flyby acts to pull the cyan trajectory downwards, closer to Titan. To determine how the initial condition should be adjusted to decrease the second flyby angle, a flyby periapsis map colored to reflect the angle ω_f at the second flyby is produced. It appears in Figure 6.29(*a*), with a zoomed view of the region near the original initial guess in Figure 6.29(*b*). Consider the colorbar in the figure, and note that negative flyby angles are colored in blue tones, while positive angles range from green through yellow and orange to red. To decrease the value of ω_f, the Sun-Saturn periapse angle ω_r must be shifted more towards the blue region. By increasing ω_r by 1.05º, such that the initial Sun-Saturn periapse angle is ω_r = 149.55º, the new value of the flyby angle of the second flyby is ω_f = -34.70º, and a 1,066 km altitude flyby is achieved. The new trajectory appears in Figure 6.30 in the Saturn-Titan rotating view (*a*) and the Saturn-centered inertial view (*b*). After the second close flyby in light blue, the trajectory escapes the vicinity of Saturn at high energy. The V_∞ with respect to Titan at the second flyby is 4.423 km/s, yielding ΔV_∞ = -0.331 km/s due to the solar gravity. The time of flight in the post-flyby revolution is 334 days. Note that no ΔV has been applied to this trajectory — the entire adjustment in V_∞ is a result of tidal acceleration acting on the post-flyby revolution, and targeting has been achieved by adjusting the orientation of the orbit in the Sun-

Saturn frame. Of course, leveraging solar gravity to reduce V_∞ is accomplished at the expense of a lengthy interval between encounters.

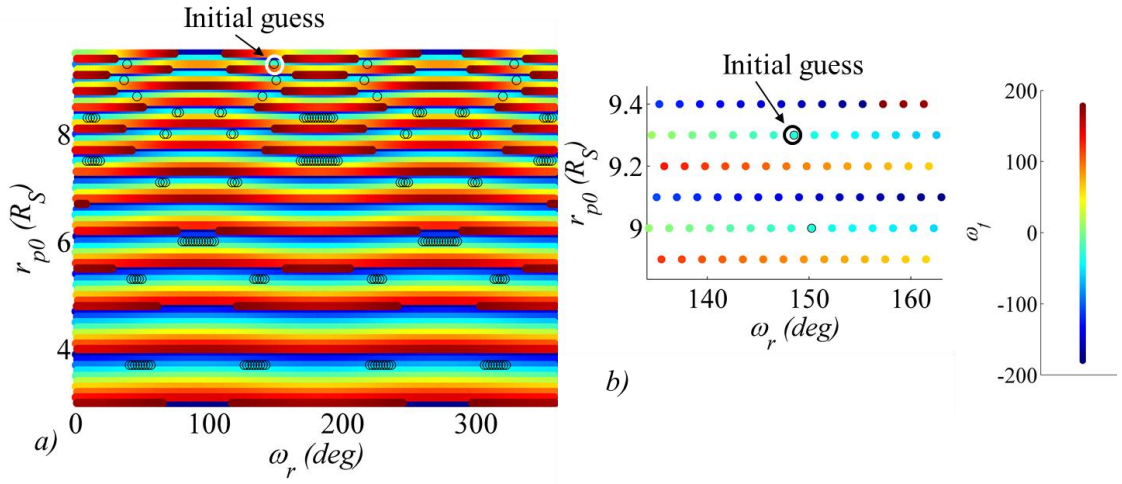

Figure 6.29 Flyby periapsis maps colored by ω_f for a 3:1 pre-flyby resonance with Titan.

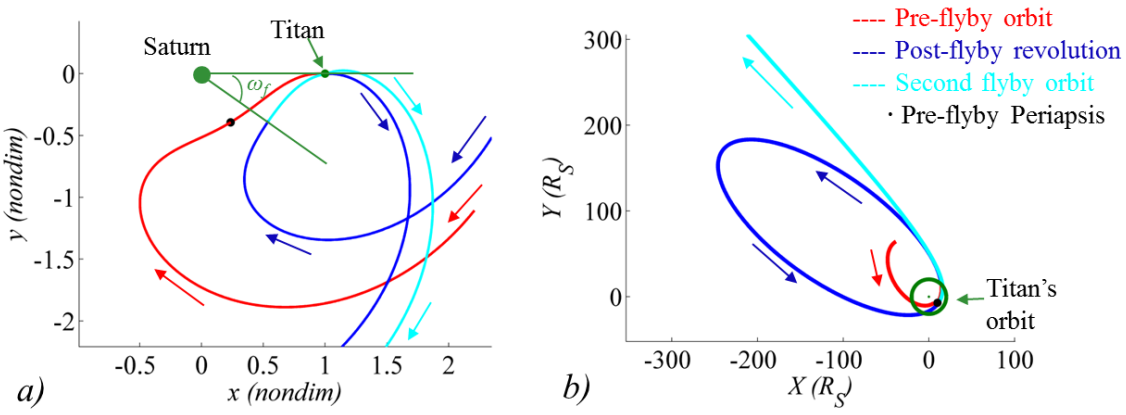

Figure 6.30 Trajectories in the Saturn-Titan rotating view (*a*) and the Saturn-centered inertial view (*b*). Initial conditions now tuned to yield a 1,066 km altitude at the second Titan flyby.

The same process is effective for the 4:1 and 5:1 pre-flyby resonant orbits. Consider a 4:1 example. Again, the trajectories that reach the second periapsis in an integer number of Titan revolutions are marked in black on the ΔV_∞ flyby periapsis map; this map appears in Figure 6.31. In this example, some of the trajectories are infeasible since the large periapse raise, a consequence of the tidal acceleration during the post-flyby revolution, causes the second periapsis

to lie beyond Titan's orbit, and no close second flyby is possible. These regions are signified by white zones in the map. An initial guess is selected in the blue region of the flyby periapsis map that corresponds to a decrease in V_∞, as desired. The selected initial condition is marked on the map by a white circle. The pre-flyby orbit is in a 4:1 resonance with Titan with an initial periapse radius $r_{p0} = 7.8\ R_S$. The periapse angle in the Sun-Saturn frame is $\omega_r = 161.89^o$, and the initial V_∞ with respect to Titan is 5.382 km/s. This initial state results in a distant second flyby of Titan; the altitude of the second flyby is 370,290 km. The trajectory appears in the Saturn-Titan rotating view and the Saturn-centered inertial view in Figure 6.32. The orbit approaches its first Titan flyby (red) and encounters the moon at a 1,000 km altitude. The post-flyby revolution (dark blue) is affected by solar gravity, and the second distant flyby occurs when the spacecraft is on the light blue path. It is notable that even this quite distant encounter, relative to a small body, does visibly impact the Saturn-centered orbit.

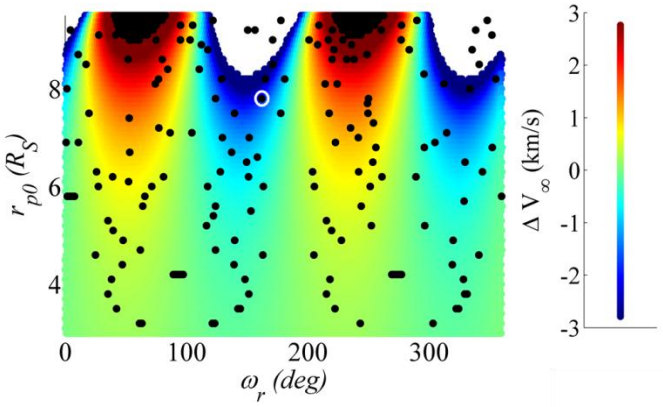

Figure 6.31 Flyby periapsis map for ΔV_∞ for a 4:1 pre-flyby resonance. Trajectories in resonance with Titan during the post-flyby revolution marked in black; initial guess circled in white.

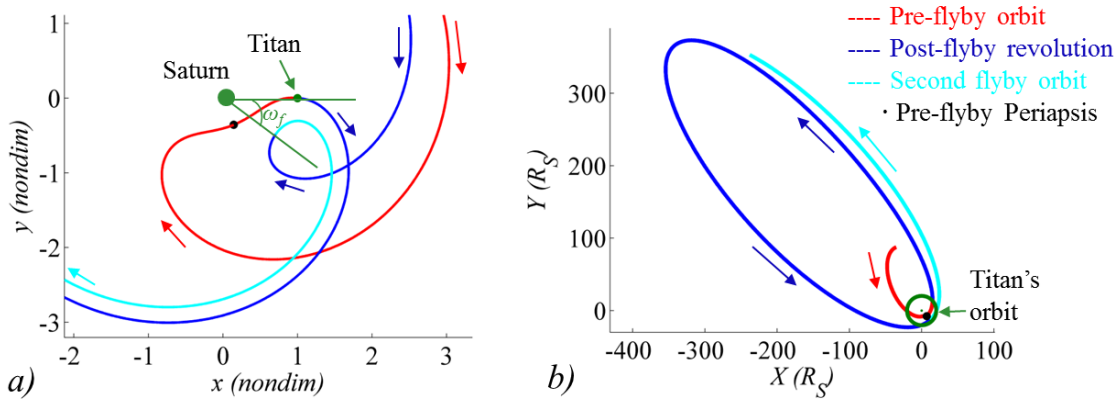

Figure 6.32 Trajectories in the Saturn-Titan rotating view (*a*) and the Saturn-centered inertial view (*b*).

As in the previous example employing a 3:1 Titan-resonant pre-flyby orbit, the second flyby in the 4:1 pre-flyby resonance case is tuned by using a periapsis flyby map colored consistent with the second flyby angle, ω_f. In this case, to shift the flyby closer to Titan, the second flyby angle, originally equal to -34.66º, must be less negative. This shift is accomplished by adjusting only the periapse angle, or by changing r_p and ω_r simultaneously. Consider the map in Figure 6.33. In either case, the color of the initial periapse point on the ω_f map must move towards a green tone to yield a less-negative flyby angle. In this example, r_p is held constant at 7.8 R_S and the original value of periapse angle, ω_r = 161.89º, is decreased to increase ω_f. The new initial periapse angle, ω_r = 161.16º, results in ω_f = -16.33º. The new trajectory possesses a 1,058 km altitude flyby at the second encounter, and V_∞ = 3.306 km/s. The relative velocity is modified such that ΔV_∞ = -2.076 km/s, a decrease that is quite significant. The time of flight of the post-flyby revolution is 732 days. Again, no maneuver is incorporated in the trajectory design. The change in V_∞ is due solely to tidal acceleration during the post-flyby revolution. Note the extreme sensitivity of the trajectory to initial periapse angle. With a change in ω_r of just 0.73º, the altitude of the second flyby is modified by over 369,000 km. The tuned trajectory appears in the rotating and inertial views in Figure 6.34. As in the 3:1 example, the trajectory escapes the vicinity of Saturn at high energy after the second Titan flyby.

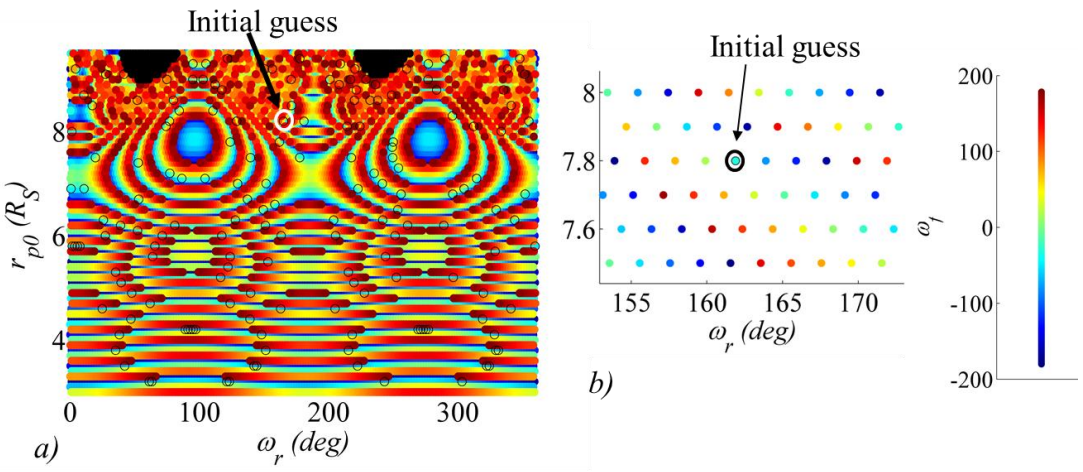

Figure 6.33 Flyby periapsis maps colored by ω_f for a 4:1 pre-flyby resonance with Titan.

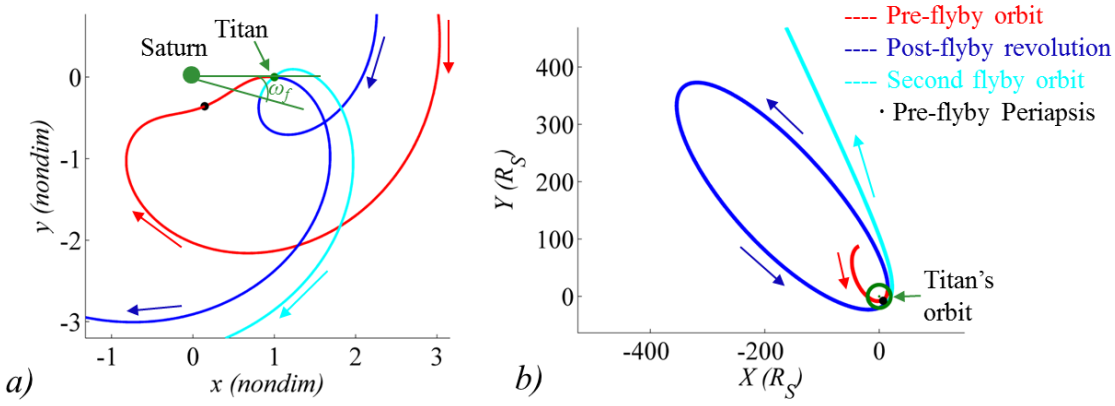

Figure 6.34 Trajectories in the Saturn-Titan rotating view (*a*) and the Saturn-centered inertial view (*b*). Initial condition tuned to yield a 1,058 km altitude at the second Titan flyby.

In a final example, the same process is employed to produce a high-energy escape originating from a 5:1 Titan-resonant orbit. The V_∞ flyby periapsis map is augmented by marking (in black) the initial states that result in post-flyby resonant trajectories. The new map appears in Figure 6.35 for the 5:1 pre-flyby resonance example. Again, the white regions in the map correspond to trajectories that are infeasible for achieving a change in V_∞ at the second flyby; these trajectories either escape or the subsequent periapse radii are raised beyond the orbit of Titan so that a second close flyby is impossible. An initial condition, selected to decrease the V_∞ with respect to Titan at the second flyby, is marked in white on the map. An initial periapse radius of 4.74 R_S is paired

with a periapse angle ω_r = 168.09º to yield a trajectory with V_∞ = 6.435 km/s at the first Titan flyby. After the post-flyby revolution, the spacecraft encounters Titan again at an altitude of 635,790 km, with a flyby angle ω_f = -55.63º. The trajectories appear in Figure 6.36. Again, a map of ω_f is computed and appears in Figure 6.37. The closest approach to Titan occurs at a negative *y*-value. One way to tune the trajectory and achieve a close encounter at the second flyby is, thus, to increase the second flyby angle, making it less negative. Once again, a map relating the initial state of the pre-flyby trajectory to the flyby angle at the second flyby is produced; it appears in Figure 6.37. The initial state on the pre-flyby trajectory is marked on the map. To increase the second flyby angle, the initial state is adjusted towards the green region on the map, by fixing r_{p0} to remain constant and decreasing the periapse angle of the initial orbit. With a new periapse angle ω_r = 167.26º, and consequently a new flyby angle ω_f = -24.55º, the altitude of the second flyby decreases to 1,089 km. The V_∞ with respect to Titan is now 3.922 km/s, for a ΔV_∞ = -2.513 km/s. The time of flight on the post-flyby revolution is 891 days. The tuned trajectory appears in Figure 6.38. Once again, the spacecraft escapes at high energy after the second Titan flyby.

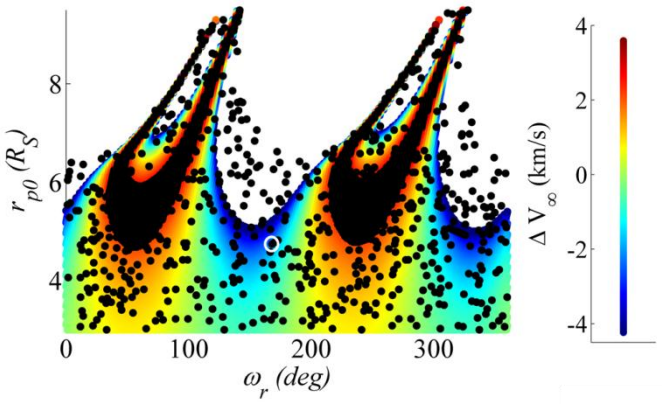

Figure 6.35 Flyby periapsis map for ΔV_∞ for a 4:1 pre-flyby resonance. Trajectories in resonance with Titan during the post-flyby revolution marked in black; initial guess circled in white.

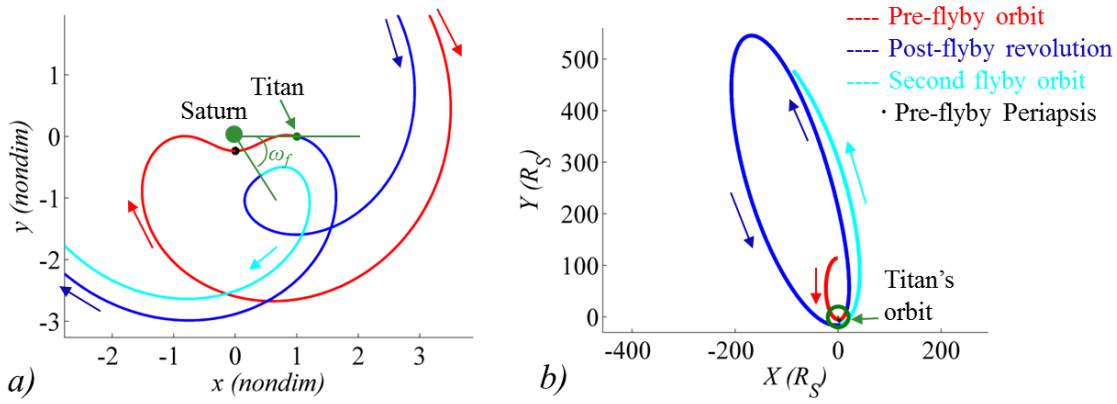

Figure 6.36 Trajectories in the Saturn-Titan rotating view (*a*) and the Saturn-centered inertial view (*b*).

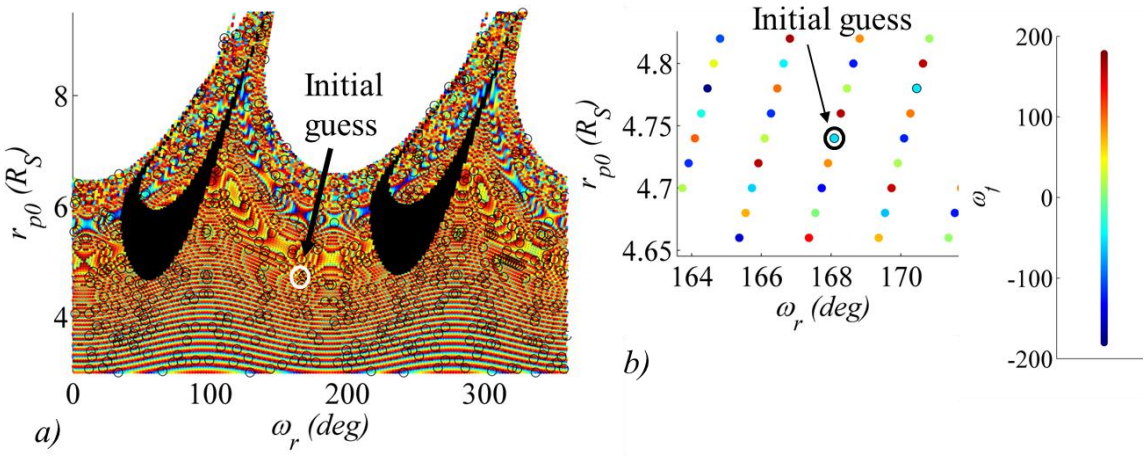

Figure 6.37 Flyby periapsis maps colored by ω_f for a 4:1 pre-flyby resonance with Titan.

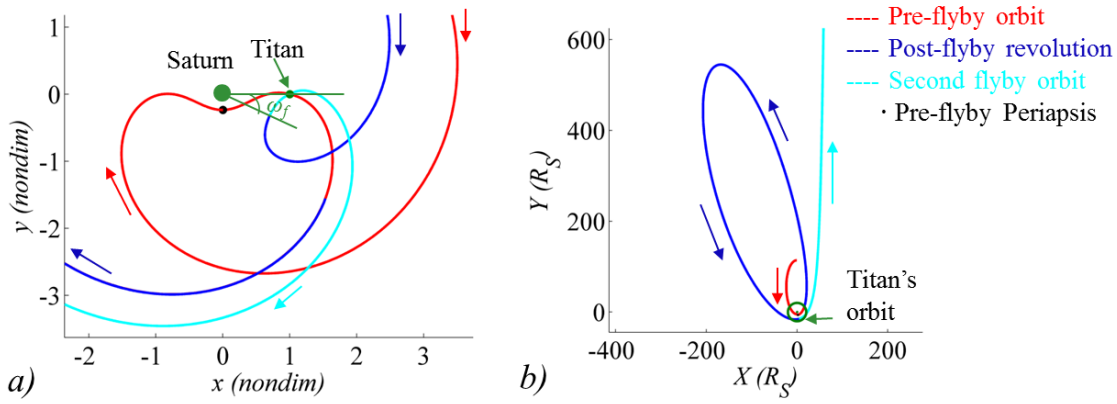

Figure 6.38 Trajectories in the Saturn-Titan rotating view (*a*) and the Saturn-centered inertial view (*b*). Initial condition tuned to yield a 1,089 km altitude at the second Titan flyby.

The procedures developed to incorporate a flyby and tidal acceleration in the design process are demonstrated using parameters based on a real-world design scenario, that is, various extended mission options in support of the Cassini spacecraft in the Saturnian system. The resulting maps are employed for designing sample trajectories related to this specific problem. The maps are computed for a specific set of conditions: a particular range of pre-flyby r_p values, a discrete set of pre-flyby semi-major axes, and a specific flyby altitude in the Sun-Saturn-Titan system, all consistent with the Cassini end-of-life options. However, these design strategies are not limited to these particular parameters and assumptions. Similar flyby periapsis Poincaré maps are applicable to other Sun-planet-moon systems for a desired range of pre-flyby semi-major axis and periapse radius values, and for a flyby altitude specified by the particular problem posed to a mission designer. However, the concepts may also be applied to a wider range of applications. Through modification of the particular subset of the parameters fixed and the quantities that are available for adjustment, maps may be created to select a set of initial conditions that lead to desired orbits based on different sets of constraints. For example, by maintaining the value of Jacobi Constant, as opposed to the pre-flyby semi-major axis, a designer may locate trajectories that satisfy a pre-flyby constraint on the Jacobi value rather than a particular pre-flyby trajectory that is resonant with Titan.

Designing flybys from a multi-body perspective provides trajectory opportunities that may be exploited to allow or enhance various mission applications. However, the multi-body approach adds complexities to basic encounter design; these complexities must be overcome to develop a procedure that is effective for preliminary trajectory design. Flyby periapsis Poincaré maps offer

a methodical process for selecting a pre-flyby orbit that results in a desired outcome after tidal acceleration affects the trajectory during the post-flyby revolution. Trajectory design remains an art — selecting and blending the appropriate maps are the keys to success.

7. CONCLUDING REMARKS

Preliminary trajectory design in a multi-body model is complicated by the extensive solution space. The lack of an analytical solution to the CR3BP equations of motion, combined with the sensitive and even chaotic nature of the design space, render the selection of initial conditions that lead to a trajectory with the desired characteristics challenging. However, retaining the multi-body nature of the problem early in the design process more accurately reflects the dynamics of the problem, especially in regimes where multiple bodies affect the spacecraft motion to a similar degree. To develop a methodical procedure for preliminary trajectory design when multiple gravity fields are incorporated early in the process requires a simplification and organization of the design space. Periapsis Poincaré maps provide an effective means for the development of a multi-body preliminary design strategy. A particular series of maps is developed in this investigation. These maps assist in establishing an understanding of the types of P_2-centered trajectories that exist at a given energy level in a variety of P_1-P_2 systems. Both long- and short-term trajectory behaviors are considered. The maps are then applied to specific mission design applications, facilitating the selection of orbits that satisfy various mission objectives. With the addition of a third gravitational body, periapsis Poincaré maps can allow the systematic preliminary design of flybys in a 4-body model.

7.1. Understanding the Tidally-Influenced Environment

The tidal gravity due to the distant larger primary exerts a significant effect on large P_2-centered trajectories, and a methodical orbit design strategy begins with the development of an improved understanding of the design space in the vicinity of the second primary. An investigation of the tidal influence in terms of P_2-centered quadrants in the rotating frame offers a framework for understanding the behavior of individual trajectories over short-term propagations. However, it is the introduction of periapsis Poincaré maps that supplies the key to visualizing the short- and long-term behavior of large sets of trajectories.

Short-term periapsis Poincaré maps offer a degree of predictability to the behavior over one or several revolutions of P_2-centered trajectories at a given value of Jacobi Constant. Well-defined lobes appear on the maps, bounding regions that deliver gateways to escape or impact. A trajectory possessing a periapsis lying within a lobe is guaranteed to escape the vicinity of P_2 or to impact onto its surface after a specific number of periapse passages, following a predictable pattern through the set of lobes. The lobes corresponding to escape are neatly outlined by the stable manifolds associated with the L_1 and L_2 Lyapunov trajectories at the same value of *J*. The size and shape of the lobes evolve, consistent with the energy level as well as the mass parameter of the P_1-P_2 system. Both planar and 3-dimensional trajectories are explored. Other maps focus on orbits that remain captured after one or more revolutions. These maps highlight trajectories with particular orbital element changes due to tidal acceleration from one periapsis to the next.

At a given value of *J*, a set of trajectories may remain in orbit about P_2 over long-term propagations, even when the ZVCs remain open at L_1 and L_2. This set of captured orbits appears as an ordered group when viewed on a periapsis Poincaré map. As the trajectories evolve over time, the set of periapse points corresponding to any given trajectory forms a pattern. When the ZVCs are open, the periapses of a captured trajectory tend to produce a well-defined, ordered shape. Various characteristics of the trajectory are predictable based on the shape of the periapse profile. Given the location of a single periapsis in *x*-*y* space, along with the associated Jacobi Constant, the trajectory periapse profile is defined and, hence, certain features of the orbit are predictable, with no propagation required. Maps are created for both planar and 3D orbits.

7.2. Designing Trajectories in the Tidally-Influenced Environment

With an improved understanding of the design space in the vicinity of P_2, preliminary construction of tidally-influenced trajectories becomes more straightforward. Periapsis Poincaré maps are again applied to the problem. Depending on the variables plotted on the map, various types of trajectories are easily identified. Initial conditions leading to quasi-periodic and quasi-frozen orbits are immediately apparent. The maps facilitate the design of trajectories that satisfy specific mission design requirements.

For example, the development of options for spacecraft disposal at the end of the Cassini mission, which initially required significant time and effort for the trial-and-error discovery of point solutions, becomes quick and methodical with the addition of periapsis Poincaré maps. Short-term maps are used to select initial conditions leading to orbits that escape Saturn towards

the inner or outer solar system, as well as Saturn impact trajectories. A combination of long- and short-term maps facilitates the design of long-term, stable, Saturn-centered options for disposal orbits. First, a short-term map is used to select a trajectory that results in a significant rise in the periapse radius. Then, a long-term map defines the maneuver required to place the spacecraft on a path that remains beyond the orbit of the moon Phoebe, for example. Similarly, periapsis Poincaré maps are applied to the problem of designing a capture trajectory at the moon Titan. Other maps identify ballistic transfer trajectories from low-Earth orbit to the vicinity of the Moon. As a design tool, periapsis Poincaré maps represent a very useful alternative to a trial-and-error selection of initial conditions for P_2-centered trajectories that are significantly influenced by the gravity of the distant larger primary.

7.3. Including the Influence of an Additional Smaller Primary

Orbits in the vicinity of P_2 are not only affected by the gravity of the distant larger primary; the effects of a close encounter with a flyby body can also significantly influence the trajectory. Gravity assists are first investigated in terms of the CR3B system with P_2 and the flyby body as the primaries. The flyby kick function offers a valuable initial guess of the flyby angle that yields a particular change in trajectory orbital elements after the flyby. One advantage of the kick function is that the estimate approximates the CR3BP, therefore incorporating the gravity of the two primaries simultaneously. Also, the analysis occurs in the rotating frame, removing the necessity of transformations between frames. Employing the initial guess supplied by the kick function, polynomials are produced that are used to calculate the flyby angle that results in a specific flyby altitude.

With an improved understanding of the dynamics of gravity assist trajectories in the CR3BP, the flyby design is combined with a tidally-influenced orbit to produce a trajectory that fully exploits its multi-body environment. As an example, the Saturn-Titan CR3BP is patched together with the Sun-Saturn CR3BP for application to extended mission scenarios for the Cassini spacecraft. Periapsis Poincaré maps are again employed for the analysis.

Tidal acceleration is also effective for changing a spacecraft velocity with respect to a flyby body, i.e., V_∞. Periapsis Poincaré maps again offer a significant advantage in design strategy as compared to trial-and-error point solutions. By combining several maps, an initial flyby is easily selected that leads to a second flyby at a significantly decreased value of V_∞. The initial

conditions selected from the maps result directly in the second flyby without requiring a targeting maneuver.

7.4. Recommendations for Future Work

There are many potential directions for future investigations into the development of preliminary multi-body trajectory design strategies based on periapsis Poincaré maps. Recommended future efforts include the following.

- *Investigate the stability of periodic and quasi-periodic orbits located from the long-term periapsis Poincaré maps*. The structure of the maps suggests that some of these orbits — those existing at the center of an island in the map — may be marginally stable, representing potential opportunities for a long-term spacecraft orbit. Others, however, do not appear to lie within an island and may be unstable, opening up the possibility of manifold-based transfers into and away from these orbits. Stability investigation could be based on eigenvalue analysis of the monodromy matrix and/or Finite Time Lyapunov Exponent (FTLE) analysis of periodic and quasi-periodic trajectories.

- *Investigate 3D and retrograde maps and trajectories*. The short-term initial condition maps and long-term periapsis Poincaré maps that have been developed to characterize the tidally influenced environment and facilitate preliminary design in the CR3BP are focused, thus far, on planar, prograde trajectories. Preliminary investigations of out-of-plane and retrograde trajectories reveal structure within the dynamical environment; further exploration may advance the understanding of the design space as well as supply tools for 3D trajectory design in the CR3BP.

- *Continue investigation of flybys from a multi-body perspective*. Continued investigations are recommended to complete the multi-body flyby analysis. First, several patterns are observed, in a particular set of scenarios, that aid in defining and explaining the differences in inbound and outbound encounters and their relative effectiveness at increasing or decreasing the Keplerian energy of spacecraft trajectories. A further examination of these differences is warranted. In addition, the use of periapsis Poincaré maps for the analysis of flybys from a multi-body perspective is, thus far, limited to the

planar case. However, in a 4-body problem involving the Sun, a planet, a moon, and a spacecraft, the four bodies will rarely share a plane. It is therefore necessary to allow for the possibility of inclined flybys in gravity assist design tools.

- *Integrate different sets of periapsis Poincaré maps into an automated software tool for preliminary orbit design*. Periapsis Poincaré maps represent a valuable tool for the visualization of large sets of trajectories in the CR3BP. They are effectively applied to the problem of preliminary trajectory design in a multi-body model. As interactive visual environments become more common, the current process might be extended by tying various maps together in a graphical software tool that allows the designer to select various orbits and propagate in real time. For both the design of P_2-centered orbits as well as the design of flybys in a 4-body model, a map-based software package could facilitate preliminary trajectory design, enabling the procedures based on periapsis Poincaré maps to be accessible to a larger number of designers.

A multi-body approach to preliminary design of trajectories in the vicinity of a smaller primary offers design options that are otherwise unavailable. However, the addition of a second or third gravitational influence significantly complicates the process of selecting initial conditions that lead to a trajectory with desired characteristics. Periapsis Poincaré maps provide a valuable tool for simplifying and organizing the design space, facilitating the preliminary design of trajectories in this regime.

LIST OF REFERENCES

LIST OF REFERENCES

[1] Broucke, R. A., "Long-Term Third-Body Effects via Double Averaging," *Journal of Guidance, Control, and Dynamics*, Vol. 26, 1, January-February 2003, pp. 27-32.

[2] Prado, A. F., "Third-Body Perturbation in Orbits around Natural Satellites," *Journal of Guidance, Control, and Dynamics*, Vol. 26, No. 1, January-February 2003, pp. 33-40.

[3] Prado, A. F., "Retrograde Orbits Perturbed by a Third Body," *Journal of the Brazilian Society of Mechanical Sciences*, Vol. 27, No. 4, October-December 2005, pp. 364-371.

[4] Scheeres, D. J., M. D. Guman and B. F. Villac, "Stabilitiy Analysis of Planetary Satellite Orbiters: Application to the Europa Orbiter," *Journal of Guidance, Control, and Dynamics*, Vol. 24, No. 4, July-August 2001, pp. 778-787.

[5] Paskowitz, M. E. and D. J. Scheeres, "Design of Science Orbits about Planetary Satellites: Application to Europa," *Journal of Guidance, Control, and Dynamics*, Vol. 29, No. 5, September-October 2006, pp. 1147-1158.

[6] Villac, B. F., D. J. Scheeres, L. A. D'Amario and M. D. Guman, "The Effect of Tidal Forces on Orbit Transfers," AAS 2001-247, AIAA/AAS Spaceflight Mechanics Meeting, Santa Barbara, California, February 2001.

[7] Moulton, F. R., *Differential Equations*, Dover, 1958.

[8] Scheeres, D. J., B. G. Williams and J. K. Miller, "Evalution of the Dynamic Environment of an Asteroid: Applications to 433 Eros," *Journal of Guidance, Control, and Dynamics*, Vol. 23, No. 3, May-June 2000, pp. 466-474.

[9] Scheeres, D. J., J. K. Miller and D. K. Yeomans, "The Orbital Dynamics Environment of 433 Eros: A Case Study for Future Asteroid Missions," *IPM Progress Report*, February 15, 2003.

[10] Hénon, M., "Numerical Exploration of the Restricted Problem. V. Hill's Case: Periodic Orbits and Their Stability," *Astronomy and Astrophysics*, Vol. 1, 1969, pp. 223-238.

[11] Hénon, M., "Numerical Exploration of the Restricted Problem. VI. Hill's Case: Non-Periodic Orbits," *Astronomy and Astrophysics*, Vol. 9, 1970, pp. 24-36.

[12] Hénon, M., "Vertical Stability of Periodic Orbits in the Restricted Problem," *Astronomy and Astrophysics*, Vol. 28, 1973, pp. 415-426.

[13] Hénon, M., "New Families of Periodic Orbits in Hill's Problem of Three Bodies," *Celestial Mechanics and Dynamical Astronomy*, Vol. 85, 2003, pp. 223-226.

[14] Hénon, M., "Families of Asymmetric Periodic Orbits in Hill's Problem of Three Bodies," *Celestial Mechanics and Dynamical Astronomy*, Vol. 93, 2005, pp. 87-100.

[15] Benest, D., "Effects of the Mass Ratio on the Existence of Retrograde Satellite in the Circular Plane Restricted Problem," *Astronomy and Astrophysics*, Vol. 32, 1974, pp. 39-46.

[16] Robin, I. A. and V. V. Markellos, "Numerical Determination of Three-Dimensional Periodic Orbits Generated from Vertical Self-Resonant Satellite Orbits," *Celestial Mechanics*, Vol. 21, 1980, pp. 395-434.

[17] Kazantzis, P. G., "Numerical Determination of Families of Three-Dimensional Double-Symmetric Periodic Orbits in the Restricted Three-Body Problem, II. Sun Jupiter Case," *Astrophysics and Space Science*, Vol. 69, 1980, pp. 353-368.

[18] Lam, T. and G. J. Whiffen, "Exploration of Distant Retrograde Orbits Around Europa," AAS 2005-110, AAS/AIAA Spaceflight Mechanics Meeting, Copper Mountain, Colorado, January 2005.

[19] Russell, R. P., "Global Search for Planar and Three-Dimensional Periodic Orbits Near Europa," *Journal of the Astronautical Sciences*, Vol. 54, No. 2, April-June 2006, pp. 199-226.

[20] Tsirogiannis, G. A., E. A. Perdios and V. V. Markellos, "Improved Grid Search Method: An Efficient Tool for Global Computation of Periodic Orbits," *Celestial Mechanics and Dynamical Astronomy*, Vol. 103, 2009, pp. 49-78.

[21] Lara, M. and R. P. Russell, "Concerning the Family "g" of the Restricted Three-Body Problem," IX Jornada de Trabajo en Mecánica Celeste, Jaca, Huesca, Spain, June 2006.

[22] Lara, M., R. P. Russell and B. F. Villac, "On Parking Solutions Around Europa," AAS 2005-384, AAS/AIAA Astrodynamics Specialist Conference, Lake Tahoe, California, August 2005.

[23] Lara, M., R. P. Russell and B. F. Villac, "Classification of Distant Stability Regions at Europa," *Journal of Guidance, Control, and Dynamics*, Vol. 30, No. 2, March-April 2007, pp. 409-418.

[24] Chauvineau, B. and F. Mignard, "Dynamics of Binary Asteroids, I. Hill's Case," *Icarus*, Vol. 83, 1990, pp. 360-381.

[25] Hamilton, D. P. and J. A. Burns, "Orbital Stability Zones about Asteroids," *Icarus*, Vol. 92, 1991, pp. 118-131.

[26] Hamilton, D. P. and A. V. Krivov, "Dynamics of Distant Moons of Asteroids," *Icarus*, Vol. 128, 1997, pp. 241-249.

[27] Carruba, V., J. A. Burns, P. D. Nicholson and B. J. Glandman, "On the Inclination Distribution of the Jovian Irregular Satellites," *Icarus*, Vol. 158, 2002, pp. 434-449.

[28] Sheppard, S. S., "Outer Irregular Satellites of the Planets and Their Relationship with Asteroids, Comets, and Kuiper Belt Objects," IAU Symposium No. 229, May 2006.

[29] Astakhov, S. A., A. D. Burbanks, S. Wiggins and D. Farrelly, "Chaos-assisted capture of irregular moons," *Nature*, Vol. 423, May 2003, pp. 264-267.

[30] Astakhov, S. A., A. D. Burbanks, S. Wiggins and D. Farrelly, "Dynamics of Capture in the Restricted Three-Body Problem," Order and Chaos in Stellar Planetary Systems, ASP Conference Series, Vol. 316, pp. 80-85.

[31] Belbruno, E. A., "Lunar Capture Orbits, a Method of Constructing Earth Moon Trajectories and the Lunar GAS Mission," AIAA 1987-1054, AIAA/DGLR/JSASS International Electric Propulsion Conference, Colorado Springs, Colorado, May 1987.

[32] Belbruno, E. A. and J. K. Miller, "Sun-Perturbed Earth-to-Moon Transfers with Ballistic Capture," *Journal of Guidance, Control, and Dynamics*, Vol. 16, No. 4, July-August 1993, pp. 770-775.

[33] Yamakawa, H., J. Kawaguchi, N. Ishii and H. Matsuo, "On Earth-Moon Transfer Trajectory with Gravitational Capture," AAS 93-633, AAS/AIAA Astrodynamics Specialist Conference, Victoria, Canada, August 1993.

[34] Kawaguchi, J., H. Yamakawa, T. Uesugi and H. Matsuo, "On Making Use of Lunar and Solar Gravity Assists in LUNAR-A, PLANET-B Missions," *Acta Astronautica*, Vol. 35, No. 9-11, 1995, pp. 633-642.

[35] Belbruno, E. A. and J. P. Carrico, "Calculation of Weak Stability Boundary Ballistic Lunar Transfer Trajectories," AIAA 2000-4142, AIAA/AAS Astrodynamics Specialist Conference, Denver, Colorado, August 2000.

[36] Howell, K. C. and M. Kakoi, "Transfers Between the Earth-Moon and Sun-Earth Systems Using Manifolds and Transit Orbits," *Acta Astronautica*, Vol. 59, 2006, 2006, pp. 367-380.

[37] Koon, W. S., M. W. Lo, J. E. Marsden and S. D. Ross, "Shoot the Moon," AAS 2000-166, AAS/AIAA Astrodynamics Specialist Conference, Clearwater, Florida, August 2000.

[38] Gómez, G., W. S. Koon, M. W. Lo, J. E. Marsden, J. Masdemont and S. D. Ross, "Invariant Manifolds, The Spatial Three-Body Problem, and Space Mission Design," AAS 2001-301, AAS/AIAA Astrodynamics Specialist Conference, Quebec City, Canada, August 2001.

[39] Gómez, G., W. S. Koon, M. W. Lo, J. E. Marsden, J. Masdemont and S. D. Ross, "Connecting Orbits and Invariant Manifolds in the Spatial Restricted Three-Body Problem," *Nonlinearity*, Vol. 17, 2004, pp. 1571-1606.

[40] Parker, J. S. and G. H. Born, "Modeling a Low-Energy Ballistic Lunar Transfer Using Dynamical Systems Theory," *Journal of Spacecraft and Rockets*, Vol. 45, No. 6, November-December 2008, pp. 1269-1281.

[41] Russell, R. P. and T. Lam, "Designing Capture Trajectories to Unstable Periodic Orbits Around Europa," AAS 2006-189, AAS/AIAA Spaceflight Mechanics Meeting, Tampa, Florida, January 2006.

[42] Howell, K. C., B. G. Marchand and M. W. Lo, "Temporary Satellite Capture of Short-Period Jupiter Family Comets from the Perspective of Dynamical Systems," AAS 2000-155, AAS/AIAA Spaceflight Mechanics Meeting, Clearwater, Florida, January 2000.

[43] Villac, B. F. and D. J. Scheeres, "Escaping Trajectories in the Hill Three-Body Problem and Applications," *Journal of Guidance, Control, and Dynamics*, Vol. 26, No. 2, March-April 2003, pp. 224-232.

[44] Paskowitz, M. E. and D. J. Scheeres, "Robust Capture and Transfer Trajectories for Planetary Satellite Orbiters," *Journal of Guidance, Control, and Dynamics*, Vol. 29, No. 2, March-April 2006, pp. 342-353.

[45] Villac, B. F. and D. J. Scheeres, "New Class of Optimal Plane Change Maneuvers," *Journal of Guidance, Control, and Dynamics*, Vol. 26, No. 5, September-October 2003, pp. 750-757.

[46] Broucke, R. A., "The Celestial Mechanics of Gravity Assist," AIAA 1988-4220, AIAA/AAS Astrodynamics Specialist Conferece, Minneapolis, Minnesota, August 1988.

[47] Strange, N. J. and J. M. Longuski, "Graphical Method of Gravity-Assist Trajectory Design," *Journal of Spacecraft and Rockets*, Vol. 39, No. 1, January-February 2002, pp. 9-16.

[48] Kloster, K. W., A. E. Petropoulos and J. M. Longuski, "Europa Orbiter Tour Design with Io Gravity Assists," *Acta Astronautica*, Vol. 68, No. 7-8, April-May 2011, pp. 931-946.

[49] Campagnola, S. and R. P. Russell, "The Endgame Problem Part 2: The Multi-body Technique and the T-P Graph," *Journal of Guidance, Control, and Dynamics*, Vol. 33, No. 2, 2010, pp. 476-486.

[50] Howell, K. C. and J. Guzmán, "Spacecraft Trajectory Design in the Context of a Coherent Restricted Four-Body Problem with Application to the MAP Mission," IAF-00-A.5.06, 51st International Astronautical Congress, Rio de Janeiro, Brazil, October 2000.

[51] Malyshkin, L. and S. Tremaine, "The Keplerian Map for the Planar Restricted Three-Body Problem as a Model of Comet Evolution," *Icarus*, Vol. 141, 1999, pp. 341-353.

[52] Zhou, J., Y. Sun, J. Zheng and M. Valtonen, "The Transfer of Comets from Near-Parabolic to Short-Period Orbits: Map Approach," *Astronomy and Astrophysics*, Vol. 364, 2000, pp. 887-893.

[53] Pan, M. and R. Sari, "A Generalization of the Lagrangian Points: Studies of Resonance for Highly Eccentric Orbits," *The Astronomical Journal*, Vol. 128, September 2004, pp. 1418-1429.

[54] Ross, S. D. and D. J. Scheeres, "Multiple Gravity Assists, Capture, and Escape in the Restricted Three-Body Problem," *SIAM Journal of Applied Dynamical Systems*, Vol. 6, No. 3, 2007, pp. 576-596.

[55] Gawlik, E. S., J. E. Marsden, S. Campagnola and A. Moore, "Invariant Manifolds, Discrete Mechanics, and Trajectory Design for a Mission to Titan," AAS 09-226, AAS/AIAA Spaceflight Mechanics Meeting, Savannah, Georgia, February 2009.

[56] Szebehely, V., *Theory of Orbits*, Academic Press, New York, 1967.

[57] Tapley, B. D., B. E. Schutz and G. H. Born, *Statistical Orbit Determination*, Elsevier Academic Press, New York, 2004.

[58] Parker, T. S. and L. O. Chua, *Practical Numerical Algorithms for Chaotic Systems*, Springer-Verlag, New York, 1989.

[59] Guckenheimer, J. and P. Holmes, *Nonlinear Oscillations, Dynamical Systems, and Bifurcations of Vector Fields*, Springer, New York, 1983.

[60] Conley, C. C., "Low Energy Transit Orbits in the Restricted Three-Body Problem," *Society for Industrial and Applied Mathematics Journal on Applied Mathematics*, Vol. 16, 1968, pp. 732-746.

[61] Koon, W. S., M. W. Lo, J. E. Marsden and S. D. Ross, "Heteroclinic Connections Between Periodic Orbits and Resonance Transitions in Celestial Mechanics," *Chaos*, Vol. 10, No. 2, June 2000, pp. 427-469.

[62] Villac, B. F. and D. J. Scheeres, "On the Concept of Periapsis in Hill's Problem," *Celestial Mechanics and Dynamical Astronomy*, Vol. 90, 2004, pp. 165-178.

[63] "Cassini Solstice Mission," [HTTP://SATURN.JPL.NASA.GOV, Accessed March, 2011]

[64] Davis, D. C., C. E. Patterson and K. C. Howell, "Solar Gravity Perturbations to Facilitate Long-Term Orbits: Application to Cassini," AAS 2007-275, AAS/AIAA Astrodynamics Specialist Conference, Mackinac Island, Michigan, August 2007.

[65] Haapala, A. and K. C. Howell, "Trajectory Design Using Periapse Poincaré Maps and Invariant Manifolds," AAS 2011-131, AAS/AIAA Spaceflight Mechanics Meeting, New Orleans, Louisiana, February 2011.

[66] Yagasaki, K., "Sun-perturbed Earth-to-Moon Transfers with Low Energy and Moderate Flight Time," *Celestial Mechanics and Dynamical Astronomy*, Vol. 90, 2004, pp. 197-212.

[67] García, F. and G. Gómez, "A Note on Weak Stability Boundaries," *Celestial Mechanics and Dynamical Astronomy*, Vol. 97, 2007, pp. 87-100.

[68] Sousa Silva, P. A. and M. O. Terra, "Dynamical Properties of the Weak Stability Boundary and Associated Sets," *Journal of Physics: Conference Series*, Vol. 246, No. 1, 2010, pp. 1-18.

[69] Sousa Silva, P. A. and M. O. Terra, "Applicability and Dynamical Characterization of WSB Associated Sets in the Lunar SOI," [http://www.scribd.com/doc/44546495/Applicability-and-dynamical-characterization-of-WSB-associated-sets-in-the-lunar-SOI, Accessed April 2011]

[70] Howell, K. C., J. M. Longuski, D. C. Davis, C. E. Patterson, M. Kakoi, J. Chen, M. Okutsu and C. H. Yam, "Encore and End-of-Life Options for the Cassini Spacecraft," *Final Report JPL 1283234, prepared for the Jet Propulsion Laboratory*, February 2007.

[71] Yam, C. H., D. C. Davis, J. M. Longuski and K. C. Howell, "Saturn Impact Trajectories for Cassini End-of-Mission," *Journal of Spacecraft and Rockets*, Vol. 46, No. 2, March-April 2009, pp. 353-364.

[72] Yam, C. H., *Design of Missions to the Outer Planets and Optimization of Low-Thrust, Gravity-Assist Trajectories via Reduced Parameterization*, Ph.D. Dissertation, Purdue University, May 2008.

[73] Byrnes, D. V. and L. E. Bright, "Design of High Accuracy Multiple Flyby Trajectories Using Constrained Optimization," *Advances in the Astronautical Sciences*, Vol. 90, No. 1, 1995, pp. 121-134.

[74] Okutsu, M., C. H. Yam, J. M. Longuski and N. J. Strange, "Cassini End-of-Life Escape Trajectories to the Outer Planets," AAS 2007-258, AAS/AIAA Astrodynamics Specialist Conference, Mackinac Island, Michigan, August 2007.

[75] Ozimek, M. T., D. J. Grebow and K. C. Howell, "Design of Solar Sail Trajectories with Applications to Lunar South Pole Coverage," *Journal of Guidance, Control, and Dynamics*, Vol. 32, No. 6, November-December 2009, pp. 1884-1897.

[76] Howell, K. C., M. Beckman and C. E. Patterson, "Representations of Invariant Manifolds for Applications in Three-Body Systems," *Journal of the Astronautical Sciences*, Vol. 54, No. 1, January-March 2006, pp. 69-93.

[77] Howell, K. C. and H. J. Pernicka, "Numerical Determination of Lissajous Trajectories in the Restricted Three-Body Problem," *Celestial Mechanics*, Vol. 41, 1988, pp. 107-124.

[78] Sweetser, T. H., "An Estimate of the Global Minimum ΔV Needed for Earth-Moon Transfer," AAS 91-101, AAS/AIAA Spaceflight Mechanics Meeting, Houston, Texas, February 1991.

[79] Parker, J. S., "Targeting Low-Energy Ballistic Lunar Transfers," AAS George H. Born Symposium, Boulder, Colorado, May 2010.

[80] Johannesen, J. R. and L. A. D'Amario, "Europa Orbiter Mission Trajectory Design," AAS 99-360, AAS/AIAA Astrodynamics Specialists Conference, Girdwood, Alaska, August 1999.

[81] Sweetser, T. H., R. Maddock, J. R. Johannesen, J. Bell, P. Penzo, A. A. Wolf, S. Williams, S. Matousek and S. Weinstein, "Trajectory Design for a Europa Orbiter Mission: A Plethora of Astrodynamic Challenges," AAS 97-174, AAS/AIAA Spaceflight Mechanics Meeting, Huntsville, Alabama, February 1997.

[82] Wolf, A. A., "Touring the Saturnian System," *Space Science Reviews*, Vol. 104, No. 1-4, 2002, pp. 100-128.

[83] Sims, J. A., J. M. Longuski and A. J. Staugler, "V_∞ Leveraging for Interplanetary Missions: Multiple-Revolution Orbit Techniques," *Journal of Guidance, Control, and Dynamics*, Vol. 20, No. 3, May-June 1997, pp. 409-415.

[84] Campagnola, S. and R. P. Russell, "The Endgame Problem Part 1: V-infinity Leveraging Technique and Leveraging Graph," *Journal of Guidance, Control, and Dynamics*, Vol. 33, No. 2, March-April 2010, pp. 463-475.

[85] Strange, N. J. and J. A. Sims, "Methods for the Design of V-Infinity Leveraging Maneuvers," AAS 2001-437, AIAA/AAS Astrodynamics Specialist Conference, Quebec City, Canada, July-August 2001.

VITA

VITA

Diane Elizabeth Craig Davis received her Bachelor of Science degree in Physics from Texas A&M University in 1999. She then studied astrodynamics at the University of Texas at Austin, graduating with a Master of Science in Engineering degree in Aerospace Engineering in 2001. Her master's thesis considered the nongravitational forces acting on the satellites of the Global Positioning System. Diane studied control systems through the Mechanical Engineering program at Georgia Tech Lorriane in Metz, France, in 2001-2002. In July 2002, Diane joined the Inner Planet Navigation group at the Jet Propulsion Laboratory in Pasadena, California. From 2002-2005, she performed navigation and orbit determination for the Mars Premier Netlander Mission, Mars Express, Rosetta, Genesis, Deep Impact, and Phoenix missions. In August of 2005 Diane started work on her Ph.D. in Astrodynamics and Space Applications in the department of Aeronautics and Astronautics at Purdue University.